UNIVERSITY OF CALIFORNIA,
IRVINE

Modeling physiological oscillations in a biologically constrained CA1 network from two perspectives: full-scale parallel network and rationally reduced Network Clamp

DISSERTATION

submitted in partial satisfaction of the requirements
for the degree of

DOCTOR OF PHILOSOPHY

in Biomedical Sciences

by

Marianne Bezaire

Dissertation Committee:
Professor Ivan Soltesz, Chair
Professor Alan Goldin
Professor Jeffrey Krichmar

2015

DEDICATION

To my husband Jeremy and my daughter Madeleine.

TABLE OF CONTENTS

LIST OF FIGURES

LIST OF TABLES

ACKNOWLEDGMENTS

I would like to thank the professors, teachers, and other students who have helped me along the way, as well as my husband, family, and friends.

Specifically, I thank my advisor and department chair, Professor Ivan Soltesz, for consistently guiding and supporting me throughout this project, and for instilling proper appreciation of interneurons. In addition, the contributions of my dissertation committee, Professors Alan Goldin and Jeffrey Krichmar, along with the additional members of my advancement committee, Professors Craig Stark and Xiangmin Xu, have been valuable and much appreciated. The current and past members of the Soltesz Lab have also played a central role in my development as a scientist and modeler. I would also like to thank the developers of the NEURON simulation software, Professors Michael Hines and Ted Carnevale, for their timely and constant support over the years. I thank those who have written me letters in support of my graduate student funding and admissions, including my advisor Professor Soltesz and Professors Jill Leutgeb, Michael Cahalan, Al Goldin, Ted Carnevale, Craig Stark, Karl Bohringer, Ted Lee, and my very supportive undergraduate research advisor Joseph Miller.

I thank my husband, Jeremy Bezaire, for his invaluable support, which came in many forms throughout the years of this project. My family and friends have also encouraged me throughout the years, and I appreciate their presence in my life.

Both the National Institutes of Health (the National Institute of Neurological Disorders and Stroke) and the National Science Foundation have supported my work. I have received funding from an NSF Graduate Research Fellowship (DGE-0808392 to me) as well as supercomputing time via the NSF-supported XSEDE program (startup allocations to me and Ivan Soltesz; research allocation to Ivan Soltesz). I was also supported by the Interdepartmental Gateway Neuroscience Program and an NIH grant (NS35915 to Ivan Soltesz).

My modeling work has been carried out on the supercomputers Stampede and Ranger at University of Texas, Trestles at San Diego Supercomputing Center and BDUC and HPC at University of California at Irvine.

Portions of Chapters 2 and 3 of this thesis/dissertation are a reprint of the material as it appears in Hippocampus. The co-author listed in this publication directed and supervised research which forms the basis for the thesis/dissertation. Portions of Figure 5.9a were adapted with original authors' permission from *Science*, Vol 321, Klausberger and Somogyi, *Neuronal Diversity and Temporal Dynamics: The Unity of Hippocampal Circuit Operations*, Figure 2, 2008. Reprinted with permission from AAAS. Experimental ivy cell histogram adapted from *Neuron*, Vol 57, Fuentealba et al., *Ivy Cells: A Population of Nitric-Oxide-Producing, Slow-Spiking GABAergic Neurons and Their Involvement in Hippocampal Network Activity*, Figure 5B, Copyright 2008, with permission from Elsevier. Experimental neurogliaform cell histogram from *Journal of Neuroscience*, Vol 30, Fuentealba et al., *Expression of COUP-TFII nuclear receptor in restricted GABAergic neuronal populations in the adult rat hippocampus*, Figure 6F, Copyright 2010, with permission.

CURRICULUM VITAE

Marianne Bezaire

EDUCATION

Doctor of Philosophy in Biomedical Sciences **2015**
University of California, Irvine *Irvine, California*

Bachelor of Science in Chemical Engineering **2005**
University of Southern California *Los Angeles, California*

RESEARCH EXPERIENCE

Graduate Student Researcher **2009–2015**
University of California, Irvine *Irvine, California*

Research Engineer **2005**
University of Washington *Seattle, Washington*

Research Intern **2004**
University of Washington *Seattle, Washington*

Research Assistant **2003–2005**
University of Southern California *Los Angeles, California*

WORK EXPERIENCE

Senior Associate Clinical Systems **2008–2009**
Amgen, Inc *Thousand Oaks, California*

Associate Clinical Systems **2006–2008**
Amgen, Inc *Thousand Oaks, California*

REFEREED JOURNAL PUBLICATIONS

Sokolova IV, Schneider CJ, Bezaire M, Soltesz I, Vlkolinsky R, Nelson GA. Proton Radiation Alters Intrinsic and Synaptic Properties of CA1 Pyramidal Neurons of the Mouse Hippocampus. **2015**
Radiation Research (2015) 183(2):208-218.

Varga C, Oijala M, Lish J, Szabo GG, Bezaire M, Marchionni I, Golshani P, Soltesz I. Functional fission of parvalbumin interneuron classes during fast network events. **2014**
eLife (2014) 3.

Lee SH, Marchionni I, Bezaire M, Varga C, Danielson N, Lovett-Barron M, Losonczy A, Soltesz I. Parvalbumin-positive basket cells differentiate among hippocampal pyramidal cells. **2014**
Neuron (2014) 82(5):1129-1144.

Bezaire MJ, Soltesz I. Quantitative Assessment of CA1 Local Circuits: Knowledge Base for Interneuron-Pyramidal Cell Connectivity. **2013**
Hippocampus (2013) 23(9):751-785.

Schneider CJ, Bezaire M, Soltesz I. Toward a full-scale computational model of the rat dentate gyrus. **2012**
Frontiers in Neural Circuits (2012) 6:83.

Case MJ, Morgan RJ, Schneider CJ, Soltesz I. Computer Modeling of Epilepsy. **2012**
Jasper's Basic Mechanisms of the Epilepsies, 4th edition.

Case M, Soltesz I. Computational modeling of epilepsy. **2011**
Epilepsia (2011) 52 Suppl 8:12-5

Case M, Soltesz I. Discreet charm of the GABAergic bourgeoisie: superconnected cells conduct developmental symphonies. **2009**
Neuron (2009) 64(6):780-782

Shastry A, Case MJ, Bohringer KF. Directing Droplets using Microstructured Surfaces. **2006**
Langmuir (2006) 22(14):6161-6167

Case MJ, Shastry A, Bohringer KF. Towards understanding contact angle hysteresis behavior of textured surfaces. **2005**
Journal of Undergraduate Research in Bioengineering (2005) 5:10-14

REFEREED CONFERENCE PUBLICATIONS

Bezaire MJ, Burk K, Soltesz I. Large-scale parallel computer model of the CA1 network: Insights into oscillatory interneuronal discharges. **2014**
International UC Irvine Epilepsy Research Center Symposium. Newport Beach, CA

Bezaire MJ, Burk K, Soltesz I. Mechanisms of interneuronal control of spontaneous oscillations in a large-scale parallel computer model of the CA1 network. **2014**
Joint Symposium on Neural Computation. Irvine, CA

Bezaire MJ, Burk K, Soltesz I. Biologically constrained CA1 model network produces physiological oscillations. **2014**
Annual Conference on the Neurobiology of Learning and Memory. Irvine, CA

Bezaire MJ, Burk K, Soltesz I. Using the NSG with a large-scale parallel computer model of the CA1 network: a case study **2014**
CNS. Quebec City, Canada

Bezaire MJ, Soltesz I. Big Data-driven full-scale parallel computer model of the CA1 network: Insights into oscillatory interneuronal discharges. **2013**
Society for Neuroscience. San Diego, CA.

Vlkolinsky R, Sokolova IV, Schneider C, Bezaire M, Soltesz I, Nelson G. Long-term changes in neuronal excitability produced by low-dose radiation. Society for Neuroscience. San Diego, CA. 2013 **2013**
Society for Neuroscience. San Diego, CA.

Bezaire MJ, Soltesz I. Interneuron type-specific contributions to CA1 network activity in a data-driven computer model **2013**
Joint Symposium on Neural Computation. Pasadena, CA.

Bezaire MJ, Soltesz I. Interneuron type-specific contributions to CA1 network activity in a data-driven computer model. **2012**
Society for Neuroscience. New Orleans, LA.

Case MJ, Soltesz I. Network mechanisms contributing to CA1 pyramidal cell subthreshold membrane potential oscillation. **2012**
Joint Symposium on Neural Computation. Riverside, CA.

Case MJ, Soltesz I. Computer modeling to understand the role of interneurons in physiological hippocampal functions. **2011**
Gordon Conference on Inhibition in the CNS. Waterville, ME.

Case MJ, Schneider CJ, Soltesz I. Parallel Computing Enables Full-Scale Modeling of the Rat Dentate Gyrus. Joint Symposium on Neural Computation. **2010**
Joint Symposium on Neural Computation. Los Angeles, CA.

Case MJ, Soltesz I. Spatial Processing in a Biologically Realistic Model of the Rat Dentate Gyrus. **2010**
Gordon Conference on the Neurobiology of Cognition. Waterville Valley, NH.

Shastry A, Case MJ, Bhringer KF. Engineering texture to manipulate droplets in microfluidic systems. **2005**
MEMS , Miami, FL

Case M, Miller JD, et al. Martian circadian rhythms: A Biosignature? **2004**
Society for Research on Biological Rhythms. Vancouver, BC.

Case M, Miller JD, et al. Mars, methane and circadian rhythms. **2004**
International Symposium on Optical Science and Technology, 49th annual meeting of SPIE. Denver, CO.

Case MJ, Miller JD, et al. Hippocampal neurogenesis and the development of circadian rhythms in locomotor and ingestive behavior in MAO knockout mice. **2004**
Society for Neuroscience Abstracts. Washington, DC.

SOFTWARE

SimTracker
`http://mariannebezaire.com/simtracker/`
MATLAB-based GUI that enables efficient design, execution, analysis, documentation, and communication of simulations

Superdeep NEURON Template
`http://senselab.med.yale.edu/ModelDB`
ModelDB entry for CA1 microcircuit model, #153280

CA1 Open Source Brain Entry
`http://opensourcebrain.org/projects/nc_ca1`
Open Source Brain entry for CA1 model

Superdeep Open Source Brain Entry
`http://opensourcebrain.org/projects/nc_superdeep`
Open Source Brain entry for CA1 microcircuit model

Bitbucket Account
`http://bitbucket.org/mbezaire`
Account for Mercurial repositories of all my code

WEBSITES

Blog
`http://mariannebezaire.com`
Professional blog about programming and neuroscience related matters

Quantitative Assessment
`http://www.ivansolteszlab.org/quantitativeassessment.html`
Graphical tour of the calculations and strategies used in the quantitative assessment

Model Explorer
`http://ivansolteszlab.org/modeling.html`
Documentation of each model, including links to code, results, analysis tools, and model characterization

ABSTRACT OF THE DISSERTATION

Modeling physiological oscillations in a biologically constrained CA1 network from two perspectives: full-scale parallel network and rationally reduced Network Clamp

By

Marianne Bezaire

Doctor of Philosophy in Biomedical Sciences

University of California, Irvine, 2015

Professor Ivan Soltesz, Chair

I developed a full-scale, biologically constrained model of hippocampal CA1 subfield that is capable of spontaneous theta and gamma oscillations with distinct interneuronal phase preferences. In addition to structural constraints on the cell numbers and connectivity, experimental observations drove the development of the electrophysiology for the nine cell types and their synapses. To characterize and experimentally constrain the model, I designed and developed a custom software tool called SimTracker. SimTracker works with my NEURON code template to enable efficient coding, simulation design and execution, and analysis of results for parallel network NEURON simulations. I also created the Network Clamp, a software tool that implements the concept of a rational method for reducing a full-scale parallel network model to a small, yet biologically constrained model whose simulations can be run on a personal computer. Here I characterize the physiological oscillations displayed by the model. Additionally, I explore the parameter-space of the model by studying its oscillatory properties while manipulating its connectivity, excitation level, and synapse kinetics. This dual approach model is well characterized, flexible and accessible, and it represents a useful collation of experimental knowledge as well as a significant technical advance in neural network modeling.

Chapter 1

Introduction

In this work, I tested the hypothesis that an anatomically and electrophysiologically constrained computer model of CA1, when given tonic excitation, can induce and maintain spontaneous theta oscillations with distinct phase preferences for each cell type. Hippocampal theta oscillations (4-12 Hz rhythmic fluctuations present in the local field potential) are important to learning and memory, and their generation and maintenance are of great interest. Several experimental preparations in vivo, and in vitro (both in hippocampal slices and isolated CA1) can produce theta oscillations. Therefore, I hypothesized that a detailed, biologically constrained, full scale model of CA1 with realistic connectivity and diverse cell types could also produce this theta rhythm. In this work, I discuss how I constrained my model and show how my constrained model is capable of generating spontaneous theta rhythms. In addition, I present the custom software I developed to manage the model constraints, simulations, and analysis of results.

1.1 Background

The hippocampus supports diverse cognitive tasks including learning, memory, and spatial processing. While performing these tasks, hippocampal neurons display a distinct pattern of membrane potential oscillations known as theta. In rodents, theta is a 4-12 Hz oscillation visible in the local field potential (LFP) (Lee et al., 1994) as well as in the firing probabilities of the hippocampal neurons (Klausberger and Somogyi, 2008). Theta occurs *in vivo* in awake and anesthetized animals, as well as in animals in the REM stage of sleep. It is also displayed *in vitro* in several hippocampal preparations, clearly involving distinct mechanisms.

In vivo, the medial septum is thought to drive the hippocampal theta rhythm (Bullock et al., 1990; Villette et al., 2010; Kowalczyk et al., 2013). Cholinergic cells in the medial septum provide slow depolarization to CA1, while GABAergic projections from the septum provide rhythmic inhibition to CA1 at the theta frequency (Lee et al., 1994). Lesions to or inactivation of the medial septum have been shown to abolish theta in vivo (Andersen et al., 1979; Givens and Olton, 1990; Soltesz and Deschenes, 1993), while stimulation of the medial septum can drive theta activity (Monmaur and Breton, 1991).

However, theta oscillations can also be seen in CA1 independent of septal inputs. For example, an isolated, full hippocampal CA1 preparation (Goutagny et al., 2009) can exhibit theta. This spontaneous oscillation indicates the CA1 network is predisposed to oscillate within the theta frequency range. Careful study of theta in other *in vitro* hippocampal preparations also supports the idea that the hippocampus may be capable of internally-generated theta (Kowalczyk et al., 2013).

The network mechanisms that enable theta (or disrupt theta in disease) are of great interest. Therefore, I chose to investigate how an isolated CA1 network might develop and sustain a theta rhythm. I built a detailed, biologically constrained computer model of an isolated CA1 network with distinct interneuron types and tested whether it was capable of producing

a spontaneous theta oscillation with distinct interneuron firing phase preferences. I found that it was capable of a theta oscillation given a tonic, arrhythmic excitatory input. I then subjected the model to various perturbations to determine the robustness of the theta activity and to characterize the role of specific network components in the theta rhythm. Finally, I compared this spontaneous theta with experimental observations of *in vivo* theta to hypothesize whether similar mechanisms were involved in the generation of both rhythms.

1.2 Specific Aims

My work accomplished three specific aims. First, I tested the hypothesis that an anatomically and electrophysiologically constrained computer model of CA1, when given tonic excitation, could induce and maintain spontaneous theta oscillations. To test this idea, I assembled the existing anatomical data about CA1 (Bezaire and Soltesz, 2013), which included realistic proportions of eight interneuron types and realistic connectivity between each type. I also consulted existing electrophysiological resources (the NeuroElectro database at `www.neuroelectro.org/`, single and paired cell electrophysiological data from other lab members, and published data about synaptic connections and ion channels) to constrain the electrophysiological properties of the model. Then I experimented with different levels of excitation to the model and found that tonic excitation to the full-scale CA1 model was sufficient for the network to develop theta and gamma rhythmic spiking. Multiple areas of the parameter space produced theta.

Next, I hypothesized that the interneuron type-specific electrophysiological and network properties were sufficient for each cell type to display a distinct preferred firing phase during theta oscillations. I found that distinct cell types showed distinct firing phases, a phenomenon also seen *in vivo* (Varga et al., 2012; Klausberger and Somogyi, 2008)

Finally, to accomplish my other two aims efficiently and to enable others to reproduce and build on my work, I designed and developed a user-friendly software package called SimTracker. SimTracker is a MATLAB-based software program that enables designing, executing, organizing, and analyzing simulations efficiently. It also interfaces with supercomputers and produces figures, tables, and websites for communicating results. Users do not need to buy a MATLAB license to use the SimTracker, and SimTracker is available for Windows, Mac, or Linux users.

1.3 Significance

Theta is a 4-12 Hz oscillation in the local field potential (LFP), present in a variety of animals including rodents and humans (Lee et al., 1994). Within CA1, theta is strongest in the stratum lacunosum-moleculare (Buzsáki, 2002). The phase of theta shifts across the layers of CA1 as a function of depth, achieving a 180^o difference between stratum lacunosum-moleculare and stratum pyramidale (Buzsáki, 2002). The LFP depends mostly on synaptic currents and general membrane conductance, with only a small component due to spiking. However, theta also modulates the spiking of many neuron types in CA1 (Klausberger and Somogyi, 2008).

Theta has been linked to learning, exploration, and recall of previously stored memories (Wang, 2010; Hasselmo, 2005). Theta is thought to help organize and segregate information. Specifically, Hasselmo et al. (2002) proposed that theta may organize encoding and retrieval functions of the hippocampus, separating them in time. Recent experimental evidence supports this proposition. Siegle and Wilson (2014) showed that optogenetic stimulation during theta rhythm differentially enhances encoding or retrieving functions, depending on the phase of stimulation. This separation appears to be necessary; theoretical studies have shown it is not possible for both processes to occur at the same time, in the same network, without

interference (Hasselmo et al., 2002), and this requirement of task separation has recently been pursued experimentally. Douchamps et al. (2013) found that disrupting cholinergic modulation of the theta rhythm, which has traditionally been thought to mediate the separation between encoding and retrieval functions, decreases the encoding of novel spatial environments.

Further, deficits in theta have been associated with deficits in learning, recall, and spatial processing. For example, a study of the effects of seizures on theta and spatial processing found a correlation between reduced theta power and deficits in spatial task performance (Chauvière et al., 2009). In addition, temporary inactivation of the medial septum that reduced hippocampal theta power also reduced performance in a spatial working memory task (Givens and Olton, 1990).

Theta is not specific to rodents; it has been observed in humans during both spatial (Kahana et al., 1999) and non-spatial tasks (Tesche and Karhu, 2000; Axmacher et al., 2010; Lega et al., 2012). In a pioneering study of theta in the human hippocampus, Ekstrom et al. (2005) showed that theta power increased during movement compared to standing still. Watrous et al. (2013) compared human and rat hippocampal low-frequency oscillations during spatial navigation, finding that humans have a lower oscillation frequency (3.4 Hz) than rats (8 Hz), as had been suggested by other studies (Lega et al., 2012). However, the human experiments were performed using virtual reality, which is associated with a decrease in oscillation frequency in rats, so it is possible that during real navigation humans would exhibit a slightly higher frequency of oscillation.

Also, theta oscillations are generally slower in larger animals and so it may be consistent with that trend for humans to have the slower theta oscillation (Lega et al., 2011). A human memory free recall task found a prominent 3 Hz theta oscillation whose power was correlated with correct responses to the task (Lega et al., 2011). They also found a higher frequency theta oscillation (around 8 Hz) whose function was not as clear. Fell et al. (2011) saw an

increase in theta band (4-8 Hz) hippocampal EEG power that was correlated with correct functioning on a memory task. In addition, Rutishauser et al. (2010) found that the spike timing of individual neurons correlated with function on a memory task: the more correlated the spike timing was to the local theta rhythm, the better the subjects performed on a memory task. Finally, Guderian et al. (2009) found higher amplitude theta oscillations prior to word presentation correlated with better memory performance later.

1.3.1 The Role of the Model

Any model is necessarily a simplified view of reality. The simplification is the model's power; the model is a tool generally used to illustrate the importance of the included characteristics (or the converse) to the behavior under study. In this work, we chose to focus on intrinsic network mechanisms. Though it is known that CA1 receives phasic input during theta (Mizuseki et al., 2009), recent optogenetic studies have shown that the oscillation in CA1 is not entirely determined by its afferents. By focusing on network properties within our CA1 network model, we systematically examined the role of various characteristics in the development and maintenance of theta.

Further, generating a highly constrained model forced us to take stock of the experimental data available. The exercise highlighted gaps in our experimental knowledge as well as provided a venue for collating experimental data for general use. Much of the anatomical data we assessed gains value and explanatory power when combined or compared to other data, as we have done in our quantitative assessment (Bezaire and Soltesz, 2013).

This detailed modeling is most effective when executed iteratively with experiments. Model results can generate new hypotheses to test experimentally. In this case, the results can refine our theory of theta and also help focus and choose the most efficacious experiments to carry out. Using a model allowed a precise and complete control over which parameters

we manipulated and to what extent. This gave us much more power than current experimental techniques and was also much faster. Therefore, models represent a useful tool for experimentalists, one that can help us achieve an overall goal of verifying a hypothesis in a physiologically relevant, biological preparation.

1.4 Experimental observations

1.4.1 Hippocampal theta in experimental preparations

in vivo

In vivo, the medial septum is thought to drive the hippocampal theta rhythm (Bullock et al., 1990; Villette et al., 2010; Kowalczyk et al., 2013). Cholinergic cells in the medial septum mainly excite pyramidal cells, while reciprocal GABAergic projections between the medial septum interneurons and the hippocampal interneurons drive the neurons of the hippocampus at the theta frequency (Lee et al., 1994). Lesions to or inactivation of the medial septum have been shown to abolish theta in vivo (Andersen et al., 1979; Givens and Olton, 1990), while stimulation of the medial septum can drive theta activity (Monmaur and Breton, 1991).

However, there have been some surprising results from a recent optogenetic study that drove septal neurons at specific frequencies and then observed their ability to entrain CA1 neurons (Ducharme et al., 2013). This study demonstrated the limits of septal control of CA1 theta, as CA1 theta behavior could be only partly attributed to septal activity, and CA1 did not always respond robustly to frequencies imposed by the septal inputs (but see Brandon et al. (2013)). Further, several groups have shown methods of obtaining theta oscillations in the absence of the medial septum (or in *in vitro* preparations), so it appears that the hippocam-

pus may be predisposed to oscillate within the theta range of frequencies. In addition, it has been found that GABAergic backprojections from the subiculum to the hippocampus can also drive theta (Jackson et al., 2014). Careful study of theta in *in vitro* hippocampal preparations also supports the idea that the hippocampus may be capable of internally-generated theta (Kowalczyk et al., 2013).

In both awake and anesthetized animals, different cell types prefer to fire at different phases during theta rhythm (Varga et al., 2012; Klausberger and Somogyi, 2008). The preferred phases vary somewhat depending on the state of the animal, and different phases have also been found by different laboratories (Table 1.1). These distinct phase preferences are likely to be a central feature that enables theta to support learning, memory, and spatial processing. Not only do various interneuron types supply precise inhibition to pyramidal cells in terms of anatomical location on the pyramidal cell, but the distinct phase preferences enable the interneurons to also supply precise inhibition in terms of timing.

in vitro

In an *in vitro* preparation, Konopacki et al. (1987) showed that the hippocampus is capable of producing theta oscillations independent of pulsed, rhythmic inputs from other brain regions. They applied carbachol, a cholinergic receptor agonist, to hippocampal slices and recorded the LFP from the granule or molecular layer of the dentate gyrus. Using the same preparation, Williams and Kauer (1997) located the theta generator in CA3 and observed that NMDA receptors were necessary to propagate theta to CA1. They also argued that carbachol-induced theta and *in vivo* theta were generated by fundamentally different mechanisms. Gillies et al. (2002) elaborated on this criticism, observing that carbachol-induced theta is independent of interneurons, but *in vivo*, theta is accompanied by strong interneuron activity (Soltesz and Deschenes, 1993).

As a more physiologically relevant alternative to carbachol-induced theta, Gillies et al. (2002) activated metabotropic glutamate receptors (mGluRs) and reduced AMPA receptor (AMPAR) activation to generate theta in CA1 independent of CA3 and other afferent activation. This theta persisted in the presence of atropine (a mAChR antagonist), so it also appeared to be independent of cholinergic mechanisms; instead, it seemed to be caused by an inhibitory network mechanism. Various network activity characteristics correlated with stratum oriens interneuron spiking; the stratum oriens interneurons seemed to have intrinsic theta generating mechanisms, and their activity was necessary for the field theta and theta-related IPSP trains.

Most relevant to my work, Goutagny et al. (2009) created an isolated, full CA1 subfield preparation in which they could elicit a spontaneous theta rhythm by applying a mild, tonic depolarization. The rhythm was detectable in the intracellular membrane potential of the pyramidal cells and interneurons, as well as the local field potential. This preparation received no input from the CA3, entorhinal cortex, or medial septum, suggesting that a full, intact CA1 was sufficient to produce theta oscillations. In identical conditions in slices, the authors were not able to detect a theta rhythm, underscoring the importance of having the entire network intact to elicit the rhythm. However, rhythmic oscillation attributed to theta could also be due to poor oxygenation, a problem in many preparations (Hajos et al., 2009). This criticism was somewhat mitigated in an earlier work that observed a slower spontaneous oscillation (around 3 Hz) and found no damage in explicit tests for damage due to poor oxygenation (Wu et al., 2002).

Given the variety of methods capable of producing the theta rhythm, there may be multiple mechanisms of theta. Several pieces of experimental evidence suggest that multiple mechanisms exist, such as the finding that theta is a traveling wave in the hippocampus, due to the difference in preferred oscillation frequency from septal to temporal poles (Lubenov and Siapas, 2009), the finding of multiple generators in the full, isolated CA1

preparation (Hajos et al., 2009), and the presence of layer-specific differences in theta power, coherence, and phase (Montgomery et al., 2009). Even in humans, there is evidence for multiple mechanisms: Watrous et al. (2011) found that variation in theta power in different electrodes was differentially correlated with movement speed, task, and view, while Mormann et al. (2008) found a gap in synchrony between the entorhinal cortex and the hippocampus in both the theta and delta bands, suggesting that there are multiple theta generators.

Given the likelihood of multiple theta generators existing and of there being multiple mechanisms for theta, it follows that theta properties such as the dominant frequency, the oscillation power, and even the phase preferences or firing rates of each neuron type may vary across the preparations that exhibit theta rhythm.

1.4.2 Interneurons in theta

The interneurons of the CA1 are generally modulated by the theta rhythm and are more likely to fire during certain phases of the rhythm, with each interneuron type having a distinct preferred phase preference (Klausberger and Somogyi, 2008).Interneuron types also exhibit distinct firing rates during theta. These firing rates and phase preferences are somewhat dependent on the state of the animal. For example, though theta can be seen in the animals both during anesthesia (urethane with ketamine and xylazine) (Klausberger et al., 2003; 2004; 2005; Fuentealba et al., 2008a; 2010) and in awake, head-fixed or freely moving animals (Varga et al., 2012; Lapray et al., 2012), the firing phase preferences shift slightly, and the interneurons fire more in the awake states (Table 1.1).

Cell Type	Firing Rate (Hz) Theta	Non	SWR	Theta Phase (^{o})	State of Animal	Ref.
ADI	8.60	0.06	0.25	156	anesth: u+k & x	Klausberger et al. (2005)
Axo-axonic	17.10	3.50	2.95	185	anesth: u+k & x	Klausberger et al. (2003)
Bistratified	5.90	0.90	42.80	1	anesth: u+k & x	Klausberger et al. (2004)
CCK+ Basket	9.40	1.60	2.70	174	anesth: u+k & x	Klausberger et al. (2005)
Ivy	0.70	1.70	0.80	31	anesth: u+k & x	Fuentealba et al. (2008a)
Ivy	2.80	2.10	5.20	46	awake, free	Lapray et al. (2012)
Ivy	2.40	3.00	6.70		awake, free	Fuentealba et al. (2008a)
NGF	6.00	2.65	2.30	196	anesth: u+k & x	Fuentealba et al. (2010)
O-LM	4.90	2.30	0.23	19	anesth: u+k & x	Klausberger et al. (2003)
O-LM	29.80	10.40	25.40	346	awake, head restraint	Varga et al. (2012)
PPA	5.75	1.95	1.50	100	anesth: u+k & x	Klausberger et al. (2005)
PV+ Basket	7.30	2.74	32.68	271	anesth: u+k & x	Klausberger et al. (2003)
PV+ Basket				234	anesth: u+k & x	Klausberger et al. (2005)
PV+ Basket	21.00	6.50	122.00	289	awake, free	Lapray et al. (2012)
PV+ Basket	25.00	8.20	75.00	307	awake, head restraint	Varga et al. (2012)
Pyramidal				20	anesth: u+k & x	Klausberger et al. (2003)
Trilaminar	0.20	0.10	69.00	trough	anesth: u+k & x	Ferraguti et al. (2005)
Double Proj.	0.90	0.55	26.93	77	anesth: u+k & x	Jinno et al. (2007)
Oriens Retro.	0.53	0.37	53.37	28	anesth: u+k & x	Jinno et al. (2007)
Radiatum Retro.	5.15	1.90	0.70	298	anesth: u+k & x	Jinno et al. (2007)

Table 1.1: Firing rates and theta phase preferences for various cell types in various conditions. Theta phase is relative to the LFP recorded in the pyramidal layer, where 0^o and 360^o are at the trough of the oscillation. non: non-theta/non-SWR state. SWR: sharp wave/ripple. u+k & x: urethane + supplemental doses of ketamine and xylazine.

1.5 Model general strategy and limitations

My strategy was to incorporate a wide array of anatomical (structural) and electrophysiological (functional) constraints when designing my model, and to characterize the model in a structured way, using the same concepts and protocols used by experimentalists to characterize real, biological samples. My goal was to make the model detailed and constrained by biology, with the exception of transient functional phenomena such as plasticity and neuromodulation. While these phenomena are clearly important for the learning and memory functions associated with theta (Bliss et al., 1993; Hasselmo, 2006; Neves et al., 2008), I hypothesized that the stable components of the network should be sufficient to produce a stable oscillation, such that the role of transient phenomena can then be reserved for the encoding and retrieval functions that happen within the framework of the theta oscillation.

Additionally, though the CA1 is expected to receive rhythmic input any time it is displaying theta, I hypothesized that such input may not be necessary to initiate and maintain the oscillation. Instead, the network may be predisposed to oscillate within the theta range, freeing the phasic input from that task. The main function of the phasic input would then not be to enforce theta, but to influence theta frequency and send the information necessary for encoding or retrieving specific memories. Such an arrangement would make the theta oscillation more robust and more sensitive to weak inputs, reminiscent of the putative function of background gamma in enabling the creation of cell assemblies from even weak inputs (Börgers et al., 2005; Kopell et al., 2010).

Also, the model does not include gap junctions. Mixed results have been found when studying the effect on theta frequency and power of blocking, knocking out, or opening gap junctions (Kowalczyk et al., 2013).

However, because of the specific approach and hypothesis, the model in its current state should not be used to study encoding and retrieval functions as in Cutsuridis et al. (2010).

Short and long-term plasticity mechanisms, as well as neuromodulation, should be added prior to any such studies. The model is currently capable of integrating inputs from CA3 and EC, so we hypothesize that the model in its present state may be capable of basic spatial processing in its current state, given adequate spatial input.

1.6 Other models

This work represents a unique approach compared to other models of the hippocampus or oscillations (or both). However, its findings are consistent with those of other models. Previous computer modeling studies have shown that spontaneous oscillations within the theta range can arise in networks that vary in their degree of biological constraint (Neymotin et al., 2011a,b). Neymotin et al. (2011b) produced a 4,200 cell neocortical model based on extended integrate-and-fire neurons connected in a straight-forward manner. Their model produced a 7 Hz theta oscillation mostly visible in the firing patterns of the excitatory cells of the model; the inhibitory neurons did not strongly follow this theta pattern in their spiking. In a more biologically constrained 1,200 cell model of the CA3, Neymotin et al. (2011a) showed that spontaneous oscillations can arise at 8.1 Hz. Their model contained pyramidal, O-LM and basket cells only. When they supplied tonic, random input to all the synapses of the model, an 8.1 Hz theta rhythm developed. This theta is apparently present just as a peak in the power spectrum from their computed LFP; it's not clear whether it is also visible in the spiking patterns of all or some of the cell types. Rotstein et al. (2005) produced a small network of conductance-based neurons, consisting of O-LM and fast-spiking cells, which was able to produce an oscillation within the theta range. In this small scale network, the bidirectional connections between the O-LM and fast-spiking cells were necessary, as was I_h (the hyperpolarization-activated depolarizing current) in the O-LM cells, and some applied, constant, bias current to each cell in the model. This network produced different

theta phase firing preferences for the two classes of cell, as seen experimentally.

Cutsuridis et al. (2010) have also built a model of the CA1 network with theta driven by rhythmic inputs from the medial septum, which they have used to study the role of theta oscillations in learning and memory. They essentially showed how theta in the network could be used to separate the phases of encoding and retrieval. Cutsuridis and Hasselmo (2012) later used this model to study the contributions of CA1 interneurons to the theta rhythm. However, they enforced different firing preferences of the interneurons by stimulating them with two sets of medial septum neurons that were active at opposite phases of the theta cycle, so the different timing of the interneurons was not emergent from the network, but rather explicitly designed and controlled by the stimulation pattern they received.

We hypothesized that an isolated, full-scale, detailed CA1 network model could also exhibit spontaneous theta and gamma rhythms as well as distinct phase preferences for each cell type. We developed a detailed, biologically constrained computer model of CA1 and found that it was capable of a theta oscillation given a tonic, arrhythmic excitatory input. Then we subjected the model to various perturbations to determine the robustness of the theta activity and to characterize the role of specific network components in the theta rhythm. Finally, we developed a reduced model that is small enough to run on a personal computer but still incorporates the biological constraints of network CA1.

Our model differs from these models in a number of specific ways. First, our model provides realistic numbers and strengths of the inputs to each cell, as well as variability in the input received by each cell. We can easily record voltage traces in our cells, see variability in the behavior of our cells, study the activity of the cells by their position and connectivity, or see the specific connections and inputs converging on a cell of interest. Our model provides unprecidented detail, documentation, and flexibility for examining many hypotheses.

1.7 Overview of the dissertation

Now we will delve into the specifics of the model. In general, this means delving into a quantification of CA1, in which we will make reasonable estimates of anatomical properties such as the proportion of each cell type, the total number of excitatory and inhibitory synapses, and the number of boutons in the whole network. Specifically, chapters 2 and 3 discuss the anatomical constraints of the model. They include the work published in Bezaire and Soltesz (2013) as well as some additional calculations required to fully constrain the interneuron-interneuron connectivity. As the data associated with Bezaire and Soltesz (2013) are rather dense, an alternative to understanding the calculation of cell numbers is to walk through the interactive graphic available at `www.ivansolteszlab.org` for an intuitive tour through the data and the assumptions used to generate the estimates of cell numbers. In addition to these population constraints, there are also morphological properties and topological constraints, also discussed in Chapter 3. Next, in Chapter 4, I discuss the electrophysiological constraints of the model.

Chapter 5 moves on to discuss the behavior of the constrained model, specifically its ability to generate and maintain spontaneous theta oscillations. I characterize many properties of the oscillations and compare them with experimental observations. I also explore what happens if the network receives timed or patterned inputs, to see under what conditions the afferents can impose a specific oscillation on the CA1 network.

In Chapter 6, I share the software program and process documentation that I have made publically available to fully document my model and ease its adoption by others who wish to carry it forward. Finally, in Chapter 7, I discuss future steps that may be taken with the model, as well as conclude my defense of my original thesis.

1.8 General methods

All simulations were performed using the NEURON simulation environment (Carnevale and Hines, 2005). We report results here from our full scale network model as well as a reduced Network Clamp approach. We implemented our model in parallel NEURON 7.3, a neural network simulator (Carnevale and Hines, 2005). The model simulations were run with a fixed time step of 0.01 or 0.02 ms, for a simulation duration of 600 or 1000 ms. We executed the model on several supercomputers, including University of Texas' Stampede, San Diego Supercomputing Center's Trestles, and University of California at Irvine's HPC. We used our custom-built, MATLAB-based SimTracker tool to design, execute, organize, and analyze the simulations (Bezaire and Soltesz, 2015). A list of abbreviations used throughout this work is given in Table 1.2

CB	calbindin
CB1R	CB1 cannabinoid receptor
CCK	cholecystokinin
CR	calretinin
COUP-TFII	COUP transcription factor 2
M2R	muscarinic acetylcholine receptor type 2
mGluR1α	metabotropic glutamate receptor type 1α
mGluR8	metabotropic glutamate receptor type 8
nNOS	neuronal nitric oxide synthase
NPY	neuropeptide Y
PV	parvalbumin
SOM	somatostatin
VIP	vasoactive intestinal polypeptide
ADI	Apical dendritic innervating
PPA	Perforant path-associated
SCA	Schaffer Collateral-associated

Table 1.2: List of abbreviations for neurochemical markers and cell types.

1.8.1 Model Development

The model contained one type of pyramidal cell (with either a simple or complex morphology) and eight types of interneurons, including PV+ basket cells, CCK+ basket cells, bistratified cells, axo-axonic cells, O-LM cells, Schaffer Collateral-associated cells, neurogliaform cells, and ivy cells. The behavior of each cell type was characterized using a current injection sweep that matched experimental conditions. Published experimental data and model cell data were generated and compared side by side (see website). Next, cells were connected using double exponential synapses, with each connection comprising a realistic number of synapses (usually 10). Connections were randomly picked from all the cells whose somata were within the axonal extent of the presynaptic cell's soma, in such a way that the bouton distribution of the cell was honored. Potential synaptic locations on the postsynaptic cell were constrained by the known target area of the presynaptic cell.

1.8.2 Stimulation

The stimulation in our model moves the cell potentials away from rest and also away from the chloride reversal potential, which is important to reveal the spontaneous, interneuron-driven oscillation. Because none of the cells spike spontaneously in our network, some stimulation was required.

We constrained the convergence of the stimulating afferents using anatomical data. We also constrained the weight of the stimulation using electrophysiological observations and by maintaining realistic firing rates for the cell types. Because we used experimental data for the constraints, we occasionally refer to our proximal inputs as coming from CA3 and our distal inputs as coming from entorhinal cortex. However, the stimulation was not patterned to resemble actual spike trains from those areas, because the focus of this paper was CA1 network in isolation from rhythmic extra-CA1 influences, though the model is organized so

that these inputs can be added and studied in detail in the future. Instead, we used random, independent Poisson-distributed spike trains. The model cells were connected to a subset of these afferents, such that they received a constant level of excitatory synaptic input.

1.8.3 Model Execution

We used Mercurial code versioning system to maintain our code across personal computers and each supercomputer that we used. With every simulation, we logged the code version used as well as all the parameter values. Simulations were run on several dozen processors (HPC), several hundred processors (Trestles), or several thousand processors (Stampede) as appropriate for the scale of the model. We began with a small scale model and, upon seeing that small networks could produce physiological oscillations, gradually increased the size to full scale while observing the network activity.

1.8.4 Analysis

We subjected each simulation to a standard analysis using our SimTracker tool. We first visually observed the presence or absence of theta or gamma oscillations in the spiking pattern of the network. Then we calculated the Fast Fourier Transform (FFT) to determine the power of any oscillations in the spike timing per cell type. After finding a dominant theta or gamma frequency, we then analyzed the level of modulation and preferred firing phase for each cell type. Finally, we calculated the firing rate of each cell type. We also surveyed all simulations together in a meta-analysis of how theta appeared within the parameter-space.

1.8.5 Accessibility

The model website is `http://www.ivansolteszlab.org/models/ca1.html`. The website includes a graphical tour of the model, links to our model code on ModelDB (published version) and Open Source Brain (working version), and model results for modelers who want to analyze our results without rerunning a simulation.

1.8.6 Network Clamp

Simulations consisted of a detailed pyramidal cell model and simple point process models of local neurons and afferents that synapsed on the pyramidal cell. The somatic voltage of the pyramidal cell was recorded. Data analysis was then performed on the somatic voltage trace. Each simulation lasted 20 s and was run with a fixed time step of 0.1 ms. The simulations were run in serial on a personal computer with 8 GB of RAM.

All analyses of data were performed using custom scripts in MATLAB, version R2014a.

To calculate the phase shifts between oscillations, each somatic voltage trace was subjected to a bandpass filter at 8 Hz. The phase shift was calculated relative to a reference timepoint (t=0) based on the average offset of the peaks of the oscillation. The phase shifts between the control trace and the disinhibited traces were then compared. The power of the oscillation at the theta frequency was computed using a Fast Fourier Transform.

The firing rate was calculated by counting the number of spikes throughout the simulation and dividing by the simulation time. A spike was registered whenever the somatic voltage potential crossed the threshold of -10 mV in the positive (depolarizing) direction.

We attached various presynaptic cells to the pyramidal cell model as described in the remainder of this section. Then we recorded the voltage in the soma and various dendritic

compartments, as well as the currents through the various ion channel mechanisms, and the spiking pattern of the pyramidal cell. These outputs were subjected to various forms of analysis as described in Chapter 5.

Chapter 2

Quantitative Assessment of Neuron Numbers

The CA1 network is one of the most studied areas in the mammalian brain. Both experimentalists and modelers are interested in the roles played by each interneuron type in the function of the CA1 network. As the field progresses in hypothesizing about and testing the roles of various CA1 interneurons and microcircuits, an idea of the relative abundance of each interneuron and its connections with other neurons has become important. To build a truly data-constrained network model, the assembly of a current knowledge base is not just important, but a requirement.

I determined that sufficient information existed about the rat CA1 region to estimate the numbers of most interneuron types. I felt this assessment was necessary to sufficiently constrain the model and also to extract the most value out of existing data. Such an assessment would be useful in modeling and for the field in general, to enable us to better quantify the role of each interneuron type in the network. Therefore, I combined experimental data from over 100 publications to estimate the fraction and absolute number of 16 types of interneu-

rons (Bezaire and Soltesz, 2013), as shown in Figure 2.1. The results of this quantitative assessment of the CA1 have enabled me to better constrain my model network based on biological observations (Table 2.2).

The knowledge base produced here, beyond constraining my model, is broadly useful. It should inspire future projects for two reasons. One, the assessment is a single-frame shot of the state of our collective knowledge. Because of the fast-moving pace of research, it will need to be updated continually in the future. Two, the information would be more accessible in an online database. By publishing the assessment in this form, I hope to lay a framework upon which others can build an online system of sharing and calculating quantitative data.

2.1 Methods of assessment

In determining the relative abundance of each interneuron type, I looked for characteristics that, when combined, uniquely identified a neuron type population. The key attribute that distinguishes the various interneuron types is the axonal arborization pattern, which defines where GABA is being delivered on the distinct axo-somato-dendritic domains of postsynaptic neurons. However, for technical reasons, quantitative neuron counts cannot be made based on axonal arborization alone. Such an approach would require that I visualize and count all neurons of a single subtype within CA1 of a given animal, with each and every neuron's axonal arbor visualized and verified as belonging to that particular neuronal subtype, which is not currently experimentally feasible. Consequently, the calculation of neuron numbers was chiefly based on expression of neurochemical markers. By necessity, I often considered co-expression of a certain marker combination as a signature of a particular interneuron type. Not all interneurons of a given type necessarily express markers reliably enough to be detected, so in general the estimates at which I arrived should be considered lower bounds. After completing my analysis, a small percentage of neurons remained undefined; this number

represents the leeway on the upper bound of the various neuron types plus the contribution of the lesser known neuron types, for which I could not estimate their number.

In some cases I used marker expression by layer to refine my estimates. While layer position is not sufficient to identify neuron types, quantitative data are often layer-specific and could be used as a guide for differentiating similar neuron types. For example, when estimating the numbers of CCK+ neurons other than basket cells, I assumed CCK+ neurons in the stratum lacunosum-moleculare were perforant path-associated cells, while those in the stratum radiatum were Schaffer Collateral-associated or apical dendritic innervating cells.

To arrive at more detailed estimates, I made assumptions about marker expression, laminar distribution, and relative abundance of various neuron types. All assumptions are listed in a separate table (Table 2.1), as well as in the text. In general, I did not account for any gradients or heterogeneity in the distribution of individual neuron types. For example, throughout the calculations I assumed the CA1 was homogenous along the septotemporal axis. I averaged observations made in dorsal and ventral CA1 where available, or in some cases took observations made in the dorsal CA1 to be representative of the entire CA1. I made these simplifications though gradients and heterogeneity in marker expression have been shown for some markers in both principal neurons and interneurons (Kosaka et al., 1987; Nomura et al., 1997a;b; Fuentealba et al., 2010). These simplifications should be revisited in models where dorsal/ventral differences are of interest. Additionally, cellular properties and connectivity can vary as a function of depth within a layer or other factors (Mizuseki et al., 2011a; Slomianka et al., 2011; Graves et al., 2012). Therefore, I made these simplifications because not enough information is available to incorporate these characteristics into our estimates, not because I think that these factors are not important for certain aspects of hippocampal function.

2.2 Estimates of neuron numbers

Combining the results of a vast literature survey and a well-documented list of assumptions (Table 2.1), I arrived at a comprehensive estimate of interneuron numbers by cell type and anatomical layer. The total estimates for each interneuron type by layer are given in Table 2.2 and shown in Figures 2.1 and 2.2. The strategies used to calculate the estimates for each cell type depend on the experimental data available and so they vary for each cell. For an interactive, graphical tour of the calculations, see `www.ivansolteszlab.org`. .

#	**Explicit, Forced Assumption**	**Sec.**
1	**11% of CA1 and CA3 cells are GABAergic interneurons.** Experimental observations range from $7 - 11\%$. We assumed 11% after calculating the number of boutons each interneuron would be required to have for all the interneurons to fully cover the GABAergic synapses on all the pyramidal cells.	2.2.1
2	**CA1 pyramidal cells are homogeneous.** CA1 pyramidal cells vary in many properties as a function of factors such as dorsal/ventral location and depth within the pyramidal layer. However, in the absence of detailed quantitative information about how the pyramidal cell bouton count and dendrites vary with these factors, we considered the data from a few CA1 pyramidal cells as representative of all pyramidal cells.	2.2.2

#	Explicit, Forced Assumption	Sec.
3	**Each CA1 pyramidal cell synapses only once onto each postsynaptic CA1 pyramidal cell.**	3.2.1
4	**Each CA1 pyramidal cell connection onto a CA1 interneuron comprises 3 synapses.**	3.2.1
	We made these assumptions to determine the divergence of each CA1 pyramidal cell. Deuchars and Thomson (1996) studied the anatomy of one pyramidal to pyramidal cell pair that was found to have two synapses, but its amplitude was over twice the average. We concluded that most pyramidal to pyramidal connections comprise one synapse. For CA1 pyramidal cell to interneuron connections, we based our assumption on an observation that CA1 pyramidal cells generally contact O-LM cells with three synapses each (Biro et al., 2005). However, in CA3, some pyramidal cell to basket cell connections included only one synapse (Sik et al., 1993; Gulyás et al., 1993) and the EPSP amplitude range of these connections (Gulyás et al., 1993) was similar to that seen in connections in CA1 (Ali et al., 1998). Yet, current clamp recordings of pyramidal cell to interneuron connections (bistratified and basket cells) in the CA1 revealed a large enough range in EPSP amplitude to suggest that at least some connections may comprise multiple synapses, especially connections onto bistratified cells (Ali et al., 1998).	

#	Explicit, Forced Assumption	Sec.
5	**Observations made in dorsal CA1 are representative of the whole CA1.**	2.1
6	**The expression of COUP-TFII in interneurons dorsally is representative of the whole CA1.** Some properties (marker expression, frequency of certain cell types) vary between dorsal and ventral CA1. Where possible, we averaged values from both sides. In some cases, only dorsal area observations were available. Therefore, our findings will be more representative of the dorsal CA1.	2.2.3

#	Explicit, Forced Assumption	Sec.
7	**All nNOS+/NPY+ cells are either ivy cells or neurogliaform cells.**	2.2.3
8	**All nNOS+/NPY+ cells with somata in the stratum oriens or pyramidale are ivy cells.**	2.2.3
9	**nNOS+/NPY+/reelin+ cells in the stratum radiatum are neurogliaform cells.**	2.2.3
10	**nNOS+/NPY+/reelin- cells in the stratum radiatum are ivy cells.**	2.2.3
11	**All ivy cells are nNOS+/NPY+ with somata in the stratum oriens, pyramidale, or radiatum.**	2.2.3
12	**All α-actinin-2+/CR- cells in the stratum lacunosum-moleculare are neurogliaform cells.**	2.2.3
	We considered nNOS and NPY to generally indicate neurogliaform family cells, though we resorted to different criteria in the stratum lacunosum-moleculare because some nNOS+/NPY+ cells there were found to not be neurogliaform family cells. Ivy and neurogliaform cells have similar marker expression profiles, so we resorted to separating them by layer and reelin expression.	

#	Explicit, Forced Assumption	Sec.
13	**Ivy and neurogliaform cells make 10 classical synapses on each postsynaptic cell.** Most neurogliaform family cell boutons do not participate in classical synapses (i.e., do not have a corresponding postsynaptic element) but instead rely on volume transmission. For our convergence calculations, we found it necessary to assume a number of corresponding postsynaptic elements (classical synapses) for each connection. We based this number on a prediction made about classical synapses on observations of neurogliaform cell to pyramidal cell connections in the neocortex.	3.2.2
14	**All stratum oriens SOM+/CB+ cells projecting to the septum are double projection cells.**	2.2.4
15	**All SOM+ cells projecting to the subiculum are either double projection or oriens-retrohippocampal cells.** Of the projection cells, four types are known to target the subiculum. We separated these into two groups by their SOM expression.	2.2.4

#	Explicit, Forced Assumption	Sec.
16	**Projection interneurons of the stratum oriens with axons in strata oriens and radiatum have the same number of local boutons as do the so-called back projection cells.**	3.2.2
17	**Projection interneurons of the stratum oriens with axons in strata oriens and radiatum have the same laminar distribution of local boutons as do conventional bistratified cells.** For several projection cell types, their cell numbers could be estimated but we had no direct observations of their bouton counts or distribution. Because their axon arbors are similar to those of the so-called back projection cells (both the laminar distribution and the small number of local targets) and conventional bistratified cells (laminar distribution), we used information from those types to estimate total bouton counts and distribution respectively, which enabled us to calculate local convergence.	3.2.2

#	Explicit, Forced Assumption	Sec.
18	**All stratum oriens-specific cell types contact their postsynaptic targets with 10 synapses each.** A light microscopy study of O-LM to pyramidal cell connections showed a range of three to 17 potential synapses per connection (Maccaferri et al., 2000). We took the average of 10 synapses per connection, assuming the potential synapses made actual contact. For projection cells whose axons mainly ramify in the strata radiatum and oriens (formerly known as oriens-bistratified cells), a connection was observed to comprise 10 potential synapses (Maccaferri et al., 2000). Therefore, we assumed that all stratum oriens-specific cells contacted their postsynaptic targets with 10 synapses.	3.2.2
19	**The ratio of PV+ basket cells:bistratified cells:axo-axonic cells within the stratum pyramidale is the same as the ratio in other layers.** In the absence of data about the composition of the PV+ cells in the stratum radiatum and oriens, we assumed they were similar to the stratum pyramidale. Though this assumption may favor PV+ basket cells, the majority of PV+ cells are located in the stratum pyramidale, and so we felt observations made in the stratum pyramidale were could be treated as broadly representative of PV+ cells in the whole CA1 without introducing significant error.	2.2.5

#	Explicit, Forced Assumption	Sec.
20	**Axo-axonic cells have an average of 7,200 boutons each.** We based this assumption on the published divergence of a single axo-axonic cell and on the observed number of synapses made for one connection onto a pyramidal cell.	3.2.2
21	**The ratio of PV+:CCK+ basket cell boutons in the entire CA1 is 1.6:1.** We averaged data regarding the relative frequency of PV+ and CCK+ basket cell boutons on pyramidal cell somata and in the pyramidal layer of the mouse CA1 (Foldy et al., 2010; Wyeth et al., 2010). We took this ratio to be representative of the total number of boutons of each basket cell type in rat CA1, for the purpose of calculating the number of CCK+ basket cells.	2.2.6
22	**Only basket cells synapse on the somata of pyramidal cells.** Though other cell types sometimes synapse on pyramidal cell somata, such as bistratified, ivy, or trilaminar cells, we assumed that their contribution was minor in our calculations of interneuronal convergence onto pyramidal cells.	3.3.1

#	Explicit, Forced Assumption	Sec.
23	**Basket cells in the stratum radiatum are likely CCK+ basket cells.**	3.2.2
24	**CCK+ basket cells are found in all layers of the CA1.** Many CCK+ basket cells are located in the stratum radiatum; therefore, we assumed unlabelled basket cells in the stratum radiatum were representative of CCK+ basket cells. However, CCK+ basket cells are also found in every other layer of the CA1, even in the stratum lacunosum-moleculare (Vida et al., 1998).	2.2.6
25	**CCK+ SCA and ADI cells are only found in the stratum radiatum; all CCK+ cells that are not basket cells in that layer are SCA or ADI cells.**	2.2.6
26	**CCK+ PPA cells are only found in the stratum lacunosun-moleculare; all CCK+ cells that are not basket cells in that layer are PPA cells.**	2.2.6
27	**Of CCK+ cells in the stratum radiatum that are not basket cells, half are SCA cells and half are ADI cells.** To gain a rough idea of the numbers of CCK+ cell types, we identified them based on their layer. However, various CCK+ cell types are found in more than one layer. For example, here we assumed that PPA cells were only in the stratum lacunosum-moleculare, but in reality they are occasionally found in the stratum radiatum and even once in the stratum oriens (Klausberger et al., 2005).	2.2.6

#	Explicit, Forced Assumption	Sec.
28	**All CCK+/VIP+ and CCK+/VGLUT3+ GABAergic cells are CCK+ basket cells.** However, ADI cells have been shown to express VGLUT3 (Klausberger et al., 2005), but it is not known what proportion of them express VGLUT3.	2.2.6
29	**CCK+ basket cells do not express CB; all CCK+/CB+ cells are non-basket cell types.**	2.2.6
30	**All the CCK+/CB- cells in the strata oriens and pyramidale are CCK+ basket cells.**	2.2.6
31	**Lesser known CCK+ cell types are found in the strata oriens and pyramidale.** Since no CCK+ basket cells have been found to express CB, we assumed that any CCK+/CB+ cells were not basket cells. Little has been published about the lesser-known CCK+ cell types, so we assumed they made up the remaining non-basket cell types in the strata oriens and pyramidale.	2.2.6
32	**The septotemporal and mediolateral bouton distribution of CCK+ basket cells is the same as for PV+ basket cells.** We made this assumption so that we could extrapolate from the slice data to a full axonal bouton count for CCK+ basket cells.	3.2.2

#	Explicit, Forced Assumption	Sec.
33	**CCK basket cells make 8 synapses per connection with other interneurons.** We made this assumption because they have been shown to make 8 synapses/connection with pyramidal cells in mouse. However, it has been shown that PV+ basket cells make only one or a few synapses per connection with interneurons despite making many synapses per connection on pyramidal cells. It is not known whether CCK+ basket cells also display this difference with connections onto interneurons, so we assumed they did not.	3.2.2

#	Explicit, Forced Assumption	Sec.
34	**All IS cells express CR or VIP or both.**	2.2.7
35	**All cells that express CR or VIP are IS I, II, or III cells, except for CCK+/VIP+ basket cells and CR+ septally projecting cells.**	2.2.7
36	**CR+/VIP- cells are IS-I or septally projecting cells, CR-/VIP+ cells are IS-II cells, and CR+/VIP+ cells are IS-III cells.**	2.2.7
37	**All VIP+ cells are CCK+/VIP+ basket cells or IS cells.** CR is generally a marker of interneuron specificity, but not all IS cells express it. Those that do not may express VIP (but so do some basket cells). Therefore, we took CR and VIP to be the most reliable markers of interneuron specificity and considered that the various combinations of the two markers identified different types of IS cells. Enkephalin may also be expressed by IS cells, but it is also expressed by non-IS cells so we have not derived any information from its expression.	2.2.7
38	**Approximately** 10% **of GABAergic cells in the CA1 express calbindin.** It has been previously estimated that 10% of GABAergic cells are CB+ (Freund and Buzsáki, 1996).	2.2.8

#	Explicit, Forced Assumption	Sec.
39	**Averaging the inputs to the CA1 from a CA3a and CA3c cell represents the inputs from an average CA3 cell.** There are known to be significant differences in bouton count and distribution from CA3a and CA3c. Since we had data from both areas, we combined it to calculate the laminar distribution and total CA1 divergence of an average CA3 pyramidal cell.	3.2.3
40	**For those cell types for which their ratio of innervation of pyramidal cells to interneurons is unknown, the bouton target ratio of 92:8 (pyramidal cell:interneuron) is adequate.** We determined the ratio as described in the methods. This ratio took into account the proportion of pyramidal cells and interneurons as well as their numbers of GABAergic input synapses. In reality, the ratio is likely to be even more skewed because some interneurons receive a significant amount of inhibition from afferent GABAergic neurons.	3.2.2

#	Explicit, Forced Assumption	Sec.
41	**Unless stated otherwise, proximally projecting cell types only contact postsynaptic pyramidal cells on basal dendrites in the stratum oriens and proximal apical dendrites in the stratum radiatum.** Some bistratified cells have been shown to synapse in the stratum pyramidale and some ivy or SCA cells to synapse in the stratum lacunosum-moleculare, but there is no quantitative data about the fractions of these cells that synapse in that layer.	
42	**Unless stated otherwise, distally projecting cell types only contact postsynaptic pyramidal cells on distal apical dendrites in the stratum lacunosom-moleculare.** This assessment still accounts for some neurogliaform cell boutons in the stratum radiatum and some O-LM cell boutons in the stratum oriens, but assumes that PPA cells only synapse in the stratum lacunosum-moleculare since there are no quantitative data about them in other layers.	3.3.1
43	**The entorhinal cortex supplies most of the excitatory inputs to the stratum lacunosum-moleculare.** Though the nucleus reuniens supplies a significant portion of excitatory inputs to the stratum lacunosum-moleculare, not enough data are available to quantify the contribution, so we have assumed that the excitatory inputs to the stratum lacunosum-moleculare are supplied by the entorhinal cortex.	3.2.3

Table 2.1: List of explicit assumptions we were compelled to make to complete our assessment.

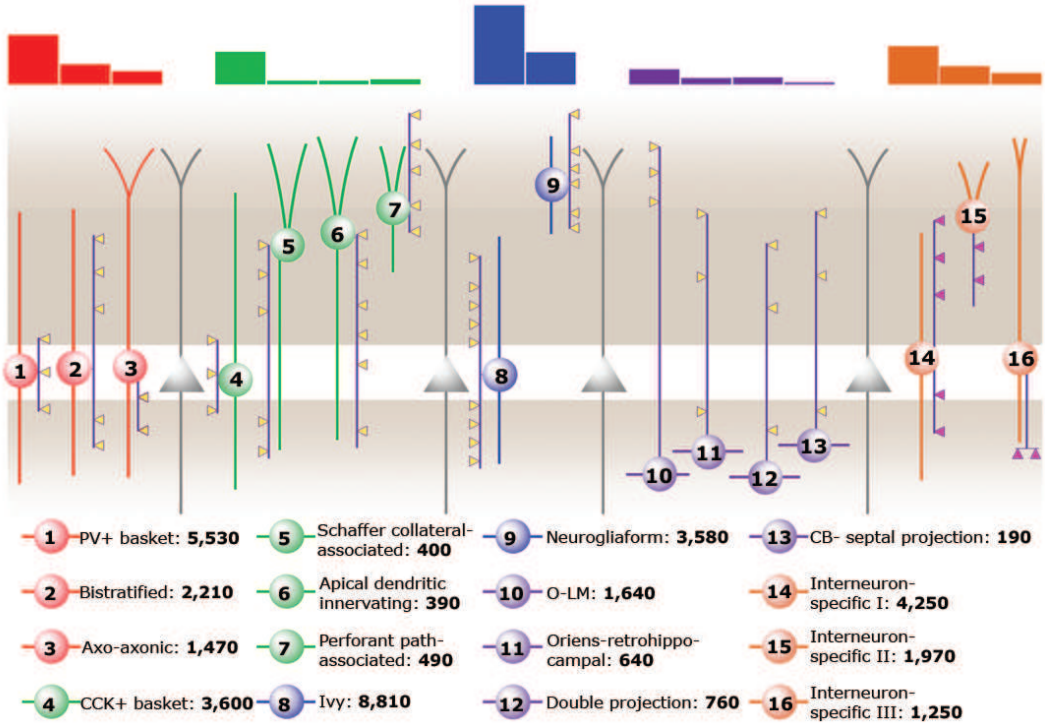

Figure 2.1: Estimate of interneuron numbers in rat CA1

To calculate the number of each interneuron type, we first needed a basis of the total number of interneurons. I combined an estimate of the total number of neurons in the rat CA1 with an observation of the fraction of neurons that were GABAergic to calculate the total number of interneurons. From there we calculated the fraction of interneurons that were each cell type, and then arrived at total cell numbers for each interneuron type.

2.2.1 Neuron Numbers, Boutons, and Divergence

Here, we began by estimating the total number of neurons in the rat CA1 as 350,000, within the range found for 30-day-old Wistar rats (320,000 - 380,000) (West et al., 1991). GABAergic interneurons constitute 7% to 11% of all hippocampal neurons (Woodson et al., 1989; Aika et al., 1994). To get a more precise estimate, we calculated the average number of boutons each interneuron would need to have available to synapse on pyramidal cells if the

Cell Type	Fraction	Total	SO	SP	SR	SLM
Neurogliaform Family	**32.2%**	**12,390**	**980**	**5,410**	**3,030**	**2,970**
Ivy	22.9%	8,810	980	5,410	2,420	0
Neurogliaform	9.3%	3,580	0	0	610	2,970
SOM Expressing	**9.3%**	**3,580**	**3,580**	**0**	**0**	**0**
O-LM	4.3%	1,640	1,640	0	0	0
Double Projection	2%	760	760	0	0	0
CB- septal proj.	0.5%	190	190	0	0	0
Oriens-retrohipp.	1.7%	640	640	0	0	0
Other SOM+ Cells*	0.9%	350	350	0	0	0
PV Expressing	**23.9%**	**9,210**	**2,200**	**6,460**	**550**	**0**
PV+ Basket	14.4%	5,530	1,320	3,880	330	0
Bistratified	5.7%	2,210	530	1,550	130	0
Axo-axonic	3.8%	1,470	350	1,030	90	0
CCK Expressing	**13.9%**	**5,370**	**1,140**	**1,070**	**1,960**	**1,200**
CCK+ Basket	9.4%	3,600	780	940	1,170	710
ADI	1%	390	0	0	390	0
SCA	1%	400	0	0	400	0
PPA	1.3%	490	0	0	0	490
CCK Misc.	1.3%	490	360	130	0	0
Interneuron Specific	**19.4%**	**7,470**	**780**	**3,190**	**1,450**	**2,050**
IS I	11%	4,250	780	1,800	780	890
IS II	5.1%	1,970	0	480	450	1,040
IS III	3.2%	1,250	0	910	220	120
Other Interneurons	**1.2%**	**480**				
TOTAL	**100%**	**38,500**	**8,680**	**16,130**	**6,990**	**6,220**

Table 2.2: Estimate of interneuron numbers in rat CA1 (Bezaire and Soltesz, 2013). Abbreviations: ADI - apical dendritic innervating, CB- calbindin, CCK - cholecystokinin, IS - interneuron specific, O-LM - oriens-lacunosum-moleculare, PPA - Perforant Path-associated, proj. - projection, PV - parvalbumin, retrohipp. - retrohippocampal, SCA - Schaffer Collateral-associated, SLM - stratum lacunosum-moleculare, SOM - somatostatin, SO - stratum oriens, SP - stratum pyramidale, SR - stratum radiatum

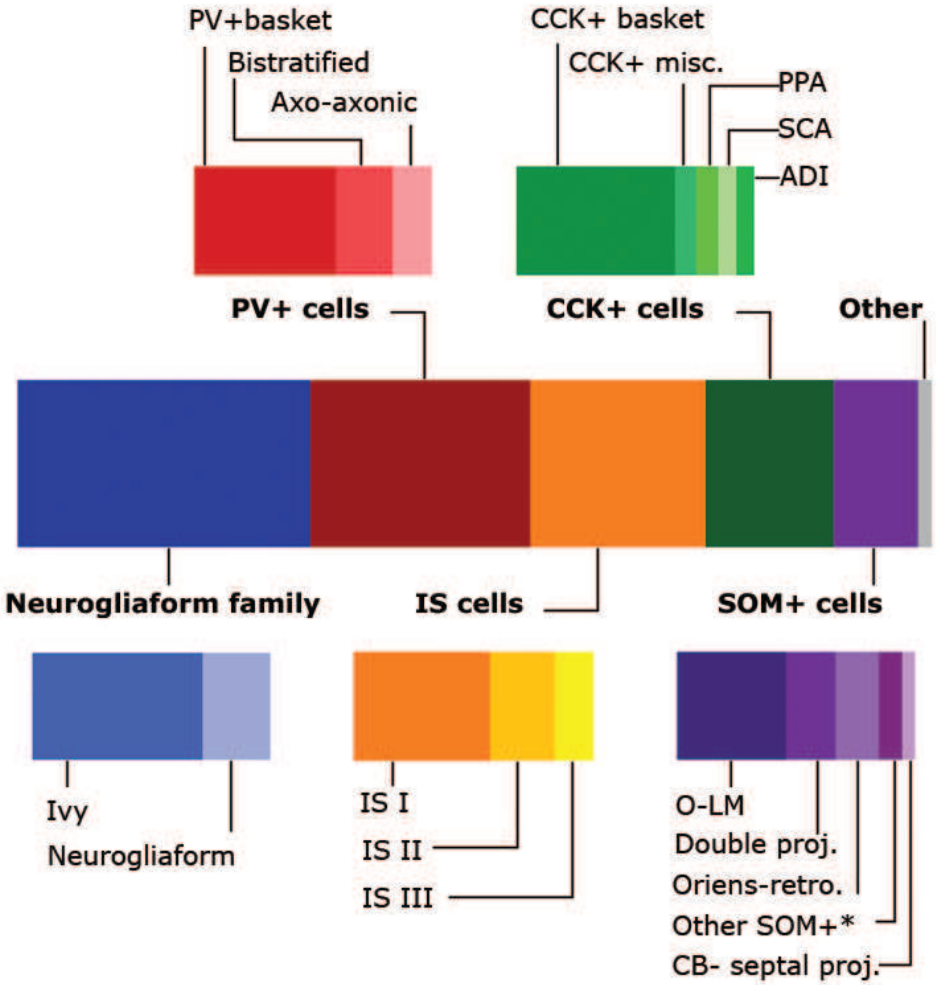

Figure 2.2: Square pie chart of interneurons

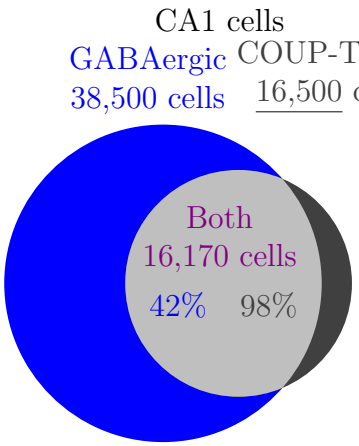

Figure 2.3: Co-expression of GABA and COUP-TFII in CA1. Known data: 42% of GABAergic cells express COUP-TFII and 98% of COUP-TFII are GABAergic (Fuentealba et al., 2010); 38,500 of CA1 cells are GABAergic (Table 2.1). Derived data: total number of COUP-TFII+ cells in the CA1 (16,500). We then used the calculated number of COUP-TFII+ cells to estimate the abundance of other classes of cells.

total fraction of GABAergic neurons were 7% or 11%. At 7%, given that CA1 pyramidal cells receive approximately 1,830 GABAergic synapses on their dendrites, somata, and proximal axons (Megías et al., 2001), each interneuron would need to have 24,310 boutons available for synapsing onto pyramidal cells. However, with a fraction of 11%, each interneuron would need only 14,810 boutons to synapse on pyramidal cells, within the range of bouton counts seen for most interneurons. Though neurogliaform family cells have many more boutons, when only the boutons contributing to classical synapses are considered (Olah et al., 2009), the numbers are also within range. Therefore, we generated the following estimates using the interneuronal fraction of 11%, for a total of 311,500 pyramidal cells and 38,500 GABAergic interneurons (note that the 11% interneuronal fraction is listed as an assumption in Table 2.1).

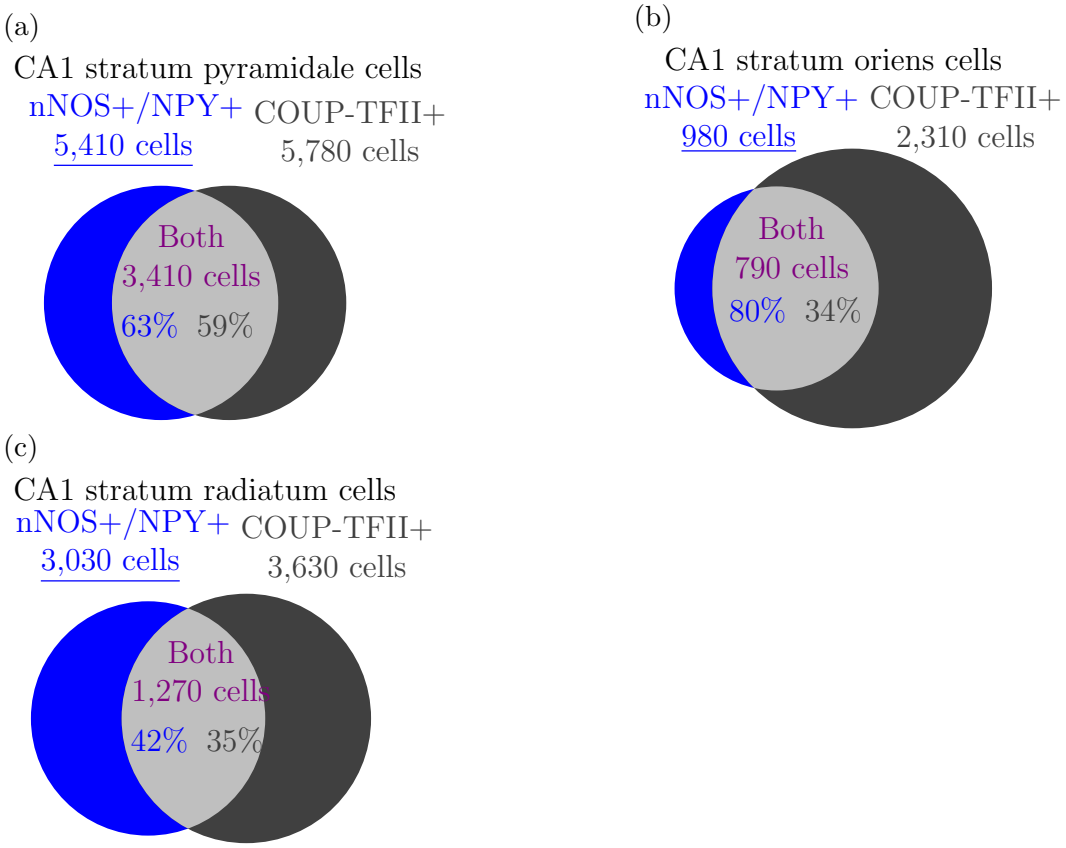

Figure 2.4: Co-expression of nNOS/NPY and COUP-TFII in distinct layers of CA1. We used the number of COUP-TFII cells in each layer and the percentage of overlap relative to each population (Fuentealba et al., 2010, see suppl. table 2) to calculate the total number of nNOS+/NPY+/COUP-TFII+ cells and then the number of nNOS+/NPY+ cells (underlined) for each layer.

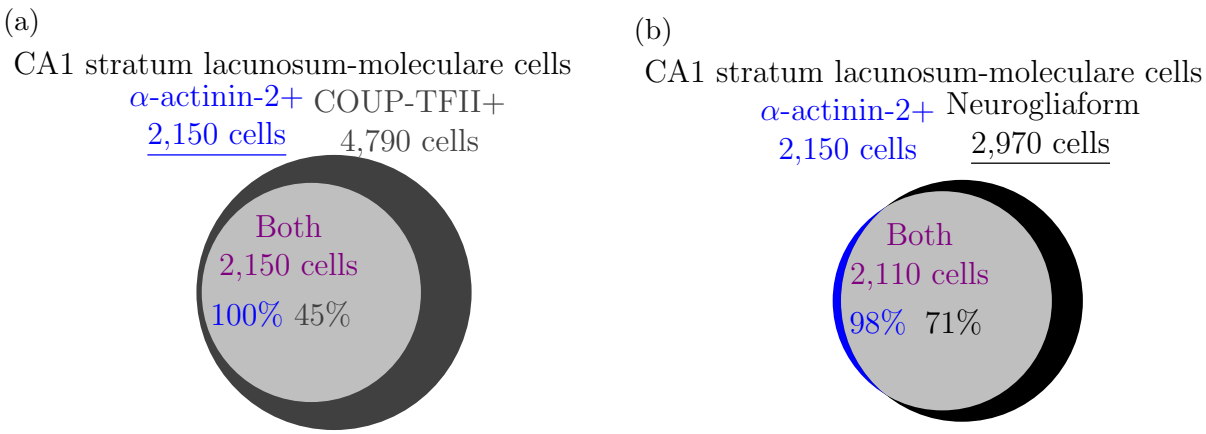

Figure 2.5: Co-expression of α-actinin-2 and COUP-TFII in CA1 stratum lacunosum-moleculare. Logic used to obtain the number of neurogliaform cells in the CA1 stratum lacunosum-moleculare. a) Given the number of COUP-TFII cells in the stratum lacunosum and the percentages of overlap (Fuentealba et al., 2010), the total number of α-actinin-2+/COUP-TFII+ and α-actinin-2+ cells can be calculated. b) Given the total number of α-actinin-2+ cells and the percentage that are likely to be neurogliaform cells (Price et al., 2005), the total number of neurogliaform cells can be calculated.

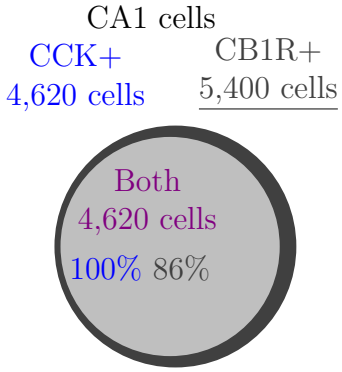

Figure 2.6: CCK and CB1 receptors in CA1. Known data: 100% of CCK+ cells express CB1R and 86% of CB1R+ cells express CCK (Katona et al., 1999b). Derived data: total number of CB1R+ cells in the CA1 $(5,400)$.

2.2.2 Calculation of Pyramidal Cells

Though CA1 pyramidal cells have recently been found to exhibit more heterogeneity than previously realized (Mizuseki et al., 2011b; Slomianka et al., 2011; Graves et al., 2012; Lee et al., 2014), in the absence of sufficient detailed, quantitative information, we considered them as one homogenous group of 311,500 cells (see assumption in Table 2.1).

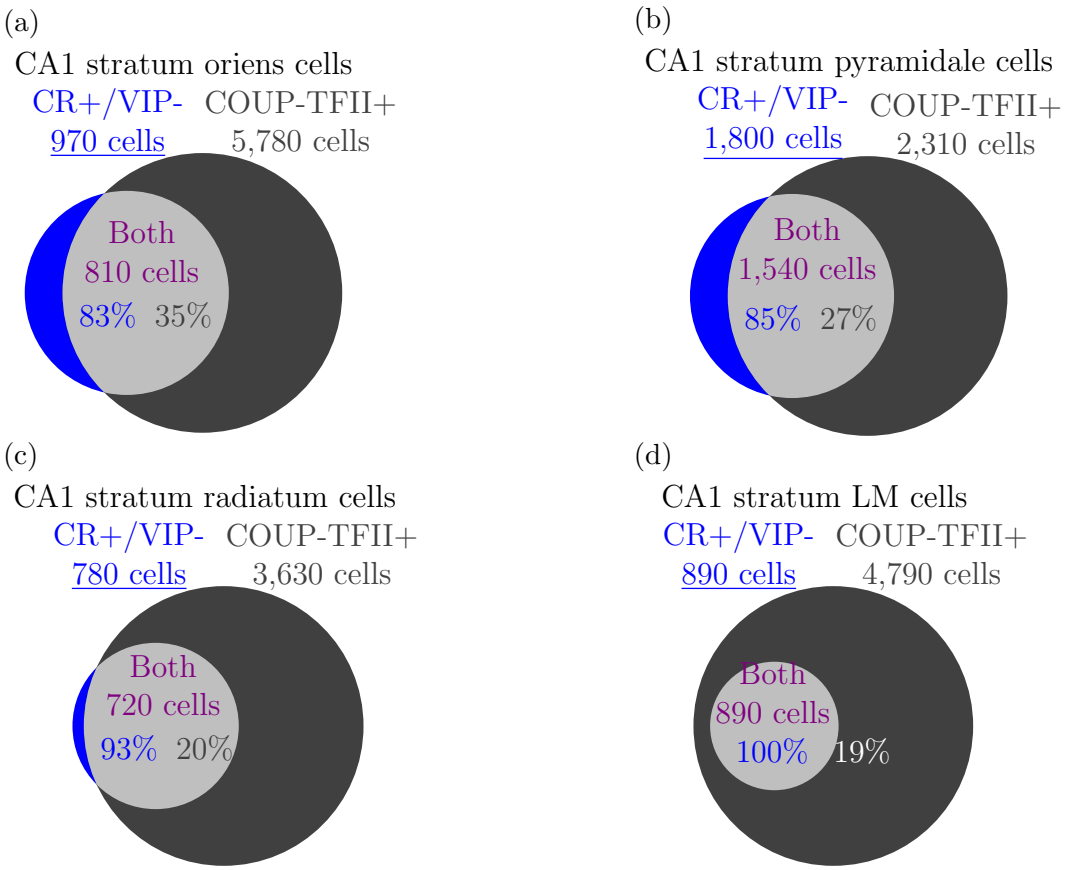

Figure 2.7: Co-expression of CR+/VIP- and COUP-TFII in distinct layers of CA1. Given the number of COUP-TFII cells in that layer and the percentage of overlap relative to each population (Fuentealba et al., 2010, see suppl. table 2), the total number of CR+/VIP-/COUP-TFII+ cells and then the number of CR+/VIP- cells (underlined) was calculated for each layer.

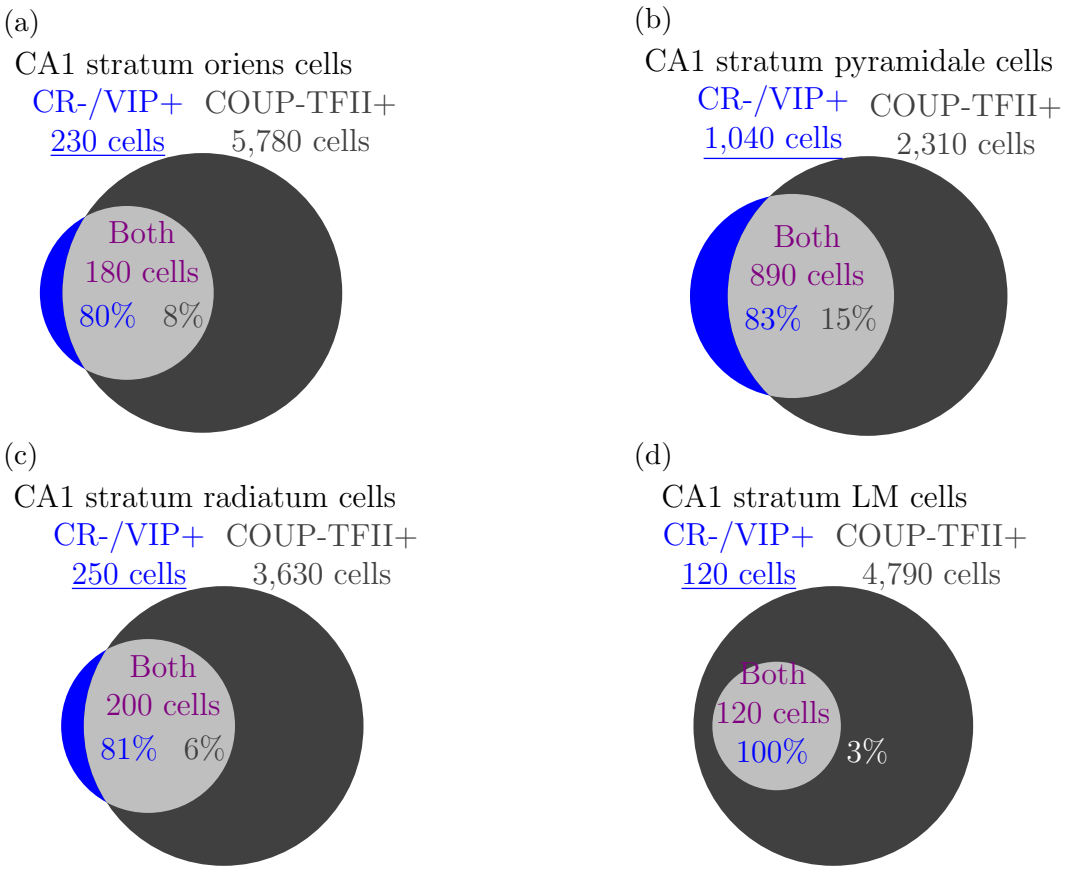

Figure 2.8: Co-expression of CR-/VIP+ and COUP-TFII in distinct layers of CA1. Given the number of COUP-TFII cells in that layer and the percentage of overlap relative to each population (Fuentealba et al., 2010, see suppl. table 2), the total number of CR-/VIP+/COUP-TFII+ cells and then the number of CR-/VIP+ cells (underlined) was calculated for each layer.

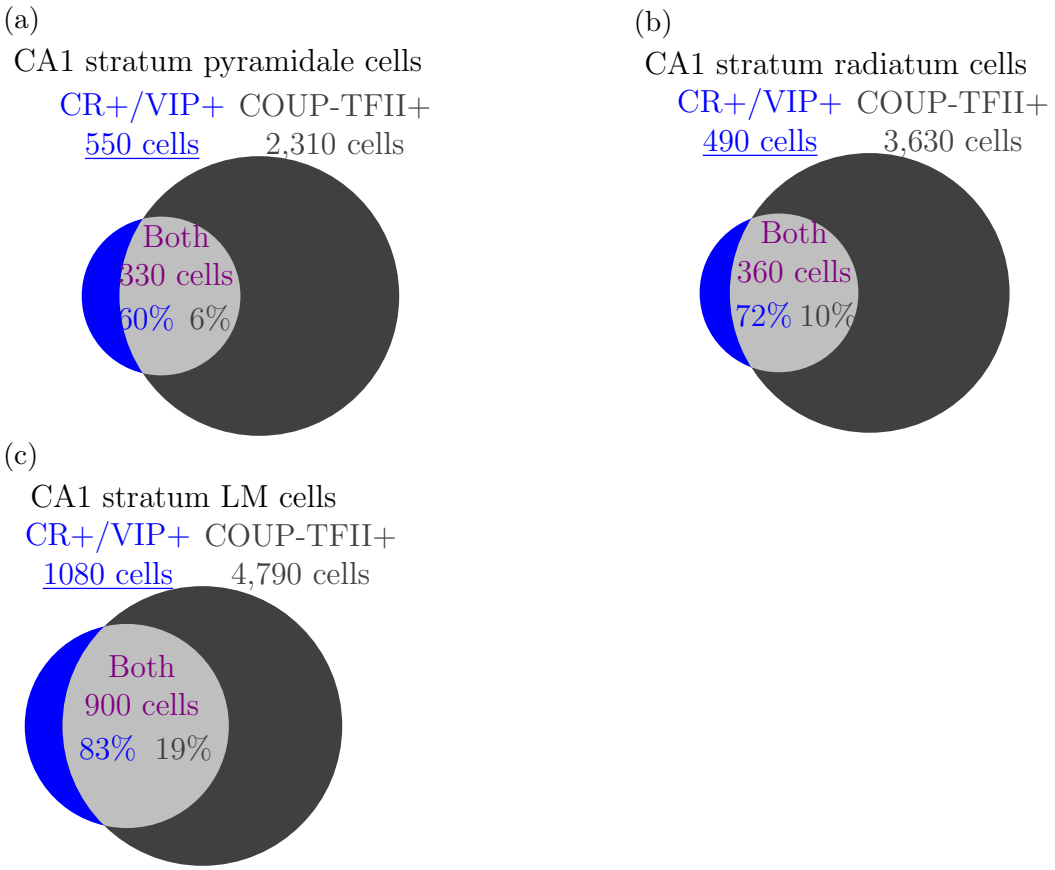

Figure 2.9: Co-expression of CR+/VIP+ and COUP-TFII in distinct layers of CA1. Given the number of COUP-TFII cells in that layer and the percentage of overlap relative to each population (Fuentealba et al., 2010, see suppl. table 2), the total number of CR+/VIP+/COUP-TFII+ cells and then the number of CR+/VIP+ cells (underlined) was calculated for each layer.

2.2.3 Calculation of Neurogliaform Family Cells

Neurogliaform family cells, including ivy and neurogliaform cells, form the most abundant group of interneurons within CA1 (for a review, see Armstrong et al. (2012)). They often express neuronal nitric oxide synthase (nNOS), neuropeptide Y (NPY), and α-actinin-2, as well as the nuclear receptor COUP-TFII (Price et al., 2005; Fuentealba et al., 2010). We first calculated the number of COUP-TFII+ cells and then used data about the co-expression of COUP-TFII with nNOS and NPY or α-actinin-2 to estimate the number of ivy and neurogliaform cells. We assumed that all nNOS+/NPY+ cells in the strata oriens, pyramidale, and radiatum were either ivy or neurogliaform cells (Table 2.1). However, Price et al. (2005) found that, in the stratum lacunosum-moleculare, some non-neurogliaform cells also expressed nNOS or, more rarely, nNOS and NPY. Therefore, in our calculations for neurogliaform cells in the stratum lacunosum-moleculare, we relied on α-actinin-2 expression only.

Though there is known to be a dorsal/ventral gradient in the expression of COUP-TFII, we assumed the expression of COUP-TFII in interneurons dorsally is representative of the whole CA1 (Table 2.1). Approximately 42% of GABAergic neurons in the CA1 express COUP-TFII (Fuentealba et al., 2010). Conversely, about 98% of COUP-TFII expressing neurons in the CA1 are GABAergic. Combining these two observations (Fig. 2.3), there are roughly 16,500 COUP-TFII expressing neurons in the CA1 and 16,170 COUP-TFII+/GABAergic neurons in the CA1. We combined this estimate of COUP-TFII+ neurons with their experimentally observed laminar distribution (Fuentealba et al. (2010), see their Supporting Information Fig. 1A) to get the total number of COUP-TFII+ neurons per layer, as shown in Table 2.3. Next, we used these numbers to calculate the number of ivy and neurogliaform cells. Because the assays looked at the coexpression of various markers with COUP-TFII, but not GABA, we performed our calculations on the basis of COUP-TFII+ neurons, rather than GABAergic COUP-TFII+ neurons. However, we considered any neurons expressing nNOS

or NPY to be GABAergic.

Ivy Cells

Ivy cells express nNOS and NPY (Fuentealba et al., 2008a) but not reelin (Fuentealba et al., 2010; Armstrong et al., 2012). Their somata are generally found in the stratum pyramidale and sometimes in the strata radiatum or oriens (Fuentealba et al., 2010; Somogyi et al., 2012). Not all ivy cells express COUP-TFII (Fuentealba et al., 2010), so nNOS/NPY expression is a better indicator of ivy cells than the presence of COUP-TFII with nNOS and NPY. No other cell type in the stratum pyramidale is known to express both nNOS and NPY, though bistratified cells express NPY (Fuentealba et al., 2008a; Klausberger et al., 2004) and interneuron-specific III cells may express nNOS (Tricoire et al., 2010).

Layer	**% cells**	**Total cells**
stratum lacunosum-moleculare	29%	4,790
stratum radiatum	22%	3,630
stratum pyramidale	35%	5,780
stratum oriens	14%	2,310

Table 2.3: Distribution of COUP-TFII expressing cells by layer. The percent of COUP-TFII expressing cells found in each layer is listed (adds to 100% of GABAergic COUP-TFII expressing cells), as well as the number of cells assuming a basis of 16,500 COUP-TFII expressing cells. Percentages from Fuentealba et al. (2010, see their suppl. fig. 1A).

.

Assay	Total	Layer				Ref.
		SO	SP	SR	SLM	
nNOS/NPY/CB	81.0%					Fuentealba et al. (2008a, Table S2)
nNOS/NPY/CR	93.3%					Fuentealba et al. (2008a, Table S2)
nNOS/NPY/SOM	80.3%					Fuentealba et al. (2008a, Table S2)
nNOS/NPY/α-actinin-2	87.6%					Fuentealba et al. (2008a, Table S2)
nNOS/reelin/NPY/SOM	73.6%	44.8%	81.7%	91.0%	55.2%	Fuentealba et al. (2010, Suppl. Table 2)
NPY/COUP-TFII/nNOS	78.1%	63.0%	78.3%	87.4%		Fuentealba et al. (2010, Suppl. Table 2)
PV/nNOS/NPY	56.7%	34.7%	54.2%	88.9%	41.2%	Fuentealba et al. (2008a, Table S1)
PV/nNOS/NPY/$GABA_AR$-α1	79.4%	94.8%	74.2%	93.5%	85.4%	Fuentealba et al. (2008a, Table S2)

Table 2.4: Percentage of NPY+ cells expressing nNOS (Fuentealba et al., 2008a; 2010). For each assay included, the calculations were made by summing all combinations including nNOS and NPY, and dividing that number by the sum of all combinations including NPY. Though the assays included other markers (listed in column 1), the calculation process was the same for each assay.

From Table 2.3, there are 5,780 COUP-TFII expressing cells in the stratum pyramidale. Approximately 59% of these cells express nNOS and NPY (Fuentealba et al. (2010), see their Supporting Information Table 2), giving a total of 3,410 COUP-TFII+/nNOS+/NPY+ cells in the stratum pyramidale. In the stratum pyramidale, 63% of nNOS+/NPY+ cells express COUP-TFII (Fuentealba et al. (2010), see their Supporting Information Table 2). Using the logic in Figure 2.4a, we determined there are about 5,410 nNOS+/NPY+ cells, the putative ivy cells, in the stratum pyramidale.

We repeated this exercise for nNOS+/NPY+ cells in the stratum oriens. Approximately 34% of the 2,310 COUP-TFII+ cells in the stratum oriens are also nNOS+/NPY+ (Fuentealba et al. (2010), see their Supporting Information Table 2). Though some projection cells may express nNOS (Sik et al., 1994) and double projection cells can express NPY (Klausberger, 2009), no other cell type in the stratum oriens is known to be nNOS+/NPY+. Therefore, we assumed all nNOS+/NPY+ cells in the stratum oriens were ivy cells (Table 2.1). Using the logic in Figure 2.4b, we estimated there are roughly 980 ivy (nNOS+/NPY+) cells in the stratum oriens.

For the ivy cells in the stratum radiatum, we first calculated the number of nNOS+/NPY+ cells. Then we considered that neurogliaform cells may also contribute to the nNOS+/NPY+ cell count in the stratum radiatum, as neurogliaform cells are often found at the border of the stratum radiatum and lacunosum-moleculare (Klausberger and Somogyi, 2008). Ivy cells predominate in the stratum radiatum (Somogyi et al., 2012): coexpression data of NPY and nNOS with reelin, a neurogliaform cell marker (see Armstrong et al. (2012)), showed reelin-expressing cells constituted only 20% of nNOS+/NPY+ cells in the stratum radiatum. Following the logic in Figure 2.4c, we determined there are 3,030 nNOS+/NPY+ cells in the stratum radiatum. Applying the observation by Somogyi et al. (2012) of reelin expression in the stratum radiatum, we calculated that 2,420 (80%) of the nNOS+/NPY+ cells are ivy cells (Table 2.1). We estimated a total of 8,810 ivy cells across strata oriens, pyramidale,

and radiatum.

Neurogliaform Cells

Neurogliaform cells are found in the stratum lacunosum-moleculare or at the border of the distal stratum radiatum (Vida et al., 1998), and they can express NPY, α-actinin-2, or nNOS (Price et al., 2005; Fuentealba et al., 2010). According to a recent report, there are at least two subsets of neurogliaform cells: those that arise from the medial ganglionic eminence (MGE) and those that arise from the caudal ganglionic eminence (CGE) (Tricoire et al. (2010), in mouse). Those cells derived from the MGE are expected to express nNOS and those from the CGE to express COUP-TFII. However, a significant coexpression of COUP-TFII and nNOS has been found for cells in all layers of the CA1 (Fuentealba et al., 2010). Further, there is evidence for a CGE origin for some nNOS+ cells (Tricoire et al. (2010), in mouse; Tricoire and Vitalis (2012) Tricoire and Vitalis, 2012). Therefore, neurogliaform cells do not necessarily cleanly separate into two groups when taking into account both neurochemical identity and origin. This may be due to interspecies differences, a dorsal/ventral gradient in expression, different methods of observation, or other factors. To estimate the expression of nNOS by neurogliaform cells, we calculated the percent of NPY+ cells in the stratum lacunosum-moleculare that co-express nNOS (Fuentealba et al. (2010), see their Supporting Information Table 2). In the stratum lacunosum-moleculare, the fraction of NPY+ cells that also express nNOS ranges from 41% to 85% (Table 2.4) depending on the combination of neurochemical markers tested in the assay (Fuentealba et al. (2010), see their Supporting Information Table 2). Data about co-expression of nNOS with α-actinin-2 were also available, though not as a function of layer. Overall, 46% to 63% of α-actinin-2+ cells throughout the CA1 expressed nNOS (Price et al. (2005); Fuentealba et al. (2008a), see their Supporting Information Table S2).

A more reliable marker of neurogliaform cells would be NPY or α-actinin-2 (Vida et al.,

1998; Ratzliff and Soltesz, 2001; Price et al., 2005). Approximately 71% of neurogliaform cells in the stratum lacunosum-moleculare express α-actinin-2 (Price et al., 2005). In the stratum lacunosum-moleculare, 100% of α-actinin-2+ cells express COUP-TFII, while 45% of COUP-TFII+ cells express α-actinin-2. We calculated the number of α-actinin-2 expressing cells in the stratum lacunosum-moleculare using the logic in Figure 2.5a, for a total of 2,150 α-actinin-2+ cells. In the stratum lacunosum-moleculare, α-actinin-2 appears to be a relatively specific marker: α-actinin-2+ cells do not co-express PV, CB, VIP, or CCK (Ratzliff and Soltesz, 2001). Only 2% of α-actinin-2+ cells in stratum lacunosum-moleculare express CR, while 43% express NPY (Ratzliff and Soltesz, 2001). Previous work has considered α-actinin-2+ cells in the stratum lacunosum-moleculare as neurogliaform cells (Fuentealba et al., 2010). We assumed that, in the stratum lacunosum-moleculare, 98% of α-actinin-2 expressing cells were neurogliaform cells (the percent of α-actinin-2+ cells that are GABAergic but do not express CR (Ratzliff and Soltesz, 2001); see Table 2.1). Using the knowledge that 71% of neurogliaform cells express α-actinin-2 (Price et al., 2005) and the logic in Figure 2.5b, we calculated there are 2,970 neurogliaform cells in the stratum lacunosum-moleculare. We then included 20% of the nNOS+/NPY+ cells in the stratum radiatum (610 reelin+ cells (Table 2.1), as calculated above in the ivy cell section), to get a total of 3,580 neurogliaform cells across the strata radiatum and lacunosum-moleculare. Because not all neurogliaform cells express nNOS, there may be even more neurogliaform cells in the stratum radiatum. However, we did not calculate the number of α-actinin-2+ cells in the stratum radiatum because data were not available about the overlap of α-actinin-2 with COUP-TFII in the stratum radiatum (Fuentealba et al., 2010).

2.2.4 Calculation of SOM+ Cells

SOM+ cells include O-LM cells and several projection cells (Maccaferri, 2005; Klausberger and Somogyi, 2008), as well as conventional bistratified cells, which will be

calculated in the PV+ cell section. Many of the projection cells have a local axonal arborization consisting of boutons primarily in the strata radiatum and oriens. These include double projection cells that project to the septum and subiculum, so-called back-projection cells that project to the CA3 and dentate gyrus, and oriens-retrohippocampal projection cells that target the subiculum (Klausberger and Somogyi, 2008). A projection cell targeting both the CA3 and the subiculum has also recently been discovered (Jinno (2009); Klausberger and Somogyi (2008), in mouse).

Layer					
SO	**SP**	**SR**	**SLM**	**Ref.**	**Notes**
85%	7%	8%		Nomura et al. (1997b)	Dorsal
92%	3%	5%		Nomura et al. (1997b)	Ventral
88.5%	5%	6.5%		Nomura et al. (1997b)	Averaged[1]
88.0%	9.1%	2.9%		Kosaka et al. (1988)	Dorsal
89.8%	6.8%	3.4%		Kosaka et al. (1988)	Ventral
89%	7.9%	3.1%		Kosaka et al. (1988)	Dorsal+Ventral
89.7%	7.3%	2.5%	0.5%	Jinno and Kosaka (2006)	Mouse
73.3%	22.8%	3.9%	0%	Fuentealba et al. (2010)	Calculated

Table 2.5: Laminar distribution of SOM within the CA1. Note that data from Nomura et al. (1997b) combines the strata radiatum and lacunosum-moleculare. 1: Calculated average of the dorsal and ventral values.

About 12% of GABAergic neurons in the CA1 express SOM (Kosaka et al., 1988). Applying this fraction to the calculation for GABAergic neurons gave 4,620 SOM+ neurons. About 89% of these cells are located in the stratum oriens (Table 2.5) (Kosaka et al., 1988; Nomura et al., 1997b), a total of 4,110 SOM+ GABAergic cells in the stratum oriens.

O-LM cells

O-LM cells, which express SOM and mGluR1α-actinin-2 (Ferraguti et al., 2004), are found in the stratum oriens (Klausberger and Somogyi, 2008). Roughly 40% of SOM+ cells in the stratum oriens are O-LM cells (Ferraguti et al., 2004), giving a total of 1,640 O-LM cells.

Double projection cells

Of the SOM+ cells in the stratum oriens, 23% project to the medial septum (Jinno (2009), in mouse), a total of 950 septally projecting SOM+ cells. Of the cells projecting to the medial septum, 80% are CB+ (Toth and Freund, 1992; Gulyás et al., 2003; Jinno, 2009). The double projection cells, which project both to the medial septum and to the subiculum, are known to express CB and SOM (Toth and Freund, 1992; Somogyi and Klausberger, 2005; Jinno et al., 2007); some also express mGluR1α-actinin-2, M2R, PV, or NPY (Jinno et al., 2007). We assumed all septally projecting, SOM+/CB+ cells were double projection cells (Table 2.1), for a total of 760 double projection cells.

Other septally projecting cells

Subtracting the SOM+/CB+ double projection cells from the total of septally projecting cells, we were left with a subset of 190 SOM+/CB-, septally projecting cells. This subset likely constitutes another group of septally projecting cells. Katona et al. (1999a) suggested that so-called back-projection cells, which are not known to express CB but often express SOM (70%, see Jinno (2009)), can project to the septum, in addition to projecting to the CA3. The observation that 18% of septally projecting cells express CR may also be relevant, as it has not been shown that double-projection cells express CR (Jinno, 2009). There is also a subset of SOM+ cells that are weakly M2R+ and may project to the septum, but this subset does not appear to express CR (Hajos and Mody, 1997; Ferraguti et al., 2005). For now, we consider the subset of 190 SOM+/CB- septally projecting cells in our calculations, noting that this cell type may also be the so-called back-projection cells or a subset of M2R+ septally projecting cells. In addition to these multiple subsets of SOM+ septal projection cells, there may be another small subset of septally projecting cells that are SOM- (Jinno et al., 2007). We do not attempt to identify or include those cells.

Oriens-retrohippocampal cells

About 34% of SOM+ cells in the stratum oriens express CB, a total of 1,400 cells (Gulyás et al., 2003). Like double projection cells, oriens-retrohippocampal cells can be SOM+/CB+ but may also express M2R (Jinno et al., 2007). We subtracted the double projection cells from the SOM+/CB+ population in the stratum oriens, leaving 640 other SOM+/CB+ cells, which we assumed were oriens-retrohippocampal cells (Table 2.1).

Other SOM+ cells

Other stratum oriens cells also express SOM (Jinno, 2009). Subtracting the estimates for O-LM, oriens-retrohippocampal, double projection, and other septally projecting cells from the total number of SOM+ cells left 880 SOM+ cells unidentified. Most of these are likely to be bistratified cells, which express SOM and PV (Klausberger et al., 2004; Baude et al., 2007) and are sometimes located in the stratum oriens (Baude et al., 2007); they will be calculated in the PV+ cell section.

2.2.5 Calculation of PV+ Expressing Cells

Approximately 26% of GABAergic neurons in the CA1 express PV (Kosaka et al., 1987). Given our previous calculation of 38,500 GABAergic cells in the CA1, 10,010 PV+ GABAergic cells reside in the CA1. These include the PV+ basket cells, bistratified cells, and axo-axonic cells. Also, up to one third of O-LM cells (Varga et al. (2012), in mouse) and double projection cells (Jinno et al., 2007) express PV, but at a weaker level (but see (Ferraguti et al., 2004), where up to 75% of mGluR1α-actinin-2+/SOM+ cells in the stratum oriens also expressed PV). Subtracting one third of the O-LM and double projection cells from the total gave 9,210 remaining PV+ cells.

Layer					
SO	**SP**	**SR**	**SLM**	**Ref.**	**Notes**
36.0%	60.0%	4.0%		Nomura et al. (1997b)	Dorsal
24.0%	69.0%	7.0%		Nomura et al. (1997b)	Ventral
30.0%	64.5%	5.5%		Nomura et al. (1997b)	Averaged[1]
40.7%	54.9%	4.5%		Kosaka et al. (1987)	Dorsal
39.4%	52.8%	7.9%		Kosaka et al. (1987)	Ventral
40.0%	54.0%	6.0%		Kosaka et al. (1987)	Dorsal+Ventral
28.4%	64.5%	6.2%	0.9%	Jinno and Kosaka (2006)	Mouse

Table 2.6: Laminar distribution of PV+ cells within CA1. Note that data from Nomura et al. (1997b) combines the strata radiatum and lacunosum-moleculare. 1: Calculated average of the dorsal and ventral values.

		Layer			
		SO[1]	**SP**	**SR**	**Total**
Cell Type	**% cells**	30.0%	64.5%	5.5%	**Cells**
PV+ basket cells	60.0%	1320	3870	330	5690
Bistratified cells	24.0%	530	1550	130	2280
Axoaxonic cells	16.0%	350	1030	90	1520
Total cells		2200	6460	550	9210

Table 2.7: Relative proportion and number of each type of PV+ cell in the CA1. Cell type percentages are from Baude et al. (2007) and laminar distribution percentages are averaged from dorsal and ventral data in Nomura et al. (1997b). Note that the percentage reported to be in the strata radiatum/lacunosum-moleculare is here attributed to the stratum radiatum only, as PV distribution data from the mouse showed that the stratum lacunosum-moleculare contained less than 1% of PV+ cells (Jinno and Kosaka, 2006, in mouse). 1: A fraction of PV+ O-LM and double projection cells was subtracted from the total PV+ cells in the stratum oriens before calculating the number of PV+ basket, bistratified, and axo-axonic cells in that layer.

While 64.5% of PV+ cells are located in the stratum pyramidale, a substantial number reside in the stratum oriens (30%, see Table 2.6) (Kosaka et al., 1987; Nomura et al., 1997b). Baude et al. (2007) gave relative percentages of PV+ basket, bistratified, and axo-axonic cells in the stratum pyramidale. We assumed the ratio held for the other layers to calculate the number of cells of each type in each layer, for a total of 5,530 PV+ basket cells, 2,210 bistratified cells, and 1,470 axo-axonic cells (Table 2.7). Note that this number of bistratified cells does not include any contributions from the GABAergic projection cells in the stratum oriens that also have boutons in the strata radiatum and oriens and, in the case of double projection cells, occasionally express PV (Jinno et al., 2007).

2.2.6 Calculation of CCK+ Cells

About 12% of the GABAergic neurons in the CA1 express cholecystokinin (CCK) (Kosaka et al., 1985), a total of 4,620 CCK+ GABAergic neurons in the CA1. CCK+ cells usually express cannabinoid receptor type 1 (CB1R) (Katona et al., 1999b; Cope et al., 2002) and often express vasointestinal protein (VIP) (Somogyi et al., 2004), vesicular glutamate transporter 3 (VGLUT3) (Somogyi et al., 2004), or sometimes calbindin (CB) (Cope et al., 2002; Somogyi et al., 2004). The presence of CB1R is generally an indicator of a CCK+ cell (Katona et al., 1999b). Therefore, CB1R expression data may be useful as a confirmation of the total number of CCK+ cells. Given the overlap of CCK and CB1R expression (Katona et al., 1999b) in the somata of CA1 interneurons (Fig. 2.6), we determined that there are 5,400 CB1R+ cells in the CA1. CB1R may be a more reliable indicator of CCK+ cells than CCK expression itself, so we based the rest of our CCK+ cell calculations on a total of 5,400 cells rather than 4,620 cells. However, we did not have detailed laminar distribution or marker expression overlap data for the CB1R+ cells, so we used the corresponding fractions from CCK+ cell studies.

CCK+ cell types include CCK+ basket cells, Schaffer Collateral-associated (SCA) cells, apical dendritic innervating (ADI) cells, and perforant path-associated (PPA) cells. ADI and SCA cells reside mostly in the stratum radiatum (Cope et al., 2002; Klausberger et al., 2005; Klausberger and Somogyi, 2008). PPA cells are found at the border of strata radiatum and lacunosum-moleculare (Klausberger et al., 2005; Klausberger and Somogyi, 2008). PPA cells are also known as R-LM cells because their cell bodies are generally found near the stratum radiatum while their axons innervate the stratum lacunosum-moleculare (Hajos and Mody, 1997).

The relative frequency of each of these cell types is unknown. To estimate the number of CCK+ basket cells, we used data about the synaptic convergence of basket cells onto pyramidal cells. Foldy et al. (2010) (in mouse) found that PV+ basket cells make about twice as many total synapses onto pyramidal cell somata as do CCK+ basket cells. However, CCK+ basket cell boutons are known to occur more frequently proximal to the soma (Foldy et al. (2010), in mouse), as evidenced by Wyeth et al. (2010), who found a ratio of 13.1:10.9 for PV:CCK boutons in the whole pyramidal cell layer of the mouse CA1. We averaged these two estimates to obtain a ratio of 1.6:1 PV:CCK boutons onto pyramidal cells. We assumed this ratio also held for the total number of PV+ basket cell and CCK+ basket cell boutons in the CA1 (Table 2.1). Because there are approximately 5,520 PV+ basket cells with 10,440 boutons each, the total number of PV+ basket cell boutons in the CA1 is 57.7 million. Therefore, we calculated the total number of CCK+ basket cell boutons as 36.0 million. As CCK+ basket cells may have about 10,000 boutons each (see synapse calculations below), we calculated a total of 3,600 CCK+ basket cells.

Using data from Pawelzik et al. (2002), we determined the laminar distribution of CCK+ cells (Table 2.8) and estimated the relative abundance of each type of CCK+ cell in each layer. We included marker coexpression data from Somogyi et al. (2004) to solve for the populations of CCK+/CB+, CCK+/VIP+, CCK+/VGLUT3+, and CCK+only cells in

Layer					
SO	**SP**	**SR**	**SLM**	**Ref.**	**Notes**
16.1%	17.7%	66.3%		Kosaka et al. (1985)	Method A
18.8%	19.7%	61.6%		Kosaka et al. (1985)	Method B
21.3%	20%	36.5%	22.2%	Pawelzik et al. (2002)	
22.6%	29.2%	39.1%	9.2%	Jinno and Kosaka (2006)	Mouse

Table 2.8: Laminar distribution of CCK within the CA1. Note that data from Nomura et al. (1997b) combines the strata radiatum and lacunosum-moleculare. Methods A and B are described in the original paper, see Kosaka et al. (1985).

each layer, which we used to refine our estimates by cell type.

We assumed (Table 2.1) the CCK+ basket cells were found in all layers of the CA1 (including the stratum lacunosum-moleculare, see Vida et al. (1998) and Elfant et al. (2008)), SCA and ADI cells in the stratum radiatum, and PPA cells in the stratum lacunosum-moleculare (Table 2.1) (Klausberger and Somogyi, 2008). We assumed some lesser-known CCK+ cell types were found only in the strata oriens and pyramidale (Table 2.1). The lesser-known types include CCK+ quadrilaminar, CCK+ bistratified cells (different from SCA cells), and CCK+ SO-SO cells, so called because both their axons and dendrites remain in the stratum oriens (Pawelzik et al., 2002). In addition, some of the CCK+ basket cells found in the stratum oriens may be horizontal basket cells (Klausberger et al., 2005).

Since CCK+ basket cells have not been shown to express CB (Cope et al., 2002; Klausberger et al., 2005; Somogyi et al., 2004), we assumed none of the CCK+/CB+ cells were basket cells (Table 2.1). We considered CCK+/CB+ cells in the stratum lacunosum-moleculare as PPA cells, CCK+/CB+ cells in the stratum radiatum as SCA or ADI cells, and CCK+/CB+ cells in the strata oriens and pyramidale as the lesser-known types mentioned above (Table 2.1). Note that PPA and SCA cells are both often found straddling the border of the strata radiatum and lacunosum-moleculare, so the laminar-based calculations for these CCK+ cell types will only give a rough approximation of each type.

We assumed all the CCK+/CB- cells in the strata oriens and pyramidale were CCK+ bas-

ket cells, including CCK+/VIP+ cells, CCK+/VGLUT3+ cells, and CCK+only cells (Table 2.1). In the strata radiatum and lacunosum-moleculare, we assumed all the CCK+/VIP+ and CCK+/VGLUT3+ cells were basket cells. However, Klausberger et al. (2005) showed that ADI cells can express VGLUT3 and a high concentration of VGLUT3+ boutons has been found at the border of the strata radiatum and lacunosum-moleculare, suggesting that PPA or SCA cells may also express VGLUT3 (Somogyi et al., 2004) (Table 2.1). After counting the CCK+/VIP+ and CCK+/VGLUT3+ cells in the strata radiatum and lacunosum-moleculare, there were still an additional 430 CCK+ basket cells to be assigned, which we assumed to be CCK+only cells. Next, we assumed all of the non-basket cells in the stratum lacunosum-moleculare were PPA cells (Table 2.1). Of the non-basket cells in the stratum radiatum, we assumed the SCA and ADI each made up half the balance (Table 2.1). This led to an estimate of 65% of SCA cells being CB+, though only 32% have been observed to be CB+ experimentally (Cope et al., 2002). The numbers of each CCK+ cell type are given in Table 2.9.

2.2.7 Interneuron-specific cells

Interneuron-specific (IS) cells only synapse on other interneurons, avoiding the pyramidal cells, and they often express calretinin (CR), VIP, or enkephalin (ENK) (Acsady et al., 1996; Acsády et al., 1996; Gulyás et al., 1996; Fuentealba et al., 2010). Recently, they have been shown to express COUP-TFII as well (Fuentealba et al., 2010). IS cells can be further divided into multiple categories. One type, known as the IS III cell, expresses both CR and VIP and has axons projecting to the stratum oriens and alveus (Acsády et al., 1996; Gulyás et al., 1996). A second type, known as the IS II cell, has axons targeting the stratum radiatum and dendrites in the stratum lacunosum-moleculare (Acsády et al., 1996; Gulyás et al., 1996). This type is known to express VIP but has not been shown to express CR (Somogyi and Klausberger, 2005). A third, broad category known as IS I includes cells

	Layer				
	SO	**SP**	**SR**	**SLM**	**Total**
Cell Type	21%	20%	37%	22%	**Cells**
CCK+ Basket	**670**	**810**	**850**	**540**	**2870**
VIP	270	200	70	40	580
VGLUT3	120	150	700	430	1400
CCK only	280	460	80	70	890
SCA	**0**	**0**	**420**	**0**	**420**
CB	0	0	220	0	220
VGLUT3	0	0	0	0	0
CCK only	0	0	200	0	200
ADI	**0**	**0**	**420**	**0**	**420**
CB	0	0	220	0	220
VGLUT3	0	0	0	0	0
CCK only	0	0	200	0	200
PPA	**0**	**0**	**0**	**490**	**490**
CB	0	0	0	270	270
VGLUT3	0	0	0	0	0
CCK only	0	0	0	220	220
Misc. CCK	**310**	**110**	**0**	**0**	**420**
CB	310	110	0	0	420
Total cells	**980**	**920**	**1690**	**1030**	**4620**

Table 2.9: Relative proportion and number of each type of CCK+ cell in CA1. Laminar distribution percentages from Pawelzik et al. (2002) and marker coexpression fractions from Somogyi et al. (2004).

Marker	Layer SO	SP	SR	SLM	Ref.	Notes
CR+	22.0%	38.0%	40.0%		Nomura et al. (1997b)	Dorsal
CR+	19.0%	34.0%	47.0%		Nomura et al. (1997b)	Ventral
CR+	20.5%	36.0%	43.5%		Nomura et al. (1997b)	Averaged[1]
CR+	14.1%	45.2%	24.8%	15.9%	Jinno and Kosaka (2006)	Mouse
CR+	19.7%	46.8%	16.9%	16.6%	Fuentealba et al. (2010)	Calculated[2]
CR+	18.8%	38.7%	12.6%	29.9%	Fuentealba et al. (2010)	Calculated[3]
VIP+	9.6%	57.7%	19.2%	13.5%	Jinno and Kosaka (2006)	Mouse
VIP+	6.0%	42.4%	19.7%	31.9%	Fuentealba et al. (2010)	Calculated[2]
CR+ or VIP+	14.6%	41.4%	18.5%	25.5%	Fuentealba et al. (2010)	Calculated[2]
CR+ and VIP-	21.9%	40.6%	17.5%	20.0%	Fuentealba et al. (2010)	Calculated[2]
CR+ and VIP+	13.9%	63.6%	15.2%	7.4%	Fuentealba et al. (2010)	Calculated[2]
CR- and VIP+	0.0%	26.0%	23.2%	50.8%	Fuentealba et al. (2010)	Calculated[2]

Table 2.10: Laminar distribution of CR and VIP within CA1. Note that data from Nomura et al. (1997b) combines the strata radiatum and lacunosum-moleculare. 1: Average of the dorsal and ventral values. 2: Calculated based on data from the marker assay: CR/COUP-TFII/PPE/VIP. 3: Calculated based on data from the marker assay: CR/CB/COUP-TFII/PV.

with dendrites spanning all layers and axons targeting the stratum radiatum, and perhaps also the stratum oriens (Acsády et al., 1996; Gulyás et al., 1996). These cells generally express CR, though a subset of them do not (Acsady et al., 1996). Additionally, a subset of VIP+ cells in mice has been found to express nNOS as well; this subset has axonal and dendritic projection patterns resembling those of an IS III cell (Tricoire et al. (2010), in mouse).

We used data about the coexpression of COUP-TFII with other markers to calculate the number of IS cells. Because some non-IS cells express ENK (Price et al., 2005), we did not consider the presence of ENK to indicate interneuron-specific cells. Instead, we characterized IS cells as those that express CR or VIP (Table 2.1) (Fuentealba et al., 2010). We used information about the co-expression of CR, VIP, and COUP-TFII (Fuentealba et al., 2010), along with our earlier calculation of COUP-TFII cells per layer, to determine the number of CR or VIP positive cells in each layer (Table 2.10). We looked at three combinations of

marker expression which we took to represent specific IS cell types. We assumed CR+/VIP- cells were IS I cells, CR-/VIP+ cells were IS II cells, and CR+/VIP+ cells were IS III cells (Table 2.1). This may underestimate the number of IS I cells, since not all of them express CR (Acsady et al., 1996). Using the logic in Figures 2.7, 2.8, and 2.9, we determined the number of CR+/VIP-, CR-/VIP+, and CR+/VIP+ cells in each layer. Considering some basket cells also express VIP, we subtracted the number of CCK+/VIP+ basket cells, assuming the remaining VIP+ cells were IS cells (Table 2.1). For each layer, we removed an equal fraction of VIP+ cells (the CCK+/VIP+ basket cells) from the CR-/VIP+ and CR+/VIP+ populations. Note that 18% of septally-projecting cells express CR (Jinno, 2009); this number may align with the 190 SOM+/CB- septally projecting cells that are not double projection cells (calculated above). We subtracted these 190 cells from the CR+/VIP- population of cells in the stratum oriens to obtain an estimate for each IS cell type in each layer (Table 2.11).

Cell Type	**SO**	**SP**	**SR**	**SLM**	**Total**
IS I cells	780	1800	780	890	4250
IS III cells	0	910	220	120	1250
IS II cells	0	480	450	1040	1970

Table 2.11: Calculated number of each IS cell type in CA1 by layer.

2.2.8 Other cells

Several cell types remain for which we have not estimated their number. Here, we provide a crude estimate of number for several types given the limited information we have about them. However, we do not include the estimates made in this section in our final count in the summary section, because the estimates are likely to contain multiple cell types and may overlap with cell populations already counted.

We have not yet addressed a few of the cell types found in the stratum radiatum. These include large calbindin cells (Klausberger and Somogyi, 2008) and radiatum-

and dentate-innervating (RADI) cells (Fuentealba et al., 2010), which both express CB. Freund and Buzsáki (1996) suggested 10% of GABAergic cells in the CA1 express calbindin (CB), for a total of 3,850 CB+ cells (Table 2.1). We subtracted the previously calculated CB+ cells (CCK+/CB+ cells and SOM+/CB+ cells) from this total, for a remainder of 1,230 CB+ cells across all layers. This represents an upper bound on the large calbindin and RADI cells. They are likely to number much fewer, because the remaining CB+ cells in the strata oriens and pyramidale may actually include some of the other cell types calculated above, for which their CB expression was unknown.

There are additional projection cells that we have not calculated. So-called back projection cells project to the CA3 and dentate gyrus and are known to express nNOS (Sik et al., 1994). They may also express SOM (Katona et al., 1999a) and may even project to the septum (see Section 2.2.4 above). Unfortunately, not enough information is known about so-called back projection cells to estimate their relative abundance or even to consider them as a distinct cell type.

There are also other projection cells that target the subiculum. We performed a rough calculation to gain an idea of the cells projecting to the subiculum, including the radiatum-retrohippocampal cells and the trilaminar cells. To do this, we combined experimental data with the above calculations for double projection and oriens-retrohippocampal cells. Both double projection and oriens-retrohippocampal cells project to the subiculum (Klausberger and Somogyi, 2008). We assumed these two cell types constituted the entire population of SOM+, subicular-projecting cells, a total of 1,400 cells (Table 2.1). Since 50% of cells in the CA1 projecting to the subiculum are SOM+ (Jinno et al., 2007; Jinno, 2009), we calculated that a total of 1,400 SOM- cells project to the subiculum. These are likely to include trilaminar cells in the stratum oriens and radiatum-retrohippocampal cells in the stratum radiatum, both of which project to the subiculum and are not seen to express SOM. However, as both of these cell types are somewhat rare, it is unlikely that they comprise the

entire group of SOM- subicular projecting cells.

No data were available to break down our estimate of trilaminar and radiatum-retrohippocampal cells into an estimate for each cell type or even by layer. Once more data become available about the laminar distribution and total number of subicular projecting cells, further identification may be possible. Radiatum-retrohippocampal projection cells have not been found to express any of the major neurochemical markers, such as SOM, VIP, nNOS, CCK, CB, PV or CR, nor any particular receptors (Jinno et al., 2007; Jinno, 2009), though 80% of them express COUP-TFII (Fuentealba et al., 2010). Therefore, it is difficult to make any estimation for this type of cell. Of note, a study marking neurons that project to the granular retrosplenal cortex found that a significant portion of the axons originated from GABAergic neurons at the border of the strata radiatum and lacunosum-moleculare (Miyashita and Rockland, 2007). Most of the cells were found to be negative for the major neurochemical markers, though a small percentage expressed M2R (Miyashita and Rockland, 2007). Some of these neurons may be radiatum-retrohippocampal cells. Also, within the strata radiatum and lacunosum-moleculare, about 5% of subicular projecting cells were negative for all tested markers (Miyashita and Rockland, 2007); these cells may correspond to some or all of the putative radiatum-retrohippocampal cells.

In both the strata oriens and radiatum, approximately half of subicular projecting cells were M2R+. These M2R+, subicular projecting cells are the putative trilaminar cells that locally innervate stratum pyramidale in addition to the strata radiatum and oriens (Sik et al., 1995; Ferraguti et al., 2005; Klausberger and Somogyi, 2008). However, trilaminar cells are considered somewhat rare, so it is not clear whether they make up the entire M2R+, subicularly projecting population. Trilaminar cells are also mGluR8-decorated (Ferraguti et al., 2005); however, there is not enough information about the prevalence of mGluR8-decorated cells to base any calculations on that property.

In addition, a population of ENK expressing cells in the stratum radiatum has recently been

found (Fuentealba et al., 2008b). This cell type projects to the subiculum as well; 11.3% of subicular projecting interneurons in the CA1 expressed ENK (Fuentealba et al., 2008b). Given our calculations of subicular projecting interneurons above (2,800), approximately 320 subicular projecting cells may express ENK.

2.3 Evaluation of Estimates

We were able to confidently estimate the numbers of the most abundant interneuron types in the CA1, including the PV+ basket, bistratified and axo-axonic cells, the O-LM cells, the CCK+ basket cells, and the neurogliaform family cells (ivy and neurogliaform). Together, these cell types constituted 70% of GABAergic interneurons in the CA1. We also estimated that interneuron-specific cells make up an additional 19% of GABAergic interneurons. By making some layer-based assumptions, we were able to estimate the numbers of an additional 5% of interneurons comprising the remaining CCK+ cell types. The remaining SOM+ cells and other projections cells were less readily quantifiable, but appeared to constitute 5% to 7% of the GABAergic interneurons, with other, more obscure cell types making up the remaining fraction (about 1%).

Regarding the calculations of cell numbers, some previous estimates exist. Freund and Gulyas (1997) estimated that CR+ cells comprise 13% of all hippocampal interneurons. By our calculations (adding IS I, IS III and possibly the small subset of CB- septally projecting cells), the CR+ cells constitute 14% to 15% of CA1 cells, roughly the same as the previous estimate. Baude et al. (2007) estimated the fraction of interneurons that were PV+ basket, bistratified, or axo-axonic cells as 12%, 5%, and 3%, respectively. We reached a similar conclusion, with fractions of 14%, 6%, and 4%, for PV+ basket, bistratified, and axo-axonic cells.

Jinno and Kosaka (2006) have provided experimental observations of the neurochemical composition per layer and laminar distribution, but for mouse hippocampus. It is not clear whether these data in rat and mouse should match, as the laminar distribution data for various markers have been shown to be somewhat different for rat (Kosaka et al., 1985; 1987; 1988; Nomura et al., 1997b; Pawelzik et al., 2002; Fuentealba et al., 2010) and mouse (Jinno and Kosaka, 2006), as seen in Tables 2.5, 2.6, 2.8, and 2.10. As more data about the expression of all markers by each interneuron type become available and standardized (hippocampome.org), it will be possible to calculate the expected neurochemical composition per layer in rat, based on the cell number estimates provided here.

In quantitatively assessing the CA1, we have taken most of our data from the rat. However, some data were not available for the rat CA1 and so we used observations made in mouse, instead. This includes the percent of SOM+ cells projecting to the medial septum.

In general, we expect that our estimates could be refined as the projection cell types become better defined and their marker combinations further characterized. In addition, more sophisticated ways are needed to distinguish the various CCK+ cell types, rather than relying on laminar position. We also look forward to more data becoming available for the lesser-known cell types, such as the large calbindin cell, RADI cell, and the enkephalin-expressing subicular projecting cell.

With this current, quantitative knowledge of CA1 cell numbers, researchers will be better able to hypothesize about and quantify the roles of the various interneuron types in network functions. In addition, the knowledge base enabled the construction of a more accurate, biologically constrained computer model of CA1, similar to the data-driven models of the dentate gyrus (Santhakumar et al., 2005; Morgan and Soltesz, 2008; Schneider et al., 2012). The assembled data also enables better contrasting of the network makeup of the CA3 and other regions with that of the CA1.

Chapter 3

Quantitative Assessment of Neural Connectivity

The concepts of divergence and convergence are useful for quantifying connectivity. The divergence of a cell is the number of outgoing synapses it makes onto other cells in the network. Anatomically, the divergence is related to the boutons of the cell. Conversely, convergence is the number of incoming synapses the cell receives from other cells in the network. The anatomical correlate is the number of postsynaptic sites on the dendrites, soma, and axon of the cell. There are experimental observations for both of these types of connectivity. Therefore, we compared the connectivity as defined by both of these concepts. We found descrepancies between the estimates obtained from each concept. To conclude, we discuss reasons for the difference in numbers and describe how we handled the discrepancies when generating constraints for our model.

3.1 Calculation of Connectivity

For many neuron types, experimental estimates existed of the total boutons per axonal arborization. We multiplied these estimates by the total number of each neuron type as calculated here to get the total number of boutons available from each cell type for synapsing on postsynaptic neurons. Then we combined these data with the pyramidal cell and interneuron electron microscopy (EM) data to obtain the final convergence and divergence estimates in terms of synapses on a pyramidal cell or interneuron. These calculations enabled us to determine the overall connectivity of each neuron type, but did not permit us to calculate the local connection probability. To do so would require knowledge of the bouton distribution within the axonal extent, as well as the density of neurons of each type and their dendritic extents. However, we have still included data on the axonal extent of each neuron type wherever possible.

The total number of synapses onto a pyramidal cell has previously been calculated. Megías et al. (2001) measured dendritic length and synapse density, multiplying the two to calculate the total synapses. They estimated the number of synapses on each type of dendrite across all layers for a pyramidal cell within the dorsal CA1 (Megías et al., 2001). Megías et al. (2001) served as the basis for our calculations of synaptic convergence onto CA1 pyramidal cells.

3.2 Divergence

3.2.1 Local divergence of pyramidal cells

We calculated the total boutons on a CA1 pyramidal cell axon using the observed axon length and bouton density (Esclapez et al., 1999). Esclapez et al. (1999) provided bouton

density measurements as a function of axonal segment branch order for CA1 pyramidal cells. Although the axonal length was computed from an axon fill in a slice, the axon fills were selected from those that appeared to be fully contained within the slice (Esclapez et al., 1999). In a representative CA1 pyramidal axonal arbor, segments of third or fourth order constituted most of the axonal length; therefore we used an average of the bouton densities of the third and fourth order segments (13.56 boutons per 100μm) multiplied by the average total axonal length (3,732μm) to obtain a total of 506 boutons per CA1 pyramidal cell within the CA1.

Takács et al. (2012) observed that 39% of local collateral boutons synapse on other pyramidal cells *in vivo*, so we calculated that each pyramidal cell makes 197 synapses onto other pyramidal cells. We were also interested in the number of synapses made per connection to calculate the total number of connections made onto other pyramidal cells. In a study of pyramidal to pyramidal cell pairs within the CA1 (Deuchars and Thomson, 1996), a pyramidal to pyramidal connection comprising two synapses was found. However, its EPSP amplitude was over twice the average amplitude of the other recorded pairs, so we assumed it was an exception. We assumed that CA1 pyramidal cell local collaterals made one synapse onto each postsynaptic pyramidal cell (Table 2.1). Therefore, we calculated that each pyramidal cell diverges to contact 197 other CA1 pyramidal cells.

Takács et al. (2012) also found that CA1 pyramidal cells make 54% of their local synapses onto interneurons. To calculate their divergence onto interneurons, we estimated the number of synapses forming each pyramidal cell to interneuron connection. Biro et al. (2005) observed that a single CA1 pyramidal cell to O-LM cell connection comprised, on average, three synapses. Although some pyramidal cell to basket cell connections in the CA3 were observed to include only one synapse (Sik et al., 1993; Gulyás et al., 1993), current clamp recordings of pyramidal cell to bistratified cell connections in the CA1 revealed a large enough range in EPSP amplitude to suggest that some connections include multiple synapses (Ali et al.,

1998). Therefore, we assumed that CA1 pyramidal cells made, on average, three synapses onto each postsynaptic interneuron (Table 2.1). We then calculated that each CA1 pyramidal cell diverges to innervate 91 interneurons. Aside from the 39% of synapses made onto other pyramidal cells and the 54% made onto interneurons, there are an additional 7% of local synapses made onto unknown targets (Takács et al., 2012). Therefore, each CA1 pyramidal cell contacts an additional 11 to 35 unknown, local targets.

	Axonal			Boutons		Laminar Distribution (%)				Divergence				
Cell	**Extent** (mm)	**Length** (μm)	**Density** (/100 μm)	**Total**	**Syn.s /Conn.**	**SO**	**SP**	**SR**	**SLM**	**Total**	**Pyr.**	**Inrn**	**Pyr. Fraction**	**Inrn. Fraction**
Neurogliaform	ML: 0.5 mm[d] ST: 1.2 mm[d]	144,000[c]	41.7[a,c,t,u]	13,200[c]	10[q]	0[c]	0[c]	17[c]	83[c]	1,320	1,228	92	93%[a]	7%[a]
Ivy	ML: 0.75 mm[e] ST: 1.31 mm[e]	176,760[c]	41.7[a,c,t,u]	16,200[c]	10[a,q]	40[e,p,c]	2[e,p,c]	50[e,p,c]	8[e,p,c]	1,620	1,507	113	93%[a]	7%[a]
Bistratified	ML: 2.09 mm[f] ST: 1.86 mm[f]	76,040[f]	21.0[c]	15,970[f,c]	10[g]	51[c,f,m]	7[c,f,m]	42[c,f,m]	0[c,f,m]	1,597	1,485	112	93%[a]	7%[a]
Backprojection	ML: 2.20 mm[h]	24,540[h]	24.8[h]	6,080[h]	10[s]	58[a,f,c]	0[a,f]	42[a,f,c]	0[a,f]	608	565	43	93%[a]	7%[a]
Double projection				6,080[h,a]	10[s]	58[a,f,c]	0[a,f]	42[a,f,c]	0[a,f]	608	559	49	92%[c,i,v]	8%[c,i,v]
Oriens retrohipp.				6,080[h,a]	10[s]	58[a,f,c]	0[a,f]	42[a,f,c]	0[a,f]	608	584	24	96%[i]	4%[i]
Trilaminar	ML: 2.45 mm[f] ST: 2.60 mm[f]	54,740[f]	28.2[f]	15,440[f,c]	10[s]	13[f,c]	17[f,c]	70[f,c]	0[f]	1,544	618	926	40%[j]	60%[j]
O-LM	ML: 0.50 mm[f] ST: 0.84 mm[f]	63,440[f]	26.6[f]	16,880[f,c]	10[s]	7[f,c]	0[f]	0[f]	93[f,c]	1,688	1,502	186	89%[o,c]	11%[o,c]
PV+ Basket	ML: 1.04 mm[f] ST: 1.19 mm[f]	46,180[f]	22.6[f]	10,440[f]	11[k] 1[f]					1,014[f,c]	943[f,c]	71[f,c]	99%[c,f]	1%[c,f]
CCK+ Basket	PD: 1 mm[l]			10,000[c,l]	8[k]	19[m]	60[m]	20[m]	1[m]	1,250	1,163	87	93%[a]	7%[a]
SCA	PD: 1.1 mm[l]			12,000[a,c,l]	6[l]	10[m,p,c]	4[m,p,c]	82[m,p,c]	4[m,p,c]	2,000	1,860	140	93%[a]	7%[a]
PPA				8,000[a,c,l]	6[l]	0[a]	0[a]	0[a]	100[a]	1,333	1,240	93	93%[a]	7%[a]
Axoaxonic	0.60 mm[n] 0.85 mm[n]			7,200[a,c,n]	6[n,c]	X[n]	X[n]			1,200[n]	1,200	0	100%[r]	0%[r]

Table 3.1: Bouton counts and laminar distribution, along with divergence, for various interneuron types. The 'density' column gives the average bouton density of the axon. The axon length and total bouton counts refer to the local (CA1 area) only. ML: medio-lateral, ST: septo-temporal, PD: proximo-distal, RC: rostro-caudal. The subscripts are as follows: a: assumed; c: calculated; d: Fuentealba et al. (2010); e: Fuentealba et al. (2008a); f: Sik et al. (1995); g: Klausberger et al. (2004); h: Sik et al. (1994); i: Jinno et al. (2007); j: Ferraguti et al. (2004); k: Foldy et al. (2010); l: Vida et al. (1998); m: Pawelzik et al. (2002); n: Li et al. (1992); o: Katona et al. (1999a), p: Szabo et al. (2012), q: Tamás et al. (2003); r: Buhl et al. (1994b); s: Maccaferri et al. (2000); t: Szabadics and Soltesz (2009); u: Armstrong et al. (2011); v: Takacs et al. (2008)

Marker	Cells Included*	Num. Cells	Synapses GABA-	GABA+
PV	All 3 types	9,200	15,322	978
CCK	CCK+ Basket	2,870	5,248	2,952
CR	IS I, II, III	6,720	1,738	462
	Hippocampal-septal	950	18,920	3,080
Weighted Avg.			9,405	1,190

Table 3.2: Total number of synapses and ratio of GABA- to GABA+ synapses for various cell types by marker (Gulyás et al., 1999; Mátyás et al., 2004; Takacs et al., 2008). The calculated number of each interneuron class is also given. We calculated the average number of GABA- and GABA+ synapses per interneuron, weighting the average by the total number of cells in each class. *We used the reported laminar distributions of the dendrites of the cells in each class to determine which interneurons to include in that class (Gulyás et al., 1999; Mátyás et al., 2004; Takacs et al., 2008).

3.2.2 Local divergence of interneurons

The divergence of interneurons (Bezaire and Soltesz, 2013) is given in Table 3.1.

To calculate both divergence and convergence as a function of neuron class (pyramidal or interneuron), we needed each interneuron's preference for innervating pyramidal cells over interneurons. For some neuron types, these data have been published. For those types for which the data were not available, we assumed they innervated their postsynaptic targets in the ratio of 92 pyramidal cell synapses to eight interneuron synapses. To arrive at this ratio, we performed the following calculation. We first calculated the average number of GABAergic synapses made onto interneurons (Table 3.2) using published data about the GABAergic synapses onto various interneuron types (Gulyás et al., 1999; Mátyás et al., 2004; Takacs et al., 2008) and our estimated neuron numbers. We weighted the number found on PV+ cells by the calculated number of PV+ basket, bistratified, and axo-axonic cells, the number found on CCK+ basket cells by the number of CCK+ basket cells, the number found on CR+ cells by the total number of IS I and IS III cells, and the number found on hippocampal-septal cells by the number of septally projecting cells to get an av-

erage of 1,274 GABAergic input synapses per interneuron (Table 3.2). We then multiplied this average by the estimated number of interneurons in the CA1 and compared it to the total number of GABAergic synapses on all pyramidal cells in the CA1. We found that GABAergic synapses onto interneurons make up only 8% of all GABAergic synapses in the CA1, while GABAergic synapses onto pyramidal cells make up the other 92%. Therefore, when the preference for innervating pyramidal cells over interneurons was not reported for a given neuron type, we assumed the ratio was 92:8 pyramidal cells:interneurons (Table 2.1).

Available local inhibitory inputs

We multiplied the total bouton estimate for each interneuron type by the total number of that interneuron from Table 2.2 and the fraction of boutons that synapse onto interneurons to arrive at the number of local inhibitory boutons available for inhibitory connections onto interneurons within the CA1.

However, this sum is not the total, as we were unable to perform this calculation for certain interneuron types for which we were missing information. For example, the contribution of the interneuron-specific interneurons were not included here because, to my knowledge, there are no published estimates of their total bouton counts. Conversely, trilaminar cells are also excluded because we do not have an estimate of their total cell number.

To continue in the presence of these gaps, we will now focus only on the cell types included in the model, for which we have both the bouton counts and the cell counts. However, our choice of focus means the model specifications for the interneuron connectivity are not to be used as overall characterizations of the *in vivo* network. Finally, we arrived at our model's total inhibitory boutons available for synapsing on interneurons by layer, as displayed in Tables 3.3 and 3.4. The eight interneuron types together contribute almost 25 million GABAergic boutons for synapsing onto other interneurons, with individual interneu-

rons contributing approximately 1000 - 9000 boutons each. As a thought experiment, how might the contribution of IS interneurons affect the total bouton count? Let's assume they contribute about 10,000 boutons each to local interneuron synapses (given that many interneurons have around 10,000 boutons, and IS cells only synapse on interneurons). Given that there are about 7,500 IS cells in the CA1, they could contribute approximately about 75 million boutons. Therefore, it is possible that IS cells contribute 75% of the local GABAergic innervation of interneurons, but they could also contribute far less.

	Ivy	Neurogliaform	O-LM	PV+ Basket	Bistratified	Axo-axonic	CCK+ Basket	SCA	Total
SLM	913421	3137798	2746428	0	0	0	28800	15360	6841807
SR	5708880	642682	0	0	1185868	0	576000	314880	8428310
SP	228355	0	0	577332	197645	0	1728000	15360	2746692
SO	4567104	0	206720	0	1439983	0	547200	38400	6799407
Total	11417760	3780480	2953148	577332	2823496	0	2880000	384000	24816216

Table 3.3: Interneuronal bouton numbers in rat CA1

	Ivy	Neurogliaform	O-LM	PV+ Basket	Bistratified	Axo-axonic	CCK+ Basket	SCA
SLM	13%	46%	40%	0%	0%	0%	0%	0%
SR	68%	8%	0%	0%	14%	0%	7%	4%
SP	8%	0%	0%	21%	7%	0%	63%	1%
SO	67%	0%	3%	0%	21%	0%	8%	1%

Table 3.4: Interneuronal bouton fractions in rat CA1

Neurogliaform family cell boutons

Neurogliaform family cells (ivy and neurogliaform cells) are known to have a much higher bouton count than other cell types. For neurogliaform family cells, we averaged two estimates of interbouton length: 2.5μm (Szabadics and Soltesz, 2009) for ivy cells in the CA3 and 2.3μm (Armstrong et al., 2011) for neurogliaform cells in the dentate gyrus for an average of 2.4μm. Also, 78% of boutons are not involved in classical synapses, instead affecting other neurons via volume transmission (Olah et al. (2009), in somatosensory cortex). Therefore, we subtracted 78% of boutons from the total bouton count to determine the number of classical synapses made by each cell. However, the boutons not participating in the classical synapses are still involved with volume transmission (Olah et al. (2009), in somatosensory cortex) and are therefore functionally relevant. Their contribution should be considered in any theoretical or computer model that includes ivy and neurogliaform synapses. For both neurogliaform and ivy cells, we assumed they made 10 classical synapses per connection (Table 2.1). This assumption is based on the observation that neurogliaform cells in the somatosensory cortex were predicted to make 10 synapses per connection, though the status of those synapses as classical (with a corresponding postsynaptic element) was not confirmed (Tamás et al., 2003).

Layer					
SO	**SP**	**SR**	**SLM**	**Ref.**	**Somata Layers**
75%	0%	25%	0%	Fuentealba et al. (2008a)	Pyramidale
6%	3%	75%	16%	Szabo et al. (2012)	Pyramidale, Radiatum
40%	2%	50%	8%	Average	

Table 3.5: Laminar distribution of ivy cell boutons. Both studies used Sprague-Dawley rats.

Ivy cell boutons The axonal extent of the ivy cells is 0.75mm in the medio-lateral direction and 1.31mm in the rostro-caudal direction (Fuentealba et al., 2008a). Their total axonal length was calculated by comparison with a bistratified cell axonal arbor. By measuring the relative axonal lengths of ivy and bistratified cells within a 100x100x70 μm volume surround-

ing the soma, ivy cells were found to have an axon length 2.2 times that of bistratified cells (Fuentealba et al., 2008a). A complete bistratified cell axon had previously been measured as 78,800 μm; therefore, we calculated a total ivy cell axon length of 176,760 μm. We calculated the total bouton count, at a density of one per every 2.4 μm, as 73,650. Considering only 22% of synapses make classical synapses (Olah et al., 2009), we calculated 16,200 boutons available for classical synapses. We assumed ivy cells made 10 classical synapses on each postsynaptic cell (Table 2.1). Therefore, they diverge to innervate 1,620 cells. Their relative preference for synapsing on pyramidal cells versus interneurons is not known, so we used the ratio of 92:8 as discussed above (Table 2.1). We calculated that they contact 1,490 pyramidal cells and 130 interneurons. Ivy cells make most of their synapses in the strata oriens and radiatum (Fuentealba et al., 2008a; Klausberger, 2009). Different studies have found different distributions for ivy cell axons, as shown in Table 3.5. We took the average of two studies (Fuentealba et al., 2008a; Szabo et al., 2012), assuming that ivy cells make 40% of their synapses in the stratum oriens and 50% in the stratum radiatum.

Neurogliaform cell boutons A neurogliaform cell filled within the confines of a 400μm slice has more boutons (13,000) than a complete fill of a basket cell axon (10,000) (Halasy et al., 1996; Vida et al., 1998). Also, within an equivalent volume, neurogliaform cell axons have a release probability about five to six times that of basket cells (Olah et al. (2009), in somatosensory cortex). Therefore, each neurogliaform cell has roughly 60,000 boutons. Because 78% of boutons are not involved in classical synapses (Olah et al. (2009), in somatosensory cortex), we determined 13,200 boutons were available for synapses. As we assumed neurogliaform cells make 10 classical synapses per connection (Table 2.1), their divergence was calculated as 1,320 cells. We assumed they innervate pyramidal cells and interneurons in a 92:8 ratio (Table 2.1) for a total of 1,214 pyramidal cells and 106 interneurons.

Neurogliaform axons concentrate around the cell in a tight, radially distributed cloud. The axonal extent of neurogliaform cells was found to be 0.5mm in the mediolateral axis and 1.2mm in the septotemporal axis (Fuentealba et al., 2010). Given the total number of boutons and calculated bouton density, we calculated the total axonal length as 144,000μm. The axons are mostly found within the stratum lacunosum-moleculare (Price et al., 2005). However, as some neurogliaform cells are found within the stratum radiatum (see above), we assumed the distribution of boutons across the strata radiatum and lacunosum-moleculare matched the distribution of somata across those two layers (83% in the stratum lacunosum-moleculare, 17% in the stratum radiatum).

O-LM cell boutons The axonal extent of O-LM cells is rather compact, only 500μm in the medio-lateral direction and 840μm in the septo-temporal direction (Sik et al., 1995). O-LM cells have a local axonal length of 62,490μm and a bouton density of 26.6/100μm (Sik et al., 1995). We calculated a local CA1 bouton count of 16,370 (Sik et al., 1995). A light microscopy study of O-LM to pyramidal cell connections showed a range of three to 17 potential synapses per connection (Maccaferri et al., 2000). We took the average of 10 synapses per connection, giving a divergence of 1,637 cells (Table 2.1). There are 74% of O-LM cell synapses made onto non-GABAergic cells, while only 9% are made on GABAergic cells and 17% are unidentifiable (Katona et al., 1999a). Of the known synaptic targets, the ratio was 89% of synapses made on pyramidal cells to 11% of synapses made on interneurons (Katona et al., 1999a) for a total innervation of 1,457 pyramidal cells and 180 interneurons. Within the CA1, most of the O-LM cell boutons are found in the stratum lacunosum-moleculare, though a variable amount can be found in the stratum oriens. Sik et al. (1995) found 93% of axon collaterals in the stratum lacunosum-moleculare and 7% in stratum oriens.

Other SOM+ cell boutons The other projection cells of the stratum oriens with local axons in the CA1 usually innervate the strata radiatum and oriens. In one case, a so-called

back-projection cell made 25,000 synapses in the hippocampus (Sik et al., 1994). Of the axon length within the hippocampus, 24.3% remained within the CA1, giving an estimate of 6,080 boutons in the CA1 (Sik et al., 1994). Here, we assumed the other projection neurons with local axon collaterals also had a similar number of boutons in the CA1 (Table 2.1). For each projection cell with axons in strata oriens and radiatum, we assumed their local boutons were distributed similarly as bistratified cells (Table 2.1), between the stratum oriens and radiatum, with 58% of their length in the oriens and 42% in the stratum radiatum (following a bistratified cell with its soma in the stratum oriens, from Sik et al. (1995)). As the few collaterals within the stratum pyramidale did not exhibit a significant number of boutons, we were concerned only with the relative proportions in the oriens and radiatum.

For some types of SOM+ cells, information was available about their relative preference for synapsing on pyramidal cells or interneurons. Oriens-retrohippocampal cells send 96% of their boutons to pyramidal cells (Jinno et al., 2007). Jinno et al. (2007) also found that double projection cells send 86% of their local boutons to pyramidal cells and 14% to interneurons, whereas Takacs et al. (2008) found that, of the known local targets of septally projecting cells, 97% are on pyramidal cells and 3% are on interneurons. We averaged these two data points to calculate that double projection cells make 92% of their local targets on pyramidal cells and 8% on interneurons. Additionally, there appears to be a subset of septally projecting cells that target interneurons locally (Gulyás et al., 2003). It is possible that interneuron-specific septally projecting cells constitute the other group of septally projecting cells mentioned above. This other group is CB- and may align with the 18% of septally projecting cells seen to express CR (Jinno, 2009).

For each of the SOM+ cell types, we assumed the cells contacted their postsynaptic targets with 10 synapses each (Table 2.1). Because we assumed the same bouton counts for double projection, so-called back projection, and oriens-retrohippocampal cells, they all had a calculated divergence of 608 cells. Their preference for innervating pyramidal cells differed,

however. Double projection cells may innervate 559 pyramidal cells and 49 interneurons, while oriens-retrohippocampal cells innervate 584 pyramidal cells and 24 interneurons.

PV+ basket cell boutons The extent of the PV+ basket cell axon was found to be 1,185μm in the septotemporal direction and 1,042μm in the medio-lateral direction (Sik et al., 1995). The total axon length was 46,180μm (Sik et al., 1995). At a density of 22.6 boutons per 100μm, the estimated total bouton count per PV+ basket cell was 10,440 (Sik et al., 1995). Most of the boutons were found within the pyramidal layer, with few found in the strata oriens or radiatum (Sik et al., 1995). Though the observed number of basket cell synapses per connection varies from 2 to 12 (Buhl et al., 1994a; 1995; Sik et al., 1995; Halasy et al., 1996; Foldy et al., 2010, in mouse), here we took PV+ basket cells to make about 11 synapses on each pyramidal cell (Foldy et al., 2010, in mouse). However, PV+ basket cells have been shown to make connections comprising single or very few synapses on other PV+ interneurons (Sik et al., 1995) (but see Cobb et al. (1997), where a basket cell innervated a bistratified cell with 12 synapses) so we assumed they made only one synapse on all connections with other interneurons (Table 2.1). Sik et al. (1995) found PV+ basket cells connect with pyramidal cells and other PV+ cells with equal probability, which we took to mean in proportion to the number of each cell type. Therefore, we calculated each PV+ basket cell contacts 1,014 other cells, 943 pyramidal cells and 71 other interneurons.

Bistratified cell boutons Bistratified cells project to the strata oriens and radiatum (Klausberger, 2009). A range of values has been found for the number of boutons present on each bistratified cell. Pawelzik et al. (2002) found a mean of 4,000 boutons, in contrast to an earlier finding of 15,970 boutons within the CA1 for a bistratified cell with its soma in the oriens (Sik et al., 1995). Additionally, Halasy et al. (1996) found that a bistratified cell axon within a 400μm slice contained 8,752 boutons; therefore, the finding of 15,970 boutons in a complete axon within the CA1 seems likely. The bistratified cell observed by Sik et al.

(1995) had a local axonal length of 76,040μm and a bouton density of 21.0 boutons per 100μm.

Bistratified cells make 10 to 11 synaptic contacts with each cell they innervate (Klausberger et al., 2004) (but see Buhl et al. (1994a) and Miles et al. (1996), where five to nine were found). Therefore, each bistratified cell diverges to contact approximately 1,597 cells. Because the relative preference for synapsing on pyramidal cells was not given, we assumed (Table 2.1) that bistratified cells synapse on pyramidal cells and interneurons in a 92:8 ratio, for a total divergence of 1,469 pyramidal cells and 128 interneurons.

Layer					
SO	**SP**	**SR**	**SLM**	**Ref.**	**Somata Layers**
42%	6%	52%	0%	Pawelzik et al. (2002)	Pyramidale, typical
53%	14%	33%	0%	Pawelzik et al. (2002)	Oriens, atypical
58%	0%	42%	0%	Sik et al. (1995)	Oriens
51%	7%	42%	0%	Average	

Table 3.6: Laminar distribution of bistratified cell boutons.

Laminar distribution data for the bistratified cell was available from both Pawelzik et al. (2002) and Sik et al. (1995); an average was calculated from the two references (Table 3.6) such that 51% of collaterals were found in the stratum oriens, 7% in the pyramidale, and 42% in the radiatum. Qualitative observations of laminar axonal distribution were also available (Fuentealba et al., 2008a; Halasy et al., 1996). The medio-lateral extent of the axon was 1.15 mm, and rostro-caudally it was 1.53mm (Klausberger et al., 2004).

Axo-axonic cell boutons An experimentally observed axo-axonic cell had an elliptically shaped axonal arbor, with a 600 by 850μm extent (Li et al., 1992). Each axo-axonic cell had multiple rows of boutons, where each row corresponded to the synapses made on one postsynaptic axon. Each row contained two to 10 boutons (Li et al., 1992), with an observed divergence of one axo-axonic cell onto 1,200 pyramidal cells (Li et al., 1992). Therefore, we calculated that each axo-axonic cell has 2,400 to 12,000 boutons and assumed an average

of 7,200 boutons per axo-axonic cell (Table 2.1). Axo-axonic cells appear to contact only pyramidal cells (Buhl et al., 1994a;b).

CCK+ basket cell boutons Comparably less information is available about CCK+ basket cell axonal arbors than PV+ basket cell axons. Axonal extent, total length, and bouton density were generally not reported, though the proximal-distal extent of a CCK+ basket cell axon was found to be 1mm (Vida et al., 1998).

The study of stratum radiatum basket cells (presumably CCK+, Table 2.1) showed that a basket cell axon within a 400 μm slice contained almost 8,000 boutons (Vida et al., 1998). We assumed (Table 2.1) the same bouton distribution as for the PV+ basket cells (20% more boutons outside the slice, as in Halasy et al. (1996)), so the overall bouton count for that cell is likely around 10,000. Though the observed number of basket cell synapses per connection varies from two to 12 (Buhl et al., 1994a; 1995; Sik et al., 1995; Halasy et al., 1996; Miles et al., 1996; Foldy et al., 2010, in mouse), here we took CCK+ basket cells to make about eight synapses per connection (Foldy et al., 2010, in mouse). It is not known whether CCK+ basket cells make fewer synapses in their connections with other interneurons (as PV+ basket cells do), so we assumed they also made eight synapses per connection with other interneurons (Table 2.1). This gave a divergence of 1,250 cells: 1,150 pyramidal cells and 100 interneurons assuming the 92:8 ratio of innervation (Table 2.1). The average laminar distribution of boutons across several CCK+ basket cells was shown to be 19% in the stratum oriens, 60% in the stratum pyramidale, 20% in the stratum radiatum, and 1% in the stratum lacunosum-moleculare (Pawelzik et al., 2002).

SCA cell boutons The axonal length and bouton density of SCA cells has not been reported. The proximal-distal extent of the axon was found to be 1.1mm (Vida et al., 1998). A 400 μm slice contained 6,000 boutons (Vida et al., 1998). By comparison, a bistratified

cell in the middle of a 400 μm slice had an axon with almost 8,800 boutons (Halasy et al., 1996). However, the full, local axonal arbor of another bistratified cell had 15,970 boutons overall (Sik et al., 1995), suggesting that the bouton distribution of bistratified cells extends significantly beyond the confines of a 400 μm slice. Therefore, we assumed the SCA cell axon was distributed similarly and also had only 50% of its boutons within the confines of the 400 μm slice (Table 2.1); we calculated a complete axon as having approximately 12,000 boutons. SCA cells make approximately six synapses per connection (Vida et al., 1998), so they may contact roughly 2,000 cells. We assumed they contact pyramidal cells and interneurons in a ratio of 92:8 for a total of 1,840 pyramidal cells and 160 interneurons. SCA cells preferentially synapse in the stratum radiatum (Vida et al., 1998; Szabo et al., 2012), with an average distribution of 82% of axons in the stratum radiatum. Table 3.7 shows the different laminar distributions that have been observed for SCA cells.

Layer				
SO	**SP**	**SR**	**SLM**	**Ref.**
0%	0.2%	97.4%	2.4%	Vida et al. (1998)
19.2%	8.2%	67.4%	5.2%	Szabo et al. (2012)
9.6%	4.2%	82.4%	3.8%	Average

Table 3.7: Laminar distribution of SCA cell boutons.

ADI cell boutons No quantitative information has been reported about ADI cell axons. ADI cell boutons are known to innervate the main apical dendrite of pyramidal cells in preference to the oblique dendrites (Klausberger et al., 2005; Klausberger, 2009). If ADI cells gave rise to one tenth of the 111 GABAergic synapses on the distal main apical dendrite of the pyramidal cells (Megías et al., 2001), each of the 390 ADI cells would need approximately 8,870 boutons.

PPA cell boutons Though a 400μm slice was found to contain 8,000 boutons, over half of them were positioned outside the CA1 (Vida et al., 1998). We used the same logic as

with the SCA cell to estimate a total of 16,000 boutons (Table 2.1). Considering half of the boutons as being within the CA1 (Vida et al., 1998) gave a total of 8,000 boutons. PPA cells are thought to make six synapses per connection as seen with SCA cells (Vida et al., 1998), for a divergence of 1,333 cells. We assumed they followed the ratio of 92:8 for innervation, for a total divergence of 1,227 pyramidal cells and 106 interneurons (Table 2.1).

IS cell boutons Bouton counts of the IS cells were not available, probably due to the difficulty of determining an average bouton density for their axon collaterals. The bouton density of IS cells varies significantly along the axons (Acsady et al., 1996). This variability in bouton density, with large lengths of axon in which few boutons are found, interspersed with sections of high bouton density, may arise because of these interneurons selectivity in only synapsing on other interneurons (Acsady et al., 1996).

Trilaminar cell boutons There was sufficient information about trilaminar cells to estimate their divergence. Trilaminar cells innervate mainly the stratum oriens and stratum radiatum, but also the stratum pyramidale (Klausberger, 2009). They should be considered distinct from other projection cells whose axons ramify mainly in the strata radiatum and oriens, the cell types formerly known as oriens-bistratified cells (Maccaferri et al., 2000). Of the synapses made within the CA1, a trilaminar cell made 70% of its synapses in the stratum radiatum, 17% in the stratum pyramidale, and 13% in the stratum oriens (Sik et al., 1995). The observed axonal length and bouton density suggested the trilaminar cell had 15,800 boutons within the hippocampal formation, with 15,440 boutons in the CA1 (Sik et al., 1995). A trilaminar cell from a different study made 40% of its synapses on pyramidal cells, while 60% were made onto interneurons (Ferraguti et al., 2005). The trilaminar cell observed in (Ferraguti et al., 2005) had a more extensive axonal projection to the subiculum and most of its axon collaterals ramified in the stratum oriens, rather than the stratum radiatum, as compared to the trilaminar cell in Sik et al. (1995). Note that the trilaminar cell from

Ferraguti et al. (2005) was considered as an oriens-retrohippocampal cell in a later study (Jinno et al., 2007). We assumed trilaminar cells contacted each postsynaptic target with 10 synapses (Table 2.1), giving a local divergence of 1,544 cells (618 pyramidal cells and 926 interneurons).

Dendrite subclass	Total Synapse number	Total GABA-	Total GABA+
Ori/dist	$12,141 \pm 3,255$	$11,735 \pm 3,147$	405 ± 108
Ori/prox	479 ± 161	246 ± 83	233 ± 78
Rad/T/prox	196 ± 33	3.8 ± 0.6	193 ± 32
Rad/T/med	340 ± 138	277 ± 112	63.0 ± 25.6
Rad/T/dist	$2,219 \pm 980$	$2,171 \pm 959$	47.6 ± 21.0
Rad/t	$14,862 \pm 3,249$	$14,425 \pm 3,154$	437.1 ± 95.6
L-M/T	565 ± 349	485.7 ± 300.0	79.6 ± 49.1
L-M/M	493 ± 175	418.0 ± 148.4	75.5 ± 26.8
L-M/t	$1,051 \pm 365$	873.0 ± 303.0	178.6 ± 62.0
Total	$32,351 \pm 5,486$	$30,637 \pm 5,259$	$1,713 \pm 261$

Table 3.8: Number of GABA- and GABA+ synapses on pyramidal cell dendrites by layer and thickness of dendrite, from Table 3 in Megías et al. (2001). T: thick, M: medium, t: thin, dist: distal, med: medial, prox: proximal, Ori: stratum oriens, Rad: stratum radiatum, L-M: stratum lacunosum-moleculare

3.2.3 Divergence of afferents

We used bouton counts and synapse counts from EM studies on the dendrites and somata of CA1 pyramidal cells to quantify their inputs (see (Megías et al., 2001); we have reproduced their data with permission in our Table 3.8). We included the contributions of afferents to the CA1 as well as the local axonal projections of CA1 pyramidal cells and interneurons. In Bezaire and Soltesz (2013), we employed a novel concept to move beyond the lack of information regarding connections onto interneurons. We calculated the convergence of afferents and intrinsic inputs onto a hypothetical average interneuron and compared it to the synapse data available for several neurochemical classes of interneuron (Gulyás et al., 1999; Mátyás et al., 2004). However, that hypothetical average was not adequate for constraining our network model, and so here we ventured further in our assumptions in order to progress

with our estimates for use in our network constraints.

Glutamatergic afferents of the CA1

Excitatory inputs arrive mainly from the CA3 (Schaffer Collaterals) and the entorhinal cortex, but also from the nucleus reuniens of the thalamus and other areas (Wouterlood et al., 1990; Sotty et al., 2003; Kajiwara et al., 2008; Klausberger and Somogyi, 2008). Here, we calculated the inputs from the Schaffer Collaterals and entorhinal cortex. The Schaffer Collaterals represent the main excitatory input to the CA1. The entorhinal cortex supplies significantly less excitatory input. There are additional, smaller excitatory inputs as well, though insufficient data exist to quantify them. For example, the subiculum is known to target all layers of the CA1 (Köhler, 1985). The amygdalar input to the CA1 is also excitatory (Klausberger and Somogyi, 2008). There are also some connections from the subiculum, presubiculum, and parasubiculum as reviewed in Van Strien et al. (2009). In addition, there is glutamatergic input from the septum (Sotty et al., 2003).

It should be noted that the count of non-GABAergic synapses received by the pyramidal cell includes synapses that are not glutamatergic (Megías et al., 2001). Some non-GABAergic synapses are contributed by the cholinergic pathway from the septum. Less commonly, the serotonergic pathwaymay innervate sparsely the pyramidal cells, though it appears to rely mostly on volume transmission to pyramidal cells (Gulyas et al., 1990; Borhegyi et al., 2004).

Schaffer Collaterals The CA3 is estimated to contain 230,000 neurons, within the range for 30-day-old Wistar rats (210,000-250,000, from West et al., 1991). Approximately 11% of neurons in the hippocampus are interneurons (Woodson et al. (1989), also see our Table 2.1), for a total of 204,700 pyramidal cells and 25,300 interneurons in the CA3.

Though the Schaffer Collaterals innervate both the strata radiatum and oriens of the CA1,

there is a gradient in innervation where the CA3c neurons prefer the stratum radiatum and the CA3a neurons prefer the stratum oriens (Amaral and Witter, 1989). The CA3c neurons also tend to synapse more temporally whereas the CA3a neurons synapse more septally (Amaral and Witter, 1989). Therefore, we averaged data from a CA3c and a CA3a neuron to calculate the average input from a CA3 neuron to the CA1. The CA3c pyramidal cell was shown to have about 39,200 boutons within the dorsal area of the ipsilateral hippocampus (Wittner et al., 2007). Approximately 70% of these boutons were found in the CA1 region, so that this single pyramidal cell may contribute 27,440 boutons to the Schaffer Collateral pathway (Wittner et al., 2007). This CA3c neuron was shown to make 94% of its Schaffer Collateral synapses in the stratum radiatum and only 3% in the stratum oriens (Wittner et al., 2007). In contrast, the CA3a neuron was shown to make 64% of its synapses in the stratum oriens, 15% in the stratum pyramidale, and 21% in the stratum radiatum (Sik et al., 1993), for a total of 15,295 boutons. The relative laminar distributions of the Schaffer Collateral boutons yielded the bouton counts per lamina shown in Table 3.9. We calculated the input of an average CA3 neuron to the Schaffer Collateral pathway, assuming that the bouton distributions for the CA3a and CA3c neurons could be taken as the extreme examples on each end of a uniform gradient (Table 2.1).

	Septal		**Temporal**	
Layer	%	**Boutons**	%	**Boutons**
Lac. Mol.	0	0	0.4	67
Radiatum	20.8	2,960	94.2	15,797
Pyramidale	15.4	2,191	2.4	402
Oriens	63.8	9,079	3	503
Total		14,230		16,770

Table 3.9: Schaffer Collateral bouton counts per CA1 pyramidal cell based on a CA3a/septal distribution or a CA3c/temporal distribution.

However, this calculated contribution is certainly low. The CA1 pyramidal cell has a total of 28,860 excitatory synapses on its dendrites in the stratum radiatum and oriens (Megías et al., 2001) (see Table 3.8), which are mainly innervated by the Schaffer Collaterals. This number

	Exc. Synapses on a CA1 Pyramidal Cell		
Layer	**Total**	**S.C. Inputs**	**Remaining**
Lac. Mol.	1776	34	1,742
Radiatum	16,878	8,871	7,547
Pyramidale		921	
Oriens	11,982	3,233	8,288
Total	**30,636**	**13,059**	**17,577**

Table 3.10: Comparison of the total available excitatory synapses on a CA1 pyramidal cell with the calculated boutons available from the Schaffer Collateral path per CA1 pyramidal cell. The remaining "unclaimed" synapses left after subtracting the Schaffer Collateral inputs are also given. Because no dendrites were reported in the pyramidal layer (Megías et al., 2001), the boutons reported in the pyramidal layer were evenly divided between the stratum radiatum and stratum oriens. S. C.: Schaffer Collateral.

is much greater than the input calculated from the average of the CA3a and CA3c neurons (Table 3.9). There are two reasons for the discrepancy. First, the contralateral CA3 axons contribute a significant number of boutons to each CA1 pyramidal cell. Second, at least in the case of the Wittner et al. (2007) axon, the axonal extent of the filled CA3 neuron may have extended outside the slices that contributed to the bouton count, so that the ipsilateral axon fill was incomplete (the axon published in Wittner et al. (2007) was reconstructed from 48 slices 70 μm thick in the ipsilateral dorsal hippocampus for a total of 39,200 boutons; earlier work by Li et al. (1994) had estimated a CA3 pyramidal cell could contribute up to 60,000 boutons to the ipsilateral hippocampus). In the case of Sik et al. (1993), the axon was reconstructed from 32 sections 60 μm thick of the ipsilateral hippocampus and was said to be a complete reconstruction of the ipsilateral axon. By comparing the total number of available synapses on the CA1 pyramidal cell dendrites in the strata radiatum and oriens with the reported bouton counts from the CA3 pyramidal cells, we estimated that the reported counts represent only 46% of the boutons expected to project to the ipsilateral and contralateral CA1 from each CA3 neuron. The comparison of Schaffer Collateral boutons per CA1 pyramidal cell and available synapses on the CA1 pyramidal cell (as calculated in Megías et al. (2001)) is shown in Table 3.10. To calculate the boutons available per CA1 pyramidal cell, we multiplied the average CA1-area bouton count by the number of CA3

pyramidal cells, took 93% of the total as synapsing on CA1 pyramidal cells (Takács et al., 2012), and then divided that total by the number of CA1 pyramidal cells.

We also considered the divergence of the CA3 pyramidal cells within the ipsilateral CA1. For pyramidal cells within the CA3c, most connections made onto CA1 pyramidal cells comprise one to two synapses (Ropireddy and Ascoli, 2011), for an ipsilateral divergence of 12,760 to 25,520 CA1 pyramidal cells. Given the total number of CA1 pyramidal cells, this range corresponded to each CA3c pyramidal cell contacting 4% to 8% of CA1 pyramidal cells ipsilaterally, in line with the 4% to 9% potential CA1 pyramidal cell connectivity determined for CA3c pyramidal cells using 3D anatomical reconstruction data (Ropireddy and Ascoli, 2011). The ipsilateral CA1 divergence for the CA3a cell, with its significantly lower bouton count in the CA1, is expected to be much lower. Though no CA3a cells were included in the work of Ropireddy and Ascoli (2011), a CA3b cell was shown to have a much lower connectivity onto the CA1 pyramidal cells % compared to connections from the CA3c cells.

Other excitatory afferents The main source of glutamatergic inputs to the stratum lacunosum-moleculare of the CA1 is the temporoammonic pathway from the entorhinal cortex (Andersen et al., 2007). This pathway is likely responsible for the majority of the excitatory synapses on the distal apical dendrites of CA1 pyramidal cells, though the glutamatergic inputs from the nucleus reuniens in the thalamus also make up a significant portion of synapses (Wouterlood et al., 1990). The input from the nucleus reuniens is differentiated by the presence of VGLUT2 in the boutons (Halasy et al., 2004). The VGLUT2+ boutons are only found in the stratum lacunosum-moleculare (Halasy et al., 2004). We do not know the relative proportion of inputs from the entorhinal cortex versus the nucleus reuniens, so we have assumed that the entorhinal cortex supplies most of the excitatory inputs (Table 2.1). Together, they contribute about 1,742 synapses, which is the number of distal apical synapses found on a pyramidal cell (Megías et al., 2001) after subtracting a small contribu-

tion of the Schaffer Collaterals to the stratum lacunosum-moleculare (see contribution from a CA3c cell, Table 3.9).

Both the medial and lateral entorhinal cortex project to the CA1, though the lateral projection appears to be stronger (Witter et al., 1988). The number of principal neurons in the entorhinal cortex layer III was found to be 250,000, with 130,000 in the medial entorhinal cortex and 120,000 in the lateral entorhinal cortex (Mulders et al., 1997). We made a cursory estimate of the divergence of the entorhinal cortical neurons to the stratum lacunosum-moleculare. We assumed that both medial and lateral parts contributed proportionally to the stratum lacunosum-moleculare-targeting temporoammonic path, and that all 1,742 of the stratum lacunosum-moleculare synapses were innervated by the temporoammonic path (Table 2.1). With those assumptions, each entorhinal cortical neuron would need to provide an average of 2,171 boutons to the stratum lacunosum-moleculare-targeting part of the temporoammonic path. Given that the nucleus reuniens input may be significant, this calculation of divergence may be overestimated.

The temporoammonic path also includes an alvear targeting component. Although there are no solid quantitative comparative data, the alvear pathway is considered a minor source of entorhinal cortical input compared to the temporoammonic pathway that targets the stratum lacunosum-moleculare directly, so it must contribute significantly fewer than 1,742 synapses to each CA1 pyramidal cell.

3.3 Convergence

3.3.1 Convergence onto pyramidal cells

Next, we calculated the convergence of various neuron types onto a CA1 pyramidal cell. We compared the calculated inputs with the observed synapses on CA1 pyramidal cell dendrites and somata (see Table 3.8, which reproduces data from Megías et al. (2001)).

Excitatory synapses

Given the calculations above, we estimated that each pyramidal cell received 13,059 to 28,697 synapses from the Schaffer Collateral pathway. Additionally, each pyramidal cell received up to 1,742 synapses from the entorhinal cortex via the stratum lacunosum-moleculare-targeting portion of the temporoammonic pathway, and a smaller number of synapses from the entorhinal cortex via the alvear pathway. Previously, we had calculated that each pyramidal cell receives 197 synapses from other local collaterals. In total, a CA1 pyramidal cell receives approximately 30,636 excitatory inputs (Megías et al., 2001). A summary of the excitatory convergence onto pyramidal cells is given in Table 3.11.

Input Type	**Calculated Boutons/ CA1 Pyr. Cell.**
Entorhinal Cortex via SLM	$< 1,742$
Schaffer Collaterals	$13,059 - 28,860$
Entorhinal Cortex via Alveus	$<< 1,742$
Local Collaterals	197

Table 3.11: Calculated convergence of excitatory synapses onto a CA1 pyramidal cell, based on observations of CA1 pyramidal cell dendrites from Megías et al. (2001). The lower end of the Schaffer Collateral range is based on the bouton counts from axonal fills of CA3 cells, while the upper end of the range is based on CA1 pyramidal cell synapse counts from Megías et al. (2001). SLM: stratum lacunosum-moleculare

Perisomatic GABA+ synapses

Basket cells are known to synapse on and around the pyramidal cell soma, with CCK+ cell synapses being found further out from the soma than PV+ basket cell synapses (Foldy et al., 2010, in mouse). There are approximately 92 synapses, all GABAergic, on the pyramidal cell body; including the proximal oriens and thick radiatum dendrites that extend up to 100 μm from the soma, there are 518 perisomatic, GABAergic synapses (Megías et al., 2001). We multiplied the number of each type of basket cell by the number of boutons (Table 3.1) to get the total number of basket cell boutons in the CA1. Then we computed the average number of boutons that can synapse on each pyramidal cell, taking into account their preference for innervating pyramidal cells as discussed earlier. That gave a total of 289 basket cell synapses per pyramidal cell. We assumed that only basket cells synapse on the soma (Table 2.1). Since only 92 of these 289 synapses are found directly on the soma, we calculated that only 32% of basket cell synapses are on the soma. This calculation is slightly lower than the 51% observed experimentally for basket cells generally (Buhl et al., 1994a), or the 48 to 77% observed for CCK+ basket cells, specifically (Pawelzik et al., 2002). Subtracting the 92 synapses found on the soma (assuming all somatic GABAergic synapses are made by basket cells, Table 2.1) gave a total of 197 proximal dendritic synapses made by basket cells. That left 229 of the 518 perisomatic synapses (somatic, proximal basal, and thick, proximal radiatum synapses) unclaimed. However, since other cell types occasionally make perisomatic synapses as well (such as trilaminar cells (Ferraguti et al., 2005), bistratified cells (Buhl et al., 1994a), or ivy cells (Fuentealba et al., 2008a)), those could account for some of the perisomatic synapses found on the pyramidal cell.

To determine the convergence of basket cells onto a pyramidal cell, we divided the total number of synapses contributed from each basket cell type by the average number of synapses per connection made by each basket cell type. The ratio of PV:CCK basket cell synapses on the soma is about 2:1(Foldy et al., 2010, in mouse). Therefore, we calculated that each

pyramidal cell is innervated by 17 PV+ basket cells and 13 CCK+ basket cells.

Axon initial segment GABA+ synapses

There are at least 25 synapses on the axon of the CA1 pyramidal cell (Megías et al., 2001). This count only includes proximal synapses, though there are likely more synapses distally (Megías et al., 2001). These axonal synapses were not included in the dendritic or somatic counts for pyramidal cells, given in Table 3.8. Dividing the total number of boutons from all axo-axonic cells by the total number of pyramidal cells in the CA1, we calculated that there are 34 axo-axonic boutons for each pyramidal cell (assuming they only innervate pyramidal cells, see (Buhl et al., 1994a;b)) and that a pyramidal cell receives input from about six axo-axonic cells on its proximal axon.

Proximal dendritic GABA+ synapses

The number of GABAergic synapses found on the proximal basal and apical dendrites of a pyramidal cell total 953 (Table 3.8) (Megías et al., 2001). A number of interneuron types synapse on these proximal dendrites of the pyramidal cell, which include the dendrites in the strata oriens and radiatum. This category encompasses bistratified cells, ivy cells, Schaffer Collateral-associated (SCA) cells, apical dendritic innervating (ADI) cells, large calbindin cells, trilaminar cells, and various projection cells (Klausberger and Somogyi, 2008). Note that some of the neurons associated with the stratum lacunosum-moleculare also synapse in the stratum radiatum. For example, neurogliaform cells located close to the strata lacunosum-moleculare/radiatum border make many of their synapses in the stratum radiatum (Vida et al., 1998). For this assessment, we generally assumed that the distally projecting neuron types only make synapses on the distal apical dendrites in the stratum lacunosom-moleculare (Table 2.1). However, we did account for the subset of neurogliaform

cells identified in the stratum radiatum as synapsing within the stratum radiatum (see neuron numbers calculation above) and a small fraction of O-LM cell axons remaining in the stratum oriens.

Bistratified cell synapses Bistratified cells synapse on the small and medium-sized dendrites, generally avoiding the main apical dendrite of the pyramidal cell (Klausberger et al., 2004). Multiplying the average number of boutons per bistratified cell by the estimated number of bistratified cells gave an average of 104 boutons per pyramidal cell, assuming that 92% of their boutons innervate pyramidal cells. Given that bistratified cells usually make 10 synapses per connection, each pyramidal cell receives input from 10 bistratified cells. The inputs from the bistratified cells represent about 7.5% of the inhibitory input synapses on the dendrites in strata oriens, pyramidale, and radiatum dendrites of the CA1 pyramidal cell.

Projection cell synapses To calculate the contributions of the double projection and oriens-retrohippocampal cells to CA1 pyramidal cell innervation, we assumed that they had a similar number of local boutons as the so-called back-projection cell (Table 2.1). We calculated that these projection cells (which make up 4% of interneurons) could supply 2% of the available inhibitory dendritic synapses on CA1 pyramidal cells. The contribution of the other projection cell types could not be calculated since their cell numbers are unknown.

Ivy cell synapses Given the number of ivy cells and the calculation of their classical bouton count, we estimated that a CA1 pyramidal cell receives 422 synapses from ivy cells. Ivy cells therefore innervate 28% of the synapses on the strata radiatum, pyramidale, and oriens dendrites of the pyramidal cell. Since ivy cells make about 10 synapses per connection, each pyramidal cell receives classical synaptic input from 42 ivy cells. If there are ivy cells that only influence pyramidal cells through volume transmission without making any classical

synapses, we have not included them in this calculation of convergence.

Stratum radiatum neurogliaform cell synapses As neurogliaform cells are often found near the border of the strata radiatum and lacunosum-moleculare, their axons sometimes fall within the stratum radiatum. Here, we made the simplifying assumption that those neurogliaform cells found in the stratum radiatum contribute their boutons to dendrites in the stratum radiatum. Earlier we had calculated that there were 610 neurogliaform cells in the stratum radiatum; therefore, they are expected to contribute a total of 24 boutons to the stratum radiatum dendrites of each CA1 pyramidal cell. Since neurogliaform cells make 10 synapses per connection, a single CA1 pyramidal cell likely receives classical synaptic input from two neurogliaform cells in the stratum radiatum. As with the ivy cells, if some neurogliaform cells contact pyramidal cells only through volume transmission but not classical synapses, they were not included in this calculation.

Schaffer collateral associated cell synapses SCA cells synapse mainly in the stratum radiatum, but also in the stratum oriens. In the stratum radiatum, SCA cells prefer to synapse on the oblique dendrites rather than the main shaft (Klausberger, 2009). We estimated that a CA1 pyramidal cell receives 14 synapses from SCA cells. Since SCA cells make about six synapses per connection, each pyramidal cell receives input from about two SCA cells.

Apical dendritic innervating cell synapses ADI cells have similar targets to SCAs but tend to innervate the main shaft more than SCA cells; in general, they prefer the large apical dendrites (Klausberger et al., 2005; Klausberger, 2009). We do not know much about the axonal length or bouton density of ADI cells. We estimated above that there are 390 ADI cells in the CA1, but without any bouton data, their convergence cannot be estimated.

Other proximal dendritic synapses Several other neurons known to innervate the basal and proximal apical dendrites have not been included here, such as so-called back projection, trilaminar, RADI, large calbindin, and some lesser-known CCK+ cell types. The numbers of these neurons are not known very precisely, nor are their bouton counts, with the exception of the bouton counts for the trilaminar cells.

Assessing the difference between interneuron boutons available for synapsing onto pyramidal cells and GABAergic synapses on pyramidal cell dendrites, we find that there are still available synapses on the dendrites for which we have not determined the source. In the stratum oriens, 290 inhibitory synapses on the basal dendrites (128 of them perisomatic) were still unclaimed. In the stratum radiatum, there were still 333 inhibitory synapses (87 perisomatic) remaining.

Distal dendritic GABA+ synapses

Neurogliaform, O-LM, and lesser well-known types such as the perforant path associated (PPA) and radiatum-retrohippocampal projection cells are known to synapse on the distal dendrites in the stratum lacunosum-moleculare (Klausberger and Somogyi, 2008). The total number of synapses made onto the distal apical dendrites of a pyramidal cell is 335 (Megías et al., 2001).

Neurogliaform cell synapses As discussed above, a large portion of neurogliaform cell boutons are found in the stratum lacunosum-moleculare. We made the simplifying assumption that all of the neurogliaform cells found in the stratum lacunosum-moleculare contributed their boutons to that layer. Therefore, 2,970 neurogliaform cells in the stratum lacunosum-moleculare contribute an average of 116 classical boutons per pyramidal cell and innervate 35% of stratum lacunosum-moleculare inhibitory synapses. It follows that

each pyramidal cell receives input from 12 neurogliaform cells in the stratum lacunosum-moleculare and 14 neurogliaform cells overall, given that neurogliaform cells have been observed to make 10 synapses per connection (Tamás et al. (2003); also, see Table 2.1). As mentioned above, if some neurogliaform cells contact pyramidal cells only through volume transmission but not classical synapses, they were not included in this calculation.

O-LM cell synapses About 99% of O-LM boutons remain in the CA1 (Sik et al., 1995), giving a total of 77 synapses per pyramidal cell (72 on the distal apical dendrites and 5 on the basal dendrites). We estimated that O-LM cells make 10 synapses per connection (Table 2.1) based on light microscopic observations (Maccaferri et al., 2000), such that eight O-LM cells converge on a single pyramidal cell.

PPA cell synapses PPA cells seem to innervate small to medium-sized dendrites mostly in the stratum lacunosum-moleculare (Vida et al., 1998; Klausberger, 2009). Accounting for the estimated number of PPA cells (490) and the local bouton count (8,000), the average number of boutons available per pyramidal cell is 12. Given that PPA cells make about six synapses per connection, we calculated a convergence of two PPA cells onto each pyramidal cell.

Other distal dendritic synapses An average of 99 distal, stratum lacunosum-moleculare dendritic synapses per pyramidal cell remain unclaimed. Some of these synapses may be innervated by the radiatum-retrohippocampal cell, but we have no bouton information for that cell so we cannot calculate its contribution.

Summary of inhibitory convergence onto pyramidal cells

Cell Type	Total Cells	Boutons/ Cell	Boutons Total	% on Pyr. Cells	Per Pyr. Cell	Boutons/ Connection	Convergence
Ivy	8,520	14,700	129.5M	93%	387	10	39
Neurogliaform	3,560	13,200	47.3M	93%	141	10	14
O-LM	1,640	16,730	27.3M	89%	78	10	8
Double Projection	760	6,080	4.6M	92%	14	10	1
Oriens retrohipp	640	6,080	3.9M	96%	12	10	1
PV+ Basket	5,520	10,400	57.4M	99%	182	11	17
Bistratified	2,210	16,020	35.4M	93%	106	10	11
Axo-axonic	1,470	7,200	10.6M	100%	34	6	6
CCK+ Basket	2,870	10,000	28.7M	93%	86	8	11
SCA	420	12,000	4.9M	93%	15	6	3
PPA	490	8,000	4.1M	93%	12	6	2
Total per Pyr. Cell			**Inhibitory Synapses**		1,067	**Convergence**	**113**

Table 3.12: Calculated convergence of interneurons onto a CA1 pyramidal cell. Note that several cell types are not included here, such as back-projection, radiatum-retrohippocampal, and more. a: all stratum oriens-specific cells were assumed to make 6 synapses/connection. b: all oriens-bistratified cells were assumed to have the same number of CA1 boutons as back-projection cells.

Cell Type	Total Boutons	Oriens		Radiatum			L-M	Soma	Axon
		Distal	Proximal	Thick prox.	Thick dist.	Thin			
Ivy	387	155	3	4	0	194	31	0	0
Neurogliaform	141	0	0	0	0	24	117	0	0
O-LM	78	5	0	0	0	0	73	0	0
Double Projection	13	8	0	0	0	5	0	0	0
Oriens retrohipp	12	7	0	0	0	5	0	0	0
Trilaminar		*	*	*		*			
Back Projection		*				*			
Radiatum retrohipp						*	*		
PV+ Basket	182	0	61	60	0	0	0	61	0
Bistratified	106	45	3	3	0	55	0	0	0
Axo-axonic	34	0	0	0	0	0	0	0	34
CCK+ Basket	86	0	27	28	0	0	0	31	0
SCA	15	1	1	0	0	12	1	0	0
ADI					*				
PPA	12	0	0	0	0	0	12	0	0
Misc CCK+		*	*	*		*	*		
Total Boutons									
Total Available	1839	405	233	193	111	437	334	92	34
Total Claimed	1067	221	95	94	0	296	235	92	34
Total Remaining	772	184	138	99	111	141	99	0	0
Percent Remaining	42%	45%	59%	51%	100%	32%	30%	0%	0%

Table 3.13: Calculated convergence of interneurons onto a CA1 pyramidal cell by layer and dendrite type. For some interneuron types, no data were available but the likely locations of their synapses are marked with an asterisk. Other interneuron types are not shown in this table. The 'Total Available' column values are based on the synapse counts on an average CA1 pyramidal cell from Megías et al. (2001). The 'Total Claimed' column gives the counts for the presynaptic cell types we have calculated in this assessment, and the 'Total Remaining' column gives the number of synapses on the average pyramidal cell remaining after subtracting the estimated innervation calculated in this assessment.

Table 3.12 summarizes the estimated convergence of interneurons onto a single CA1 pyramidal cell, while Table 3.13 details convergence by layer. Although a CA1 pyramidal cell has been shown to have about 1,840 inhibitory synapses on its dendrites, soma, and axon, we only calculated 1,118 inhibitory inputs. Therefore, 39% of the inhibitory inputs remain unspecified by our calculations. There are several possible reasons for this discrepancy. We should consider that axonal fills of interneurons may be incomplete, or bouton density may be higher, or the fraction of boutons that participate in classical synapses from neurogliaform family neurons may be much higher, or the fraction of CA1 neurons that are interneurons may be higher than previously reported. Though some afferent projections to the CA1 are GABAergic, they mainly target interneurons rather than pyramidal cells (Freund and Antal, 1988; Gulyas et al., 1990; Melzer et al., 2012, in mouse), so we do not consider them significant here.

3.3.2 Convergence onto interneurons

Some experimental observations have been made regarding inputs to interneurons. While in Bezaire and Soltesz (2013) we used the concept of a hypothetical average interneuron to enable accounting for boutons and input synapses onto interneurons, the concept does not offer sufficient detail for model implementation. Therefore, we took a different strategy to arrive at estimates of inputs onto each interneuron type in our model.

This consisted of using an estimated or experimentally determined dendritic length and synapse density of the cells, in each layer, and distributing the available boutons evenly across all potential input synapses in that layer.

For some neurochemical classes of interneuron, the input synapse numbers have been calculated (Table 3.14). These classes include CCK+, PV+, CB+, and CR+ cells. The CCK+ cell class represents CCK+ basket cells only. The PV+ class was heterogeneous, but the mor-

Marker	Total Synapses	Percent GABA+	Non GABAergic	GABAergic
PV	16,300	6%	15,322	978
CCK	8,200	36%	5,248	2,952
CB	3,800	29%	2,698	1,102
CR	2,200	21%	1,738	462
HS*	22,00	14%	18,920	3,080

Table 3.14: Total number of synapses and ratio of GABA- to GABA+ for various cell types by marker (Gulyás et al., 1999; Mátyás et al., 2004; Takacs et al., 2008). * Hippocampal-septal cells, classified by their projection target rather than a marker expressed.

phological traits varied smoothly such that there were no distinctive groups (Gulyás et al., 1999) (Gulyás et al., 1999); it is likely that multiple PV+ cell types are included. The identity of the CB+ cell class was unclear. Judging from their dendritic distribution, the Type 1 neurons (Gulyás et al., 1999) could be large calbindin cells or perhaps CB+ bistratified cells. Since they do not have many dendrites in the stratum lacunosum-moleculare, they seem less likely to be SCA or PPA cells. The Type 2 neurons mentioned here but not analyzed look to be double projection cells (Gulyás et al., 1999). The CR+ cell type is likely to include multiple interneuron-specific cell types (Gulyás et al., 1999).

Excitatory afferents

Input Type	Calculated Boutons/ CA1 Pyr. Cell.
Entorhinal Cortex via Stratum Lacunosum-Moleculare	$< 1,394$
Schaffer Collaterals	$7,952 - 17,576$
Local Collaterals	2,211
Total	**11,557 - 21,181**

Table 3.15: Calculated convergence of excitatory synapses onto a hypothetical average interneuron in the CA1. There are also inputs from the entorhinal cortex via the alveus, as well as from other afferents.

Takács et al. (2012) found that 93% of Schaffer Collateral synapses were made onto pyramidal cells, while 7% of synapses were made onto interneurons. We started with the number of Schaffer Collateral synapses on pyramidal cells and used the ratio to determine the Schaf-

fer Collateral synapses available for interneurons. This gave an average of 7,952 to 17,476 Schaffer Collateral synapses onto each interneuron (Table 3.15), depending on whether we counted only the observed boutons on the CA3 neurons or what we calculated must be the total number based on the available CA1 pyramidal cell synapses in the strata radiatum and oriens.

Performing the same exercise with the remaining stratum lacunosum-moleculare inputs (assuming they are all from the entorhinal cortex, Table 2.1) gave an additional 1,394 entorhinal cortical boutons available per interneuron, since 9% of the entorhinal cortical input to the stratum lacunosum-moleculare synapses on interneurons (Takács et al., 2012). Additionally, there are 2,211 boutons per interneuron from the local collaterals of the CA1. This gave a total of 11,557 to 21,081 excitatory inputs (Table 3.15), much higher than most of the observed values in those classes reported in Table 3.2, where the weighted average gives 9,461 excitatory inputs per interneuron. Note that it does not include entorhinal cortical inputs coming from the alvear pathway (in which the fraction of synapses made onto interneurons is high, at 21%, see Takács et al. (2012)), so the actual number of available excitatory boutons may be even higher. Additionally, interneurons receive non-GABAergic input from subcortical sources. They also receive some cholinergic input from the septum, and serotonergic and glutamatergic input from theraphe Gulyas et al. (1990); Freund et al. (1990); Freund and Gulyas (1997); Varga et al. (2009). Of course, not all interneurons receive inputs from all excitatory sources, so there may be a significant variation in total number of excitatory inputs across all interneuron types.

Convergence by cell type

An excellent recent qualitative review of interneuron-interneuron connectivity is given in Chamberland and Topolnik (2012) and a detailed analysis of specific connections seen in the literature is underway as part of the Hippocampome project (hippocampome.org). In

Layer	Synapse Density Excitatory	Inhibitory	Dendritic Length
Lm M	143.44	27.89	213.92
Lm t	126.75	28.97	441.74
Rad T	444.68	39.13	255.27
Rad M	416.01	16.67	1712.61
Rad t	133.5	12.14	401.36
Pyr M	*	*	248.28
Ori T	568.45	44.49	21.13
Ori M	344.95	16.13	685.81
Ori t	325.08	23.46	367.63
Total	304.89	20.72	4347.75
Somatic	40.7	18.09	1006.01

Table 3.16: PV+ cell synapse densities and dendritic lengths. Synapse densities are given in terms of synapses per 100 μm length of dendrite or per 100 μm^2 area of soma surface. Somatic entry in dendritic length column is area in μm^2. Data from Gulyas et al. (1991).

the meantime, we estimated the convergence onto specific interneuron types as given in the following sections.

Convergence onto PV+ cells Experimental data from Gulyas et al. (1991) has been reproduced in Table 3.16 in the form of input synapse density and dendritic length. I used it to calculate the total number of input synapses for PV cells, given in Table 3.17, arriving at a total of 14,609 excitatory synapses and 1,050 inhibitory synapses. I used the same number of inputs for PV+ basket cells, axo-axonic cells, and bistratified cells as Gulyas et al. (1991) found no distinctive groups within their dataset.

Convergence onto CCK+ cells Table 3.18 reproduces data from Mátyás et al. (2004). As with the PV+ cells in a previous work, all CCK+ cells were lumped together in experimental observations, so we used the same convergence data for CCK+ basket cell and Schaffer Collateral-associated cell.

My calculated convergence estimates are given in Table 3.19.

Layer	Excitatory	Inhibitory
Im M	307	60
Lm t	560	128
Rad T	1135	100
Rad M	7125	285
Rad t	536	49
Pyr	856	40
Ori T	120	9
Ori M	2366	111
Ori t	1195	86
Total	14200	868
Somatic	409	182
AIS		10

Table 3.17: My calculation of total synapses, which differs somewhat from the totals calculated by Gulyas et al. (1991). Note that the AIS number is just taken directly from their paper since the synapse density and AIS length were not reported, only the final number.

	Synapse Density		Dendritic
Layer	Excitatory	Inhibitory	Length
LMt	85.07	57.55	803.47
LMm	88.78	60.81	487.71
RLMt	80.96	42.24	375.68
RLMm	86.77	36.71	271.12
Rt	64.68	13.92	466.02
Rm	87.76	35.21	1821.76
RM	71.81	45.11	477.03
RT	94.86	137.03	110.99
PM	48.77	67.68	155.77
PT	56.58	107.2	154.84
OT	82.26	140.52	20.16
OM	84.02	62.24	137.36
Om	78.05	28.67	521.48
Ot	90.61	24.51	534.92
Total			6338.31
Soma*	3.4	16.12	966

Table 3.18: CCK+ cell synapse density and dendritic lengths. Synapse densities are given in terms of synapses per $100\mu m$ length of dendrite or per $100\mu m^2$ area of soma surface. Somatic entry in dendritic length column is area in μm^2. Data from Mátyás et al. (2004)

Layer	Excitatory	Inhibitory
LMt	684	462
LMm	433	297
RLMt	304	159
RLMm	235	100
Rt	301	65
Rm	1599	641
RM	343	215
RT	105	152
PM	76	105
PT	88	166
OT	17	28
OM	115	85
Om	407	150
Ot	485	131
Total	5191	2757
Soma*	33	156
AIS	1	5

Table 3.19: CCK+ cell synapse calculations. My calculation of total synapses differs somewhat from the totals calculated by Mátyás et al. (2004) at the end of their paper. Note that the AIS number is just taken directly from their paper since the synapse density and AIS length were not reported, only the final number

	Dendritic Length	
Layer	Neurogliaform	Ivy
SLM	895.8	75.1
SR	1885.5	1758.6
SP	0	49.6
SO	0	51.2
Total	2781.4	1934.4
Somatic	254.6	385.7

Table 3.20: Ivy and Neurogliaform dendritic lengths are given in μm. Somatic entry in dendritic length column is area in μm^2.

	Synapse Density	
Layer	Excitatory	Inhibitory
SLM	88.7	31.7
SR	154.5	27.1
SP	123.7	42.5
SO	133.7	24.9
Somatic	17.8	15.9

Table 3.21: Ivy and Neurogliaform synapse densities are given in terms of synapses per $100\mu m$ length of dendrite or per $100\mu m^2$ area of soma surface.

Convergence onto neurogliaform family cells We calculated the dendritic lengths and somatic area of ivy and neurogliaform cells in Table 3.20.

Then I took the average of all dendritic synapse densities, regardless of cell class, and used that average to calculate the average synaptic density from the interneuron data that we have (Mátyás et al., 2004)and arrived at the estimates given in Table 3.21.

	Synapses	
Layer	Excitatory	Inhibitory
SLM	67	24
SR	2717	477
SP	61	21
SO	68	13
Total	2913	534
Somatic	69	61

Table 3.22: Ivy cell synapse estimates.

Layer	Synapses Excitatory	Inhibitory
SLM	795	284
SR	2913	511
SP	0	0
SO	0	0
Total	3708	795
Somatic	45	41

Table 3.23: Neurogliaform cell synapse estimates.

Layer	Dendritic Length
SO	4165.68
Somatic	3007.78

Table 3.24: O-LM cell dendritic lengths are given in terms of synapses per $100\mu m$ length of dendrite or per $100\mu m^2$ area of soma surface. Somatic entry in dendritic length column is area in μm^2.

Convergence onto OLM cells The dendrites of O-LM cells are confined to the stratum oriens. The dendritic length and somatic area were reported by Kispersky et al. (2012) and are given in Table 3.24. We used the CB+ cell density from Gulyas et al. (1991), averaging medium and thin dendritic densities for Table 3.25 to arrive at the total convergence given in Table 3.26. The observed CB+ cell fraction of 36% for GABAergic synapses fits with the observations of OLM cell inputs from Blasco-Ibez and Freund (1995), which stated that greater than 60% of incoming synapses appeared to be innervated by CA1 pyramidal cells.

Layer	Synapse Density Excitatory	Inhibitory
SO	53.02	29.58
somatic	12.75	17.97

Table 3.25: O-LM synapse densities are given in terms of synapses per $100\mu m$ length of dendrite or per $100\mu m^2$ area of soma surface. Somatic entry in dendritic length column is area in μm^2.

Layer	Synapses Excitatory	Inhibitory
SO	2209	1232
somatic	383	540

Table 3.26: O-LM cell synapses.

Layer	Synapse Density Excitatory	Inhibitory	Dendritic Length
Lm M	75.31	16.14	0
Lm t	****	****	554.13
Rad T	85.36	23	377.19
Rad M	93.93	18.04	387.86
Rad t	49.73	11.48	118.06
Pyr M	42.53	28.36	232.73
Ori T	66.39	29.7	86.87
Ori M	61.36	20.06	375.81
Ori t	37.89	7.98	146.82
Total	72.83	19.02	2279.47
Somatic	14.22	11.55	

Table 3.27: CR+ cell synapse densities are given in terms of synapses per $100\mu m$ length of dendrite or per $100\mu m^2$ area of soma surface. Dendritic lengths are in terms of μm and the somatic entry in the dendritic length column is area in μm^2.

Convergence onto other cells For other cells not included in the model, there is limited convergence information. CR+ cells are likely interneuron-specific (IS) cells, so we used the CR+ cell information from Gulyas et al. (1991), shown here in Table 3.27. The total synapses per CR+ cell are given in Table 3.28.

There are 7,470 IS cells and about 504 input synapses per each IS cell (assuming the CR+ cell bouton info from Gulyas et al. (1991) applies), so there are almost 4 million additional input boutons required onto IS cells. Of course, the IS cells also contribute a certain number of boutons to the inhibition of other interneurons. With our earlier estimate of 75 million boutons contributed by IS cells, there would be enough local inhibitory boutons available for full coverage of all CA1 local, GABAergic input synapses.

There are a few other miscellaneous cell types, including other CCK+ cells and some stratum-

Layer	Synapses Excitatory	Inhibitory
SLM	417	89
SR	745	170
SP	99	66
SO	344	113
total	1605	439
somatic	77	57
axonic	0	8

Table 3.28: CR+ cell synapses.

oriens cells. Using the CCK+ cell info, we expect the other 1,370 CCK cells (PPA, ADI, and miscellaneous CCK+ cells) need an additional 4 million GABAergic synaptic inputs, and the remaining 2,420 stratum-oriens cells require an additional 4.3 million GABAergic synaptic inputs (assuming CB+ cell properties apply to these cells).

Therefore, we expect that the total GABAergic boutons in CA1 (local and afferent) required for innervating interneurons would be about 43 million, as given in Table 3.29. If this coverage needed to be achieved entirely with local boutons, then the remaining cell types for which we do not know the boutons would need to contribute an average of 1928 boutons each to local inhibitory innervation (if we exclude any contribution from trilaminar cells, since we don't know their total cell number). This number is well within the range of bouton numbers seen in individual interneuron axons.

Post-syn. Type	Ivy	NGF.	O-LM	Dbl. Proj.	CB- septal proj.	Oriens-retrohipp.	Other SOM+*	PV+ B.
# Cells	5530	8810	3580	1640	760	190	640	350
Dend. Inputs	868	534	795	1232	1087	1087	1087	1087
Soma. Inputs	177	61	41	540	142	142	142	142
AIS Inputs	10	8	8	8	7	7	7	7
Total Per Cell	1055	603	844	1780	1236	1236	1236	1236
Total Per Type	5834150	5312430	3021520	2919200	939360	234840	791040	432600
Fraction	14%	12%	7%	7%	2%	1%	2%	1%

(continued)

Post-syn. Type	Bis.	Axo.	CCK+ B.	ADI	S.C.-A	PPA	CCK Misc.	IS I	IS II	IS III	Total
# Cells	2210	1470	3600	390	400	490	490	4250	1970	1250	38020
Dend. Inputs	868	868	2757	2757	2757	2757	2757	438	438	438	24612
Soma. Inputs	177	177	156	156	156	156	156	57	57	57	2692
AIS Inputs	10	10	5	5	5	5	5	8	8	8	131
Total Per Cell	1055	1055	2918	2918	2918	2918	2918	503	503	503	27435
Total Per Type	2331550	1550850	10504800	1138020	1167200	1429820	1429820	2137750	990910	628750	42794610
Fraction	5%	4%	25%	3%	3%	3%	3%	5%	2%	1%	

Table 3.29: Inhibitory convergence onto interneurons in rat CA1

3.4 Comparing Convergence and Divergence

Overall, the 8 interneuron types have 25 million boutons available for synapsing locally onto other interneurons, while the 8 types expect 33 million boutons to innervate their input synapses. So we have achieved 76% inhibitory synaptic coverage of the interneurons (as compared to 59% inhibitory synaptic coverage of pyramidal cells). The inhibitory divergence and convergence of interneurons are graphically depicted in Figure 3.1. In our model, we have not considered the contributions of the missing types, especially IS cells, nor the inputs needed to inhibit the missing types. However, we have created two alternate model connectivities, one with the inhibitory synapse numbers calculated here and one with scaled up values for inhibitory synapses to achieve full inhibitory coverage of pyramidal cells. This differences between the behavior of these networks are discussed in Chapter 5.

3.4.1 Subset selectivity

It is informative to consider the results of our calculations in light of some experimental observations about inhibitory connections. Gulyas et al. (1991) observed that PV cells receive about 27% of their inhibitory inputs from other PV cells. Does that imply that PV cells have some selectivity in their innervation, preferring to innervate other PV cells?

By layer, the fraction of interneuron-targeting boutons supplied by PV cells is given in Table 3.30. It totals 14%, but is completely absent in SLM, so in the layers where the boutons are present, it is generally higher. In the pyramidale layer, PV+ boutons comprise 28% of inhibitory boutons. Experimentally, Gulyas et al. (1991) found that the GABAergic innervation of PV+ cells by PV+ boutons is at least 27.6%, but probably higher. With the minimum value, there is some selectivity of PV+ cells for each other.

For CCK+ cells, 4% -28% of GABAergic inputs were from other CCK cells (Gulyas et al.,

Layer	Fraction
SLM	0%
SR	14%
SP	28%
SO	21%
Total	14%

Table 3.30: Of the inhibitory boutons targeting other interneurons, PV boutons make up about 14% overall.

Layer	Fraction
SLM	1%
SR	11%
SP	63%
SO	9%
Total	13%

Table 3.31: Of the inhibitory boutons targeting other interneurons, CCK boutons make up about 13% overall.

1991). Given that the calculated fraction of available boutons that are CCK+ is about 13%, there doesn't seem to be any particular preference of CCK cells for other CCK cells (Table 3.31).

3.4.2 Gaps in experimental data

In estimating the connectivity of the CA1, we performed an initial calculation of the excitatory and inhibitory convergence onto CA1 pyramidal cells, as well as onto a hypothetical average interneuron. The calculation revealed that we could only account for about half of the excitatory and inhibitory inputs to CA1 pyramidal cells based on known afferent and interneuron axon data and our calculated cell numbers. We were surprised by the magnitude of the difference and hope that the exposure of this difference will drive more experiments to fill in this gap of our knowledge. In contrast to the pyramidal cell, the convergence onto the hypothetical average interneuron aligned with or exceeded our expectations based on the observed input synapses for several classes of interneurons.

More in vivo axon fills of interneurons would help refine the divergence calculations for axo-axonic cells, CCK+ cells, and interneuron-specific cells. Also, convergence data in the form of what percent of inhibitory inputs onto pyramidal cells are associated with the various neurochemical markers would provide a validation of our convergence calculations and could explain the source of the remaining 39% of GABAergic inputs that were unknown in this assessment. Further quantification of excitatory inputs is also necessary, especially those targeting the stratum lacunosum-moleculare.

3.4.3 Potential reasons for gaps

As mentioned above, possible candidates for this discrepancy include incomplete axonal fills, more neurogliaform family cell boutons participating in classical synapses, or more GABAergic cells (a higher fraction of CA1 cells being GABAergic). We must also consider the inputs of GABAergic projection cells onto inhibitory synapses on interneurons.

3.4.4 How we address the gaps for our model

We first calculated the inhibitory inputs in the reduced model. We chose the number of cells converging, the number of synapses per connection, and the total number of synapses from each interneuron type based on our quantitative assessment (Bezaire and Soltesz, 2013). As this only accounted for 59% of the inputs, we also ran the model with the "full" approach, where most of the cell types had proportionally increased their numbers synapsing onto the pyramidal cell (Table 4.2).

3.5 Connectivity values used in the model

Because not all CA1 interneuron types were included in the model and due to other differences, our model connectivity does not precisely match the expected connectivity *in vivo*.

3.5.1 Interneuron to interneuron connectivity

Our model implementation of the inhibition of interneurons was less experimentally constrained than the other connectivity properties in the model. To arrive at reasonable estimates, we focused on the available inhibitory inputs (divergence) and contrasted that info with the inhibitory input synapses onto each interneuron type. At the most cursory level, we estimated that, for our 8 model interneuron types only, there are about 25 million local GABAergic boutons available from the 8 types to synapse on them. For those 8 types, we expect that they would receive about 33 million GABAergic input synapses. Now, many or perhaps most of these inputs could actually come from the interneuron-selective interneurons. However, those cells are not included in the model, and therefore we have a lower level of inhibition (and may be missing inhibition at specific phases during theta).

We began by calculating the total convergence onto our 8 interneuron types, given in Table 3.29, and contrasting that with the divergence information from Table 3.3. Since some types are missing from our model network, we realize that these interneurons would not make all of their connections with the 8 interneuron types, and that these types would receive other inputs, so this model connectivity is a bit different than in vivo connectivity. However, for simplification, we are making all connections between these 8 interneuron types only. In general, the types that we have left out are also likely to to be projection neurons or to be smaller populations of neurons, so they are less likely to receive significant input or make significant contributions to local inhibition. The broad exception to this is the IS cells.

There are limited data available about which interneurons each IS cell type targets (Tyan et al., 2014), so we assumed that all interneurons receive approximately the same fraction of IS inputs. Therefore, we determined the percent of coverage that our available boutons achieved across all of our model interneuron expected inputs, and used that same fraction for each of our interneurons.

In general, for each cell type's boutons, we distributed them evenly among the input synapses for all cell types in that layer. The two exceptions were PV+ boutons and neurogliaform family boutons. We introduced a PV skew to ensure that the overall PV+ synaptic innervation onto PV+ cells was 28% of the GABAergic innervation, as observed in Gulyas et al. (1991). Due to that skew, PV+ cells were more likely to receive inputs from PV+ cells and less likely to receive input from other cell types, whereas PV- cells were more likely to receive inputs from PV- cells and less likely to receive inputs from PV+ cells. We set this skew to 30% to achieve the 28% metric.

We also diverted some of the ivy cell boutons available for synapsing on olm cells to synapse on other ivy cells in the stratum oriens, because we had 100% coverage of OLM cells without connecting all of the ivy cell inputs to them. Neurogliaform cells only innervated pyramidal cells and other neurogliaform cells, though there is evidence *in vivo* that they innervate other interneurons, including PV+ cells (Booker et al., 2013).

Our final model interneuron connectivity came out to be as shown in Tables 3.33 (connections) and 3.32 (synapses). This resulted in coverage of inhibitory synapses ranging from 67% to 100% for the various cell types in the model, as shown in Table 3.34.

Synapses	Ivy	Neurogliaform	O-LM	PV+ Basket	Bistratified	Axo-axonic	CCK+ Basket	SCA
Ivy	258	281	1270	238	238	238	958	1024
Neurogliaform	35	172	0	92	92	92	500	508
O-LM	10	127	62	77	77	77	402	402
PV+ Basket	8	0	0	39	39	39	38	24
Bistratified	32	29	276	156	156	156	136	141
Axo-axonic	0	0	0	0	0	0	0	0
CCK+ Basket	63	25	161	94	94	98	280	217
SCA	13	14	11	7	7	7	34	38

Table 3.32: Local inhibitory synaptic innervation of interneurons in model CA1

Connections	Ivy	Neurogliaform	O-LM	PV+ Basket	Bistratified	Axo-axonic	CCK+ Basket	SCA
Ivy	26	28	127	24	24	24	96	102
Neurogliaform	4	17	0	9	9	9	50	51
O-LM	1	13	6	8	8	8	40	40
PV+ Basket	8	0	0	39	39	39	38	24
Bistratified	3	3	28	16	16	16	14	14
Axo-axonic	0	0	0	0	0	0	0	0
CCK+ Basket	8	3	20	12	12	12	35	27
SCA	2	2	2	1	1	1	6	6

Table 3.33: Inhibitory intra-connectivity in model CA1

Cell Type	Ivy	Neurogliaform	O-LM	PV+ Basket	Bistratified	Axo-axonic	CCK+ Basket	SCA
Model Inputs	424	646	1782	711	711	711	2354	2346
Expected Inputs	603	844	1780	1055	1055	1055	2918	2918
Coverage	70%	77%	100%	67%	67%	67%	81%	80%

Table 3.34: Inhibitory coverage of interneurons in the model

3.6 Use of non-rat or non-hippocampal data

We preferred to use entirely rat, hippocampal data for this anatomical assessment, but in some cases we did not have enough rat data to proceed. For those calculations where comparable mouse hippocampal data existed, we used the mouse data instead and noted it in the calculation. One such instance was the ratio of PV+ basket cell boutons to CCK+ basket cell boutons. We used this ratio to calculate the total number of CCK+ basket cells, and it was averaged from two experiments done in mouse. In addition, the number of synapses per connection made by PV+ basket cells and CCK+ basket cells onto pyramidal cells was taken from mouse data. We are not aware of published differences between rat and mouse regarding the projection cells or the basket cell connectivity.

For a few data points, we relied on data from other parts of the brain than the CA1. This occurred for the neurogliaform family bouton properties: the fraction of boutons forming classical synapses (taken from somatosensory cortex) and the density of boutons (taken from the dentate gyrus and CA3). We are not aware of significant differences between neurogliaform cells of the somatosensory cortex and the CA1. However, we have taken care to note the fraction of boutons forming classical synapses in the assumption table. Because the bouton densities in the dentate gyrus and CA3 were similar, we believe that the bouton densities of neurogliaform family cells in the CA1 will also be similar to the those in the dentate gyrus and CA3.

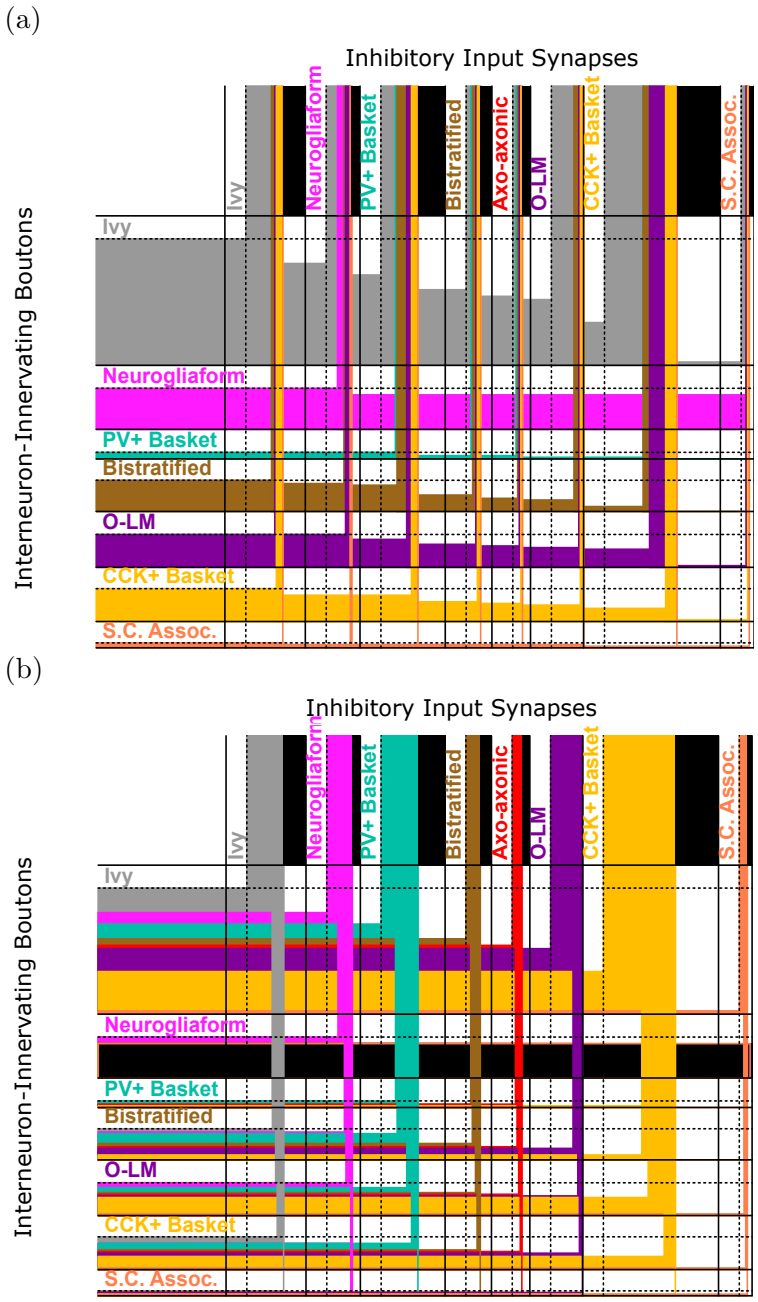

Figure 3.1: (a) Divergence and (b) convergence of inhibitory cells onto other interneurons, by type. The inhibitory divergence and convergence of each interneuron is quantitatively represented by the height (divergence) or width (convergence) of the color-coded area. Black widths represent the experimentally-based estimate of inhibitory input synapses that are not innervated by boutons due to the discrepancy in experimental data about interneuronal divergence and inhibitory convergence as discussed in the main text; not enough inhibitory boutons were available on the model interneurons to achieve full coverage of all inhibitory input synapses except to O-LM cells.

3.7 Impact of morphology and network topology on connections

The locations of the synapses on the postsynaptic cell were influenced by the morphology of the cell and by model logic that constrained the available locations based on the presynaptic cell type. In addition, the specific cells available for connecting were constrained by their distance from each other (soma to soma), as each cell had a set 3-dimensional position within the network and each presynaptic cell had a set axonal bouton distribution and extent. The details of how these properties were used to set realistic connection locations and topology are given in the following sections.

3.7.1 Morphology of single cells

Table 3.35 gives the lengths and areas of the soma and dendrites for each model cell type, as well as the number of compartments used in the model. Figure 3.2 shows the morphology of each model cell. Note that the surface area of most model cell types is significantly smaller than their biological counterparts. We scaled the membrane capacitance and resistance accordingly, so that our model cells still had similar electrophysiological personalities as their biological counterparts. In this way, we were able to adequately mimic the electrical behavior of the cells while reducing the computational load required for simulations.

3.8 Locations of incoming synapses

When connecting cells, each postsynaptic cell has many potential synapse locations available. A certain number of them are randomly picked for use. More details about the potential locations and actual locations chosen used are given in the following sections 3.8.1 and 3.8.2.

(a) CCK+ basket and S.C.-Assoc.

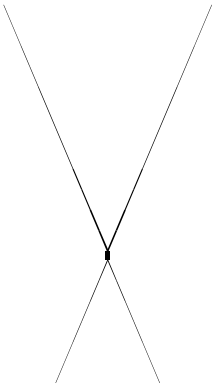

(b) OLM

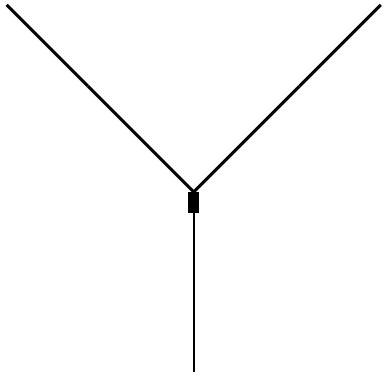

(c) Pyramidal (Simple)

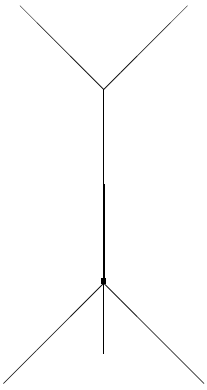

(d) Pyramidal (Complex)

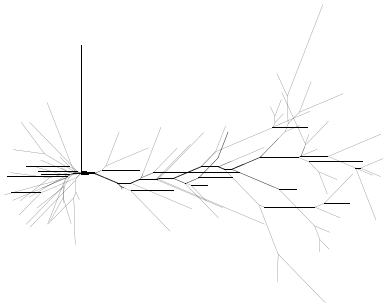

(e) PV+ and neurogliaform family

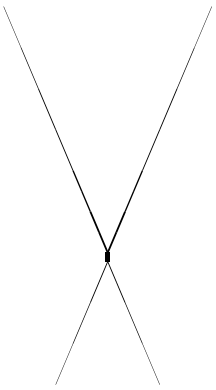

Figure 3.2: Various cell morphologies used

Cell Type	Somatic Area	Dendritic Area	Dendritic Length	Compartments
Axo-axonic	628.3	11309.7	1800.0	17
Bistratified	628.3	11309.7	1800.0	17
CCK+ basket	628.3	9479.8	1800.0	17
Ivy	628.3	11309.7	1800.0	17
Neurogliaform	628.3	11309.7	1800.0	17
O-LM	628.3	4718.3	500.6	4
PV+ basket	628.3	11309.7	1800.0	17
Pyramidal (complex)	421.0	15946.5	9995.2	202
Pyramidal (simple)	314.2	9124.9	1502.5	15
S.C.-Assoc.	314.2	9479.8	1800.0	17
Pyramidal (simple)	314.2	9124.9	1502.5	15

Table 3.35: Morphology of cells included in the model

3.8.1 Potential synaptic locations

The spatial resolution of the cells is temporarily set to a high value, and the possible synapse locations are enumerated along all the dendrites, with a constant density over all possible locations. Then, the spatial resolution is set to a lower value to be used throughout the simulation. All the synapses are shifted to the nearest node. This has the effect of reducing the unique locations of the synapses, but making the number of synapses on each compartment correlate better with the length of the compartment (instead of blindly choosing to put in the middle of each segment only).

Also, each possible compartment that is within a specified distance from the soma is a candidate for receiving a synapse. Each potential synapse location is added to a list for that synapse type (that particular combination of presynaptic and postsynaptic cell). Then whenever a synapse is needed, the list of potential synapses is consulted - the total length of the list is passed into a random number generator so that any synapse in the list could potentially be selected. A uniform distribution is used and returns an integer describing an index into the list. That particular synapse is then connected to the presynaptic cell's spike detector.

3.8.2 Choosing random locations

We allowed the presynaptic cell to synapse on the pyramidal cell n times as shown in Table 4.2, where n equaled the number of synapses per connection reported in the literature for that cell type (Bezaire and Soltesz, 2013). Synapse locations were randomly chosen from among all the possible dendritic, somatic, and axonic locations where that presynaptic cell type has been experimentally observed to synapse (Table 3.36). Note that the various dendritic sections are shown in Figure 3.3.

Presynaptic Cell Type	**SLM Dendrites**	**SR Dendrites**	**SO Dendrites**	**Peri-Somatic**	**Axon**
Pyramidal			X		
Axoaxonic					X
Bistratified		X	X		
CCK+ Basket				X	
Ivy		X	X		
Neurogliaform	X				
O-LM	X				
PV+ Basket				X	
SCA		X			

Table 3.36: Possible synapse locations for various presynaptic cell types; Figure 3.3 shows the categories of dendrites by color.

3.8.3 Actual synaptic locations used

The actual synapse location used for each connection in the model is not routinely recorded into the output because the dataset would be too large. However, this information can be easily be determined for all connections to and from cells of interest. The model also contains code to track these data for every cell, but that option should only be used for very small networks as it generates so much data.

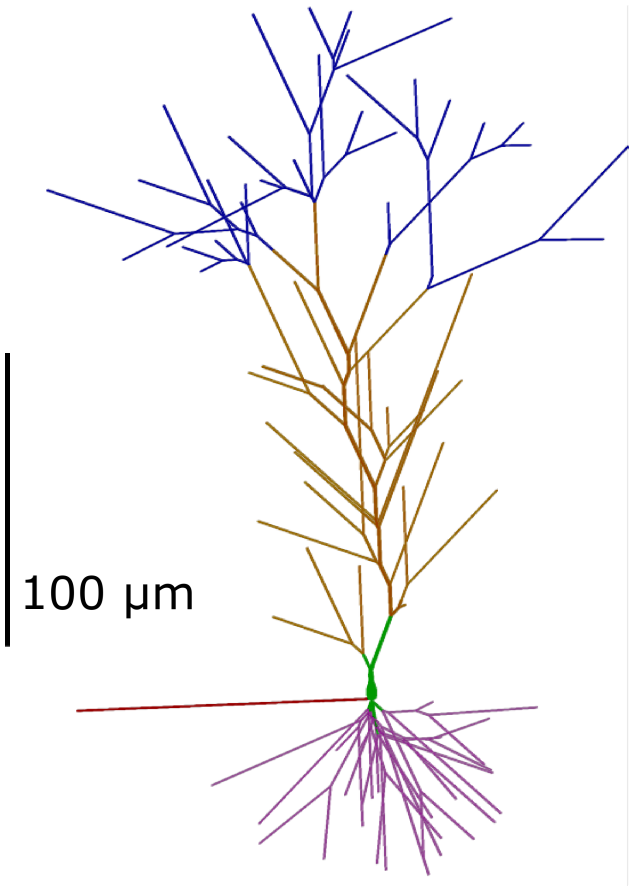

Figure 3.3: Sections of pyramidal cell dendrites. Blue: distal apical, orange: proximal apical, green: perisomatic, red: axon, lilac: basal.

3.9 3D arrangement of cells

The cells were arranged in a prism, distributed evenly throughout their specified layer, with their position completely specified by the dimensions of the prism and the unique ID (gid) of the cell (Figure 3.4). To accomplish this, we compiled x, y, and z positioning algorithms and then called them, passing in the cell's gid, whenever the cell's position was required. The formulae used in the positioning algorithms are given in Equations . Their equations can easily be replaced by parametric surface equations that are capable of modeling a more realistic, 3D shape of the CA1 if desired.

(a)

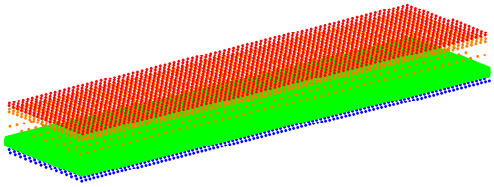

(b)

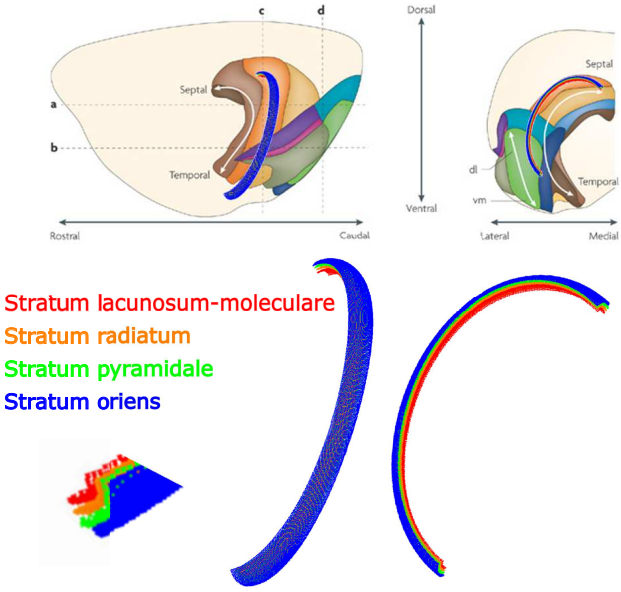

Figure 3.4: (a) The model has a 3D arrangement of neurons with realistic dimensions. (b) Parametric equations can also be used to assign cell positions efficiently while maintaining a realistic shape of the network.

3.10 Axonal Distributions of the cells

In our model, cells can be connected if the soma of the postsynaptic cell falls within the area of the axonal extent of the presynaptic cell. We used normal distributions to determine the connections between cells, such that after all connections are made, for each cell type, the distances from each presynaptic cell soma to each postsynaptic cell soma follow a normal distribution. Figure 3.5 gives an example axonal distribution for each presynaptic cell type onto an example pyramidal cell.

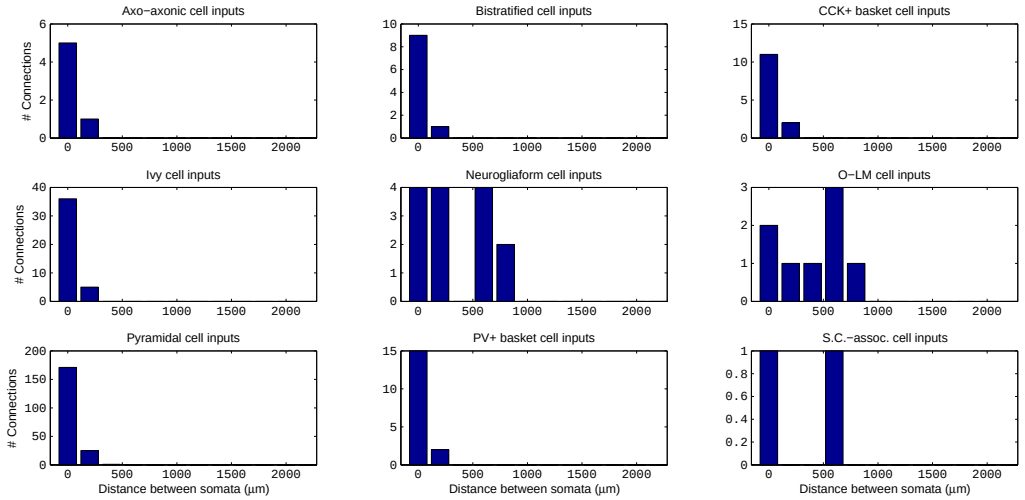

Figure 3.5: For the cells connecting to a single pyramidal cell in the model, the distribution of distance between each presynaptic cell soma and the postsynaptic pyramidal cell soma are plotted.

Chapter 4

Electrophysiological Properties of CA1 Neurons and Synapses by Type

For each of the eight interneuron types in my model, as well as the CA1 pyramidal cells, I fit my model cells to experimental electrophysiological data to ensure that I have biologically constrained neurons that behave realistically. The model cells and their comparisons with experimental cells are described here. First I discuss the ion channels used in the model cells and the model cells themselves. Then I describe the model implementation of the synaptic mechanisms found on the postsynaptic cell, through which the connectivity functions of the model are implemented.

While fitting some cells, I altered the kinetics of the voltage-gated channels associated with the cell type to achieve the characteristic firing pattern of that cell. I considered this allowable because the channel models that we work with are not necessarily precise representations of those found in the biological hippocampal neurons. In general, the ion channel models developed from experimental data may be from widely varying preparations including differing temperatures, reagents, animal types, and nervous system areas. Therefore, I felt that it was

acceptable to adjust channel timing and dependence on voltage within reasonable bounds to achieve the experimentally observed properties at the cellular level. However, this made it all the more important to fully characterize the behavior of the ion channels so that their behavior and contributions to the cell behavior could be fully understood. Therefore, in the following section each ion channel is fully described, including its origins (experimental constraints and model creaters) and its behavior in a uniform preparation (channel type at uniform density inserted into a uniformly-sized somatic compartment at the same calcium concentration, temperature, axial and specific membrane resistance, and capacitance).

4.1 Components of single cells

In this section, we describe subcellular mechanisms such as ion channels and other calcium mechanisms. We included many ion channels found in principle cells and interneurons of the CA1 (Table 4.1). A detailed characterization of each ion channel's properties, along with a description of the strategy used to generate the ion channel model, is given in the following subsections. Except for the L-type calcium channel, the ion channels all use a quasi-ohmic equation to express the driving force that sets the instantaneous conductance of the channel. The L-type calcium channel takes into account a dependence on the calcium concentration that leads to inwardly rectifying behavior, and it does this by using a GHK-style equation to calculate the driving force on the channel. All other channels used a quasi-ohmic calculation of their driving force.

We fixed some channel bugs from previous implementations, which are detailed in the sections on the individual ion channels that were affected (Sections 4.1.1 and 4.1.3). We also removed most temperature dependence equations (q10 equations) from the cells because they were not being used correctly. We found that the baseline temperature being used in these equations often did not match the temperature used in the experimental preparation on which the

channel was based, but had instead been changed to another value, such as 6.3^{o}C, the default temperature in the NEURON simulation program, to circumvent any alteration in channel behavior from the behavior at the temperature of the experimental preparation used to characterize the channel.

To directly compare the behavior of each channel, we subjected each to the same conditions and characterization protocol, as shown in the figures below. The protocol consisted of inserting the channel at a density of .001 S/cm^2 into a cylindrical membrane compartment of size 16.8 μm height by 16.8 μm diameter at 34^{o}C, with an internal calcium concentration of 5.e-6 mM and an external concentration of 2 mM. The reversal potentials were set to E_{Na}=+55 mV, E_K=-90 mV, $E_{Ca^{2+}}$=+140 mV, and E_{HCN}=-35 mV .

Channel	**Description**	**Model Type**
$Ca_{v,L}$	L-type Calcium	GHK
$Ca_{v,N}$	N-type Calcium	Quasi-ohmic
HCN	Hyperpolarization-activated, Cyclic Nucleotide-gated	Quasi-ohmic
HCN_{OLM}	Hyperpolarization-activated, Cyclic Nucleotide-gated for O-LM cells	Quasi-ohmic
HCN_p	Hyperpolarization-activated, Cyclic Nucleotide-gated for pyramidal cells	Quasi-ohmic
$K_{Ca,S}$	Small (SK) Calcium-activated potassium	Quasi-ohmic
$K_{dr,fast}$	Fast delayed rectifier potassium	Quasi-ohmic
$K_{dr,fast,ngf}$	Fast delayed rectifier potassium for neurogliaform family cells	Quasi-ohmic
$K_{dr,p}$	Delayed rectifier potassium for pyramidal cells	Quasi-ohmic
$K_{dr,slow}$	Slow delayed rectifier potassium	Quasi-ohmic
$K_{v,A}$	A-type voltage activated potassium	Quasi-ohmic

$K_{v,A,dist,p}$	A-type voltage activated potassium for distal pyramidal dendrites	Quasi-ohmic
$K_{v,A,ngf}$	A-type voltage activated potassium for neurogliaform family cells	Quasi-ohmic
$K_{v,A,olm}$	A-type voltage activated potassium for O-LM cells	Quasi-ohmic
$K_{v,A,prox,p}$	A-type voltage activated potassium for proximal pyramidal dendrites	Quasi-ohmic
$K_{v,Ca,B}$	Big (BK) Calcium-activated, voltage dependent potassium	Quasi-ohmic
$K_{v,Group}$	Multiple slower voltage dependent potassium	Quasi-ohmic
leak	Leak	Quasi-ohmic
Na_v	Voltage dependent sodium	Quasi-ohmic
$Na_{v,bis}$	Voltage dependent sodium for bistratified cells	Quasi-ohmic
$Na_{v,ngf}$	Voltage dependent sodium for neurogliaform cells	Quasi-ohmic
$Na_{v,p}$	Voltage dependent sodium for pyramidal cells	Quasi-ohmic

Table 4.1: Ion channels included in the model

4.1.1 Calcium channels

The calcium channels and other calcium mechanisms have previously been used in Soltesz Lab models (Santhakumar et al., 2005; Dyhrfjeld-Johnsen et al., 2007; Morgan and Soltesz, 2008) and given their own calcium current that operates separately from the calcium currents through other channels. The purpose of that arrangement was to be able to model local calcium dynamics, assuming that the various calcium channel types had isolated calcium concentrations even though the channels could possibly be intermixed within a compartment. We removed the unique calcium currents , returning the channel to its original state, because

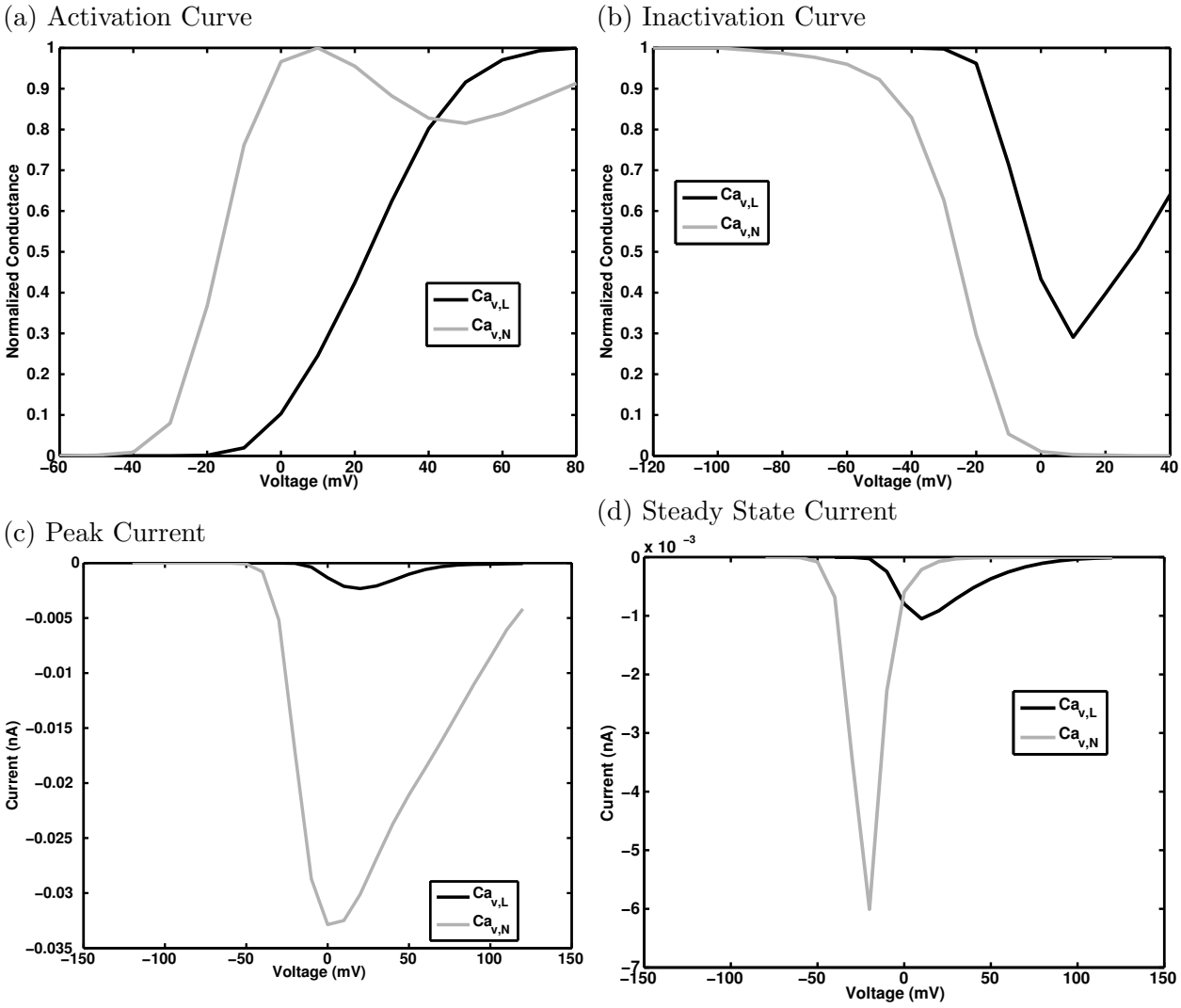

Figure 4.1: Calcium channel currents.

we were not interested in local calcium pools and the two channel types that we use are not necessarily even placed in the same compartments, rendering the change unnecessary.

In Figure 4.1, the differing behavior of the N-type and L-type calcium channels can be seen. The L-type channel is not significantly inactivating; in contrast, the N-type channel inactivates.

$Ca_{v,L}$ Channel This channel model was developed by Jaffe et al. (1994) and has been used in many other models implemented by Migliore. It uses the GHK equation to calculate

driving force such that there is inward rectification of the channel caused by a mild dependence on calcium concentration. The equations for this channel were based on activation data from CA1 and CA3 hippocampal neurons in adult guinea pigs, at room temperature. The voltage of half-activation was shifted by −10 mV to account for ionic differences in the bath of the experimental preparation compared to the model condition.

$Ca_{v,N}$ Channel This channel was also developed by Jaffe et al. (1994), using the same preparation as that for the $Ca_{v,L}$ channel. However, it was later modified by Aradi and Holmes (1999), replacing the GHK calculation for a quasi-ohmic calculation of the driving force. In addition, its behavior was altered somewhat compared to previous implementations such as Morgan and Soltesz (2008) and Santhakumar et al. (2005). Their implementations contained a typo in the channel definition that caused its equations to differ from those presented in Aradi and Holmes (1999), and had the effect of reducing the conductance of the channel below its intended magnitude.

The channel had a slightly decreased conductance at high levels of activation, as shown in Figure 4.1. This odd behavior has been present since the replacement of the GHK calculation with a quasi-ohmic expression. However, it may not have too large of an effect since it only happens at very depolarized potentials, potentials that are likely to be achieved only at the peak of the action potential.

4.1.2 HCN channels

While HCN channels are technically gated by the presence of cyclic nucleotides, it is not common practice to include the gating in HCN channel models used in network modeling. Instead, only the voltage-dependent activation (the hyperpolarizing preference) is included. In addition, the mixed cation current of Na+ and K+ is not explicitly modeled. Instead,

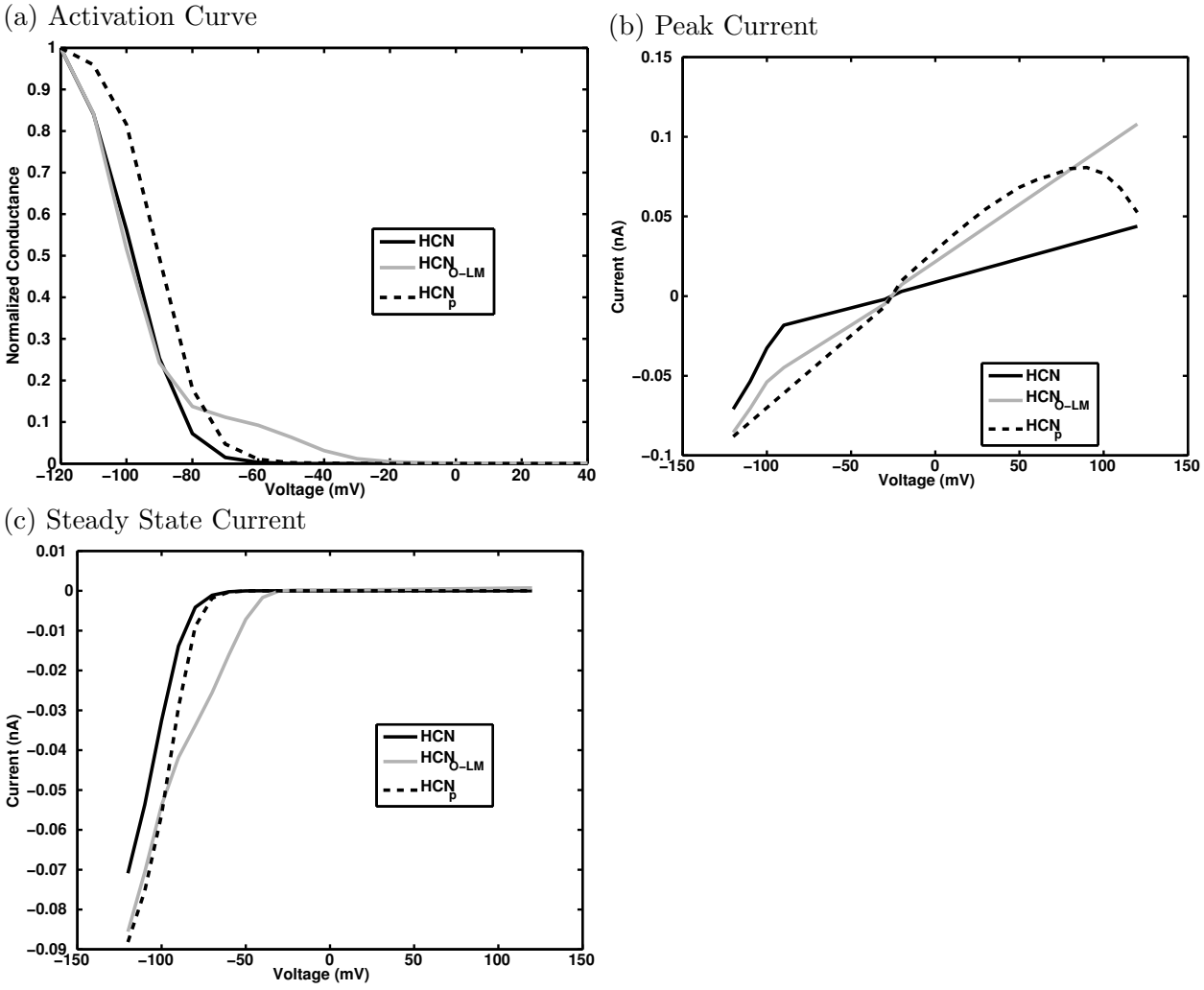

Figure 4.2: HCN channel currents.

either a fake "'h"' ion is invented or a non-specific current is used. This has the side effect of rendering the reversal potentials of Na+ and K+ unable to affect the driving force of the H current.

None of these channel models included an inactivating component. Also, because they are hyperpolarization-activated, the protocol used to characterize the inactivating of other channels was used to characterize the activation of the HCN channels. In Figure 4.2, the differing behavior of the HCN channels can be seen.

HCN Channel In Chen et al. (2001), the HCN current was experimentally observed in CA1 pyramidal cells of Sprague-Dawley rats at room temperature. They then developed a model channel based on their observations, which included fast and slow components and used separate, artificial ion definitions for each. We kept only the slow component as the cells that included this channel were displaying a non-physiological, oscillating sag when both components were included.We further modified the channel by adjusting the calculation of the slow component slightly (removing some of the voltage dependence, which further decreased the oscillation of the sag) and by replacing the fake ion definition with a non-specific current (which did not further affect the channel behavior).

HCN_{OLM} Channel This model was developed by Saraga et al. (2003) based on data from young Sprague-Dawley rats at a warm room temperature. It was then used in an O-LM cell model by Cutsuridis et al. (2010), which we incorporated into our model. It included an artificial "'h"' ion and we found that this ion could not be replaced with a non-specific current without altering the conductance of the channel slightly. This may be due to the inability of the non-specific current to take into account local ion shortages near the membrane . Unlike the previous HCN model, this one only ever had a single time constant.

HCN_p Channel This model, based on experimental data from adult Sprague-Dawley rats at 23^o or 33^o (Magee, 1998) was implemented by Cutsuridis et al. (2010) for their pyramidal cell model. It uses a non-specific current.

4.1.3 Potassium channels

A variety of potassium channels were included. For the delayed rectifier and A-type potassium channels, multiple varations were produced for disparate cell types. The variations enabled us to tune their thresholds and voltage dependence to produce the different voltage

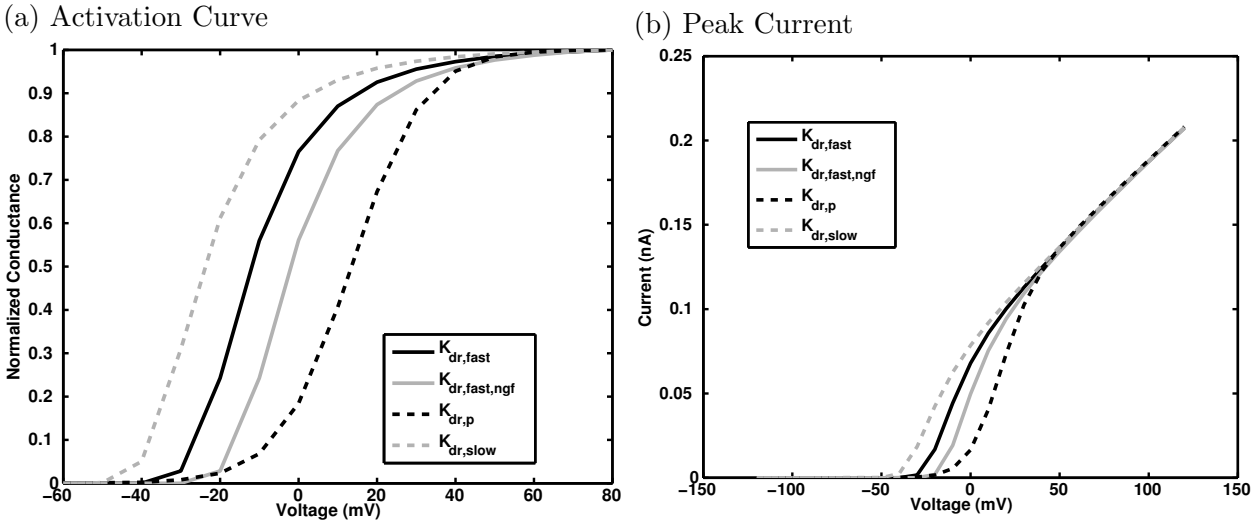

Figure 4.3: Delayed rectifier potassium channel currents.

dependence and AP thresholds of the cells into which we placed them. The leak channel is also included here since it mostly conducts potassium.

Delayed Rectifier Potassium Channels

The delayed rectifiers did not include an inactivating component. If they do inactivate, it is likely to happen after several seconds of voltage clamp, a condition that is not usually physiologically relevant.

In Figure 4.3, the differing behavior of the delayed rectifiers can be seen.

$\mathbf{K}_{dr,fast}$ Channel This fast delayed rectifier potassium channel was originally implemented by Yuen and Durand (1991). They based it on a model of a fast delayed rectifier in a squid axon, and then adjusted the equation parameters until their model action potential wave form matched that of an experimental mouse cell. Their model was later modified by Aradi and Holmes (1999), shifting the voltage dependence slightly.

$K_{dr,fast,ngf}$ Channel This is a variation of the $K_{dr,fast}$ channel, which I shifted by -10 mV to better match the action potential waveform and threshold of the neurogliaform family cells, which tend to have a higher threshold than other cells.

$K_{dr,p}$ Channel This channel was implemented by Migliore, based on experimental data from hippocampal cells in rat pups at room temperature (Klee et al., 1995). It has been used in many models since then, including Poolos et al. (2002). .

$K_{dr,slow}$ Channel This model was originally implemented by Yuen and Durand (1991) based on data from Storm (1990). It is meant to serve as a combination of slow delayed rectifier current and M-type potassium current. It was modified by Aradi and Holmes (1999).

A-type Potassium Channels

The A-type potassium channel is a transient, quickly-inactivating channel that activates near the action potential threshold. It has the effect of delaying action potential onset and increasing action potential threshold, and it can modulate early repolarization after an action potential (Storm, 1990).

$K_{v,A}$ Channel This channel model was developed by Migliore et al. (1995), using some equations from Borg-Graham (1991) as a starting point. They modified those equations to take into account data from Ficker and Heinemann (1992) and Numann et al. (1987), which enabled their model cell to better display the burst behavior they were studying.

$K_{v,A,dist,p}$ Channel This channel was also developed by Migliore et al. (1995); it was used in the CA1 pyramidal cell model of Poolos et al. (2002) and was based on experimental

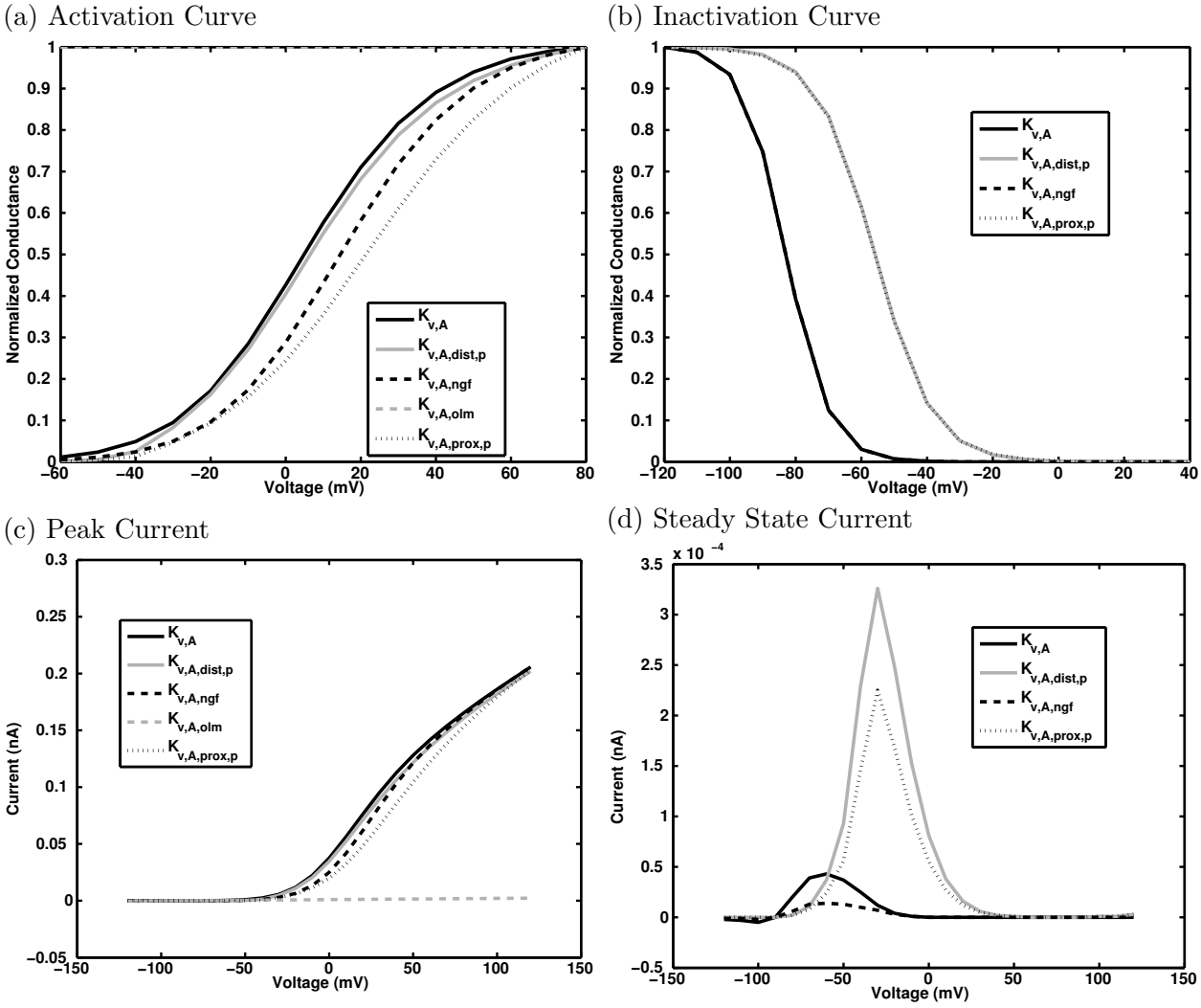

Figure 4.4: A-type potassium channel currents.

observations of rat hippocampal pyramidal cell from Klee et al. (1995).

$\mathbf{K}_{v,A,prox,p}$ Channel This channel model was also developed by Migliore et al. (1995) and is similar to the $\mathrm{K}_{v,A,dist,p}$ channel, differing slightly in timing and voltage.

$\mathbf{K}_{v,A,ngf}$ Channel A variation of the KvA A-type channel developed by Migliore et al. (1995). I modified its activation and inactivation equations, offseting them by +10 mV to be compatible with the high-threshold neurogliaform cell family, for use in neurogliaform and ivy cells.

$\mathbf{K}_{v,A,olm}$ Channel This channel was used in the O-LM cell by Cutsuridis et al. (2010), originally implemented by Saraga et al. (2003) based on experimental data from the McBain lab and others.

Other Potassium Channels

The leak and KCaS channels are not voltage activated nor inactivating. While KvCaB was voltage-dependent, it was also Ca^{2+} gated. KvGroup had voltage-dependent activation and had no inactivating component.

$\mathbf{K}_{Ca,S}$ Channel This calcium-activated potassium channel is also known as the small or "'SK"' channel. The model was first developed by Yuen and Durand (1991), and altered by Aradi and Holmes (1999) based on data from Beck et al. (1997), Latorre et al. (1989), Sah (1996), and Lancaster et al. (1991).

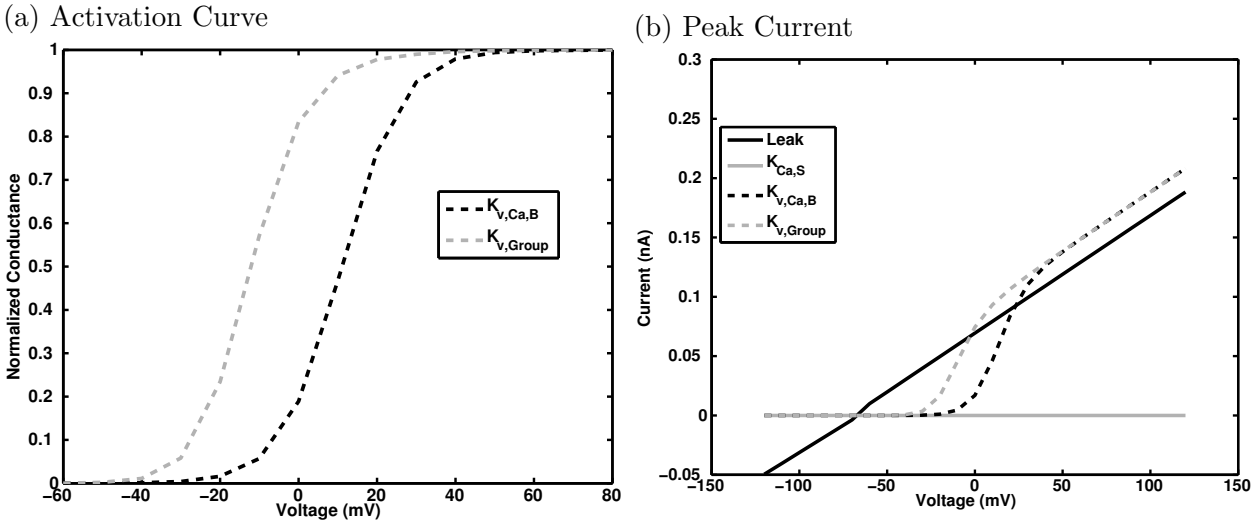

Figure 4.5: Other potassium channel currents. Because they didn't have a voltage-sensitive inactivation component, only the activation curve, which is equivalent to the IV Peak curve, need be shown here.

$\mathbf{K}_{v,Ca,B}$ Channel Also known as the big ("'BK"') channel, this potassium channel is both voltage dependent and calcium-gated. It was implemented by Migliore et al. (1995) based on a model from Moczydlowski and Latorre (1983). A variation of this model used in other Soltesz Lab models (Santhakumar et al., 2005), (Morgan and Soltesz, 2008) contained a bug such that it did not update the calcium concentration at each time step, rendering it essentially calcium-independent (it only sampled the calcium concentration once at the beginning of the simulation, when the internal concentration of each cell was likely to be very low due to no spiking activity occurring yet). After fixing the bug, the channel contributed much more current during spiking activity and became calcium dependent as in the original Migliore implementation.

In Figure 4.5, the behavior of these other channels is shown as a function of voltage. Figure 4.6shows the calcium-gated potassium channels as a function of internal Ca^{2+} concentration.

$\mathbf{K}_{v,Group}$ Channel This is a modified version of the fast delayed rectifier potassium channel, with the parameters adjusted to match the channel model given in Lien and Jonas (2003).

(a) KvCaB Activation Curve

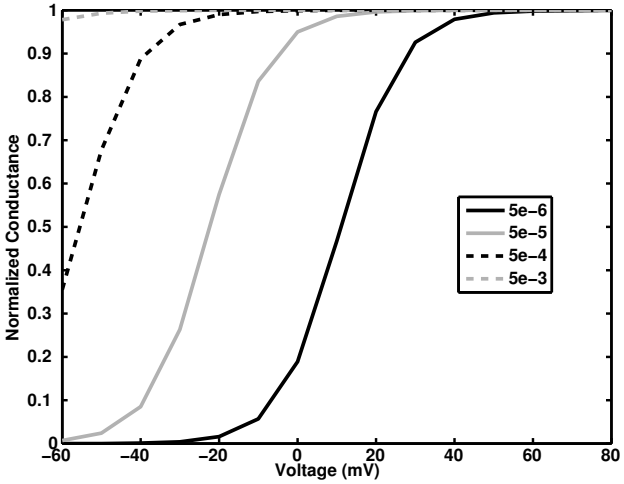

(b) KvCaB Peak Current

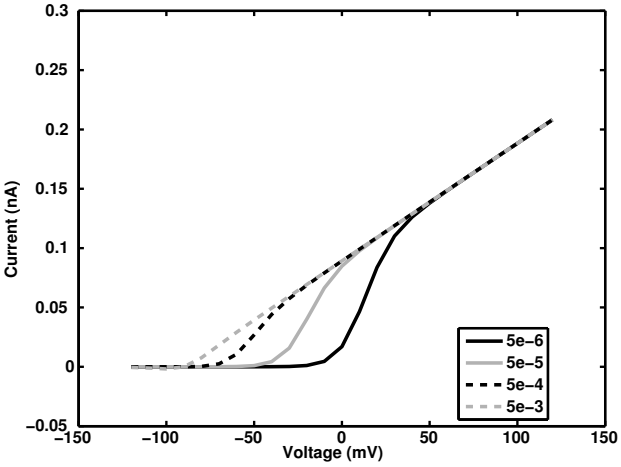

(c) KCaS Peak Current

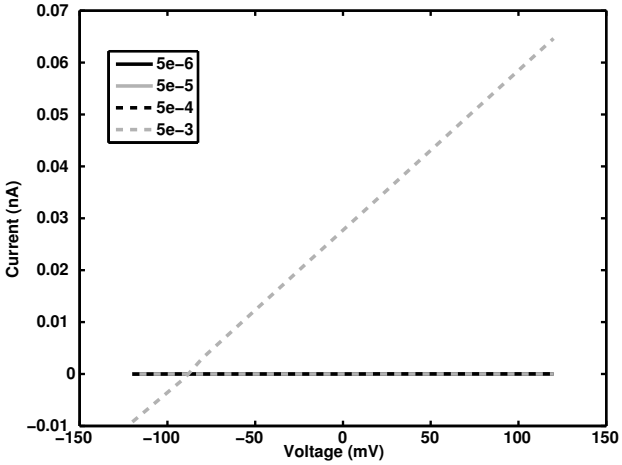

Figure 4.6: Calcium-dependent potassium channel dependence on calcium concentration. (a) The normalized conductance of the channels are plotted as a function of test voltage step and calcium concentration. (b) and (c) The current-voltage relation is shown at several calcium concentrations for (b) KvCaB channel and (c) KCaS channel. Note that the KCaS channel is only active at the highest calcium concentration and is not dependent on voltage (although the voltage continues to set the driving force) when it is active.

However, while the channel was presented in that paper as a model of the Kv3.1b channel, the methods used in that paper to experimentally characterize the current are likely to have included multiple potassium channel types. Specifically, they added 300 uM of 4-AP, which they indicated was a low enough dose that it would block only Kv3.1b channels. Then they subtracted the intracellular potential recording of the cell in the presence of that blocker from the control recording and attributed that entire difference to Kv3.1b. But Campanac et al. (2013) used only 5-10 uM of 4-AP to block Kv1.1 channels, so at least two potassium channel types, and possibly others, must have been blocked in Lien and Jonas (2003). Therefore, more than one potassium channel type contributes to the dynamics of the model channel they fit, hence our name of KvGroup.

leak Channel A very simple channel that employs a non-specific current and is quasi-ohmic. It should generally have its reversal potential set near to (but not hyperpolarized relative to) the potassium reversal potential and should be used to implement the specific membrane resistance by setting its conductance to the reciprocal of the membrane resistance.

4.1.4 Sodium channels

As with the potassium channels, we made several variations of the fast activating, fast-inactivating sodium channel so that each cell type contained a version with a compatible threshold for the cell, enabling the cell to display its physiological AP threshold.

In Figure 4.7, the differing behavior of the sodium channels can be seen.

Na_v Channel This channel model was originally developed by Yuen and Durand (1991) and then modified by Aradi and Holmes (1999).

(a) Activation Curve

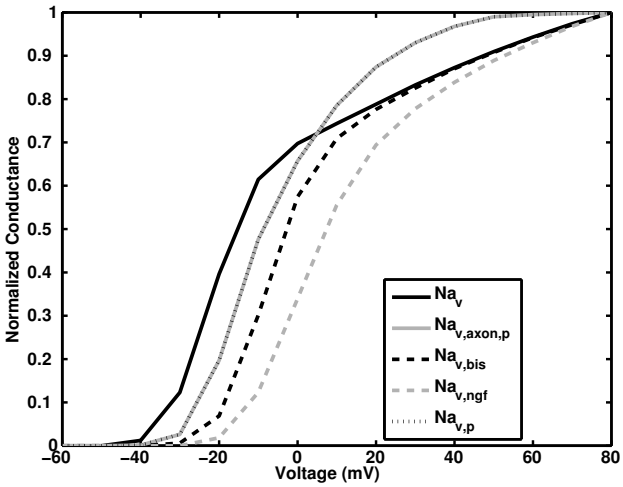

(b) Inactivation Curve

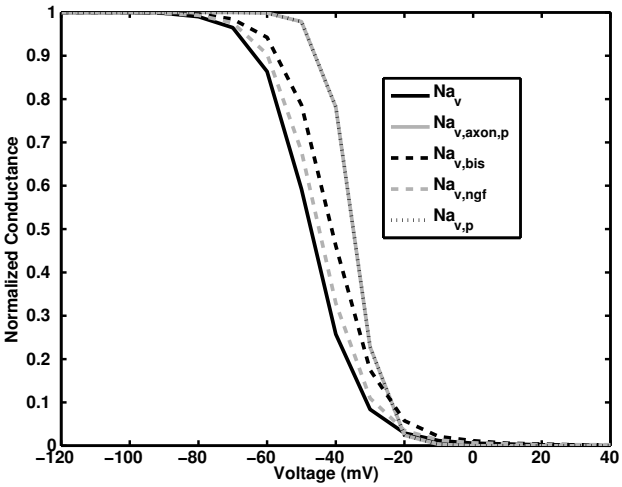

(c) Peak Current

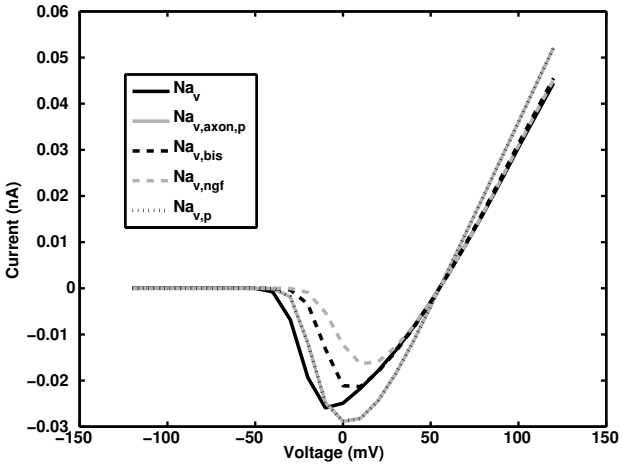

(d) Steady State Current

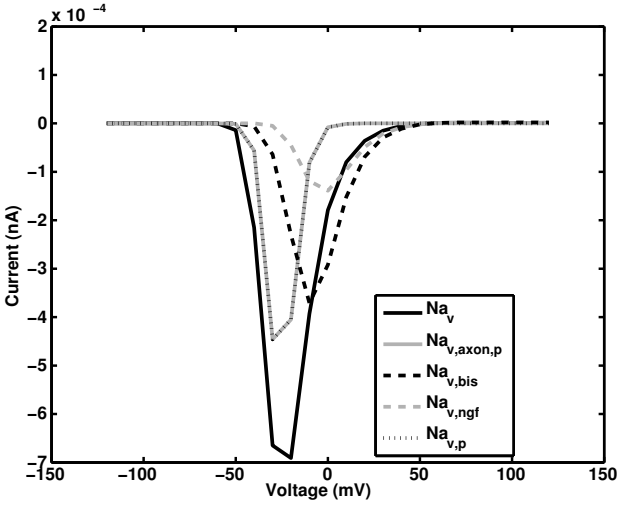

Figure 4.7: Sodium channel voltage dependence. The normalized conductance of the sodium channel is plotted as (a) a function of test voltage step to show activation and (b) as a function of holding voltage prior to the test step to show inactivation.

$Na_{v,bis}$ Channel This channel is modified from ch_Nav to have a slightly higher threshold, which makes it suitable for bistratified cells. The voltage dependence of its activation has been shifted by -5 mV and of its inactivation has been shifted by -3 mV. Additionally, the coefficients have been adjusted as well.

$Na_{v,ngf}$ Channel This channel is modified from ch_Nav to have a much higher threshold, which makes it suitable for neurogliaform family cells. Its activation and inactivation voltage dependences have been offset by about -19 mV, and the coefficients have been slightly modified as well.

$Na_{v,cck}$ Channel This channel is modified from ch_Nav to have slightly different kinetics. While the voltage dependence has not been much changed, the coefficients have been significantly adjusted to achieve more realistic CCK+ cell behavior.

$Na_{v,p}$ Channel This channel is from Migliore et al. (1999) and used in Poolos et al. (2002). It contains both a fast and an optional slow inactivating component. In general, we did not use the slow, inactivating option so that this channel model was essentially equivalent to the Na_v channel for axons used in Poolos et al. (2002).

4.1.5 Other calcium mechanisms

We did not include special calcium mechanisms in the model, such as those necessary to model calcium buffering, diffusion, or internal stores. Such mechanisms are complex enough to be beyond the scope of this work, although they would be useful in studying single cell dynamics, such as when using our network clamp tool described in Chapters 5 and 6.

4.2 Matching experimental conditions when fitting the model cell

As with our ion channel models, we wished to characterize our model cells in experimental terms. For each model cell type, we had at least one experimental observation available (albeit in a mouse preparation). In general we matched the current injection level for the current sweeps, as well as the duration of the injection. We did not, however, take into account any baseline current injected to push the cell to a certain resting potential prior to the beginning of the sweep, nor did we account for any bath or pipette ion concentrations that resulted in a divergence of reversal potentials from physiological values. Nor did we correct for the junction potential inherent in all patch clamp experiments, except in a small CA1 microcircuit model published in Lee et al. (2014).

Our rationale for not including the junction potential is that we were not sure whether to trust the calculated, estimated junction potential based on plugging the list of reagents into AxoClamp's Junction Potential Calculator. Nor did most publications report the junction potential of their preparation. Therefore, though we would prefer to account for this shift in potential of the cell, because it is not widely reported in experimental literature, we have disregarded it.

Additionally, most experimental publications do not report the reversal potentials caused by their choice of reagents when reporting whole cell patch clamp data, so we have again assumed that any reversal potential differences can be ignored. Nor did we account for a baseline current injection, since many experiments never documented it and I only discovered from talking to experimentalists that often a baseline current is injected and not reported in the methods.

4.2.1 Properties that are fit

We focused on the firing rate and rheobase (current threshold) as the most important properties to fit. However, we also tracked the input resistance, membrane time constant, sag properties, and many others to see how well they matched the experimental data. Below is a table comparing experimental and model electrophysiological properties for all neurons. Note that the experimental data is generally from mouse cells, which may be smaller than the rat neurons that our model cells represent.

A detailed explanation of all properties that were characterized is given in the description of our SimTracker tool, section 6.4.

A summary of how we characterized the various electrophysiological properties of the cells is given in our description of the Experimental Data tool in Section 6.4. Our strategy for fitting the cells based on experimental data is given next.

4.3 Combining components into a working cell model

To fit our cells, we used a combination of trial and error as well as NEURON's Multiple Run Fitter (MRF). In theory, our recommended strategy for fitting took the following form, although we did occasionally deviate from this form depending on the circumstances of the fitting. In general, the values for later properties depended on parameter values that were set by fitting earlier, more general properties.

1. Match the RMP and the input resistance. Parameters to adjust:
    - leak channel conductance (or the specific membrane resistance)
    - reversal potential

2. Match the membrane time constant. Parameters to adjust:

    - capacitance

3. Match the hyperpolarization properties (sag amplitude and timing). Parameters to adjust:

    - HCN channel conductance
    - HCN channel reversal potential
    - HCN channel kinetics

4. Match the properties of the transient peak during depolarization (amplitude and decay time constant). Parameters to adjust:

    - T-type Ca^{2+} channel conductance
    - T-type Ca^{2+} channel kinetics

5. Match the rheobase and firing curve. Parameters to adjust:

    - Na+ channel conductance
    - K+ channel conductance
    - L-type and N-type Ca^{2+} channel conductance

6. Match action potential properties (width, threshold, amplitude). Parameters to adjust:

    - Na+ channel kinetics
    - K+ channel kinetics
    - L-type and N-type Ca^{2+} channel kinetics

Pyramidal Cell Model

We used two different pyramidal cell morphologies in our simulations. For some networks, we tested a realistic morphology from a pyramidal cell model previously used to study I_h (Poolos et al., 2002), available online from ModelDB, accession # 9769 Hines et al. (2004). The model contained detailed morphology, including 187 sections of dendrites, 13 somatic sections, and 2 axonal sections. In addition, several subcellular mechanisms were present, such as A-type and delayed rectifier K+ channels, a Na+ channel, a HCN channel, and leak channels. We adjusted the calculation of the reversal potential for the HCN channel such that it was never more negative than -90 mV.

We also employed a simpler morphology pyramidal cell model in some of our simulations. We adapted the pyramidal cell model used by Cutsuridis et al. (2010) so that it had a slightly lower, more realistic firing rate. We accomplished this by giving it the electrophysiological properties from the other pyramidal cell model we used. We performed most structured parameter space exploration with model networks containing this cell type, as it required less memory to model its simple morphology.

The differences in results achieved between networks using each of the models is given in Chapter 6.

Interneuron Cell Models

We included 8 types of interneurons in our network model. Many of the cell types were developed from scratch, as existing models were not available on ModelDB. These included the neurogliaform family cells (neurogliaform and ivy), the CCK+ basket cell, and the Schaffer Collateral-Associated cell. For the OLM cell and the PV+ cells, we modified existing CA1 cell models published by others.

(a) Experimental current sweep

(b) Complex model current sweep

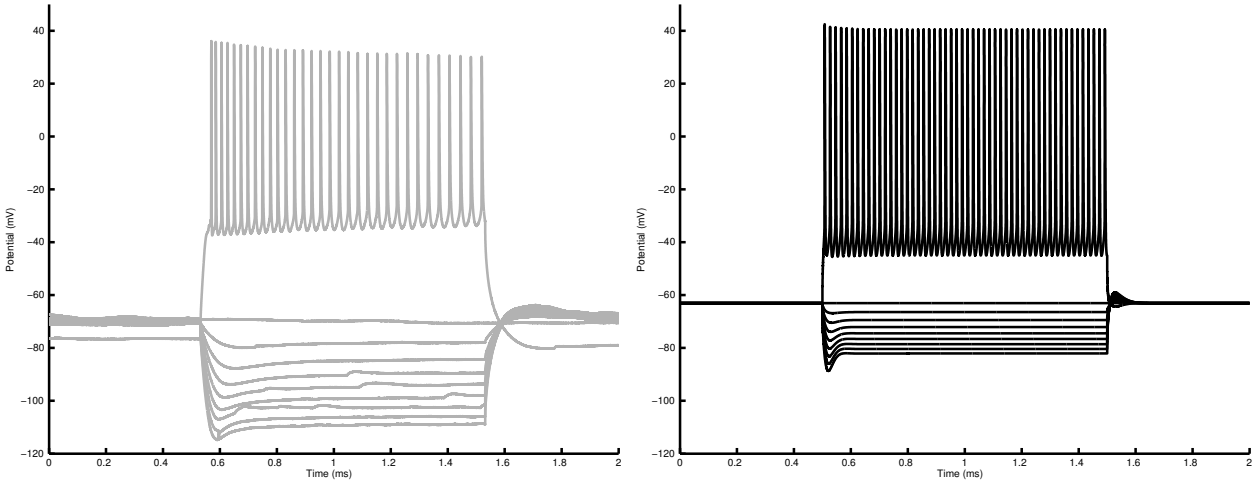

(c) Simple model current sweep

(d) Firing rate

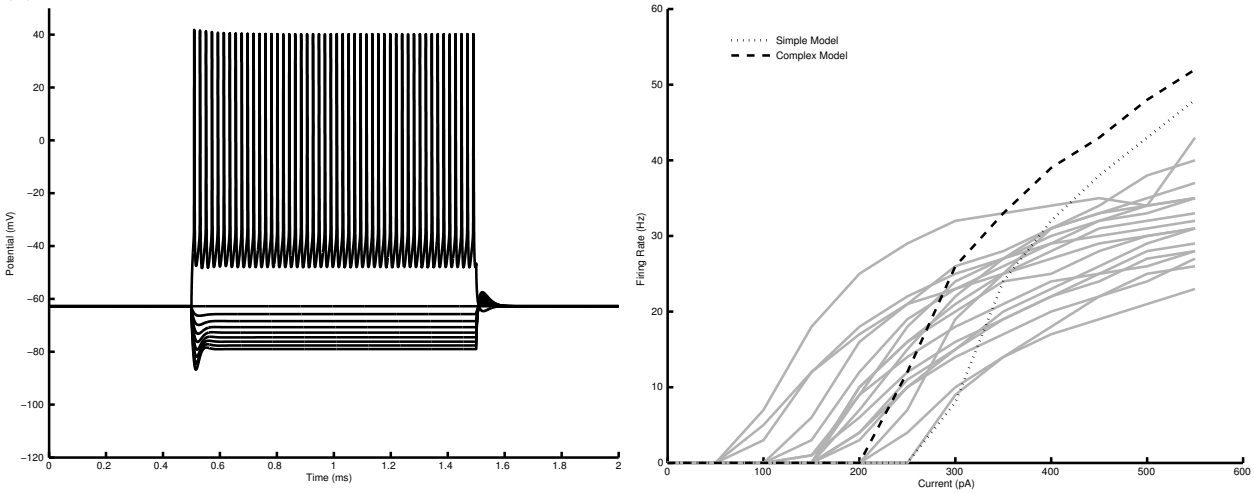

Figure 4.8: Pyramidal cell firing characterization.

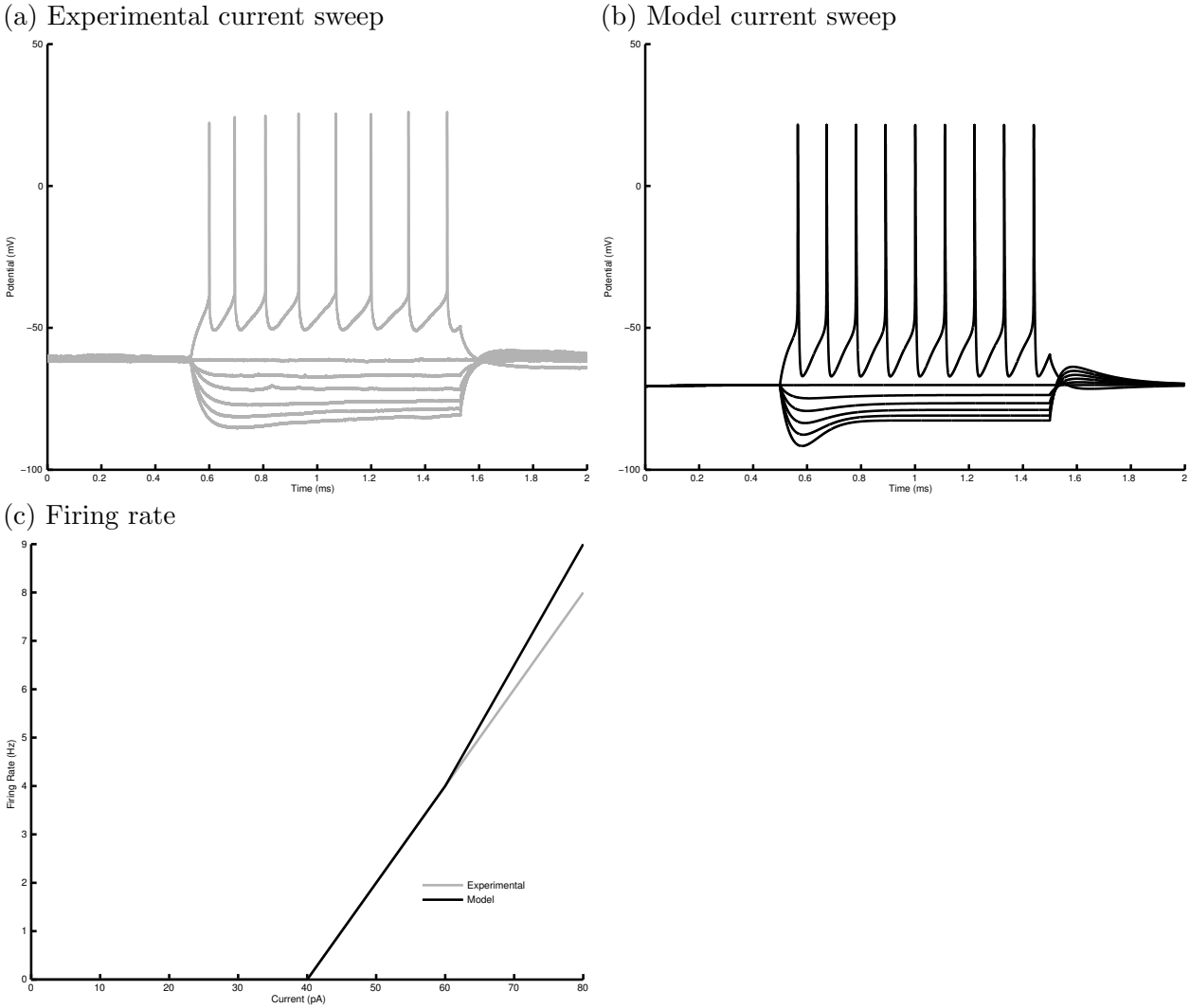

Figure 4.9: CCK+ basket cell firing characterization.

Using these distinct electrophysiological profiles for each cell type enabled us to introduce variability into the model network. Although we did not introduce variability within each cell type, the variability across cell types enabled us to study the network's mechanisms of theta in a more biologically relevant manner.

CCK+ Cells

I developed my own cell models for the CCK+ basket cell and the Schaffer Collateral Associated cell, as we had not used these types before. I prioritized fitting the sag amplitude,

(a) Experimental current sweep

(b) Model current sweep

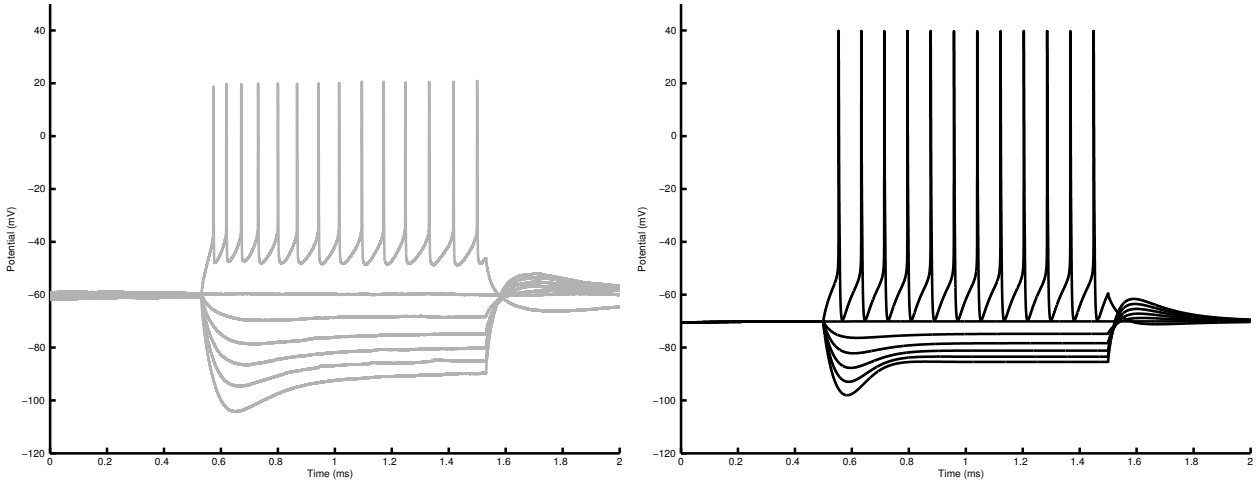

(c) Firing rate

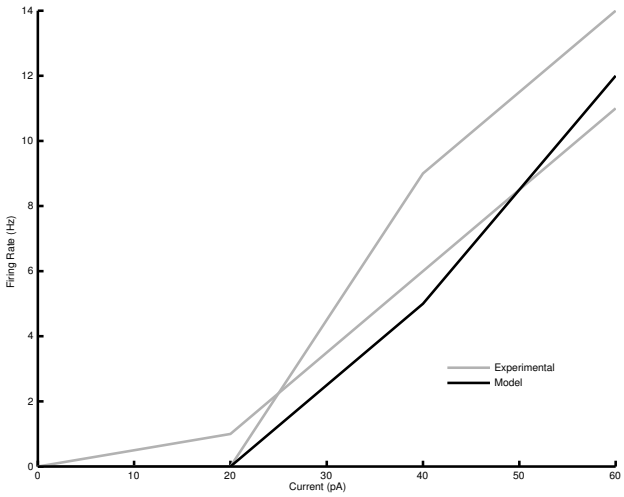

Figure 4.10: Schaffer Collateral-associated cell firing characterization.

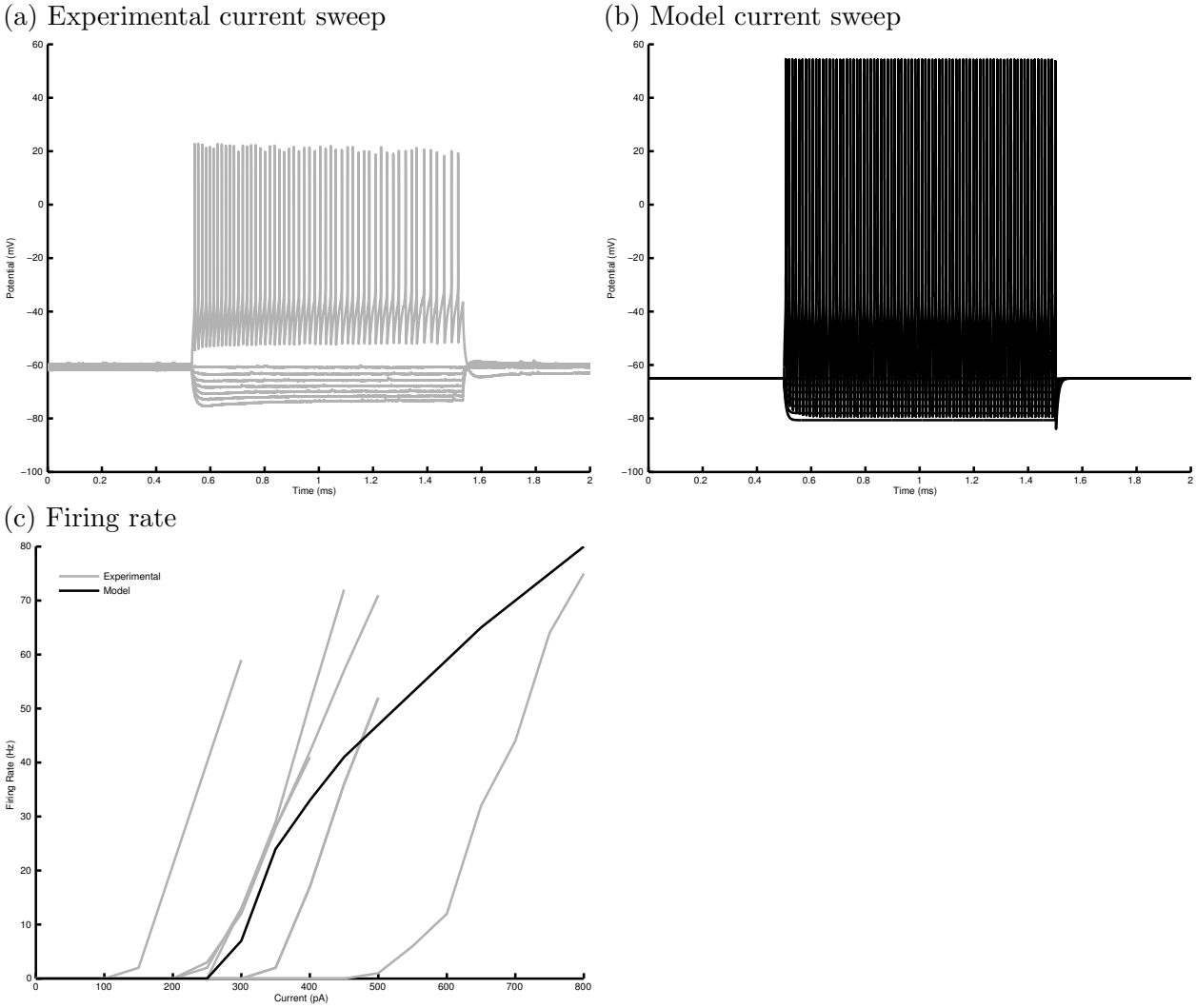

Figure 4.11: PV+ cell firing characterization.

rheobase, and firing rate of some experimental mouse cells from Lee et al. (2010). The comparison of the model cell with the experimental cells is shown in Figure 4.9 for the CCK+ basket cell and Figure 4.10 for the Schaffer Collateral-Associated cell.

PV+ Cells

I took the CA1 PV+ cell models from Cutsuridis et al. (2010) as a starting point and modified them so that they better fit the experimental cell observations from our lab. For the PV+ basket cell, I lowered the Na_v concentration to better match the firing rate found in

(a) Experimental current sweep

(b) Model current sweep

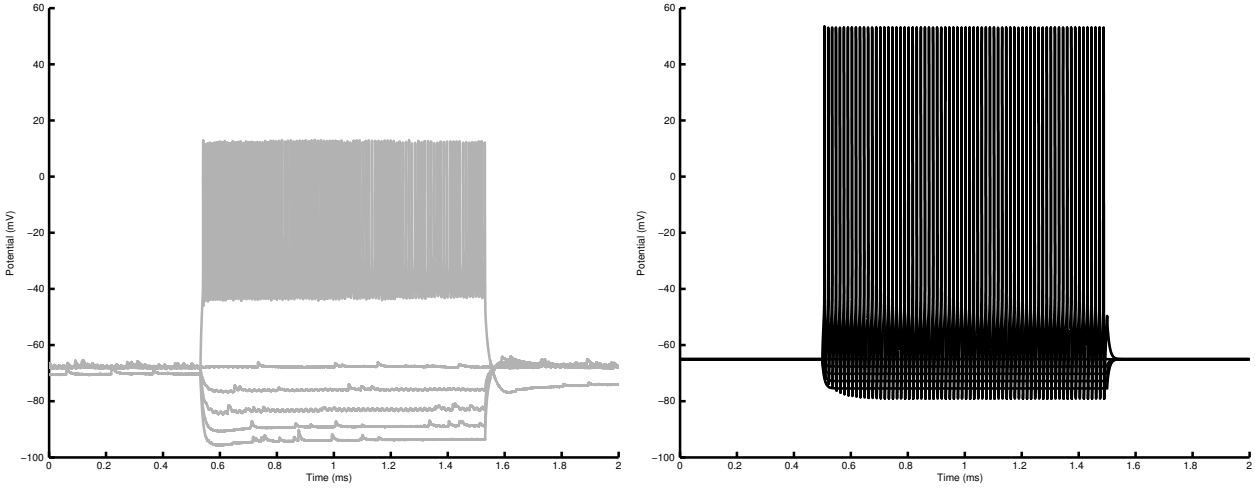

(c) Firing rate

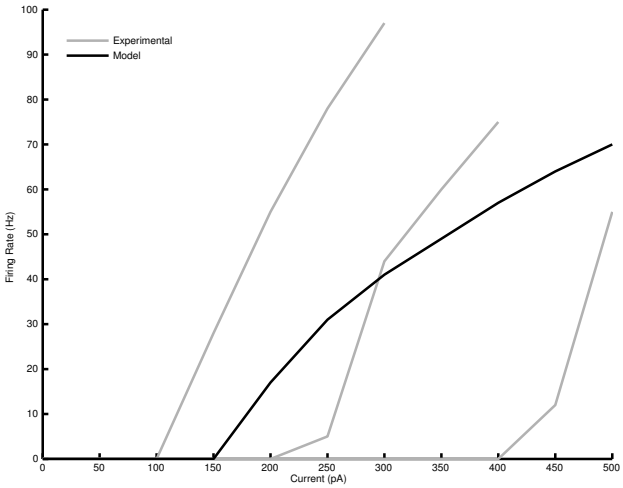

Figure 4.12: Axoaxonic cell firing characterization.

(a) Experimental current sweep

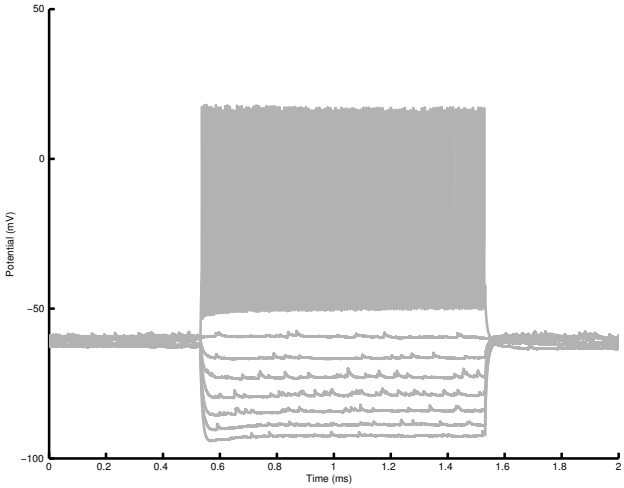

(b) Model current sweep

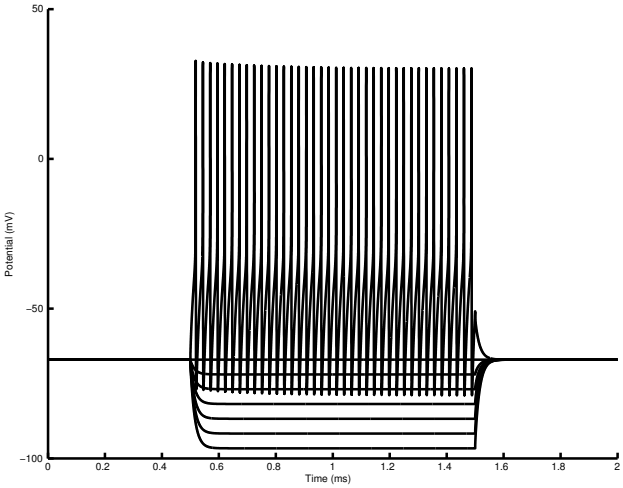

(c) Firing rate

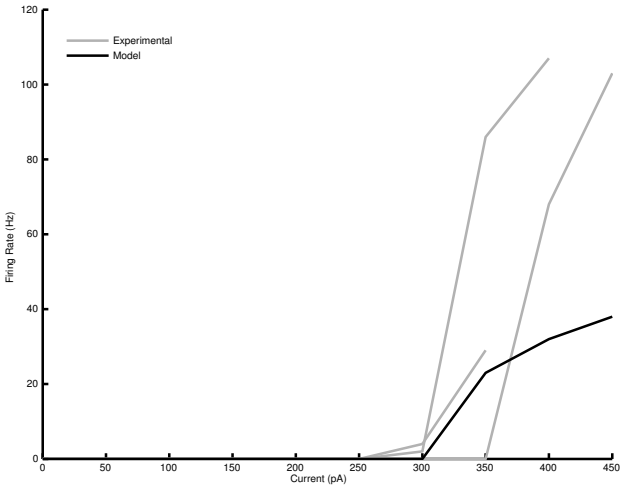

Figure 4.13: Bistratified cell firing characterization.

the experimental PV+ basket cells from our lab (mouse cells). For the axo-axonic cell, a different Na_v channel was used, the one used in the axon of the pyramidal cell, to better fit the firing rate of the experimental axo-axonic cells. The bistratified cell was modified even more, and given a different Na+ channel with a higher activation threshold so that the higher action potential threshold observed in these cells experimentally could be recreated. The firing rates and current sweeps of the cells are given in Figures 4.11 (PV+ basket cell), 4.13 (bistratified cell), and 4.12 (axo-axonic cell).

OLM Cell

I started out with the O-LM cell model from Cutsuridis et al. 2009 (ModelDB 123815), which they had modified from Saraga et al 2003 (Model DB 28316). However, I substituted ion channels from my other cells for the ones originally with the O-LM cell, because the originals caused an unphysiological resonance in response to any inhibitory synaptic input; the cell would oscillate dozens of millivolts, amplifying with time, in response to a single input. After substituting other ion channels, that behavior disappeared. The rebound spikes remained, though spontaneous activity was not seen.I also increased the specific membrane resistance and some of the potassium channel densities to achieve a higher firing frequency without depolarization block. The firing rate and current sweep are shown in Figure 4.14.

Neurogliaform Family Cells

I developed a neurogliaform family cell model to represent both neurogliaform and ivy cells. The two cells are both members of the neurogliaform family and have similar electrophysiological behavior. The ivy and neurogliaform cell have significantly depolarized action potential thresholds compared to other interneuron types. This special characteristic required me to design special sodium and potassium channels with depolarized activation and inacti-

(a) Experimental current sweep

(b) Model current sweep

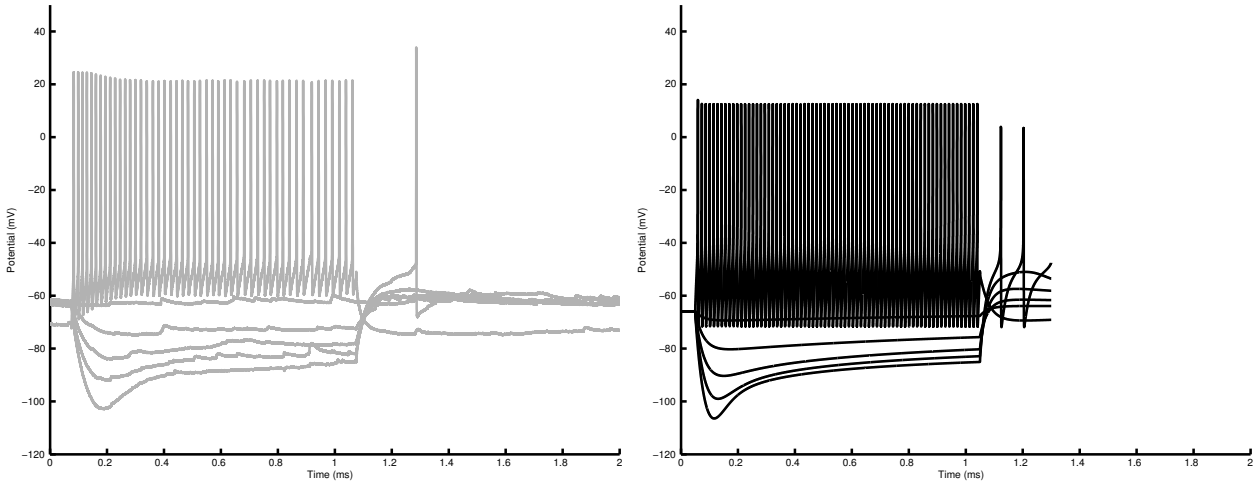

(c) Firing rate

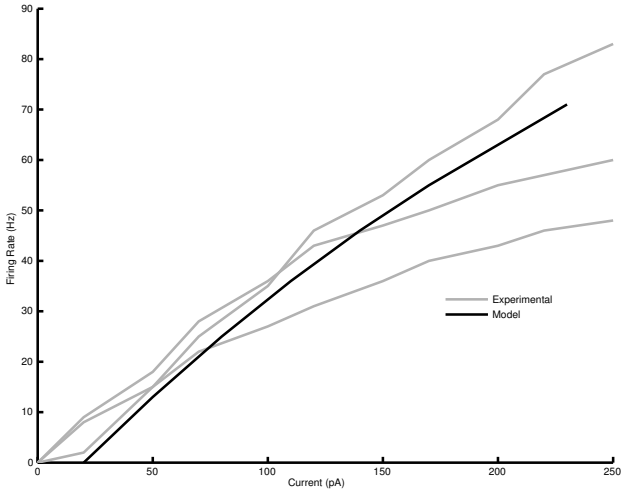

Figure 4.14: O-LM cell firing characterization.

(a) Experimental current sweep

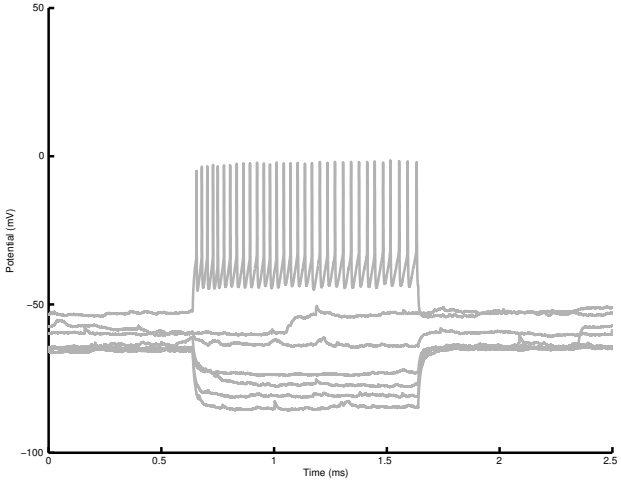

(b) Model current sweep

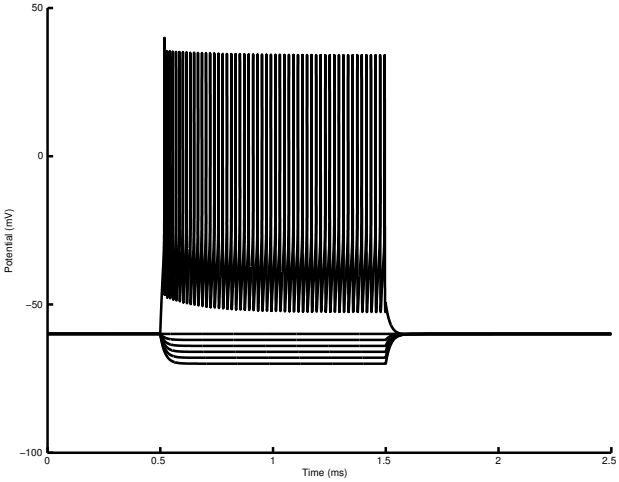

(c) Firing rate

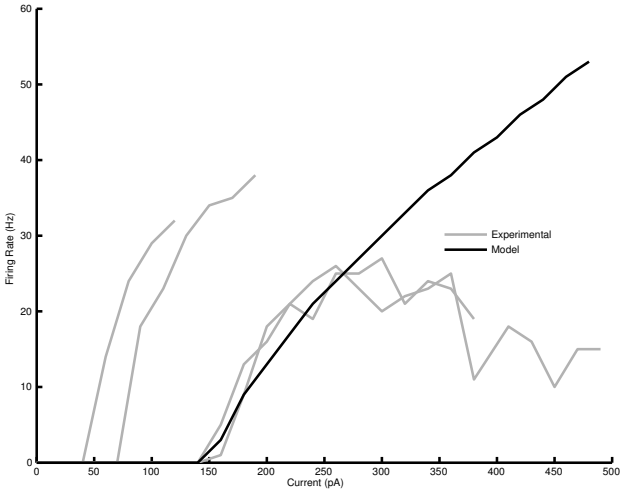

Figure 4.15: Neurogliaform cell firing characterization.

(a) Experimental current sweep

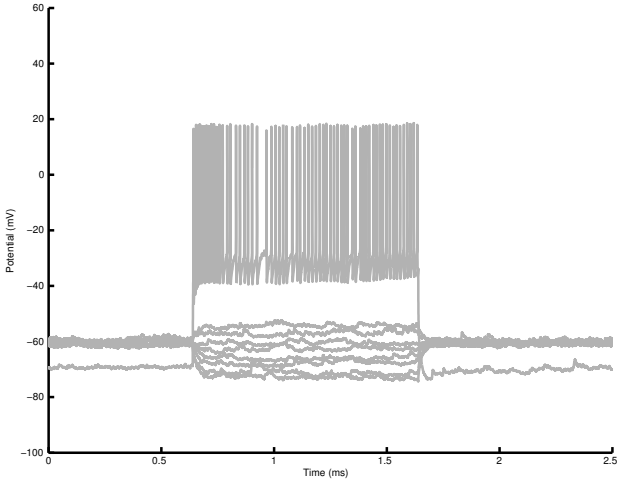

(b) Model current sweep

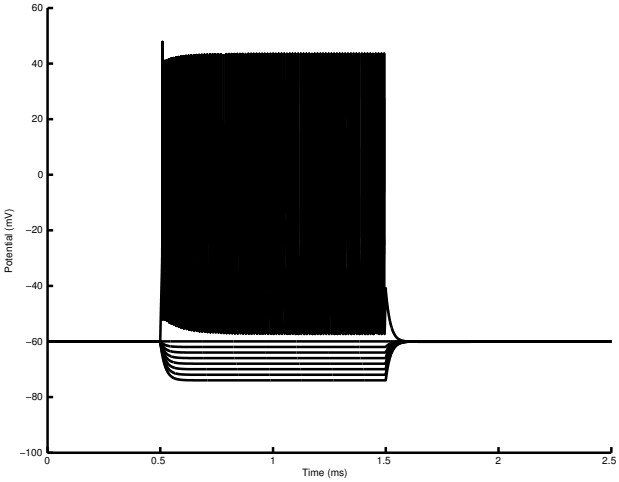

(c) Firing rate

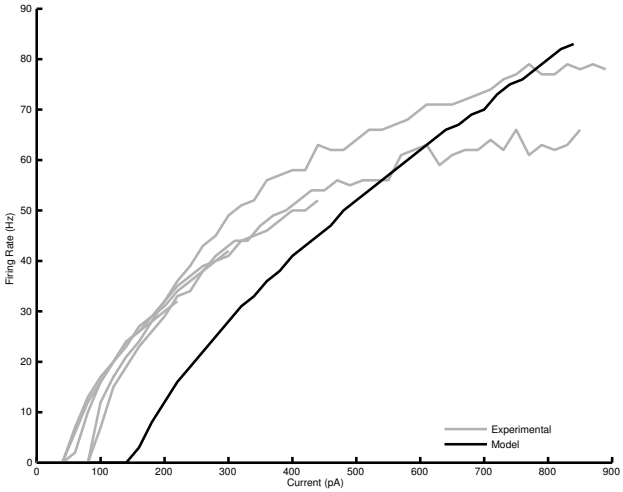

Figure 4.16: Ivy cell firing characterization.

vation voltage dependence. I successfully produced these ion channels and used them in the ivy and neurogliaform cell models to produce the characteristic action potential waveform, including the late-spiking property, the depolarized action potential threshold, and the minimal afterhyperpolarization (AHP; hyperpolarization after spike), as shown in Figure 4.16 for ivy cells and Figure 4.15 for neurogliaform cells.

Our model ivy cell appeared to have slightly more of an AHP than the biological cells, and the subthreshold ramp depolarization back to threshold was more linear in the biological cells than in our model cell. We then obtained the current v. firing frequency curve for the model ivy cell and compared it with the firing rate curves of several biological ivy cells. At low levels of depolarized current injection, the model ivy cell had similar firing frequencies. However, its curve was much steeper and so it had much higher firing frequencies with larger current injections than did the biological ivy cells. However, within the range of excitation the ivy cell is likely to receive within the context of the network model, where the ivy cells fired generally at lower than 5 Hz, it behaved similarly to biological ivy cells.

Neurogliaform Cell

As mentioned above, we used the same model for our ivy and neurogliaform cells. A comparison of the model neurogliaform cell with the biological cells is given in Figure 4.15. There was a broad range of excitability in the biological neurogliaform cells.

4.4 Components of Connections

In addition to constraining the numbers, distributions, and locations of connections (see Chapter 3), we also constrained and characterized the properties of individual connections and synapses. We did this by performing "'paired recordings"' of our model cell connections

and comparing the resulting postsynaptic current (or potential) with experimental data.

4.4.1 Using experimental data to fit a model synapse

When making pairs, we took into account the experimentally observed number of synapses in a connection. Using electron microscopy, various experimentalists found that connections involving different presynaptic and postsynaptic combinations comprised different numbers of synapses (Tamás et al., 2003; Klausberger et al., 2004; Maccaferri et al., 2000; Foldy et al., 2010). We designed our model connections to use these experimentally determined numbers of synapses in each connection. Then we matched experimental conditions for voltage clamp paired recording and compared our results with the experimental results. Specifically, we matched the holding potential of the postsynaptic cell and the reversal potential of the synapses involved in the recording. We used the Nernst equation to calculate the reversal potentials for ions of interest when fitting pairs, unless they were explicitly given in the publication. As with our single cell characterizations, we ignored the contribution of the junction potential. We inactivated the sodium channels in the model while fitting the synapses to prevent the occurrence of action currents (in many experimental conditions, the chloride reversal potential was significantly depolarized).

Then we fired the presynaptic cell and recorded the current response in the postsynaptic cell. For each cell type, we tested 10 different connections (where each connection was composed of an experimentally determined number of randomly placed synapses). We then determined the kinetics ($10 - 90\%$ rise time and decay time constant) and amplitude of the response of each of the 10 connections and altered our synapse parameters by hand so that the average of these properties matched the experimentally determined averages. The parameters that we altered were the rise and decay time constants as well as the weight (maximum conductance) of the individual synapses. Our parameter values and resulting

weights and kinetics are given in Table 4.5; the weights and kinetics are generally within 5% of the experimentally determined values (Tables 4.3 and 4.4). For reasons that are not understood, the rise time of the O-LM cell to pyramidal cell connection could not be tuned to produce a rise time as fast as that seen experimentally; the rise time of the model synapse was 10% longer than the rise time observed experimentally.

Cell Type	Synapses/Conn.	Reduced Approach		Full Approach	
		Convergence	Total Synapses	Convergence	Total Synapses
Axo-axonic	6	6	36	6	36
Bistratified	10	10	100	18	180
CCK+ Basket	8	13	104	23	184
Ivy	10	42	420	73	730
NGF	10	14	140	25	250
O-LM	10	8	80	15	150
PV+ Basket	11	17	187	30	330
SCA	6	2	12	3	18
Total		112	1,079	187	1,842

Table 4.2: Number of cells of each type converging onto the model CA1 pyramidal cell, along with the number of synapses per cell connection and the total number of synapses from each cell type, for both the reduced and the full approaches. Note that the number of synapses per connection stays the same in both approaches. Number of neurons converging and number of synapses per connection based on estimates from Bezaire and Soltesz (2013)

For the neurogliaform cell, we fit the $GABA_A$ and $GABA_B$ components separately, as there were data available for each component (Table 4.4, (Price et al., 2008)). Because only the time of peak current was given for the $GABA_B$ component of the neurogliaform cell, we estimated the decay kinetics.

Presynaptic Cell	Holding Pot. (mV)	Junction Pot. (mV)	10-90% Rise Time (ms)	Decay τ (ms)	Ampl. (pA)	Reversal Pot. (mV)	Ref.
Axoaxonic cell	−70	+4.6	0.80	11.20	308.0	$E_{Cl-} = +7$	Maccaferri et al. (2000)
Bistratified cell	−70	+4.6	2.00	16.10	150.0	$E_{Cl-} = +7$	Maccaferri et al. (2000)
CCK+ basket cell	−70	+10.8	0.63	6.47	115.4	E_{Cl-} = -26	Lee et al. (2010)
Ivy cell	−50	+15.0	2.80	16.05	8.0	E_{Cl-} = -88	Fuentealba et al. (2008a)
O-LM cell	−70	+4.6	6.20	20.8	26.0	$E_{Cl-} = +7$	Maccaferri et al. (2000)
PV+ Basket cell	−70	+10.8	0.59	5.35	65.44	E_{Cl-} = -26	Foldy (2007)
SCA cell	−70	+10.8	1.43	8.30	60.2	E_{Cl-} = -26	Lee et al. (2010)

Table 4.3: Table of paired recording data. Note that the ivy cell entry only includes the $GABA_A$ component. Pot.: potential

Receptor Type	Holding Pot. (mV)	Junction Pot. (mV)	Peak Time (ms)	Decay τ (ms)	Ampl. (pA)	Reversal Pot. (mV)	Ref.
$GABA_A$	-50 mV	+15 mV	29 ms	50 ms	4.9	-89	Price et al. (2008)
$GABA_B$	-50 mV	+15 mV	187 ms		1.9	-91	Price et al. (2008)

Table 4.4: Table of data from a CA1 neurogliaform cell to pyramidal cell pair. Note that peak current times rather than rise times were given, and that a decay time constant was only given for the $GABA_A$ component.

Cell Type	Model Parameters				Sim. Synapse Properties		
	Weight (uS)	**Syn.s**	τ_1 **(ms)**	τ_2 **(ms)**	**Ampl. (pA)**	**10-90% Rise**	**Decay**
PV+ Basket	$1.86e-4$	11	0.40	4.8	66.19	0.60	5.24
CCK+ Basket	$4.50e-4$	8	0.40	5.8	116.15	0.60	6.40
SCA	$8.50e-4$	6	0.46	3.9	58.48	1.36	8.28
Axo-axonic	$1.00e-3$	6	0.3	8.5	308.0	0.79	10.64
Bistratified	$5.10e-4$	10	0.42	11	149.40	1.97	16.49
O-LM	$1.20e-3$	10	0.25	7.5	27.03	6.84	19.82
Neuroglia. (A)	$1.45e-4$	10	8	39	4.88	29.60	50.01
Neuroglia. (B)	$4.30e-5$	10	180.00	200.0	1.86	189.20	*
Ivy (A)	$7.70e-5$	10	2.9	3.1	16.50	2.65	8.35

Table 4.5: Table of model IPSC parameters from fits to experimental data from Table 4.3. The 'Model Parameters' column gives the values of each synapse parameter that enabled the best fit of the experimental data. The actual characteristics of the model synapses under experimental conditions are given the 'Sim. Synapse Properties' column. * unable to compute unless run really long simulation.

Cell Type	Model Parameters				Sim. Synapse Properties		
	Weight (uS)	**Syn.s**	τ_1 **(ms)**	τ_2 **(ms)**	**Ampl. (mV)**	**10-90% Rise**	**H.W.**
CA1 Pyr. Cell	$8.10e-4$	1	0.05	3.5	0.71	2.95	16.10
Ento. Cortex	$1.50e-4$	1	0.50	3.0	0.25	7.38	22.40
CA3 Pyr. Cell	$1.00e-4$	1	0.50	3.0	0.20	3.66	15.86

Table 4.6: Table of model EPSP parameters from fits to experimental data from Table 4.3. The 'Model Parameters' column gives the values of each synapse parameter that enabled the best fit of the experimental data. The actual characteristics of the model synapses under experimental conditions of current clamp are given the 'Sim. Synapse Properties' column. H.W.: width at half amplitude

	PV+ B.	**CCK+ B.**	**S.C.-Assoc.**	**Axo.**	**Bis.**	**O-LM**	**NGF.**	**Ivy**
PV+ B.	D	X	X	X	D			X
CCK+ B.	X	X	X	X	X	X		X
S.C.-Assoc.	X	X	D	X	X	X	X	X
Axo.								
Bis.	X	X	X	X	X	X		X
O-LM	X	X	D	X	D	X	D	
NGF.							D	
Ivy	X	X	X	X	X	X	X	X

Table 4.7: Possible interneuron to interneuron connectivity. "X" indicates connections that we have put into the model without direct biological constraints. "D" indicates connections in the model constrained by experimental data.

After fitting each connection type under the corresponding experimental conditions, we then characterized all of the connections under a uniform, physiological condition so that we could directly compare the behavior of each connection. We chose to hold the postsynaptic cell at -50 mV to simulate mild excitation, to use the ion reversal potentials used in our single cell current sweeps and ion channel characterization (E_{Na+}=+55 mV, E_{K+}=-90 mV, $E_{Ca^{2+}}$=+140 mV, and E_{HCN}=-35), and to set the synaptic reversal potentials to 0 mV for excitatory synapses, -60 mV for $GABA_A$ synapses, and -90 mV for $GABA_B$ synapses.

Inhibitory Synapses onto Pyramidal Cells

Paired recordings were available for each interneuron connection onto pyramidal cells. We fit the experimental data under the experimental conditions for each cell type (Table 4.5).

Inhibitory Synapses onto Interneurons

Few paired recordings have been published for interneuron to interneuron connections. Table 4.7 gives the possible interneuron-interneuron pairs that were included in the full network model. Those pairs for which we have experimental data are marked with a "D". Those which we estimated at are marked with an "X". For the estimated ones, our justifications are listed in the appendix, as well as some parameter variations that we tested for each one.

Excitatory Synapses

The CA1 pyramidal cell in this model received excitatory input from other CA1 pyramidal cells, the entorhinal cortex, and the CA3. The CA1 pyramidal cell to CA1 pyramidal cell connection was characterized using a sharp electrode current clamp recording (Deuchars and Thomson, 1996). Though sharp electrode recordings are known to be leaky,

we didn't have enough information to correct for leakage. We assumed the reversal potential was 0. The cells were current clamped such that their resting voltage was between -67 and -70 mV. The mean PSP was 0.7 mV and the 10-90 % rise time was 2.7 ms, while the width of the EPSP at half maximum of the amplitude (half-width) was 16.8 ms. In our model, the current clamp was set to - 0.06 nA so the cell rested at about -67. The resulting EPSP amplitude was 0.71 mV, the 10-90 % rise time was 2.95 ms, and the half-width was 16.10 ms, as given in Table 4.6. We achieved this using a weight of 8.1e-4 μS, and synapse time constants of 0.05 and 3.5.

We fit the CA3 and entorhinal cortical afferents similarly. Assuming that the afferents make one synapse per connection with each pyramidal cell, we use the data from experiments that showed a single synapse was capable of causing a 0.2 mV change (EPSP) or was equivalent to injecting 4.3 - 5.6 pA of current (EPSC) (Magee and Cook, 2000). Because the amount of current injected was not provided in the experimental protocol, in our model we current clamped the pyramidal cell with 0 nA injected current.

For both afferents, we used a 10-90% rise time of 0.5 ms and a decay tau of 3 ms. Figure shows EPSCs obtained under physiological conditions, but with Nav channels inactivated. (With Nav channels allowed to activate during the EPSC, all three excitatory input types could cause action potentials).

The experimental data we were fitting used stimulation protocols intended to excite one synapse, so we fit the data using one synapse. However, actual connections, especially from the CA3, may comprise multiple synapses (Ropireddy and Ascoli, 2011). Therefore, after fitting the data using a single synapse, we altered the connectivity to assume that each connection from the CA3 and entorhinal cortex comprises two synapses.

Chapter 5

Spontaneous Theta Oscillations Arise in a Model CA1 Network

5.1 Results

Cell numbers as well as convergence and divergence of the model connectivity (Figure 5.1) are based on the quantitative assessment discussed in Chapters 2 and 3. To conduct the assessment, we surveyed over 100 experimental publications for anatomical data about CA1. Then we combined immunohistochemical data about laminar distribution and coexpression of markers to estimate the number of each interneuron type in CA1. Next, we extracted from the experimental literature bouton and input synapse counts for each cell type. We multiplied these counts by our estimated number of each cell and totaled the available input synapses and boutons, GABAergic and other, by layer of CA1. Then we determined the number of connections each cell type was likely to make with every other cell type based on the results of our quantitative assessment. When actually determining which cells of the model to connect, we distributed all cells evenly in 3D space and enabled random connectivity

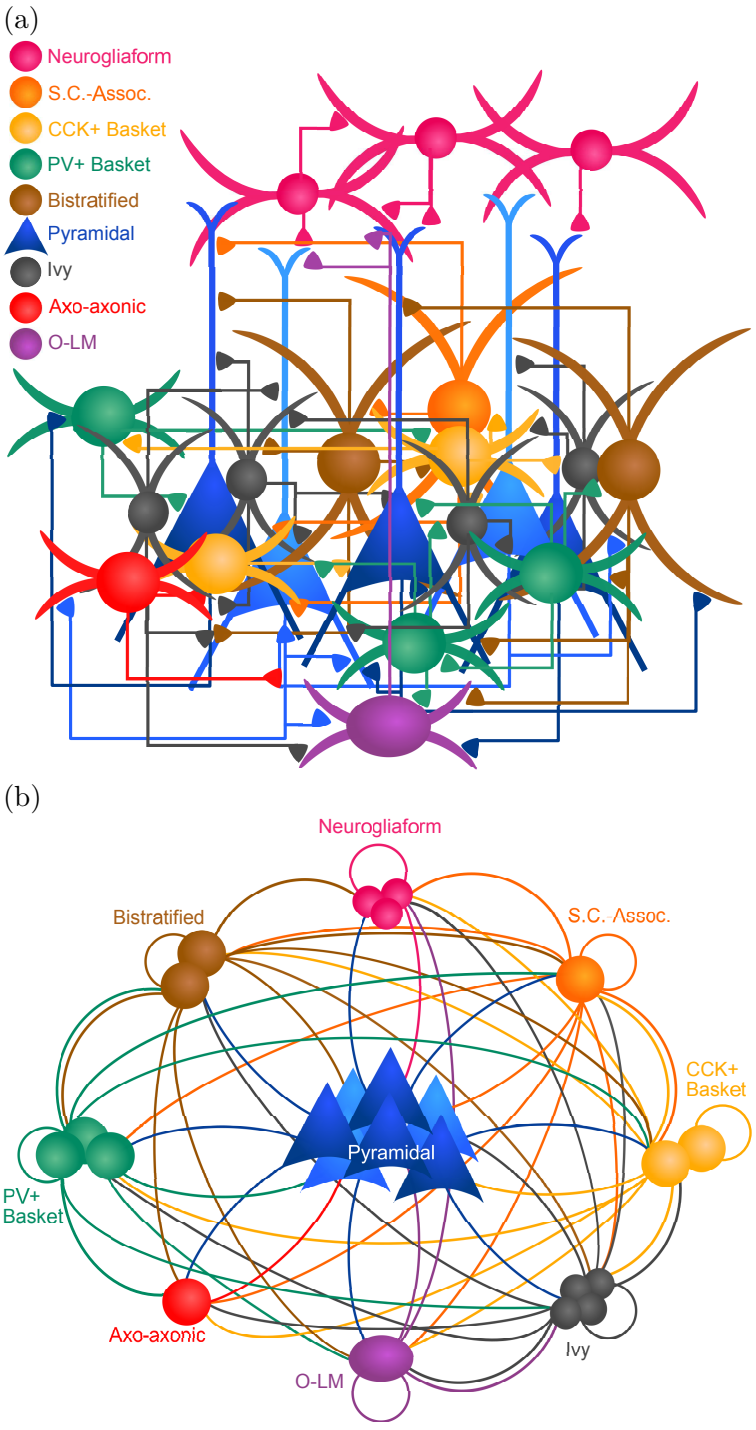

Figure 5.1: Intrinsic connectivity within CA1 network. (a) Model cells form synapses at experimentally observed locations on post-synaptic cells. (b) Each cell type innervates and receives connections from other cell types in a biologically constrained manner.

for cell connections where the postsynaptic cell body fell within the axonal extent of the presynaptic cell. Each time a connection was established between two cells, the presynaptic cell innervated the experimentally observed number of synapses on the postsynaptic cell. The synapse locations were randomly chosen from all possible places on the cell where the presynaptic cell type had been experimentally observed to innervate.

In addition to constraining our model to experimental cell and connection numbers, we also constrained the electrophysiology of individual cells and synapses (Figure 5.2). We first analyzed whole cell current injection traces of experimental cells of each type included in the model, calculating standard activate and passive electrophysiological properties. Then we fit our model cells to the experimental data, even subjecting the model cells to the same current injection protocols so we could directly compare their properties to those of the experimental cells. After fitting the single cell properties, we simulated experimental paired recordings to characterize the connections between our model cells. Where experimental data existed for paired recordings, we matched the experimental holding potential and synapse reversal potential, then performed 10 different paired recordings. We characterized the synapse properties including the synaptic amplitude, 10% - 90% rise time, and decay time constant. Finally, we fit our averages to the experimental data.

As the experimental data used to constrain the model were substantial and we wanted an intuitive way for people to view the constraints we used, how well the model fit the constraints, and the source of the constraints, we built a website for the model. The website enables anyone to intuitively browse the model's properties in a standard format for detailed information about cell types, ion channels, connectivity, comparison of model to experimental data, experimental data sources, simulation results, and more.

We implemented the model in parallel NEURON (Carnevale and Hines, 2005) and executed the simulations on supercomputers, including University of Texas' Stampede, UC Irvine's HPC, and San Diego Supercomputing Center's Trestles. Additional details are given in the

methods section in Chapter 1, section 1.8. All model results, characterizations, and experimental comparisons are available on our model website at `http://www.ivansolteszlab.org/models/ca1.html`.

5.1.1 Constrained network configuration displays physiological oscillations

After constraining the network based on published experimental observations, we chose reasonable estimates for the remaining unconstrained parameters, namely the synapse amplitudes for most incoming connections onto interneurons. We ran the network simulation with a variety of realistic amplitude levels for the interneurons. In a fraction of the total network configurations we used, we found that a spontaneous theta rhythm developed. We looked in depth at one such network where the oscillation was particularly prominent, which we called the Basic network configuration. This configuration contained pyramidal cells with complex morphology and realistic connectivity based on the calculations from Bezaire and Soltesz (2013). Further details about the various network configurations studied are available in section 5.1.3.

When given arrhythmic, tonic excitation, the Basic network configuration displayed oscillations in both the theta and gamma frequency ranges (Figures 5.3 and 5.6). The pyramidal cell spikes exhibited peak power at the theta frequency of 8.30 Hz. Within the gamma frequency range, they displayed some power at 25.15 Hz, but several interneuron types displayed their highest power at the gamma frequency of 25.15 Hz. Gamma was most obvious in PV+ interneurons, though the CCK+ basket cells displayed noticeable gamma power as well (Figure 5.6).

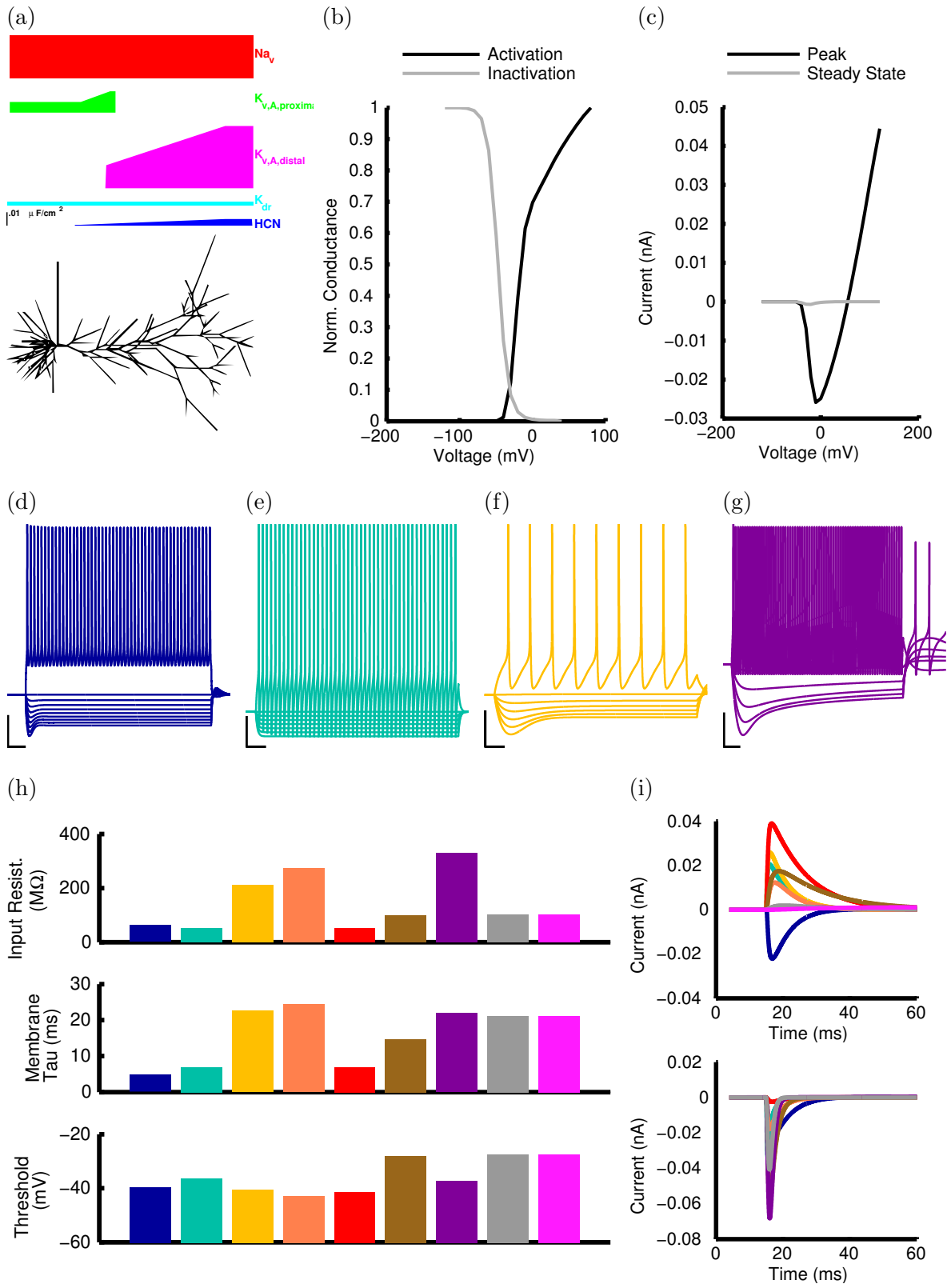

Figure 5.2: The electrophysiology of the model is biologically constrained and fully characterized. (a) The pyramidal cell models contained five ion channel types, some of which had varying densities along the dendrites of the cell (top). The morphology of the complex pyramidal cell, taken from (Poolos et al., 2002), is shown (bottom). (b) and (c) The behavior of each ion channel is physiological and characterized in experimental terms including (b) the activation and inactivation curves and (c) the peak and steady-state current-voltage relationship. (h) The electrophysiological properties of the cells, both active and passive, were characterized. (d-g) The current injection sweep is shown for several model cells, including

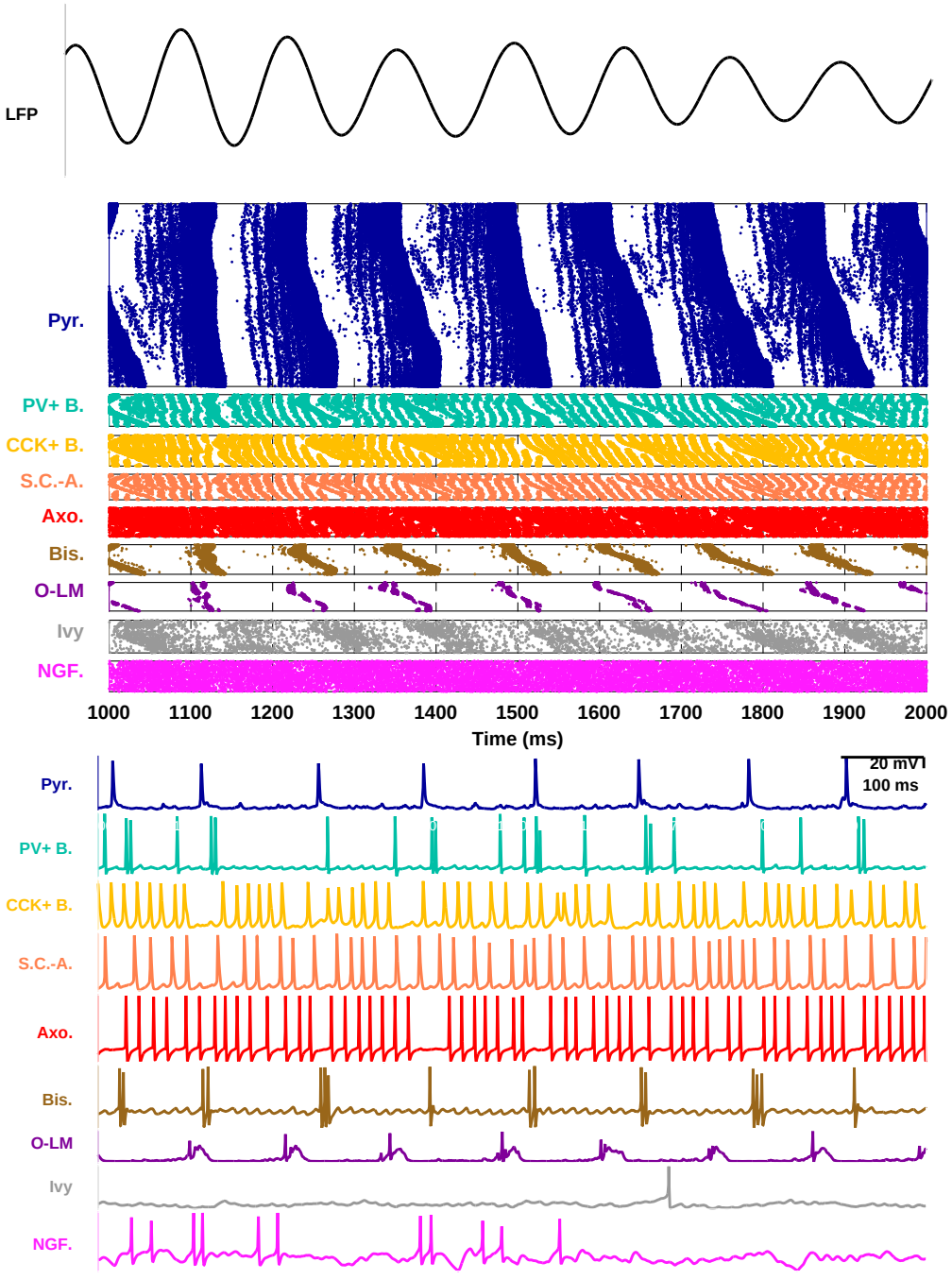

Figure 5.3: When given tonic excitation, the physiologically-connected Basic network configuration spontaneously displays theta and gamma oscillations. (Top) The calculated LFP analogue based on the pyramidal cells of the network displays a theta oscillation. (Middle) The oscillations are apparent in the spike times of the cells. Each cell's spikes are displayed horizontally at a given y-axis position per cell. (Bottom) A somatic, intracellular potential trace is shown for one cell of each type.

(a) 0.30 Hz

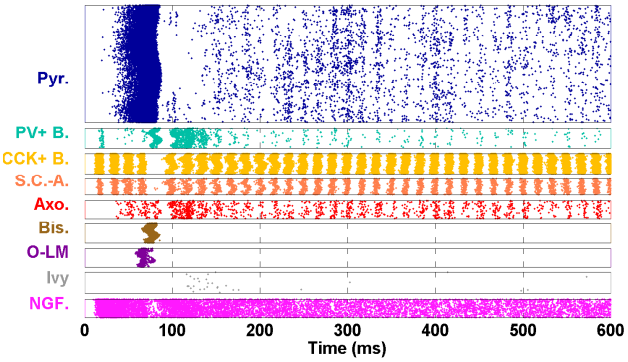

(b) 0.40 Hz

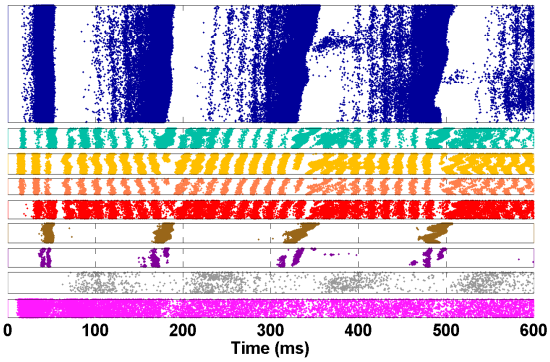

(c) 0.45 Hz

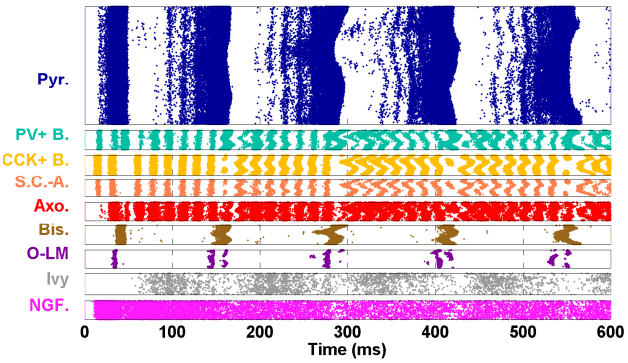

(d) 0.475 Hz

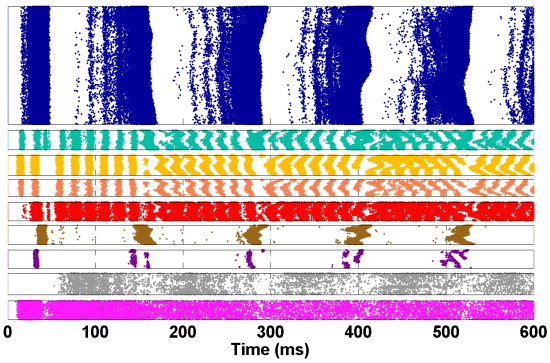

(e) 0.50 Hz

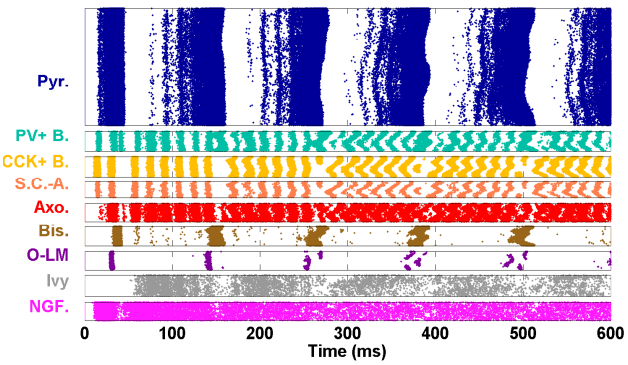

(f) 0.55 Hz

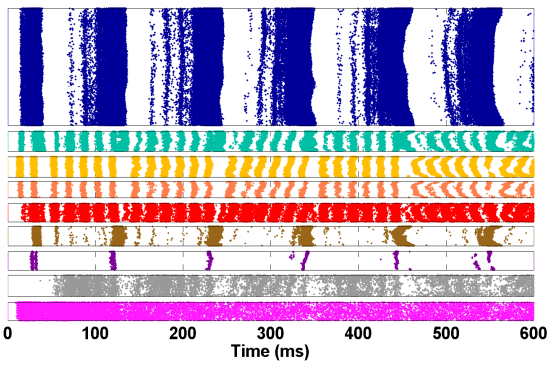

(g) 0.65 Hz

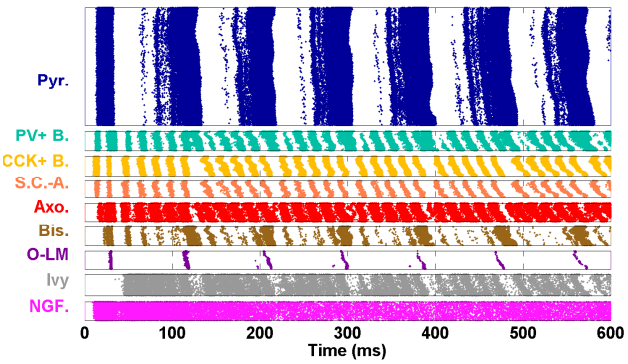

5.1.2 Oscillatory properties depend on excitation level

Next, we varied the excitation level of the network by increasing or decreasing the mean Poisson frequency of our randomly generated afferent spike trains. In the Basic network configuration, the oscillatory properties varied as a function of excitation level (Figure 5.7b). Between 0.4 Hz and 0.65 Hz, the oscillation frequency steadily rose. We took the Fast Fourier Transform of the pyramidal cell spike times and found that the power at the peak theta frequency steadily rose as well (Figure 5.7b), in correlation with the total number of spikes, as expected. In general, theta oscillations were only apparent within a small range of excitation levels dependent on the particular network configuration. When the excitation level fell below a mean Poisson frequency of 0.4 Hz in the Basic network configuration, the theta oscillation fell apart because several interneuron types were no longer adequately excited and became silent. The remaining types became less inhibited and fired at a higher rate. Although the theta oscillation disappeared, most of the interneurons that were still sufficiently excited to spike settled into a gamma rhythm that was even displayed in the pyramidal cell firing (Figure 5.4a).

5.1.3 Multiple network configurations exhibit theta and gamma

In addition to varying the stimulation level, we employed two distinct connectivity sets in the model. First, we set the convergence and divergence of the pyramidal cells to match the numbers calculated in the quantitative assessment (Bezaire and Soltesz, 2013). The convergence onto the pyramidal cells was calculated based on the synapse densities and dendritic lengths observations from Megías et al. (2001) and then compared with the calculated diver-

Figure 5.4 *(preceding page)*: Spike rasters of the Basic network simulations at various levels of afferent excitation. Note the disappearance of the theta oscillation with the lowest excitation level of 0.3 Hz in (a).

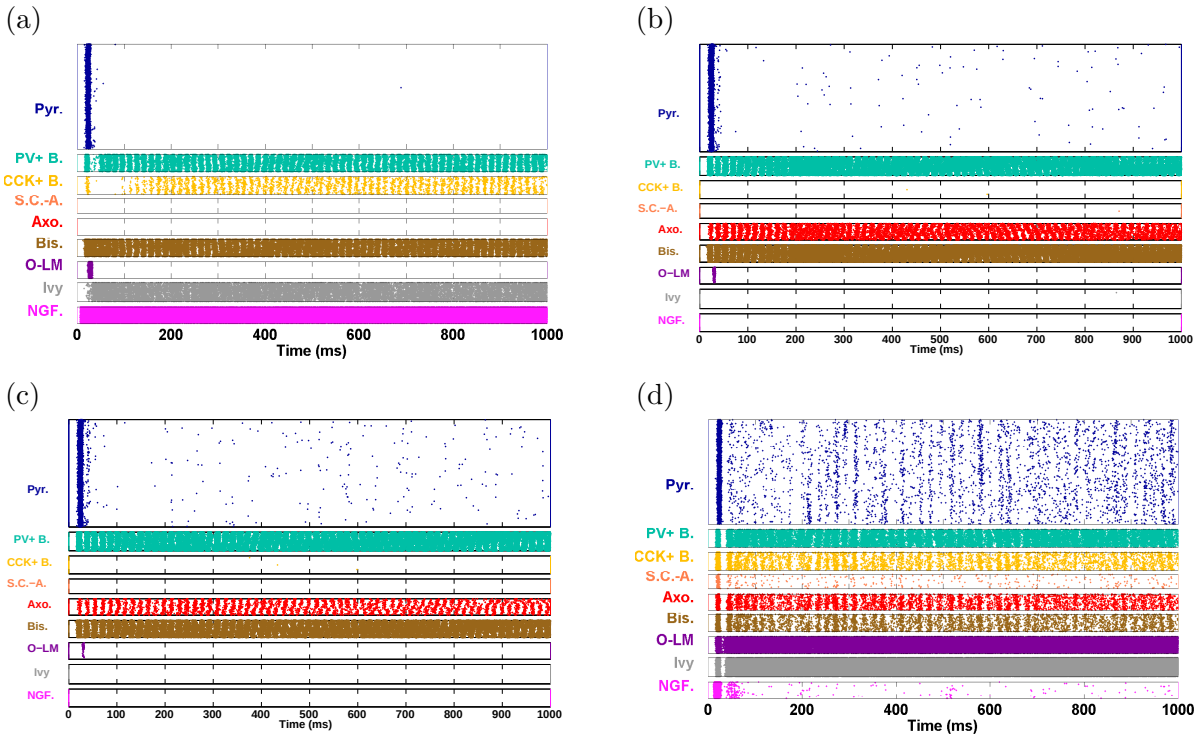

Figure 5.5: With reduced interneuronal variability, the theta oscillation disappears. Successive reductions are applied here from a to d. (a) The electrophysiological diversity is reduced so all interneurons have the same electrophysiology of the PV+ basket cells. (b) Next, the diversity of the excitatory input synapses to all interneurons is reduced so they all receive the same excitatory synapse weights as the PV+ basket cells. (c) Then, the diversity of the inhibitory input synapse weights to all interneurons is reduced so they all receive the same inhibitory synapse weights as the PV+ basket cells. (d) Finally, the diversity of the convergence onto the interneurons is reduced so they all receive the same synapse numbers as the PV+ basket cells.

gence of the interneurons and afferents onto the pyramidal cells. As noted in the quantitative assessment, there were not enough inhibitory boutons available to fully innervate all of the expected GABAergic input synapses on the pyramidal cells or interneurons; about 30% of expected inhibitory input synapses onto the pyramidal cells did not receive any inhibitory boutons. Because it has not yet been resolved which interneurons supply these synapses, we employed two different connectivity sets in our network model (calculated and full coverage). The *calculated* connectivity used the connection numbers for the inhibitory connections onto pyramidal cells from the quantitative assessment directly (Bezaire and Soltesz, 2013). In contrast, the *full coverage* connectivity scaled up the numbers of some of the inhibitory convergence onto the pyramidal cell to achieve full coverage of all expected inhibitory input synapses onto pyramidal cells, as given in Megías et al. (2001). We also used two different pyramidal cell models in our simulations: either a detailed morphology pyramidal cell model with over 200 compartments, from Poolos et al. (2002), or a simplified pyramidal cell model with similar electrophysiology, modified from Cutsuridis and Hasselmo (2012).

Throughout this work, we followed three network configurations in particular. Aside from the Basic network configuration described already, we also focused on two network configurations we will call ScaledUp and SimplePC, the spiking activity and the FFTs of which are given in Figure 5.6. The ScaledUp model included the detailed pyramidal cell morphology but with the scaled up number of inhibitory connections to its pyramidal cells. The SimplePC model contained the calculated number of inhibitory connections onto pyramidal cells and a simpler morphology pyramidal cell model. The simulation execution time and the memory requirement for the SimplePC model were quite a bit lower than for the other two models, due to the simpler pyramidal cell morphology used.

We found that almost all cell types in each simulation displayed a peak in power within the theta range, the gamma range, or both ranges, and that the peak frequency in each range was generally shared by all cell types within that network. In addition, the peak theta

frequencies were similar across the networks (Basic = 8.30, ScaledUp = 7.08, SimplePC = 6.59). For the three simulations of interest, they achieved their oscillations with a variety of firing rates for each cell type, though the rates are within a physiological range when compared to the experimentally observed rates found in published literature (Figure 5.6c). For the other configurations aside from Basic, we found that the level of stimulation provided to the model did not have a straightforward correlation with the theta frequency or normalized power, hinting at the presence of non-linear network dynamics due to the connections between interneuron types. In general, increasing the afferent firing rate differently affects each interneuron type due to the different input resistances of the interneurons. While the interneurons may achieve a particular steady state firing rate at one level of excitation, when the excitation is raised, a few interneuron types may become proportionally more excited relative to the rest of the network, enabling them to fire strongly enough to shut down other interneuron types.

Network	**Theta Freq.**	**Theta Power**	**Gamma Freq.**	**Gamma Power**
Basic	8.30	4155.18	25.15	2777.37
ScaledUp	7.08	40.59	51.03	37.77
SimplePC	6.59	12.82	29.54	4.91

Table 5.1: FFT theta and gamma properties for the pyramidal cell spikes from all pyramidal cells of the highlighted networks.

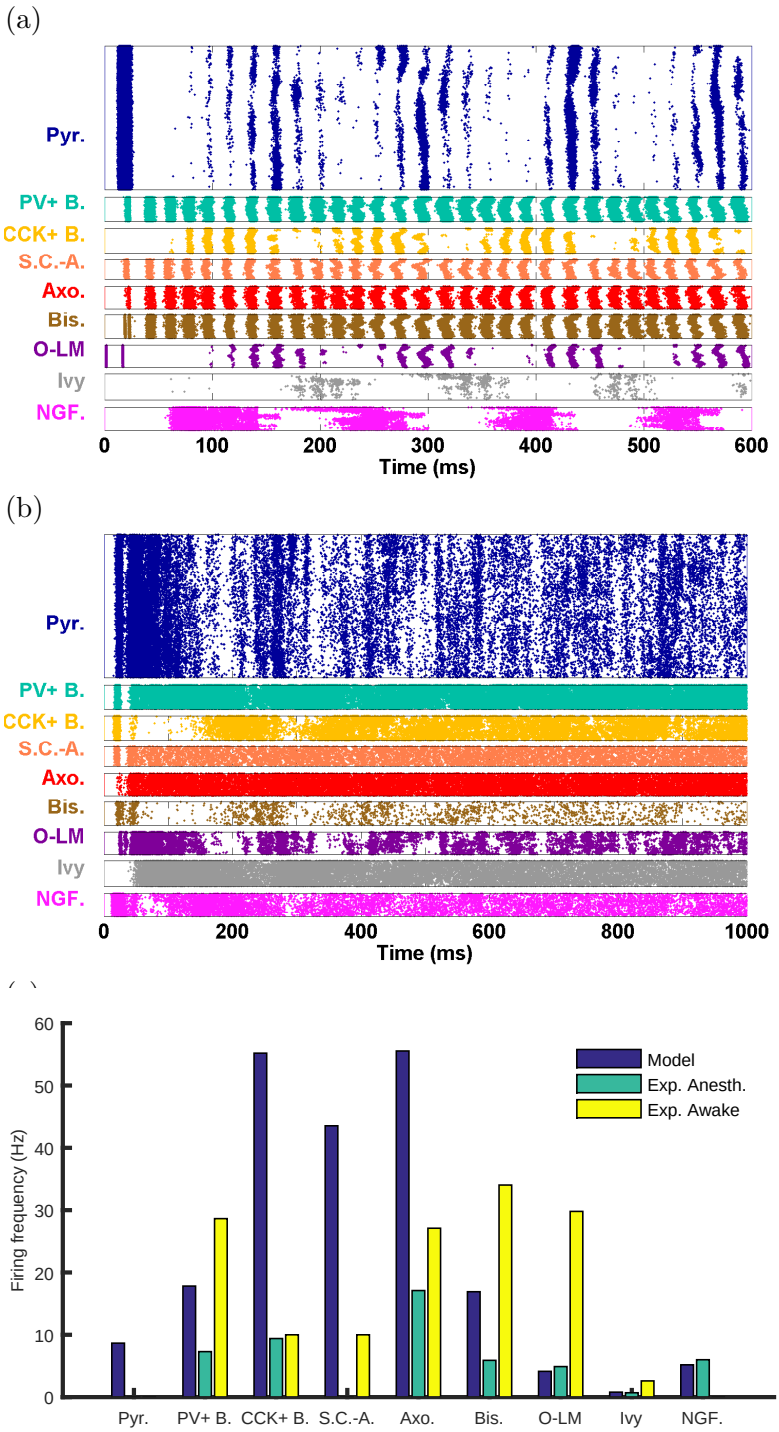

Figure 5.6: Multiple network configurations can generate theta oscillations. (a, b) The spike rasters are shown for two other network configurations, (a) ScaledUp and (b) SimplePC. (c) Firing rates of experimental and model cells during theta oscillations. Both awake-state and anesthetized firing rates are shown for each cell type, as found in experimental literature. The firing rates for each model network configuration were also included. Model firing rates were generally similar to anesthetized firing rates *in vivo*.

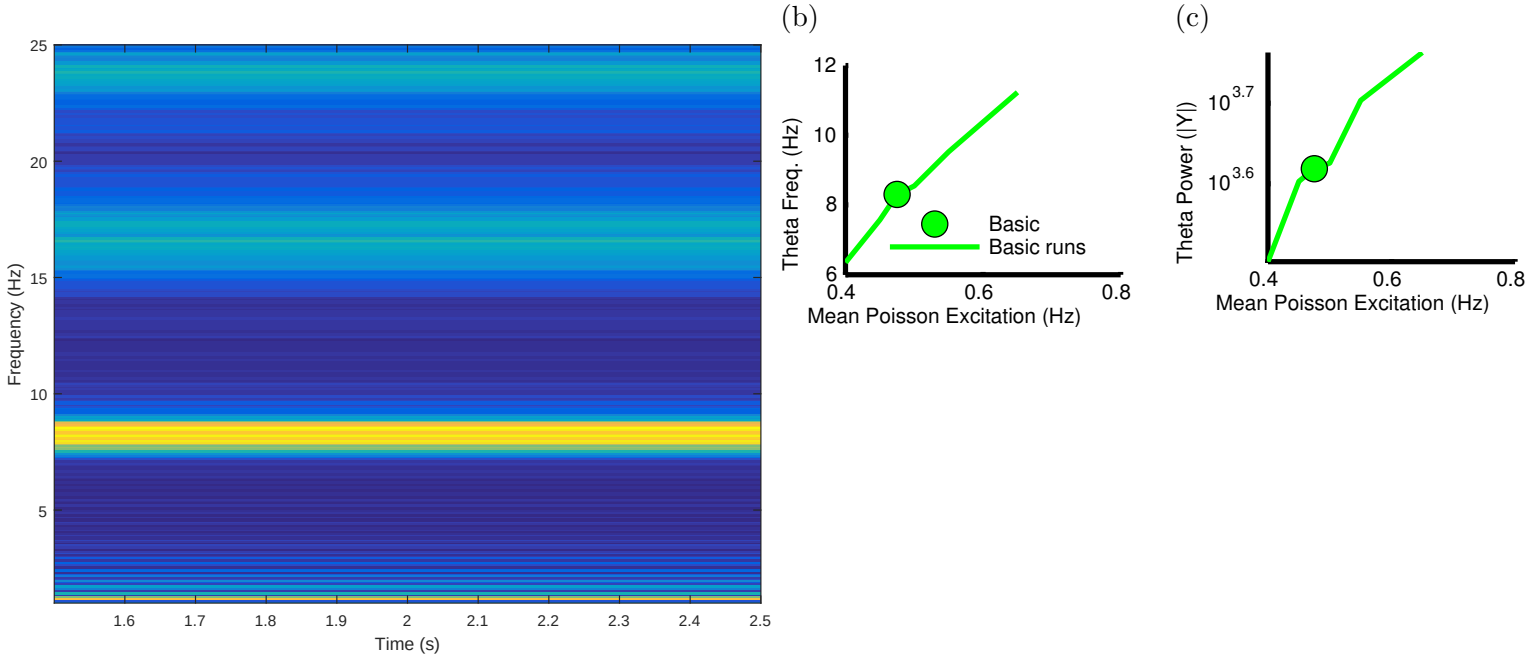

Figure 5.7: Network solutions with a variety of physiological firing rates can achieve theta and gamma oscillations. (a) The FFT power of each cell type's spikes is shown for the Basic network. (b - c) In the Basic configuration, varying tonic excitation level alters the theta properties within a small range of excitation levels. Increased excitation corresponds with increased theta frequency b and increased theta power c.

5.1.4 Model manipulations

Next, we manipulated various aspects of the network to characterize their contributions to the spontaneous oscillations. We reduced the interneuronal diversity of the network, altered the network connectivity, or altered the synapse kinetics and amplitudes. Out of infinite possibilities for manipulating the network, we chose these three disparate approaches to highlight the flexibility of the model implementation. As the model is now available online with thorough documentation and is compatible with a user-friendly simulation helper (SimTracker), we encourage others to use the model to answer their own questions about the role of various network components in CA1 function.

Reduced diversity

We reduced the interneuron diversity of the network in a variety of ways. First, we replaced the electrophysiological profiles of the different interneuron types with a single electrophysiological profile (Figure 5.8a). In each case, the theta power dropped drastically and the visible theta pattern in the spike raster disappeared. Because this may alternatively be due to inappropriate excitation levels, for one profile we also matched the excitatory afferent weights, all incoming synaptic weights, and the convergence onto each cell to that of the replacement type. While having a incoming connectivity that corresponded to the electrophysiological profile enabled all the cell 'types' to better participate, it did not restore the theta rhythm (Figure 5.5).

.

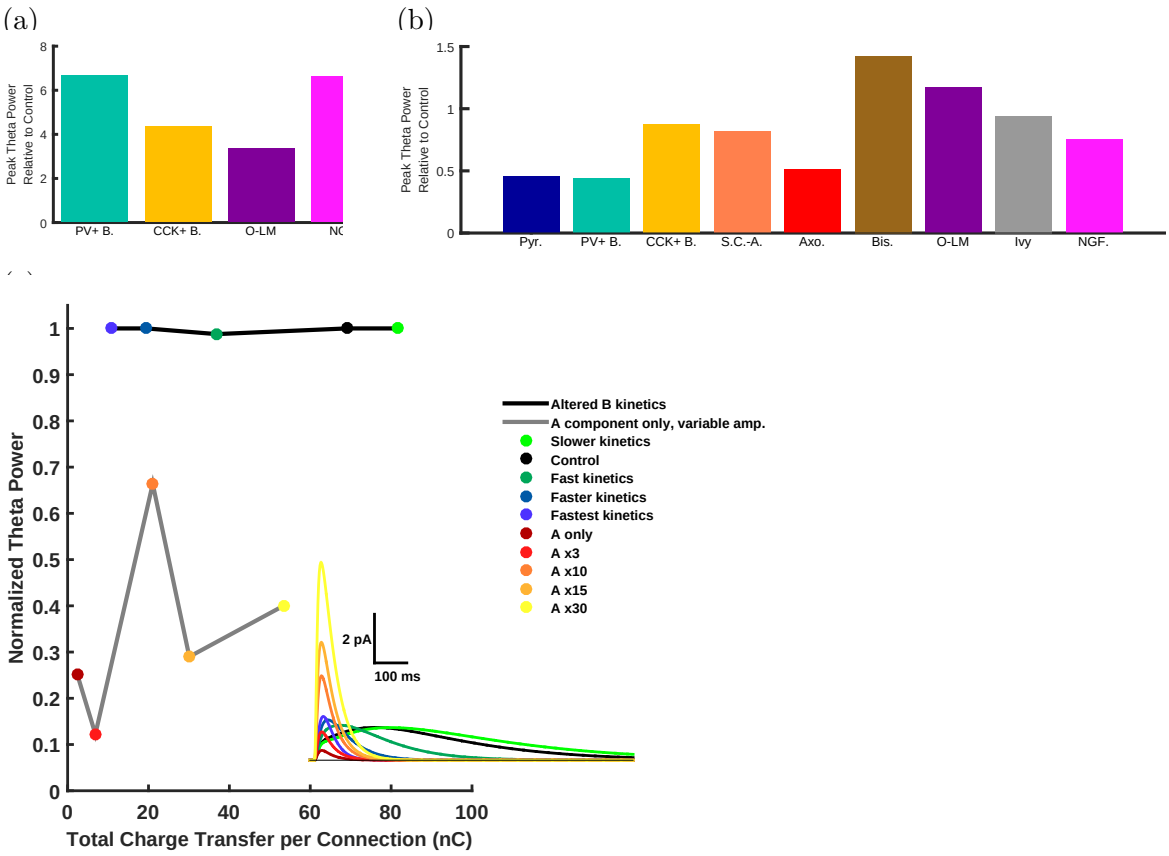

Figure 5.8: Network manipulations in the SimplePC configuration often reduced theta power. (a) Setting the electrophysiological profiles of all interneurons to that of a single cell type (PV+ basket, CCK+ basket, O-LM or neurogliaform cell) significantly reduced theta power, frequency, or both. (b) Removing the outputs of each cell type in turn had differing effects on theta power and frequency depending on cell type.(c) Characterization of the effect on theta oscillations of the $GABA_{A,B}$ synapses innervated by neurogliaform cells. Inset shows the IPSC of a neurogliaform to pyramidal cell connection, for each synapse variation. Even when a $GABA_{A,only}$ connection was strengthened sufficiently to induce a comparable total charge transfer per connection, the slower kinetics of the $GABA_{A,B}$ synaptic connections better supported theta oscillations. Blue to green data represent $GABA_{A,B}$ synaptic connections with slower or faster $GABA_B$ kinetics than the control. Red to yellow data represent $GABA_{A,only}$ synaptic connections with stronger synapse amplitudes.

Contribution of individual cell types

We also characterized the contribution of each cell type to the spontaneous oscillation by removing that cell type's outgoing connections and observing the effect. We found that removing different cells differently affected the theta oscillation. Schaffer Collateral-associated had a small effect as characterized by this test, which was not surprising given their small number (400 cells). Bistratified cells somewhat more surprisingly did not have a large effect, probably because the coincident inhibition from the O-LM cells remained intact. While the theta power remained high with the loss of PV+ basket cell outputs, in fact the normalized power was reduced and the theta frequency dropped to the lowest end of the range. The other cell types had noticeably lower theta power, though the frequency was not as affected as it was with the PV+ basket cell cut.

For characterization of the PV+ basket cell role, we additionally removed only PV+ basket cell synapses onto interneurons or only PV+ basket cell synapses onto pyramidal cells. We found that the greater disruption resulted from removing the synapses onto pyramidal cells, although there was a mild change in the network when PV+ basket cell connections to other interneurons were removed.We also removed the PV+ basket cell to pyramidal cell connections from the ScaledUp network configuration and found that while theta also fell apart, a strong gamma remained.

Contribution of $GABA_B$

$GABA_B$ is suspected to play a role in the phase preferential firing of interneurons and in a computer model was found to help differentiate between spatial trajectories with identical starting points (Wallenstein and Hasselmo, 1997; Sohal and Hasselmo, 1998). Also, in a preparation used to study LTP, Mott and Lewis (1991) found that the disinhibition activity of $GABA_B$ was necessary to the induction of LTP. Therefore, we examined the role of

$GABA_B$ in the theta oscillations of our model network.

Postsynaptic $GABA_B$ was included in our model for inhibitory synapses innervated by neurogliaform cells (Olah et al., 2009). Although ivy cells are part of the neurogliaform cell family and may also provide $GABA_B$ mediated inhibition (Bezaire and Soltesz, 2013), their potential $GABA_B$ component has not been experimentally characterized, so we only included a $GABA_A$ component for synapses made by ivy cells. The postsynaptic $GABA_B$ component provided by the neurogliaform cells is likely to be the largest contribution to the network dynamics attributed to postsynaptic $GABA_B$, as it has been experimentally observed that the $GABA_B$ inhibition activated by tempero-ammonic inputs (assumed to be innervating neurogliaform cells) was stronger and produced larger effects on spike timing than the proximal $GABA_B$ inhibition activated by the Schaffer Collateral input (Kohl and Paulsen, 2010; Kwag and Paulsen, 2009).

Next, we removed the $GABA_B$ component from our neurogliaform synapses and found that it dramatically decreased the theta power. However, this could be due simply to a general decrease in inhibition. Therefore, we next tried increasing the weight of the remaining $GABA_A$ component until it achieved a similar total charge transfer as the intact $GABA_{A,B}$ synapse. While the theta power increased with stronger $GABA_A$ synapses, it was still lower than that achieved with a similar charge transfer via $GABA_{A,B}$ synapses.

We first altered the rise and decay time constants of the $GABA_B$ synapse component and we found that quickening the kinetics of the $GABA_B$ synaptic component decreased the theta power (Figure 5.8c) while having a minimal effect on theta frequency. Next, we removed the $GABA_B$ component altogether and found a significant drop in the theta power. This may be due to a general decrease in inhibition, so we next increased the weight of the remaining $GABA_A$ component until it achieved a similar total charge transfer as the intact $GABA_{A,B}$ synapse. While the theta power increased with stronger $GABA_A$ synapses, it remained lower than in networks containing $GABA_{A,B}$ synapses capable of similar total charge transfer

(Figure 5.8c). For the neurogliaform synapses in our model network, receiving equivalent charge transfer more quickly is not as effective for maintaining the theta rhythm.

5.1.5 Distinct theta phase preferences and modulation levels

When we analyzed the firing rate of each cell type as a function of phase at the theta frequency, we found that, in each network, the neurons displayed distinct firing phase preferences segregated by neuron type (Figure 5.9). These firing phase preferences were compared to the experimentally observed phase preferences published in the literature for each cell type (Table 1.1). We found that different network configurations led to different phase preferences, which we had suspected given that different experimental preparations (awake animals versus anesthetized animals) also displayed somewhat differing phase preferences. As the spontaneous theta observed in our network is a different state than the theta displayed in vivo in the presence of rhythmic input, we expected our interneurons to display different phase preferences. However, there were some similarities present across the different network configurations. One, the O-LM cells and bistratified cells often fired around the time at which the pyramidal cells fired. Two, the neurogliaform and ivy cell synapse phase preferences were consistently shifted from each other. Three, the PV+ cell phases were generally distinct among themselves while in two out of three cases, the CCK+ cells had similar phases.

It is also important to note that, while the cells displayed firing phase preferences, they fired at other phases as well, though at a lower level (Figure 5.9). This distribution of spikes across different phases is also seen experimentally, as well as the differing levels of modulation by theta and gamma that is seen across different interneuron types experimentally.

We were able to achieve theta in smaller networks as well; however the smaller networks required a higher level of convergence and stronger connectivity between cell types than is

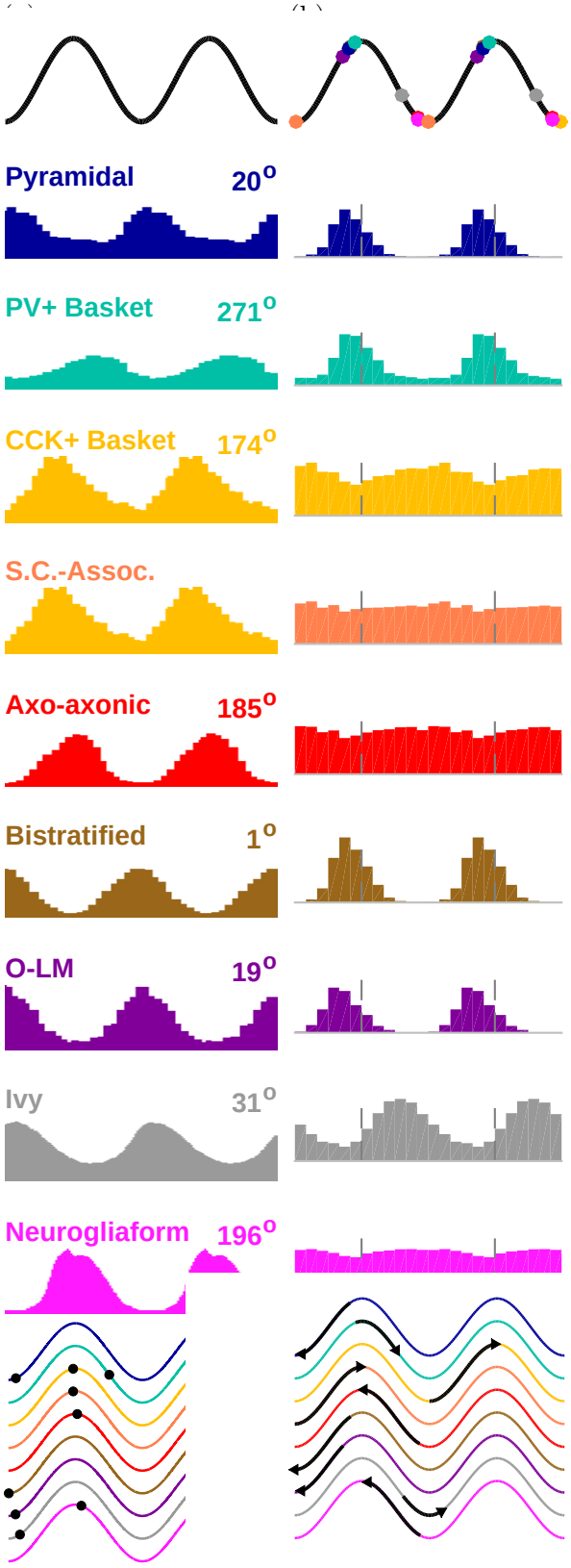

Figure 5.9: Model cell types display distinct theta phase preferences in their spike times. (Top) Theta phase preference is shown in reference to an idealized, hypothetical stratum pyramidale LFP wave. (Middle) Firing probability as a function of theta phase (double plotted for two theta periods) is shown per cell type. (Bottom) The shift in phase required to match anesthetized phase preferences is shown for each cell type. These data are displayed for (a) anesthetized experimental data and (b) Basic network. Experimental data used for CCK+ basket cell and Schaffer Collateral-Associated cell are categorized as CCK+ cells in

seen physiologically. Using connection strengths that are stronger than warranted for the synapses could render the network better able to synchronize its cells than in reality, so we considered it necessary to also achieve the oscillation in the full-scale network with relevant synapse weights and numbers. However, we also wanted some way to study a reduced version of the model on a personal computer while still maintaining the experimentally constrained connectivity. This led to the development of the Network Clamp.

5.1.6 Network Clamp

We wanted some way to study a reduced version of the model on a personal computer while still maintaining the experimentally constrained connectivity. This led to the development of the Network Clamp. The Network Clamp is a rational way to incorporate the biological detail of the network model into a manageable model that can be run on a personal computer. It can also be used to answer questions about how the network activity influences single cells. The concept of the Network Clamp is to observe a single cell in its natural state, essentially receiving all of the incoming connections that it would receive in a network, and to receive the synaptic input from those connections as they would be active in the network (Figure 5.10a). The Network Clamp enables a modeler to use realistic connectivity onto the cell of interest, and also to design realistic in vivo inputs, to use actual recorded spike trains for input or to replay a network model result into a cell. In a sense, one can visualize Network Clamp as if a single cell were to be dissected out of the full-scale network, with all of its input synapses still attached to its membrane (Figure 5.10a), so that these inputs can be then driven according to their natural pattern of activity during theta (or other) oscillations.

We previously applied this cookie-cutter technique to create a microcircuit model of CA1 pyramidal and PV+ basket cells (Lee et al., 2014) to study the effects of interneuronal connectivity specificity. Now we have taken this idea even further by zooming in on a single

pyramidal cell with all of its incoming connectivity still intact. Here we Network Clamped a simple pyramidal cell using the SimplePC connectivity, so that the cell received inputs from over 7,000 afferent cells. Locally, almost 200 synapses were innervated by other CA1 pyramidal cells, and over 1000 GABAergic synapses were innervated by CA1 interneurons, preserving the convergence determined in the quantitative assessment (Bezaire and Soltesz, 2013). We programmed the presynaptic cells to fire on average at their experimentally observed rates and to display phase preferential firing at their experimentally observed phases during an 8 Hz theta oscillation. Then we ran a 20 second long simulation while recording the intracellular potential from the soma of the pyramidal cell (Figure 5.10b). As expected, the cell displayed a prominent 8 Hz theta oscillation in its membrane potential (Figure 5.10c).

We then used the Network Clamp to explore the contributions of network inhibition onto the pyramidal cell. Experimentally using optogenetics, the role of PV+ inhibition and SOM+ inhibition have recently been compared (Royer et al., 2012). We wanted to check whether we obtained similar results in our model with PV+ disinhibition and SOM+ disinhibition. To do this, we either cut the connections from PV+ cells (PV+ basket, bistratified, and axo-axonic cells) or cut the connections from SOM+ cells (bistratified and O-LM cells) and compared the resulting pyramidal cell spikes and membrane potential oscillations.

We found with the PV+ disinhibition, the cell fired at a much higher rate than baseline (Figure 5.10a, inset) and also tended to fire at any phase and to be unmodulated by the rhythm. In contrast, with the SOM+ disinhibition, though the cell fired somewhat more than in the baseline simulation (Figure 5.10a, inset) and the phase shifted (Figure 5.10d), the cell remained far more phase-locked to the theta oscillation than in the case of the PV+ disinhibition (Figure 5.10e). Because the firing during PV+ disinhibition was so high, we decided to also run each simulation with inactive sodium channels to observe the membrane potential oscillation independent of spikes. We found that the theta rhythm was much more disrupted during PV+ disinhibition than during SOM+ disinhibition (Figure 5.10f). This

result corresponds to the observations made in a recent experiment that used optogenetics to selectively block PV+ inhibition or SOM+ inhibition *in vivo* in CA1 (Royer et al., 2012).

Commensurate with these differences, when we took the FFT of the cell's membrane potential in each simulation, the PV+ disinhibition caused a significant drop in FFT power at 8 Hz while the SOM+ disinhibition actually slightly increased the power as it removed the inhibition experienced by the cell at its most depolarized, further amplifying the membrane potential oscillation.

5.1.7 Model performance

Another benefit of the Network Clamp can be seen when observing the performance of the model code. The full scale model was well parallelized; the execution time decreased in direct proportion to the number of processors used to execute the simulation. The model also scaled well, with the execution time and memory usage correlating strongly with the number of cells and synapses in the simulation. A full scale model simulation lasting 1 s could be executed on 4,000 Stampede processors in 3.5 hours using a complex pyramidal cell or 40 minutes using a simple pyramidal cell.

Although the code is quite efficient and enables modelers to run their network simulations quickly, it is still a slow endeavor when compared with other models. In contrast, the Network Clamp is extremely fast and convenient to run. To run a 20 s Network Clamp simulation on a personal computer in serial required 33 minutes with the complex pyramidal cell morphology and 22 minutes with the simple morphology. Using a multithreaded single cell simulation would further reduce the time required for a Network Clamp simulation.

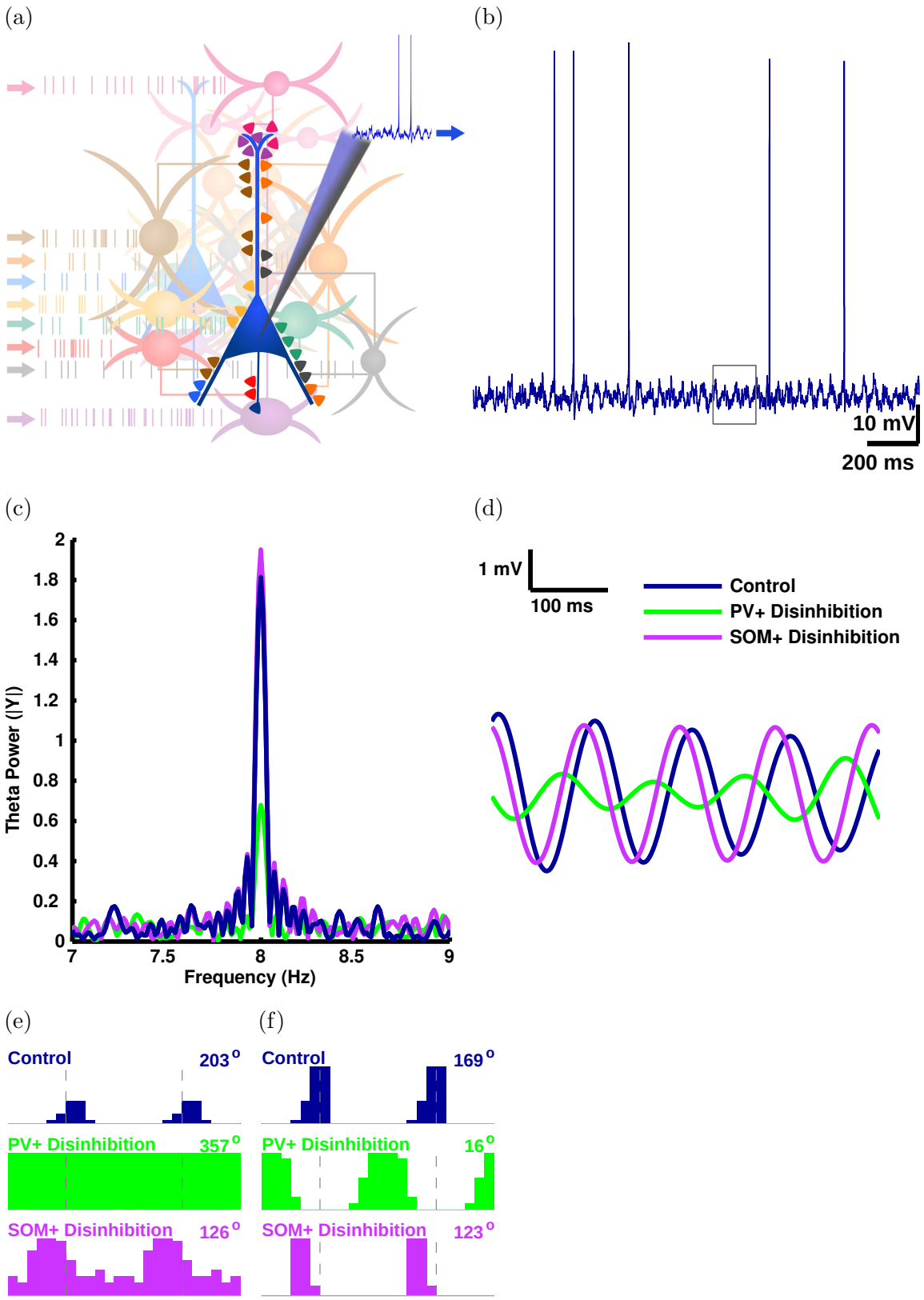

Figure 5.10: Network Clamp of a pyramidal cell shows greater disruption in theta phase for PV+ disinhibition than for SOM+ disinhibition. (a) Network Clamp diagram shows realistic spike trains in all cells converging on the pyramidal cell of interest. The cell's somatic membrane potential is recorded using an intracellular current clamp. (b) Given phasic inhibition and tonic excitation, the pyramidal cell membrane potential displays robust theta oscillations. (c) When 50% of PV+ inputs are removed, theta power of the membrane potential drops much more than when 50% of SOM+ inputs are removed. (d) Filtered

5.2 Discussion

The model was found to be capable of spontaneous oscillations, often within the theta and gamma range. It was able to display theta and gamma concurrently, along with distinct phase preferences per cell type. We had hypothesized that the network should be capable of these, and that the diversity of interneurons is likely to play a role. We found that indeed, in our model, the variation in cell inputs and electrophysiology obtained simply by constraining the behavior to experimental observations was sufficient to enable distinct phase preferences.

Not all tested connectivity or stimulation protocols resulted in oscillations. The majority of our network configurations did not display any stable oscillation. Only about % displayed theta. Of all the network configurations, % displayed gamma and an overlapping % displayed theta and gamma (% of theta-producing networks also displayed gamma and % of gamma-producing networks also displayed theta). When a network did not display theta, it was often because entire cell-type populations were overactive or silent. When we constrained the excitation level of each interneuron type to achieve physiologically relevant firing rates, we found it much more likely that the network would display theta (% of networks with physiologically relevant interneuronal firing rates displayed theta).

5.2.1 Model constraints

While there is a wealth of experimental data available to constrain the cells and connections of CA1, there are also some gaps in our knowledge. For example, there were paired recordings available that we used to characterize synapses from and to pyramidal cells, and a few interneuron-interneuron connections, but there are very few available for connections between interneurons, and we see that there are actually a significant number of connections between interneurons (Bezaire and Soltesz, 2013). Also, for the synapses that have been

characterized, it is not always clear how the junction potential contributed to the recorded responses, so behavior of the synapse may diverge in vivo. In addition, though we have used current injection sweeps from firing rate characterizations performed in our and others' labs (Maccaferri et al., 2000; Lee et al., 2014; 2010; Krook-Magnuson et al., 2011) to constrain the electrophysiology of our cells, we have not investigated the full variability within each cell type, nor directly considered the effect of morphology and morphological diversity on cell behavior.

The connectivity and cell numbers data used in our model were systemically obtained and discussed in Bezaire and Soltesz (2013). As with the synapse data, there remains much to be learned about the anatomical structure and abundance of the connections between various interneurons. Our model is structured in such a way that it can easily be updated when new anatomical data become available to further constrain the network.

5.2.2 Relevance to experimental data

We hypothesized that the model would be capable of distinct phase preferences. Though there are many inputs to the network that are phasic and sometimes interneuron-selective (afferents, neuromodulators, etc), we surmised that unique phase preferences should be a built-in property of the network for robustness, as the phasic inputs to the model are likely required to convey learning or memory, and may need to be an additional input, not the fundamental mechanism to drives phase preferences.

With such a model, we showed that not only is the network inherently supportive of theta and gamma oscillations, but it also enables phase preferences without any phasic input to the model. In an intact animal, there are phasic inputs from CA3, entorhinal cortex, and other cortical areas, as well as from the medial septum and other neuromodulatory inputs. Therefore, we expect that these phasic inputs can influence the phase preferences seen in

vivo. However, they are not necessary to achieve unique phase preferences.

In our model, different network configurations resulted in different phase preferences. For some cell types, the phase preferences diverged from what is seen in vivo, but this divergence was not surprising. The model most closely resembles the isolated CA1 experimental preparation (Goutagny et al., 2009), without the rhythmic excitatory and inhibitory infuences from brain regions connected to the CA1, including the septum, CA3, entorhinal cortex, and thalamus; we do not yet know the phases of each interneuron type in this experimental preparation.

We found that the slow kinetics of the postsynaptic $GABA_B$ component of neurogliaform synapses was important for our spontaneous theta rhythm, independently of the large total charge transfer that occurs at those synapses. There are several reasons to suspect that $GABA_B$ contributes even more to network dynamics than what our model captured. Recent experimental studies have observed postsynaptic $GABA_B$ receptors on perisomatically-targeting parvalbumin-expressing interneurons (Booker et al., 2013). Because we only included a $GABA_B$ component for neurogliaform cells, and because our model neurogliaform cells only synapsed onto other neurogliaform cells and pyramidal cells, it is likely that postsynaptic $GABA_B$ plays an even greater role in network dynamics than our model predicts. In addition, the phase preferential firing of different interneurons means that high levels of GABA may be present in and around synapses at various times during theta (Kohl and Paulsen, 2010), allowing for a stronger extrasynaptic $GABA_B$ response than what has been recorded in paired experimental preparations. Finally, many cells have presynaptic $GABA_B$ receptors (Booker et al., 2013).

While postsynaptic $GABA_B$ inhibits pyramidal cells and some interneurons, presynaptic $GABA_B$ autoreceptors only inhibit interneurons, though they affect interneuronal synapses onto both interneurons and pyramidal cells. Therefore any network manipulations that reduce $GABA_B$ activity may actually enable the other interneurons to provide greater inhi-

bition during specific phases, increasing the amplitude of the theta oscillation. As inhibition is crucial to theta generation (Soltesz and Deschenes, 1993; Ylinen et al., 1995), it is not surprising that a network manipulation reducing presynaptic $GABA_B$ and increasing the activity of most interneurons would lead to greater theta power (Leung and Shen, 2007). The reduction of presynaptic $GABA_B$ in vivo may have a similar effect to adding tonic excitation to the model to enable spontaneous theta oscillations.

Relevance of the Network Clamp to experimental data

Our finding that the PV+ inhibition served a role of modulating spike and potential phase, and that removing the PV+ inhibition led to a greater phase shift than removing SOM+ inhibition, is consistent both with our full scale network and with experimental observation (Royer et al., 2012). In the full scale network, removing the output of PV+ basket cells greatly reduces normalized theta power in the FFT computed from the spike times (to 29% of the value for the control network), while removing the output of O-LM cells only drops the power to 45% of control. In the Network Clamp, PV+ disinhibition causes the theta power of the membrane potential oscillation to drop to 38% of baseline. In contrast, SOM+ disinhibition actually causes a slight increase in theta power, likely due to the removal of inhibition at the pyramidal cell's most depolarized potential, causing a larger amplitude oscillation.

5.2.3 Reduced models

We used two ways of reducing our model for development and testing on a personal computer. We scaled down the network so that it had a few hundred cells connected to each other instead of several hundred thousand cells. We also introduced another method of reduction, which we are naming 'Network Clamp'. The Network Clamp provides a way to test network

manipulations on a smaller scale before employing them in a full-scale model, as well as a way to investigate questions about single cell dynamics. The benefit of the network clamp as opposed to a smaller-scale network model is that it preserves the convergence of the network, whereas a smaller network model either sacrifices the number of incoming connections or ramps up the connectivity (or weights) to maintain the same level, but then artificially increases the synchrony of the network. One important aspect of the network clamp is that it can only be used to study the first-order effects of any network manipulations; the resulting changes in the cell's firing rate do not influence its inputs at all, though they (or those of other cells in the network) do alter the input spike trains in real life and in a network model. This trait can also be a benefit; the reaction of the network to changes can be examined piecemeal to understand what is the immediate effect of a change, and what is a reaction to the immediate effect as the network settles into a new steady state.

5.2.4 Model accessibility

Our model is public, well documented, and also well characterized in experimentally relevant terms. Model cells sometimes are found to behave much differently than expected when subjected to experimental current sweep protocols or paired synapse recordings. We implemented a standard, thorough characterization strategy for each cell and made it available in an accessible, intuitive, and interactive website. Our ultimate goal is to have each model component constrained by standardized experimental data derived from a standard experimental protocol. Until that becomes a reality, we believe it is important to clarify the experimental constraints we used, show how well our model fits those constraints, and also to fully characterize the model components especially in the absence of available experiental data.

Chapter 6

SimTracker Software Tool and Model Code Template

Close to a thousand network simulations and more than a thousand network component simulations were executed to complete this work, and so simulation organization and documentation quickly became a problem. Further, it was difficult to keep track of all the constraints used in the model and how well the model fit them. Getting an objective, quantitative sense of how each component of the model worked was difficult without a standard way to assess model components. Finally, analyzing model results was tedious and susceptible to unnecessary variation. All of these issues were resolved with the introduction of SimTracker.

The SimTracker MATLAB tool (Figure 6.1) supports the process of designing, executing, organizing, documenting and analyzing simulations, as well as organizing and documenting results. SimTracker works with Mercurial, an established code versioning system, to track the exact code used to perform each simulation. It allows the user to specify configuration sets of cell numbers, connectivity, synapse kinetics, and all parameters used in the simulation

(Figure 6.5). These two abilities together allow complete documentation and replication of any simulation.

In addition, SimTracker serves as an organizer of simulations and their results. It can archive, reload, and back up simulation results. It also serves to ensure that the code version on the supercomputer where code will run matches the version on the user's personal computer, and takes care of generating and submitting the job script to the supercomputer's batch queueing system. When the simulation has completed, SimTracker can be prompted to download all the results from the supercomputer. SimTracker can also be used with the Neuroscience Gateway (NSG); it will package the simulation directory in the format necessary for submission to the NSG and can extract the results from an NSG output package.

SimTracker can produce a variety of outputs for each simulation, ranging from spike rasters to connectivity matrices to single cell traces. Almost every figure produced in the previous chapters of this work was generated by SimTracker. Each time that SimTracker produces a figure from a simulation, it logs which simulation produced the figure, the name of the figure file, and its location. Logging the details of figure generation enables better tracking of figure origins that becomes important once many simulation results are produced.

SimTracker	`http://mariannebezaire.com/SimTracker/`
Sumatra	`http://neuralensemble.org/sumatra/`
NeuroTools	`http://neuralensemble.org/NeuroTools/`
NeuroConstruct	`http://www.neuroconstruct.org/`
Neuronvisio	`http://www.ncbi.nlm.nih.gov/pmc/articles/PMC3368231/`
Lancet	`http://ioam.github.io/lancet/`
Neural Query System	`http://www.ncbi.nlm.nih.gov/pmc/articles/PMC2683631/`

Table 6.1: Some tools that aid in various aspects of neural network modeling.

Within SimTracker are three other tools: CellClamp (Figure 6.2), discussed in section 6.2, NetworkClamp (Figure 6.3), discussed in section 6.3, and ExperimentalData (Figure 6.4), discussed in section 6.4. CellClamp allows characterization of model components via commonly used experimental protocols. In contrast, NetworkClamp allows one to place a 'Net-

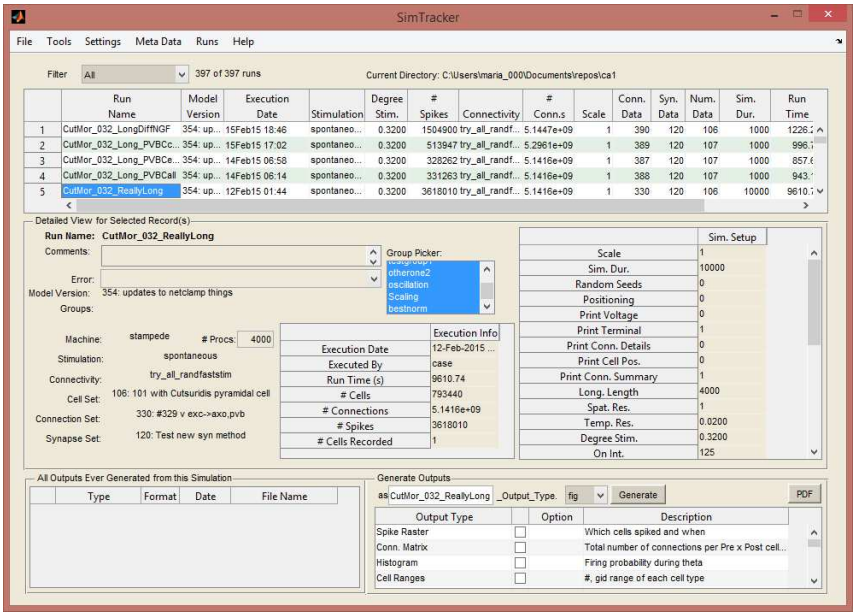

Figure 6.1: SimTracker software

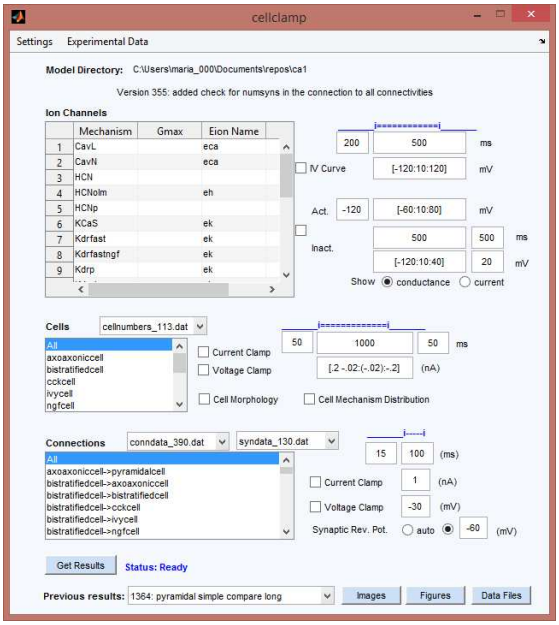

Figure 6.2: CellClamp software

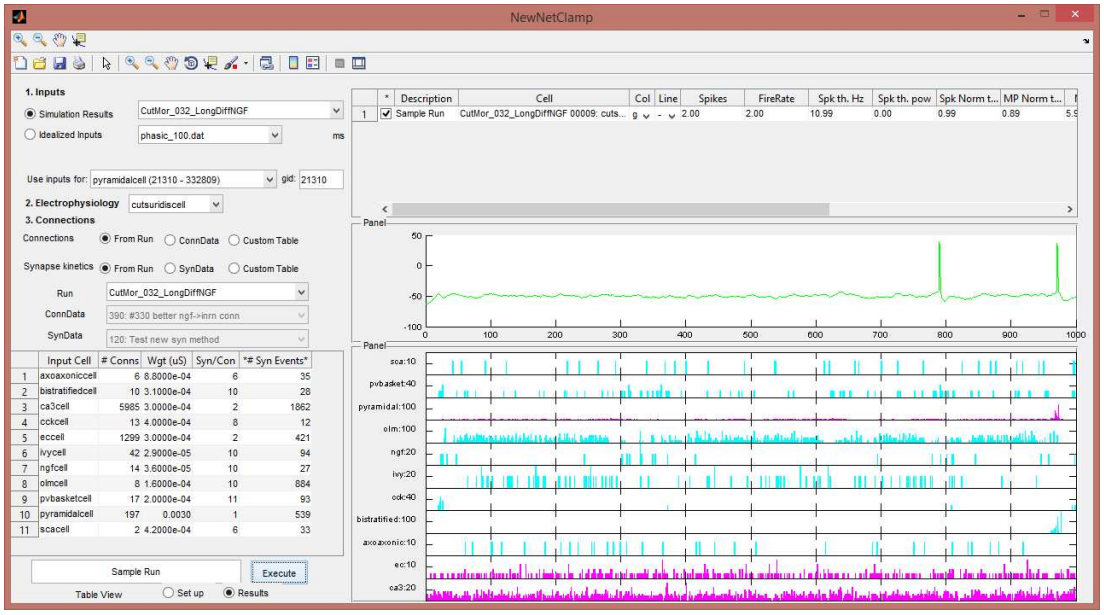

Figure 6.3: Network Clamp software

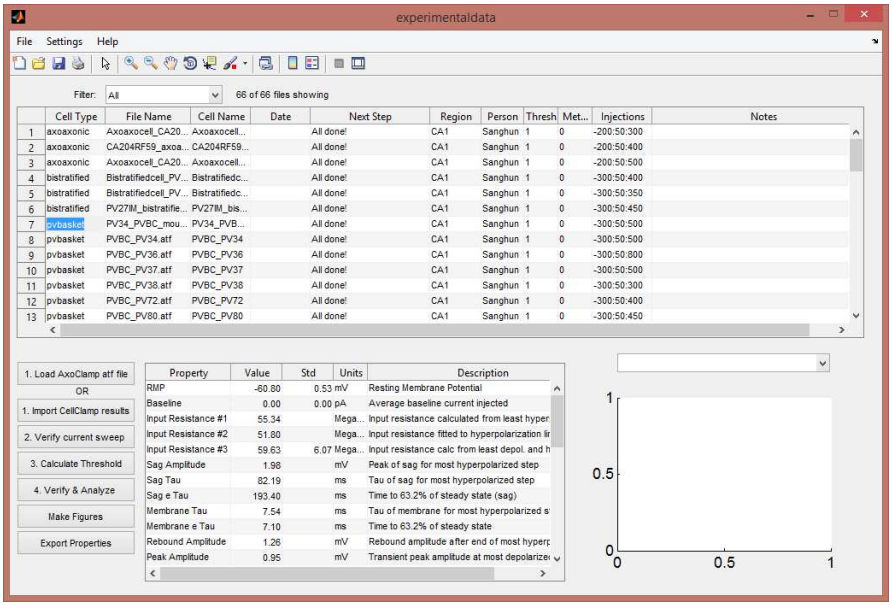

Figure 6.4: Experimental Data software

(a)

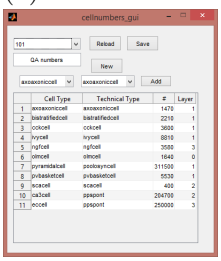

(b)

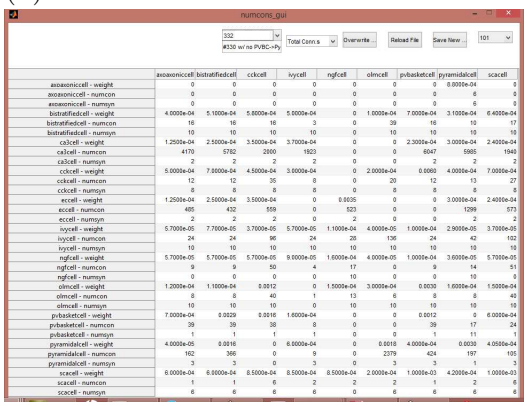

(c)

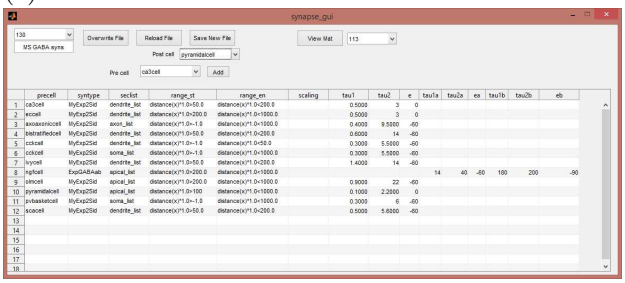

Figure 6.5: Parameter sets for the cell numbers, connections, and synapse kinetics can be designed.

work Clamp' on a single cell within a network, a concept discussed in Chapter 5. ExperimentalData supports uploading an AxoClamp atf file from an experimental current injection sweep and then analyzes various electrophysiological properties of the cell, reporting them in a variety of formats. It can also analyze the output from a CellClamp current injection sweep performed on a model cell.

Though a variety of other simulation helpers exist (Table 6.1), SimTracker is unique in that it supports the entire NEURON model development process in a highly structured manner. Its structure enables it to provide such strong support throughout the modeling process that even inexperienced modelers can quickly characterize their model components, become comfortable with the inner workings of the model, and analyze results efficiently. SimTracker supports integration of experimental data at every step of the model development process (Table 6.2).

Because SimTracker is MATLAB-based, it has flexibility in how it interfaces with other programs, and users of moderate experience with programming can customize it to fit their own development process. Some of the applications SimTracker already works in complement with include NEURON (including the Multiple Run Fitter), the batch queuing software of several supercomputers, outputs of experimental data from pClamp, Mercurial, and Excel.

Users do not need MATLAB to use SimTracker. Compiled, stand-alone versions of SimTracker exist for Windows (32-bit and 64-bit), Mac, and Linux operating systems. In addition, the MATLAB code used to create SimTracker is available for people with MATLAB who wish to customize SimTracker. SimTracker has been tested by several users on Windows and Linux, using both the compiled and the uncompiled versions. Additional issues found within SimTracker can be reported via an online issue-tracker at `https://bitbucket.org/mbezaire/simtracker`. SimTracker will be made available within SimToolsDB, a known database for simulation helpers, as well as MATLAB Central. In addition, it will be advertised on `http://ivansolteszlab.org` and `http://mariannebezaire.com` and potentially listed on other websites as appropriate.

The tool is actively used by its developer and so it will continue to be supported in the near future. Eventually, the unique functions provided by the tool may be accomplished by other resources, such as model characterization by NeuroConstruct or Open Source Brain, or simulation and results organization by Neuroscience Gateway or a similar project. The tool itself may inspire further development of other resources or development of new resources to accomplish the same tasks. Until that time, the tool will remain useful and supported.

6.1 Stepwise use of SimTracker

SimTracker aids each step of the modeling process, from simulation design to results analysis. Below, I briefly walk through the use of SimTracker for an average simulation. Additional information about SimTracker is available at `http://mariannebezaire.com/SimTracker/`.

6.1.1 Design

SimTracker supports simulation design by displaying the possible parameters and parameter sets that can be defined, and by listing the possible choices where appropriate. In addition, SimTracker stores the parameter and parameter set values for each executed simulation. Later, these values can be referred back to or they can be used to conduct meta-analyses of simulations. Users can also select from the available code versions associated with the model if they need to revisit a previous version to run a variation. Chosen parameters are prominently displayed along with the name for each simulation. Users can also design a whole family of runs simultaneously, where only one parameter value changes, and specify all possible values of that parameter.

6.1.2 Execution

After designing a simulation, the user can efficiently execute the simulation on their personal computer or on a supercomputer. If the user chooses to execute the code on a supercomputer, SimTracker will ensure the supercomputer is using the desired code version, check that all the required files are available on the supercomputer, set all the necessary parameters to the user's chosen values, create a custom job-script for use by that supercomputer for that particular simulation, and submit the simulation to the batch queue for the supercomputer, reporting back to the user when all of that has been complete. This streamlined process cuts

out many opportunities for error by ensuring that the desired simulation is the one that is run, with all parameters and code versioning as expected. It also saves the user from the tedious task of file management and job-script creation.

6.1.3 Retrieving and storing results

When the simulation is executed on a supercomputer, the results must be retrieved from the supercomputer. SimTracker handles this task, finding and downloading the results to a standardized location on the user's personal computer. Then all simulation results, regardless of where the simulation was executed, are available on the user's personal computer. Each results folder is named for the name of the simulation and contains standard result files that can be read by SimTracker (or other custom scripts that the user may wish to run). SimTracker displays the status of every simulation, whether the simulation has been designed, submitted to a supercomputer, or has been executed with results downloaded to the personal computer. In addition to storing simulation results, SimTracker also stores and displays simulation metadata, including which computer executed the simulation and how many processors were used, the date and time of execution, the user name of the person who executed the simulation, and the time taken to run the simulation.

6.1.4 Analysis of results

Once the results of a simulation are available, SimTracker lists the available analyses when the simulation is selected in SimTracker. Which analyses are available depends on which results files the user specified should be generated, but there are always some standard outputs available for every simulation, such as the spike raster, which shows the spike times of every cell in the model. Other outputs include:

- **Spike histogram** - Histogram of spikes per time, by cell type
- **Connection matrix** - Matrix of connections between each cell type in the model, including total number of connections, divergence, and convergence
- **Firing rates** - Average firing rate of each cell type
- **FFT** - FFT power at each frequency, based on spike times for each cell type
- **Intracellular trace** - Intracellular whole cell recording for select cells
- **Axonal distributions** - Density of axonal connections as a function of distance from the soma, for select cells
- **Incoming synaptic activity** - Synaptic event histograms by incoming synapse type, for select cells
- **Oscillatory phase preferences** - Oscillatory spike phase preference histograms and compasses
- **Run time** - Average and standard deviation of time required for each processor per stage of simulation
- **Memory requirement** - Memory usage of the model as a function of simulation stage

6.1.5 Figure generation

In the course of analysis, SimTracker will produce MATLAB-based figures. However, these figures can also be exported in a variety of formats including pdf, eps, bmp, jpg, and more. Each time a figure is saved, its name, location, and associated simulation is logged for future reference. If users later need to remember what parameters were in play for the simulation displayed in a particular figure, they can reference this log within SimTracker.

Experimental Data	Model Development	SimTracker Tool
Ion channel activation/inactivation curves	Subcellular mechanisms	CellClamp
Single cell current injections	Model cell electrophysiological profiles Biological cell characterization	CellClamp ExperimentalData
Paired synapse recordings	Synapse amplitudes and kinetics	CellClamp
Cell fills, axonal and dendritic lengths and synapse densities	Structural connectivity between cells (divergence and convergence)	SimTracker Connections Tool
In vivo theta observations	Model characterization, validation, analysis and communication	SimTracker, NetworkClamp, and WebsiteMaker

Table 6.2: SimTracker enables integration of biological data at each step of model development.

6.1.6 Customization of the tool

For users with MATLAB, the scripts that created the SimTracker are available and can be freely customized (with attribution according to the license terms). Even users of the compiled version have some flexibility in how they use the tool, with a variety of settings accessible for changing. Users can always add supercomputers or change the settings of supercomputers; in addition they can change which outputs are available, the parameter defaults, some behaviors of SimTracker, and more.

6.2 CellClamp

CellClamp enables characterization of various network components in experimental terms. For example, for ion channels, it can produce activation and inactivation curves as well as a current-voltage relation. To characterize single cells, it allows current clamping at various levels, and will analyze the sag, steady state voltage shift, and firing rate as a function of current injection. For synapses between cells, it performs current or voltage clamped paired

recordings (mimicking the experimental holding potential or baseline current injection, as well as the reversal potential of the dominant ion through the synapse) and analyzes the maximum conductance and kinetics of the synapse.

6.2.1 Ion channels

CellClamp can characterize ion channels in experimental terms. It accomplishes this by inserting a given ion channel into the membrane of an otherwise empty cell soma (single compartmental model). The ion channel files within the model directory (any file starting with 'ch_') are all listed in the table of ion channels available to be characterized. The user can design the current sweep levels for the activation, inactivation, and current-voltage curves. In addition, the channel density can be set by specifying the maximum conductance of the channel per area, and the reversal potential of the channel can also be set. There are other adjustable settings that affect all channel simulations, including the temperature, the axial resistance and the soma size. After the simulations complete, CellClamp will display the activation/inactivation curve and the current-voltage relation (see examples in Chapter 4).

6.2.2 Single cells

As with the ion channels, the cells of the model can also be characterized in experimental terms by CellClamp. The user can specify a series of current injection levels, along with the duration and start time of the injection. After executing the current injection sweep, CellClamp will display the firing rate curve and several other electrophysiological analyses of the cell. For detailed analysis, the simulation results can be imported into the ExperimentalData tool of SimTracker and characterized in the same manner as experimental cells. CellClamp can also prepare a session for NEURON's Multiple Run Fitter tool, so that a

model cell can be optimized to a particular experimental cell recording.

6.2.3 Synapses and connections

The connections between cells can be characterized in experimental terms as well. Because connections are usually characterized using paired patch clamp recordings, CellClamp includes analogues to paired current clamp and voltage clamp recordings. To match the experimental conditions, the user can specify a holding potential for the postsynaptic cell (including the junction potential contribution if desired) and can set the reversal potential of the synapse as well. The connection will include a set number of synapses as determined by the connectivity dataset used and the synapses will have the kinetics set by the kinetics dataset used. Ten different connections will be recorded and their results will be averaged. At the end of the simulation, the rise time, decay time constant, and synaptic amplitude are calculated and displayed along with the PSC or PSP.

6.3 Network Clamp Tool

NetworkClamp is used to implement the Network Clamp concept described in Chapter 5. A particular cell within the network is chosen and receives all the same connections that it would receive within the full network. Then specially designed inputs are given to the cell by stimulating its input cells with specific spike trains. The spike trains may either be the exact spike times of those cells within the full network, or some idealized trains (for example, spike trains with oscillatory properties constrained by experimental observation during theta), or actual spike trains from experiments. Then, the cell of interest is recorded (usually in the soma) and its intracellular trace and spike times are displayed. In NetworkClamp, it is very easy to perform parameter sweeps, systematically adjusting various aspects of the incoming

connections or synaptic activity to observe their effect on the cell of interest.

6.4 Experimental Data Tool

The Experimental Data tool is used to characterize biological and model cells in experimental terms. It reads in AxoClamp atf files from current injection sweeps and calculates many passive and active electrophysiological parameters based on the imported AxoClamp data. In addition, it can read in CellClamp results from single model cells and perform the same calculations on the model cells. Finally, it can export its results to the website directory for display on a model website.

More details are given below regarding the calculations of electrophysiological properties. First, a variety of methods exist for calculating the threshold of action potentials. Some considerations for calculating action potential threshold are given below.

Action Potential Threshold or Onset

The action potential threshold is defined as the membrane potential where, once reached, the cell will experience an action potential. This concept may be different from that of spike onset, which is the potential at which the action potential begins. Using spike onset or emperical threshold measures may overestimate the threshold Platkiewicz and Brette (2010).

Experimentally, the spike threshold varies somewhat as a function of input and previous behavior. Generally, it becomes more depolarized with more activity, as the Na_v channels inactivate. Platkiewicz and Brette (2010) differentiates between thresholds for slow inputs and fast inputs.

Model cells often fail to capture this variability in spike threshold. Models would have

more realistic thresholds (including variability seen in real life), if their Na channels were fit focusing on the spike initiation voltage range, rather than the whole voltage range (more depolarized potentials play a role in the spike shape, but not much in the spike initiation) Platkiewicz and Brette (2010).

It should also be noted that most cells will have a higher threshold *in vivo* than *in vitro*, due to the higher conductance state of the cell in vivo. In vivo, the conductance of the cell is several times larger due to all the synaptic input.

6.4.1 Approaches to Calculation of Threshold

I gave the user an option to pick between three methods and to adjust the parameters for the chosen method, as explained in the list below.

1. **The change in the derivative of the potential (Atherton and Bevan, 2005)** Take the derivative of the potential trace with respect to time. Then calculate the standard deviation of that derivative for the 50 ms prior to the action potential. The point at which the derivative exceeds the mean + 2 standard deviations is considered the threshold. Note that the number of standard deviations to be exceeded can be changed within the Analysis Settings and does not have to be an integer.

2. **The derivative threshold (Cooper et al., 2003; Metz et al., 2005)** Take the derivative of the potential trace with respect to time. Then set a cutoff point of the derivative, such as 30 mV/ms, and the point at which it is exceeded (within the 50 ms previous to the spike) is considered the threshold. Note that the cutoff point can be changed within the Analysis Settings and does not have to be an integer.

3. **The maximum of the second derivative (Mainen et al., 1995)** Take the second derivative of the potential trace with respect to time. Find the maximum of it (within

the 50 ms previous to the spike) and use that point as the threshold.

From my experience, calculation method 1 worked the most reliably, with 2 often producing the same result, while 3 frequently got stuck at the peak of the action potential.

6.4.2 Calculation of Other Cell Properties

In addition to the action potential threshold, many other cell properties were calculated. The properties and their calculation strategy are given below:

RMP: Resting Membrane Potential The average potential of the cell when no current is being injected (or when only the baseline current is being injected)

Baseline: Average baseline current injected The amplitude of a constant current injection that occurs throughout all experimental characterizations, or 0 if no baseline current is injected.

Input Resistance #1: Input resistance calculated from least hyperpolarized step The change in potential (most hyperpolarized potential subtracted from resting membrane potential) divided by the change in current injection (current injection step subtracted from the baseline current injection), from the smallest hyperpolarizing current injection.

Input Resistance #2: Input resistance fitted to hyperpolarization line The change in potential for each hyperpolarizing step is divided by the current injection for that step, and the results are fitted to a straight line and then the slope is used as the input resistance.

Input Resistance #3: Input resistance calculated from least depolarized and hyperpolarized steps The change in potential for each step is divided by the change

in current injection for that step and the results are averaged. For the hyperpolarized step, the potentials used are resting membrane potential and the most hyperpolarized potential during current injection. For the depolarized step, the potentials used are the resting membrane potential and the most depolarized potential during current injection.

Sag Amplitude: Peak of sag for most hyperpolarized step The difference between the most hyperpolarized potential occurring during current injection and the steady state potential reached by the end of the current injection.

Sag Tau: Tau of sag for most hyperpolarized step The value of tau achieved from the best fit of the trace from the most hyperpolarized current injection. The equation used in the fit is set within the Analysis Settings dialog, the section on fitting sag tau line. The portion of the trace used to fit the line starts at the most hyperpolarized potential on the trace and continues until the trace reaches steady state.

Sag e Tau: Time to 63.2% of steady state (sag) The time taken for the trace to reach 63.2% of its steady state value as compared to the potential at the most hyperpolarized point on the trace. As with the calculation of the Sag Tau, the most hyperpolarized current injection step is used for this calculation.

Membrane Tau: Tau of membrane for most hyperpolarized step The membrane time constant is calculated as the value of tau achieved from the best fit of the trace from the most hyperpolarized current injection. The equation used in the fit is set within the Analysis Settings dialog, the section on fitting the membrane time constant from a hyperpolarized potential. The portion of the trace used to fit the line starts at the time the current injection starts and continues up to the most hyperpolarized potential of the trace.

Membrane e Tau: Time to 63.2% of steady state The time taken for the trace to

reach 63.2% of its most hyperpolarized potential, as compared to the initial voltage at the start of the current injection. As with the calculation of Membrane Tau, the most hyperpolarized current injection step is used for this calculation.

Rebound Amplitude: Rebound amplitude after end of most hyperpolarized step The difference between the most depolarized potential after the end of the current injection and the resting membrane potential, for the most hyperpolarized current injection.

Peak Amplitude: Transient peak amplitude at most depolarized quiet step The difference between the most depolarized potential during current injection and the resting membrane potential, for the most depolarized current injection without spikes.

Peak Decay Tau: Transient peak decay time constant at most depolarized quiet step The time constant fit to the decay of the transient depolarized peak (using the fit equation specified in the Analysis Settings) for the most depolarized current injection without spikes.

Pre Rheobase: Most depolarized step without any spikes The most depolarized current injection level that has no spiking.

Rheobase: Least depolarized step with spikes The least depolarized current injection level where at least one spike occurs.

Delay to 1st Spike: At rheobase, spike time after injection starts For the least depolarized current injection level, the number of milliseconds after the current injection starts to the time the potential crosses the action potential threshold.

First Reg. Spiking: Least depolarized step with regular spiking (at least 3 spikes) The least depolarized current injection level where the cell spiked at least 3 times.

ISI: Average of all ISIs at first regular spiking step The average interspike interval (ISI) considering all ISIs occurring during the least depolarized current injection with at least 3 spikes.

Threshold: Avg. threshold of first 3 spikes (first regular spiking step) The average interspike interval (ISI) considering only the first 3 ISIs occurring during the least depolarized current injection with at least 3 spikes.

Spike Amplitude: Avg. amplitude of first 3 spikes (first regular spiking step) The average spike amplitude considering only the first 3 spikes occurring during the least depolarized current injection with at least 3 spikes.

Half-Width: Avg. duration of first 3 spikes at half amplitude (first regular spiking step) The average spike duration at half the maximum amplitude considering only the first 3 spikes occurring during the least depolarized current injection with at least 3 spikes.

Fast AHP Amplitude: Avg. fast AHP of first 3 spikes (first regular spiking step) The average amplitude of the fast AHP (if one exists) considering only the first 3 spikes occurring during the least depolarized current injection with at least 3 spikes.

Slow AHP Amplitude: Avg. slow AHP of first 3 spikes (first regular spiking step) The average amplitude of the slow AHP considering only the first 3 spikes occurring during the least depolarized current injection with at least 3 spikes.

ADP Amplitude: Avg. ADP of first 3 spikes (first regular spiking step) The average amplitude of the afterdepolarization (if one exists) considering only the first 3 spikes occurring during the least depolarized current injection with at least 3 spikes.

6.5 Model code organization

The model code has a modular organization, enabling quicker understanding and debugging. The code is organized in the following manner:

1. **cells directory** - contains a separate template file for each cell type
2. **connectivity directory** - contains one file for each method of connecting model cells
3. **datasets directory** - contains separate files for each possible parameter set defining cell numbers, numbers of connections, or synapse kinetics
4. **jobscripts directory** - contains downloaded job scripts and output files from supercomputers
5. **setupfiles directory** - contains various standard code modules for executing the simulation
6. **stimulation directory** - contains one file for each method of stimulating the model
7. **main.hoc** - the main code file for executing the simulation
8. **subcellular mechanisms** - various mod files defining ion channels, synapses, and other compiled mechanisms

In addition, the results are stored within the same directory as a code, within their own subdirectories:

1. **cellclamp_results directory** - contains a separate directory for each CellClamp simulation

2. **networkclamp_results directory** - contains a separate directory for each network simulation upon which the Network Clamp simulations are based, and within that directory are found separate results folders for each Network Clamp simulation

3. **results directory** - contains a separate directory for each simulation

Each results folder contains standard results files for that run, which can be analyzed using built-in functions in SimTracker. This organization both of the results and of the model code increases the efficiency of the user and also allows faster debugging. In addition, it increases the usability of the code and of SimTracker.

6.6 Impact

For the life of most of this work, SimTracker has been an irreplaceable resource to ensure consistency, efficiency, and organization of the model. It is a great tool for assisting new modelers as well. It provides support and a model structure that is helpful for users new to modeling concepts, especially for those familiar with experimental principles but not with coding. There is much potential for SimTracker to support new users and to also be reviewed by people designing other tools or websites who are looking for use cases to determine required functionality for their systems.

Chapter 7

Conclusion and Future Directions

Our model is unique in that it incorporates many more biological constraints than previous models. In addition, our model spontaneously produces theta oscillations, gamma oscillations, and distinct phase preferences for each interneuron type. Though our model is large and detailed, we have made it very accessible by introducing the network clamp and by characterizing the model in experimental terms and displaying the constraints, experimental comparisons, and resulting model behavior in an intuitive, interactive way on our website.

Our model represents a new approach to modeling, one whose benefits are increasingly recognized in the broader community. The nature of the model renders it usable for an almost infinite number of questions with no or few updates to the existing code. This style of modeling contrasts with previous models whose properties and scope were chosen with a very focused, specific question. Such models are effective and powerful in answering their chosen question. However, many are not designed to be reused to study other questions unrelated to the initial one. While our model development was also driven by a question, because of our large scope and the broad significance of the question asked, the model will be useful for diverse other questions including the study of memory tasks, spatial processing,

high frequency oscillations, and epileptic phenomena.

I have structured the model so that new data can easily be incorporated. As data gathering and data mining tools become more powerful and prevalent in neuroscience, we are achieving an abundance of accessible, reusable data. This represents both a challenge and an opportunity for modeling: how can we best use and maintain such data sets? In this work, I have shown how biological constraints can be incorporated and displayed to users without being overwhelming. I have produced a software tool that allows others to employ this same modeling strategy, one that can also be used to generate use cases for others wishing to produce resources for large scale modelers.

Modeling the CA1 network at full scale presented another challenge. We felt that a full scale network was necessary to answer our question of whether an isolated model network can initiate and maintain theta oscillations. If we had used a smaller network, we would have been forced to choose between having lower levels of synaptic input (due to fewer incoming connections) or we would have had to scale up the connections between cells (either the numbers of connections or the weights), so that the effect of any one cell on another one was much stronger than found in vivo. Neither of these options felt appropriate for studying the ability of the network to exhibit synchronized, rhythmic firing. By running the model at full scale, we were able to maintain realistic connectivity numbers and strengths, while also relying on the natural rates of synaptic input to each cell type.

Of course, our model is not an exact replica of a biological CA1 network. There are parameters that are not yet described well enough for all the cell types to be included, such as gap junctions, short-term plasticity, and sub-layer specific connectivity. For the purpose of our model question, we found that the lack of these in the model means that the theta and gamma do not require these properties. We fully expect that additional network properties will be discovered experimentally, ones that are also not included in our model. Although we view our model as the most complex currently available model of the hippocampus, it

will need to be continuously updated in the future to include additional properties.

We are making our code and software tool publically available to anyone for reuse or refinement. As additional knowledge is gained about CA1, it can be incorporated into our model. Also, anyone can use the model to answer their own question about CA1 network activity or to specifically ask more questions about the mechanism of spontaneous theta generation that we found in the model. It is our hope that other modelers will find our model readily accessible and understandable, and that they will feel free to use the model to study any questions they may have about theta or other network phenomena.

Bibliography

L. Acsady, D. Arabadzisz, and T.F. Freund. Correlated morphological and neurochemical features identify different subsets of vasoactive intestinal polypeptide-immunoreactive interneurons in rat hippocampus. *Neuroscience*, 73:299–315, 1996.

L. Acsády, T.J. Görcs, and T.F. Freund. Different populations of vasoactive intestinal polypeptide-immunoreactive interneurons are specialized to control pyramidal cells or interneurons in the hippocampus. *Neuroscience*, 73:317–334, 1996.

Y. Aika, J.Q. Ren, K. Kosaka, and T. Kosaka. Quantitative analysis of GABA-like-immunoreactive and parvalbumin-containing neurons in the CA1 region of the rat hippocampus using a stereological method, the disector. *Exp Brain Res*, 99(2):267–276, 1994.

Afia B Ali, Jim Deuchars, Hannelore Pawelzik, and Alex M Thomson. CA1 pyramidal to basket and bistratified cell EPSPs: dual intracellular recordings in rat hippocampal slices. *J Physiol*, 507(1):201–217, 1998.

DG Amaral and MP Witter. The three-dimensional organization of the hippocampal formation: a review of anatomical data. *Neurosci.*, 31:571–591, 1989.

P Andersen, HB Bland, T Myhrer, and PA Schwartzkroin. Septo-hippocampal pathway necessary for dentate theta production. *Brain research*, 165(1):13–22, 1979.

Per Andersen, Richard Morris, David Amaral, Tim Bliss, and John O'Keefe. *The Hippocampus Book*. Oxford University Press, New York, 2007.

Ildikó Aradi and William R Holmes. Role of multiple calcium and calcium-dependent conductances in regulation of hippocampal dentate granule cell excitability. *Journal of computational neuroscience*, 6(3):215–235, 1999.

Caren Armstrong, Janos Szabadics, Gabor Tamas, and Ivan Soltesz. Neurogliaform cells in the molecular layer of the dentate gyrus as feed-forward γ-aminobutyric acidergic modulators of entorhinal-hippocampal interplay. *The Journal of Comparative Neurology*, 519: 1476–1491, 2011.

Caren Armstrong, Esther Krook-Magnuson, and Ivan Soltesz. Neurogliaform and ivy cells: A major family of nNOS expressing GABAergic neurons. *Front Neural Circuits*, 6, 2012.

Jeremy F Atherton and Mark D Bevan. Ionic mechanisms underlying autonomous action potential generation in the somata and dendrites of GABAergic substantia nigra pars reticulata neurons in vitro. *The Journal of neuroscience : the official journal of the Society for Neuroscience*, 25(36):8272–81, September 2005. ISSN 1529-2401. doi: 10.1523/JNEUROSCI.1475-05.2005. URL `http://www.jneurosci.org/content/25/36/8272?ijkey=2186d3880821029ed72da99bcfabdc8e343fe842&keytype2=tf_ipsecsha`.

Nikolai Axmacher, Melanie M Henseler, Ole Jensen, Ilona Weinreich, Christian E Elger, and Juergen Fell. Cross-frequency coupling supports multi-item working memory in the human hippocampus. *Proceedings of the National Academy of Sciences*, 107(7):3228–3233, 2010.

A. Baude, C. Bleasdale, Y. Dalezios, P. Somogyi, and T. Klausberger. Immunoreactivity for the GABA_A receptor α1 subunit, somatostatin and connexin36 distinguishes axoaxonic, basket, and bistratified interneurons of the rat hippocampus. *Cereb. Cortex*, 17:2094–2107, 2007.

H Beck, H Clusmann, T Kral, J Schramm, U Heinemann, and CE Elger. Potassium currents in acutely isolated human hippocampal dentate granule cells. *The Journal of physiology*, 498(Pt 1):73–85, 1997.

Marianne J Bezaire and Ivan Soltesz. Quantitative assessment of CA1 local circuits: knowledge base for interneuron-pyramidal cell connectivity. *Hippocampus*, 23(9):751–785, 2013. URL `http://www.ncbi.nlm.nih.gov/pubmed/23674373`.

Marianne J Bezaire and Ivan Soltesz. Simtracker. *in preparation*, 2015.

A.A. Biro, N.B. Holderith, and Z. Nusser. Quantal size is independent of the release probability at hippocampal excitatory synapses. *J Neurosci*, 25(1):223–232, 2005.

J. M. Blasco-Ibez and T. F. Freund. Synaptic input of horizontal interneurons in stratum oriens of the hippocampal ca1 subfield: Structural basis of feed-back activation. *European Journal of Neuroscience*, 7(10):2170–2180, 1995. ISSN 1460-9568. doi: 10.1111/j.1460-9568.1995.tb00638.x. URL `http://dx.doi.org/10.1111/j.1460-9568.1995.tb00638.x`.

Tim VP Bliss, Graham L Collingridge, et al. A synaptic model of memory: long-term potentiation in the hippocampus. *Nature*, 361(6407):31–39, 1993.

Sam A Booker, Anna Gross, Daniel Althof, Ryuichi Shigemoto, Bernhard Bettler, Michael Frotscher, Matthew Hearing, Kevin Wickman, Masahiko Watanabe, Ákos Kulik, et al. Differential gabab-receptor-mediated effects in perisomatic-and dendrite-targeting parvalbumin interneurons. *The Journal of Neuroscience*, 33(18):7961–7974, 2013.

LYLE J Borg-Graham. Modeling the non-linear conductances of excitable membranes. *Cellular Neurobiology: A Practical Approach*, 13:247–275, 1991.

Christoph Börgers, Steven Epstein, and Nancy J Kopell. Background gamma rhythmicity and attention in cortical local circuits: a computational study. *Proceedings of the National Academy of Sciences of the United States of America*, 102(19):7002–7007, 2005.

Z. Borhegyi, V. Varga, N. Szilagyi, D. Fabo, and T.F. Freund. Phase segregation of medial septal GABAergic neurons during hippocampal theta activity. *J Neurosci*, 24(39):8470–8479, 2004.

M. P. Brandon, M. L. Donegan, J. K. Leutgeb, and S. Leutgeb. Optogenetic control of the hippocampal theta rhythm. In *Society for Neuroscience Abstracts*, 2013.

EH Buhl, K Halasy, and P Somogyi. Diverse sources of hippocampal unitary inhibitory postsynaptic potentials and the number of synaptic release sites. *Nature*, 368:823–828, 1994a.

EH Buhl, ZS Han, Z Lorinczi, VV Stezhka, SV Karnup, and P Somogyi. Physiological properties of anatomically identified axo-axonic cells in the rat hippocampus. *J Neurophysiol*, 71(4):1289–1307, 1994b.

EH Buhl, SR Cobb, K. Halasy, and P. Somogyi. Properties of unitary IPSPs evoked by anatomically identified basket cells in the rat hippocampus. *Euro. J. Neurosci.*, 7(9): 1989–2004, 1995.

TH Bullock, G Buzsaki, and MC McClune. Coherence of compound field potentials reveals discontinuities in the ca1-subiculum of the hippocampus in freely-moving rats. *Neuroscience*, 38(3):609–619, 1990.

György Buzsáki. Theta oscillations in the hippocampus. *Neuron*, 33(3):325–340, 2002.

Emilie Campanac, Célia Gasselin, Agnès Baude, Sylvain Rama, Norbert Ankri, and Dominique Debanne. Enhanced intrinsic excitability in basket cells maintains excitatory-inhibitory balance in hippocampal circuits. *Neuron*, 77(4):712–722, 2013.

Nicholas T. Carnevale and Michael L. Hines. *The NEURON Book*. Cambridge University Press, New York, 2005.

S. Chamberland and L. Topolnik. Inhibitory control of hippocampal inhibitory neurons. *Front. Neurosci.*, 6, 2012.

Laetitia Chauvière, Nadia Rafrafi, Catherine Thinus-Blanc, Fabrice Bartolomei, Monique Esclapez, and Christophe Bernard. Early deficits in spatial memory and theta rhythm in experimental temporal lobe epilepsy. *The Journal of Neuroscience*, 29(17):5402–5410, 2009.

Kang Chen, Ildiko Aradi, Niklas Thon, Mariam Eghbal-Ahmadi, Tallie Z Baram, and Ivan Soltesz. Persistently modified h-channels after complex febrile seizures convert the seizure-induced enhancement of inhibition to hyperexcitability. *Nature medicine*, 7(3):331–337, 2001.

S.R. Cobb, K. Halasy, I. Vida, G. Nyiri, G. Tamas, E.H. Buhl, and P. Somogyi. Synaptic effects of identified interneurons innervating both interneurons and pyramidal cells in the rat hippocampus. *Neuroscience*, 79(3):629–648, 1997.

Donald C. Cooper, Shannon J. Moore, Nathan P. Staff, and Nelson Spruston. Psychostimulant-Induced Plasticity of Intrinsic Neuronal Excitability in Ventral Subiculum. *J. Neurosci.*, 23(30):9937–9946, October 2003. URL `http://www.jneurosci.org/content/23/30/9937?ijkey=bba0073959eb46d596e582ed90735ad510912972&keytype2=tf_ipsecsha`.

D.W. Cope, G. Maccaferri, L.F. Marton, J.D.B. Roberts, P.M. Cobden, and P. Somogyi. Cholecystokinin-immunopositive basket and Schaffer collateral-associated interneurones target different domains of pyramidal cells in the CA1 area of the rat hippocampus. *Neuroscience*, 109:63–80, 2002.

Vassilis Cutsuridis and Michael Hasselmo. GABAergic contributions to gating, timing, and phase precession of hippocampal neuronal activity during theta oscillations. *Hippocampus*, 2012.

Vassilis Cutsuridis, Stuart Cobb, and Bruce P Graham. Encoding and retrieval in a model of the hippocampal ca1 microcircuit. *Hippocampus*, 20(3):423–446, 2010.

J. Deuchars and A.M. Thomson. CA1 pyramid-pyramid connections in rat hippocampus in vitro: Dual intracellular recordings with biocytin filling. *Neuroscience*, 74:1009–1018, 1996.

Vincent Douchamps, Ali Jeewajee, Pam Blundell, Neil Burgess, and Colin Lever. Evidence for encoding versus retrieval scheduling in the hippocampus by theta phase and acetylcholine. *The Journal of Neuroscience*, 33(20):8689–8704, 2013.

G. Ducharme, B. Amilhon, S. D. Glasgow, A. Adamantidis, and S. Williams. Modulation of hippocampal theta rhythm by optogenetic control of gabaergic projections from the medial septum. In *Society for Neuroscience Abstracts*, 2013.

Jonas Dyhrfjeld-Johnsen, Vijayalakshmi Santhakumar, Robert J Morgan, Ramon Huerta, Lev Tsimring, and Ivan Soltesz. Topological determinants of epileptogenesis in large-scale structural and functional models of the dentate gyrus derived from experimental data. *Journal of neurophysiology*, 97(2):1566–1587, 2007.

Arne D Ekstrom, Jeremy B Caplan, Emily Ho, Kirk Shattuck, Itzhak Fried, and Michael J Kahana. Human hippocampal theta activity during virtual navigation. *Hippocampus*, 15 (7):881–889, 2005.

D. Elfant, B.Z. Pál, N. Emptage, and M. Capogna. Specific inhibitory synapses shift the balance from feedforward to feedback inhibition of hippocampal ca1 pyramidal cells. *Eur. J. Neurosci.*, 27:104–113, 2008.

Monique Esclapez, June C. Hirsch, Yezekiel Ben-Ari, and Christophe Bernard. Newly formed excitatory pathways provide a substrate for hyperexcitability in experimental temporal lobe epilepsy. *J. Comp. Neurol.*, 408:449–460, 1999.

Juergen Fell, Eva Ludowig, Bernhard P Staresina, Tobias Wagner, Thorsten Kranz, Christian E Elger, and Nikolai Axmacher. Medial temporal theta/alpha power enhancement precedes successful memory encoding: evidence based on intracranial eeg. *J Neurosci*, 31 (14):5392–5397, 2011.

F. Ferraguti, P. Cobden, M. Pollard, D. Cope, R. Shigemoto, M. Watanabe, and P. Somogyi. Immunolocalization of metabotropic glutamate receptor 1α (mGluR1α) in distinct classes of interneuron in the CA1 region of the rat hippocampus. *Hippocampus*, 14:193–215, 2004.

F. Ferraguti, T. Klausberger, P. Cobden, A. Baude, J.D.B. Roberts, P. Szucs, A. Kinoshita, R. Shigemoto, P. Somogyi, and Y. Dalezios. Metabotropic glutamate receptor 8-expressing nerve terminals target subsets of GABAergic neurons in the hippocampus. *J. Neurosci.*, 25(45):10520–10536, 2005.

E Ficker and U Heinemann. Slow and fast transient potassium currents in cultured rat hippocampal cells. *The Journal of physiology*, 445(1):431–455, 1992.

Foldy. Foldy. *Nat. Neurosci.*, 2007.

Csaba Foldy, Sang-Hun Lee, Robert J. Morgan, and Ivan Soltesz. Regulation of fast-spiking basket cell synapses by the chloride channel ClC-2. *Nature Neuroscience*, 13:1047–1049, 2010.

T.F. Freund and M. Antal. GABA-containing neurons in the septum control inhibitory interneurons in the hippocampus. *Nature*, 336(6195):170–173, 1988.

T.F. Freund and A.I. Gulyas. Inhibitory control of GABAergic interneurons in the hippocampus. *Can J Physiol Pharmacol*, 75(5):479–487, 1997.

T.F. Freund, A.I. Gulyas, L. Acsady, T. Gorcs, and K. Toth. Serotonergic control of the hippocampus via local inhibitory interneurons. *Proc Natl Acad Sci U S A*, 87(21):8501–8505, 1990.

Thomas F. Freund and Gyorgy Buzsáki. Interneurons of the hippocampus. *Hippocampus*, 6: 347–470, 1996.

P. Fuentealba, R. Begum, M. Capogna, S. Jinno, L.F. Márton, J. Csicsvari, A. Thomson, P. Somogyi, and T. Klausberger. Ivy cells: a population of nitric-oxide-producing, slow-spiking GABAergic neurons and their involvement in hippocampal network activity. *Neuron*, 57:917–929, 2008a.

P. Fuentealba, R. Tomioka, Y. Dalezios, L.F. Marton, M. Studer, K. Rockland, T. Klausberger, and P. Somogyi. Rhythmically active enkephalin-expressing GABAergic cells in the CA1 area of the hippocampus project to the subiculum and preferentially innervate interneurons. *J Neurosci*, 28:10017–10022, 2008b.

Pablo Fuentealba, Thomas Klausberger, Theofanis Karayannis, Wai Yee Suen, Jojanneke Huck, Ryohei Tomioka, Kathleen Rockland, Marco Capogna, Michle Studer, Marisela Morales, and Peter Somogyi. Expression of COUP-TFII nuclear receptor in restricted

GABAergic neuronal populations in the adult rat hippocampus. *Journal of Neuroscience*, 30:1595–609, 2010.

MJ Gillies, RD Traub, FEN LeBeau, CH Davies, T Gloveli, EH Buhl, and MA Whittington. A model of atropine-resistant theta oscillations in rat hippocampal area ca1. *The Journal of physiology*, 543(3):779–793, 2002.

Bennet S Givens and David S Olton. Cholinergic and gabaergic modulation of medial septal area: effect on working memory. *Behavioral neuroscience*, 104(6):849, 1990.

Romain Goutagny, Jesse Jackson, and Sylvain Williams. Self-generated theta oscillations in the hippocampus. *Nature neuroscience*, 12(12):14911493, December 2009. ISSN 1097-6256. doi: 10.1038/nn.2440. URL `http://dx.doi.org/10.1038/nn.2440`.

A.R. Graves, S.J. Moore, E.B. Bloss, B.D. Mensh, W.L. Kath, and N. Spruston. Hippocampal pyramidal neurons comprise two distinct cell types that are countermodulated by metabotropic receptors. *Neuron*, 76(4):776–789, 2012.

Sebastian Guderian, Björn H Schott, Alan Richardson-Klavehn, and Emrah Düzel. Medial temporal theta state before an event predicts episodic encoding success in humans. *Proc Nat Acad Sci U S A*, 106(13):5365–5370, 2009.

A. I. Gulyas, K. Toth, P. Danos, and T.F. Freund. Subpopulations of GABAergic neurons containing parvalbumin, calbindin D28k, and cholecystokinin in the rat hippocampus. *J Comp Neurol*, 312:371–378, 1991.

A.I. Gulyas, T.J. Gorcs, and T.F. Freund. Innervation of different peptide-containing neurons in the hippocampus by GABAergic septal afferents. *Neuroscience*, 37(1):31–44, 1990.

A.I. Gulyás, R. Miles, A. Sík, K. Tóth, N. Tamamaki, and T.F. Freund. Hippocampal pyramidal cells excite inhibitory neurons through a single release site. *Nature*, 366(6456): 683–687, 1993.

A.I. Gulyás, N. Hájos, I. Katona, and T.F. Freund. Interneurons are the local targets of hippocampal inhibitory cells which project to the medial septum. *Euro. J. Neurosci.*, 17: 1861–1872, 2003.

Attila I Gulyás, Norbert Hájos, and Tamás F Freund. Interneurons containing calretinin are specialized to control other interneurons in the rat hippocampus. *The Journal of neuroscience*, 16(10):3397–3411, 1996.

Attila I. Gulyás, Manuel Megías, Zsuzsa Emri, and Tamas F. Freund. Total number and ratio of excitatory and inhibitory synapses converging onto single interneurons of different types in the CA1 area of the rat hippocampus. *The Journal of Neuroscience*, 19:10082–10097, 1999.

N Hajos and I Mody. Synaptic communication among hippocampal interneurons: properties of spontaneous IPSCs in morphologically identified cells. *J. Neurosci.*, 17:8427–8442, 1997.

Norbert Hajos, Tommas J Ellender, Rita Zemankovics, Edward O Mann, Richard Exley, Stephanie J Cragg, Tamás F Freund, and Ole Paulsen. Maintaining network activity in submerged hippocampal slices: importance of oxygen supply. *European Journal of Neuroscience*, 29(2):319–327, 2009.

K. Halasy, T. Hajszan, É.G. Kovács, T.T. Lam, and C. Leranth. Distribution and origin of vesicular glutamate transporter 2-immunoreactive fibers in the rat hippocampus. *Hippocampus*, 14(7):908–918, 2004.

Katalin Halasy, Eberhard H. Buhl, Zoltan Lorinczi, Gabor Tamás, and Peter Somogyi. Synaptic target selectivity and input of gabaergic basket and bistratified interneurons in the CA1 area of the rat hippocampus. *Hippocampus*, 6:306–329, 1996.

M Hasselmo, Clara Bodelón, and B Wyble. A proposed function for hippocampal theta rhythm: separate phases of encoding and retrieval enhance reversal of prior learning. *Neural computation*, 14(4):793–817, 2002.

Michael E Hasselmo. What is the function of hippocampal theta rhythm?linking behavioral data to phasic properties of field potential and unit recording data. *Hippocampus*, 15(7): 936–949, 2005.

Michael E Hasselmo. The role of acetylcholine in learning and memory. *Current opinion in neurobiology*, 16(6):710–715, 2006.

M.L. Hines, T. Morse, M. Migliore, N.T. Carnevale, and G.M. Shepherd. Modeldb: A database to support computational neuroscience. *J. Comput. Neurosci.*, 17:7–11, Jul-Aug 2004.

Jesse Jackson, Bénédicte Amilhon, Romain Goutagny, Jean-Bastien Bott, Frédéric Manseau, Christian Kortleven, Steven L Bressler, and Sylvain Williams. Reversal of theta rhythm flow through intact hippocampal circuits. *Nature neuroscience*, 2014.

DAVID B Jaffe, WILLIAM N Ross, JOHN E Lisman, NECHAMA Lasser-Ross, HIROYOSHI Miyakawa, and DANIEL Johnston. A model for dendritic ca^ 2^+ accumulation in hippocampal pyramidal neurons based on fluorescence imaging measurements. *Journal of neurophysiology*, 71:1065–1065, 1994.

S. Jinno. Structural organization of long-range GABAergic projection system of the hippocampus. *Front Neuroanat*, 3:1–9, 2009.

S. Jinno and T. Kosaka. Cellular architecture of the mouse hippocampus: A quantitative aspect of chemically defined GABAergic neurons with stereology. *Neurosci Res*, 56:229–245, 2006.

Shozo Jinno, Thomas Klausberger, Laszlo F. Marton, Yannis Dalezios, J. David B. Roberts, Pablo Fuentealba, Eric A. Bushong, Darrell Henze, György Buzsáki, and Peter Somogyi. Neuronal diversity in GABAergic long-range projections from the hippocampus. *J. Neurosci.*, 27:8790–8804, 2007.

Michael J Kahana, Robert Sekuler, Jeremy B Caplan, Matthew Kirschen, and Joseph R Madsen. Human theta oscillations exhibit task dependence during virtual maze navigation. *Nature*, 399(6738):781–784, 1999.

R Kajiwara, FG Wouterlood, A Sah, AJ Boekel, LT Baks te Bulte, and MP Witter. Convergence of entorhinal and CA3 inputs onto pyramidal neurons and interneurons in hippocampal area CA1 - an anatomical study in the rat. *Hippocampus*, 18:266–280, 2008.

I Katona, L Acsády, and TF Freund. Postsynaptic targets of somatostatin-immunoreactive interneurons in the rat hippocampus. *Neurosci.*, 88:37–55, 1999a.

Istvan Katona, Beata Sperlagh, Attila Sik, Attila Kafalvi, E. Sylvester Vizi, Ken Mackie, and Tamas F. Freund. Presynaptically located cb1 cannabinoid receptors regulate gaba release from axon terminals of specific hippocampal interneurons. *The Journal of Neuroscience*, 19:4544–4558, 1999b.

Tilman J. Kispersky, Fernando R. Fernandez, Michael N. Economo, and John A. White. Spike resonance properties in hippocampal o-lm cells are dependent on refractory dynamics. *The Journal of Neuroscience*, 32(11):3637–3651, 2012. doi: 10.1523/JNEUROSCI.1361-11.2012. URL `http://www.jneurosci.org/content/32/11/3637.abstract`.

Thomas Klausberger. GABAergic interneurons targeting dendrites of pyramidal cells in the CA1 area of the hippocampus. *European Journal of Neuroscience*, 30:947–957, 2009.

Thomas Klausberger and Peter Somogyi. Neuronal diversity and temporal dynamics: The unity of hippocampal circuit operations. *Science*, 321:53–57, 2008.

Thomas Klausberger, Peter J. Magill, László F. Márton, J. David B. Roberts, Philip M. Cobden, György Buzsáki, and Peter Somogyi. Brain-state- and cell-type-specific firing of hippocampal interneurons *in vivo*. *Nature*, 421:844–848, 2003.

Thomas Klausberger, László F Márton, Agnes Baude, J David B Roberts, Peter J Magill, and Peter Somogyi. Spike timing of dendrite-targeting bistratified cells during hippocampal network oscillations *in vivo*. *Nat. Neurosci.*, 7:41–47, 2004.

Thomas Klausberger, Laszlo F. Marton, Joseph O'Neill, Jojanneke H. J. Huck, Yannis Dalezios, Pablo Fuentealba, Wai Yee Suen, Edit Papp, Takeshi Kaneko, Masahiko Watanabe, Jozsef Csicsvari, and Peter Somogyi. Complementary roles of cholecystokinin- and parvalbumin-expressing GABAergic neurons in hippocampal network oscillations. *J. Neurosci.*, 25:9782–9793, 2005.

R Klee, E Ficker, and U Heinemann. Comparison of voltage-dependent potassium currents in rat pyramidal neurons acutely isolated from hippocampal regions ca1 and ca3. *Journal of neurophysiology*, 74:1982–1982, 1995.

Michael M Kohl and Ole Paulsen. The roles of gaba b receptors in cortical network activity. *Advances in pharmacology*, 58:205–229, 2010.

C. Köhler. Intrinsic projections of the retrohippocampal region in the rat brain. I. the subicular complex. *J. Comp. Neurol.*, 236(4):504–522, 1985.

Jan Konopacki, M Bruce MacIver, Brian H Bland, and Sheldon H Roth. Carbachol-induced eeg thetaactivity in hippocampal brain slices. *Brain research*, 405(1):196–198, 1987.

Nancy Kopell, Mark A Kramer, Paola Malerba, and Miles A Whittington. Are different rhythms good for different functions? *Frontiers in human neuroscience*, 4, 2010.

T. Kosaka, K. Kosaka, K. Tateishi, Y. Hamaoka, N. Yanaihara, J.-Y. Wu, and K. Hama. GABAergic neurons containing CCK-8-like and/or VIP-like immunoreactivities in the rat hippocampus and dentate gyrus. *J Comp Neurol*, 239:420–430, 1985.

T. Kosaka, H. Katsumaru, K. Hama, J.-Y. Wu, and C.W. Heizmann. GABAergic neurons containing the Ca2+-binding protein parvalbumin in the rat hippocampus and dentate gyrus. *Brain Res*, 419:119–130, 1987.

T. Kosaka, J.-Y. Wu, and R. Benoit. GABAergic neurons containing somatostatin-like immunoreactivity in the rat hippocampus and dentate gyrus. *Exp Brain Res*, 71:388–398, 1988.

Tomasz Kowalczyk, Renata Bocian, and Jan Konopacki. The generation of theta rhythm in hippocampal formation maintained in vitro. *European Journal of Neuroscience*, 37(5): 679–699, 2013.

Esther Krook-Magnuson, Lillian Luu, Sang-Hun Lee, Csaba Varga, and Ivan Soltesz. Ivy and neurogliaform interneurons are a major target of μ-opioid receptor modulation. *The Journal of Neuroscience*, 31(42):14861–14870, 2011.

Jeehyun Kwag and Ole Paulsen. The timing of external input controls the sign of plasticity at local synapses. *Nature neuroscience*, 12(10):1219–1221, 2009.

B Lancaster, RA Nicoll, and DJ Perkel. Calcium activates two types of potassium channels in rat hippocampal neurons in culture. *The Journal of neuroscience*, 11(1):23–30, 1991.

Damien Lapray, Balint Lasztoczi, Michael Lagler, Tim James Viney, Linda Katona, Ornella Valenti, Katja Hartwich, Zsolt Borhegyi, Peter Somogyi, and Thomas Klausberger. Behavior-dependent specialization of identified hippocampal interneurons. *Nat. Neurosci.*, ?:?, 2012.

Ramon Latorre, Andres Oberhauser, Pedro Labarca, and Osvaldo Alvarez. Varieties of calcium-activated potassium channels. *Annual Review of Physiology*, 51(1):385–399, 1989.

M.G. Lee, J.J. Chrobak, A. Sik, R.G. Wiley, and G. Buzsaki. Hippocampal theta activity following selective lesion of the septal cholinergic system. *Neuroscience*, 62(4):1033 – 1047, 1994.

Sang-Hun Lee, Csaba F́oldy, and Ivan Soltesz. Distinct endocannabinoid control of GABA release at perisomatic and dendritic synapses in the hippocampus. *J. Neurosci.*, 30:7993–8000, 2010.

Sang-Hun Lee, Ivan Marchionni, Marianne Bezaire, Csaba Varga, Nathan Danielson, Matthew Lovett-Barron, Attila Losonczy, and Ivan Soltesz. Parvalbumin-positive basket cells differentiate among hippocampal pyramidal cells. *Neuron*, 2014.

Bradley C Lega, Joshua Jacobs, and Michael Kahana. Human hippocampal theta oscillations and the formation of episodic memories. *Hippocampus*, 22(4):748–761, 2011.

Bradley C Lega, Joshua Jacobs, and Michael Kahana. Human hippocampal theta oscillations and the formation of episodic memories. *Hippocampus*, 22(4):748–761, 2012.

L Stan Leung and Bixia Shen. Gabab receptor blockade enhances theta and gamma rhythms in the hippocampus of behaving rats. *Hippocampus*, 17(4):281–291, 2007.

X-G Li, P. Somogyi, J. M. Tepper, and G. Buzsáki. Axonal and dendritic arborization of an intracellularly labeled chandelier cell in the CA1 region of rat hippocampus. *Exp. Brain Res.*, 90:519–525, 1992.

X.-G. Li, P. Somogyi, Dr. A. Ylinen, and G. Buzsáki. The hippocampal ca3 network: An in vivo intracellular labeling study. *J. Comp. Neurol.*, 339:181–208, 1994.

Cheng-Chang Lien and Peter Jonas. Kv3 potassium conductance is necessary and kinetically optimized for high-frequency action potential generation in hippocampal interneurons. *The Journal of neuroscience*, 23(6):2058–2068, 2003.

Evgueniy V Lubenov and Athanassios G Siapas. Hippocampal theta oscillations are travelling waves. *Nature*, 459(7246):534–539, 2009.

Gianmaria Maccaferri. Stratum oriens horizontal interneurone diversity and hippocampal network dynamics. *J. Physiol.*, 562:73–80, 2005.

Gianmaria Maccaferri, J. David, B. Roberts, Peter Szucs, Carol A. Cottingham, and Peter Somogyi. Cell surface domain specific postsynaptic currents evoked by identified GABAergic neurones in rat hippocampus *in vitro*. *J. Physiol.*, 524:91–116, 2000.

Jeffrey C Magee. Dendritic hyperpolarization-activated currents modify the integrative properties of hippocampal ca1 pyramidal neurons. *The Journal of neuroscience*, 18(19):7613–7624, 1998.

Jeffrey C. Magee and Erik P. Cook. Somatic EPSP amplitude is independent of synapse location in hippocampal pyramidal neurons. *Nat. Neurosci.*, 3:895–903, 2000.

Zachary F. Mainen, Jasdan Joerges, John R. Huguenard, and Terrence J. Sejnowski. A model of spike initiation in neocortical pyramidal neurons. *Neuron*, 15(6):1427–1439, December 1995. ISSN 08966273. doi: 10.1016/0896-6273(95)90020-9. URL `http://www.sciencedirect.com/science/article/pii/0896627395900209`.

Ferenc Mátyás, Tamas F. Freund, and Attila I. Gulyás. Convergence of excitatory and inhibitory inputs onto CCK-containing basket cells in the CA1 area of the rat hippocampus. *European Journal of Neuroscience*, 19:1243–1256, 2004.

M. Megías, Zs. Emri, T.F. Freund, and A.I. Gulyás. Total number and distribution of inhibitory and excitatory synapses on hippocampal CA1 pyramidal cells. *Neuroscience*, 102:527–540, 2001.

S. Melzer, M. Michael, A. Caputi, M. Eliava, E.C. Fuchs, M.A. Whittington, and H. Monyer. Long-range-projecting GABAergic neurons modulate inhibition in hippocampus and entorhinal cortex. *Science*, 335(6075):1506–1510, 2012.

Alexia E Metz, Tim Jarsky, Marco Martina, and Nelson Spruston. R-type calcium channels contribute to afterdepolarization and bursting in hippocampal CA1 pyramidal neurons. *The Journal of neuroscience : the official journal of the Society for Neuroscience*, 25(24):5763–73, June 2005. ISSN 1529-2401. doi: 10.1523/JNEUROSCI.0624-05.2005. URL `http://www.jneurosci.org/content/25/24/5763?ijkey=d8e5c52dea199141b6f797da6aef6b485505cdad&keytype2=tf_ipsecsha`.

M Migliore, EP Cook, DB Jae, DA Turner, and D Johnston. Computer simulations of morphologically reconstructed ca3 hippocampal neurons. *Journal of neurophysiology*, 73 (3), 1995.

Michele Migliore, DA Hoffman, JC Magee, and D Johnston. Role of an a-type k+ conductance in the back-propagation of action potentials in the dendrites of hippocampal pyramidal neurons. *Journal of computational neuroscience*, 7(1):5–15, 1999.

Richard Miles, Katalin Tóth, Attila I Gulyás, Norbert Hájos, and Tamas F Freund. Differences between somatic and dendritic inhibition in the hippocampus. *Neuron*, 16:815–823, 1996.

Toshio Miyashita and Kathleen S Rockland. GABAergic projections from the hippocampus to the retrosplenial cortex in the rat. *Euro J Neurosci*, 26(5):1193–1204, 2007.

K. Mizuseki, K. Diba, E. Pastalkova, and G. Buzsaki. Hippocampal CA1 pyramidal cells form functionally distinct sublayers. *Nat Neurosci*, 14:1174–1181, 2011a.

K. Mizuseki, K. Diba, E. Pastalkova, and G. Buzsaki. Hippocampal CA1 pyramidal cells form functionally distinct sublayers. *Nat Neurosci*, 14:1174–1181, 2011b.

Kenji Mizuseki, Anton Sirota, Eva Pastalkova, and György Buzsáki. Theta oscillations provide temporal windows for local circuit computation in the entorhinal-hippocampal loop. *Neuron*, 64:267–280, 2009.

E Moczydlowski and R Latorre. Gating kinetics of ca2+-activated k+ channels from rat muscle incorporated into planar lipid bilayers. evidence for two voltage-dependent ca2+ binding reactions. *The Journal of general physiology*, 82(4):511–542, 1983.

P Monmaur and P Breton. Elicitation of hippocampal theta by intraseptal carbachol injection in freely moving rats. *Brain research*, 544(1):150–155, 1991.

Sean M Montgomery, Martha I Betancur, and György Buzsáki. Behavior-dependent coordination of multiple theta dipoles in the hippocampus. *The Journal of Neuroscience*, 29(5): 1381–1394, 2009.

Robert J Morgan and Ivan Soltesz. Nonrandom connectivity of the epileptic dentate gyrus predicts a major role for neuronal hubs in seizures. *Proceedings of the National Academy of Sciences*, 105(16):6179–6184, 2008.

Florian Mormann, Hannes Osterhage, Ralph G Andrzejak, Bernd Weber, Guillén Fernández, Juergen Fell, Christian E Elger, and Klaus Lehnertz. Independent delta/theta rhythms in the human hippocampus and entorhinal cortex. *Frontiers in human neuroscience*, 2, 2008.

David D Mott and Darrell V Lewis. Facilitation of the induction of long-term potentiation by gabab receptors. *Science*, 252(5013):1718–1720, 1991.

WH Mulders, MJ West, and L Slomianka. Neuron numbers in the presubiculum, parasubiculum, and entorhinal area of the rat. *J. Comp. Neurol.*, 385:83–94, 1997.

Guilherme Neves, Sam F Cooke, and Tim VP Bliss. Synaptic plasticity, memory and the hippocampus: a neural network approach to causality. *Nature Reviews Neuroscience*, 9 (1):65–75, 2008.

T. Nomura, T. Fukuda, Y. Aika, C.W. Heizmann, P.C. Emson, T. Kobayashi, and T. Kosaka. Distribution of nonprincipal neurons in the rat hippocampus, with special reference to their dorsoventral difference. *Brain Res*, 751:64–80, 1997a.

T. Nomura, T. Fukuda, Y. Aika, C.W. Heizmann, P.C. Emson, T. Kobayashi, and T. Kosaka. Laminar distribution of non-principal neurons in the rat hippocampus, with special reference to their compositional difference among layers. *Brain Res*, 764:197–204, 1997b.

RE Numann, WJ Wadman, and RK Wong. Outward currents of single hippocampal cells obtained from the adult guinea-pig. *The Journal of physiology*, 393(1):331–353, 1987.

Szabolcs Olah, Miklos Fule, Gergely Komlosi, Csaba Varga, Rita Baldi, Pal Barzo, and Gabor Tamás. Regulation of cortical microcircuits by unitary GABA-mediated volume transmission. *Nature*, 461:1278–1281, 2009.

H. Pawelzik, D.I. Hughes, and A.M. Thomson. Physiological and morphological diversity of immunocytochemically defined parvalbumin-and cholecystokinin-positive interneurones in CA1 of the adult rat hippocampus. *J. Comp. Neurol.*, 443(4):346–367, 2002.

Jonathan Platkiewicz and Romain Brette. A threshold equation for action potential initiation. *PLoS computational biology*, 6(7):e1000850, January 2010. ISSN 1553-7358. doi: 10.1371/journal.pcbi.1000850. URL `http://www.pubmedcentral.nih.gov/articlerender.fcgi?artid=2900290&tool=pmcentrez&rendertype=abstract`.

NP Poolos, M Migliore, and D Johnston. Pharmacological upregulation of h-channels reduces the excitability of pyramidal neuron dendrites. *Nat. Neurosci.*, 5:767–774, 2002.

Christopher J. Price, Bruno Cauli, Endre R. Kovacs Akos Kulik, Bertrand Lambolez, Ryuichi Shigemoto, and Marco Capogna. Neurogliaform neurons form a novel inhibitory network in the hippocampal CA1 area. *J. Neurosc.*, 25:6775–6786, 2005.

Christopher J. Price, Ricardo Scott, Dmitri Rusakov, and Marco Capogna. $GABA_B$ receptor modulation of feed-forward inhibition through hippocampal neurogliaform cells. *J. Neurosci.*, 28:6974–6982, 2008.

A.D.H. Ratzliff and I. Soltesz. Differential immunoreactivity for α-actinin-2, an N-methyl-D-aspartate-receptor/actin binding protein, in hippocampal interneurons. *Neuroscience*, 103:337–349, 2001.

Deepak Ropireddy and Giorgio A Ascoli. Potential synaptic connectivity of different neurons onto pyramidal cells in a 3D reconstruction of the rat hippocampus. *Front Neuroinform*, 5, 2011.

Sébastien Royer, Boris V Zemelman, Attila Losonczy, Jinhyun Kim, Frances Chance, Jeffrey C Magee, and Gy'orgy Buzsáki. Control of timing, rate and bursts of hippocampal place cells by dendritic and somatic inhibition. *Nat. Neurosci.*, 15:769–775, 2012.

Ueli Rutishauser, Ian B Ross, Adam N Mamelak, and Erin M Schuman. Human memory strength is predicted by theta-frequency phase-locking of single neurons. *Nature*, 464 (7290):903–907, 2010.

Pankaj Sah. Ca¡ sup¿ 2+¡/sup¿-activated k¡ sup¿+¡/sup¿ currents in neurones: types, physiological roles and modulation. *Trends in neurosciences*, 19(4):150–154, 1996.

Vijayalakshmi Santhakumar, Ildiko Aradi, and Ivan Soltesz. Role of mossy fiber sprouting and mossy cell loss in hyperexcitability: a network model of the dentate gyrus incorporating cell types and axonal topography. *Journal of neurophysiology*, 93(1):437–453, 2005.

F Saraga, CP Wu, L Zhang, and FK Skinner. Active dendrites and spike propagation in multicompartment models of oriens-lacunosum/moleculare hippocampal interneurons. *The Journal of physiology*, 552(3):673–689, 2003.

Calvin J Schneider, Marianne Bezaire, and Ivan Soltesz. Toward a full-scale computational model of the rat dentate gyrus. *Frontiers in neural circuits*, 6, 2012.

Joshua H Siegle and Matthew A Wilson. Enhancement of encoding and retrieval functions through theta phase-specific manipulation of hippocampus. *Elife*, 3:e03061, 2014.

A. Sik, N. Tamamaki, and T.F. Freund. Complete axon arborization of a single CA3 pyramidal cell in the rat hippocampus, and its relationship with postsynaptic parvalbumin-containing interneurons. *Euro. J. Neurosci.*, 5(12):1719–1728, 1993.

A. Sik, M. Penttonen, A. Ylinen, and G. Buzsáki. Hippocampal CA1 interneurons: an in vivo intracellular labeling study. *The Journal of Neuroscience*, 15:6651–6665, 1995.

Attila Sik, Aarne Ylinen, Markku Penttonen, and Gyorgy Buzsáki. Inhibitory ca1-ca3-hilar region feedback in the hippocampus. *Science*, 265:1722 – 1724, 1994.

L. Slomianka, I. Amrein, I. Knuesel, J.C. Sørensen, and D.P. Wolfer. Hippocampal pyramidal cells: the reemergence of cortical lamination. *Brain Struct. Funct.*, 216(4):301–317, 2011.

Vikaas S Sohal and Michael E Hasselmo. Changes in gabab modulation during a theta cycle may be analogous to the fall of temperature during annealing. *Neural computation*, 10(4): 869–882, 1998.

I Soltesz and M Deschenes. Low-and high-frequency membrane potential oscillations during theta activity in ca1 and ca3 pyramidal neurons of the rat hippocampus under ketamine-xylazine anesthesia. *Journal of neurophysiology*, 70:97–97, 1993.

J. Somogyi, A. Baude, Y. Omori, H. Shimizu, S. El Mestikawy, M. Fukaya, R. Shigemoto, M. Watanabe, and P. Somogyi. GABAergic basket cells expressing cholecystokinin contain vesicular glutamate transporter type 3 (VGLUT3) in their synaptic terminals in hippocampus and isocortex of the rat. *Euro J Neurosci*, 19:552–569, 2004.

J. Somogyi, A. Szabo, P. Somogyi, and K. Lamsa. Molecular analysis of ivy cells of the hippocampal CA1 stratum radiatum using spectral identification of immunofluorophores. *Front Neural Circ*, 6, 2012.

P. Somogyi and T. Klausberger. Defined types of cortical interneurone structure space and spike timing in the hippocampus. *J Physiol*, 562:9–26, 2005.

F. Sotty, M. Danik, F. Manseau, F. Laplante, R. Quirion, and S. Williams. Distinct electrophysiological properties of glutamatergic, cholinergic and GABAergic rat septohippocampal neurons: novel implications for hippocampal rhythmicity. *J Physiol*, 551(3):927–943, 2003.

Johan F Storm. Potassium currents in hippocampal pyramidal cells. *Progress in brain research*, 83:161–187, 1990.

Janos Szabadics and Ivan Soltesz. Functional specificity of mossy fiber innervation of GABAergic cells in the hippocampus. *The Journal of Neuroscience*, 29:4239–4251, 2009.

A. Szabo, J. Somogyi, B. Cauli, B. Lambolez, P. Somogyi, and K.P. Lamsa. Calcium-permeable AMPA receptors provide a common mechanism for LTP in glutamatergic synapses of distinct hippocampal interneuron types. *J Neurosci*, 32(19):6511–6516, 2012.

Virag T Takacs, Tamas F Freund, and Attila I Gulyas. Types and synaptic connections of hippocampal inhibitory neurons reciprocally connected with the medial septum. *Euro J Neurosci*, 28(1):148–164, 2008.

Virág T. Takács, Thomas Klausberger, Peter Somogyi, Tamás F. Freund, and Attila I. Gulyás. Extrinsic and local glutamatergic inputs of the rat hippocampal CA1 area differentially innervate pyramidal cells and interneurons. *Hippocampus*, 22:1379–1391, 2012.

Gabor Tamás, Andrea Lorincz, Anna Simon, and Janos Szabadics. Identified sources and targets of slow inhibition in the neocortex. *Science*, 299:1902–1905, 2003.

CD Tesche and J Karhu. Theta oscillations index human hippocampal activation during a working memory task. *Proceedings of the National Academy of Sciences*, 97(2):919–924, 2000.

K. Toth and TF Freund. Calbindin D28k-containing nonpyramidal cells in the rat hippocampus: Their immunoreactivity for GABA and projection to the medial septum. *Neuroscience*, 49(4):793–805, 1992.

L. Tricoire and T. Vitalis. Neuronal nitric oxide synthase expressing neurons: a journey from birth to neuronal circuits. *Front Neural Circ*, 6, 2012.

L. Tricoire, K.A. Pelkey, M.I. Daw, V.H. Sousa, G. Miyoshi, B. Jeffries, B. Cauli, G. Fishell, and C.J. McBain. Common origins of hippocampal ivy and nitric oxide synthase expressing neurogliaform cells. *J Neurosci*, 30:2165–2176, 2010.

Leonid Tyan, Simon Chamberland, Elise Magnin, Olivier Camiré, Ruggiero Francavilla, Linda Suzanne David, Karl Deisseroth, and Lisa Topolnik. Dendritic inhibition provided by interneuron-specific cells controls the firing rate and timing of the hippocampal feedback inhibitory circuitry. *The Journal of Neuroscience*, 34(13):4534–4547, 2014.

NM Van Strien, NLM Cappaert, and MP Witter. The anatomy of memory: an interactive overview of the parahippocampal-hippocampal network. *Nat. Rev. Neurosci.*, 10(4):272–282, 2009.

Csaba Varga, Peyman Golshani, and Ivan Soltesz. Frequency-invariant temporal ordering of interneuronal discharges during hippocampal oscillations in awake mice. *PNAS*, Plus, 2012.

V. Varga, A. Losonczy, B.V. Zemelman, Z. Borhegyi, G. Nyiri, A. Domonkos, B. Hangya, N. Holderith, J.C. Magee, and T.F. Freund. Fast synaptic subcortical control of hippocampal circuits. *Science Sig*, 326(5951):449, 2009.

Imre Vida, Katalin Halasy, Csaba Szinyei, Peter Somogyi, and Eberhard H. Buhl. Unitary IPSPs evoked by interneurons at the stratum radiatum-stratum lacunosum-moleculare border in the CA1 area of the rat hippocampus in vitro. *The Journal of Physiology*, 506: 755–773, 1998.

Vincent Villette, Frédérique Poindessous-Jazat, Axelle Simon, Clément Léna, Elodie Roullot, Brice Bellessort, Jacques Epelbaum, Patrick Dutar, and Aline Stéphan. Decreased rhythmic gabaergic septal activity and memory-associated θ oscillations after hippocampal amyloid-β pathology in the rat. *The Journal of neuroscience*, 30(33):10991–11003, 2010.

Gene V Wallenstein and Michael E Hasselmo. Gabaergic modulation of hippocampal population activity: sequence learning, place field development, and the phase precession effect. *Journal of Neurophysiology*, 78(1):393–408, 1997.

Xiao-Jing Wang. Neurophysiological and computational principles of cortical rhythms in cognition. *Physiological reviews*, 90(3):1195–1268, 2010.

Andrew J Watrous, Itzhak Fried, and Arne D Ekstrom. Behavioral correlates of human hippocampal delta and theta oscillations during navigation. *Journal of Neurophysiology*, 105(4):1747–1755, 2011.

Andrew J Watrous, Darrin J Lee, Ali Izadi, Gene G Gurkoff, Kiarash Shahlaie, and Arne D Ekstrom. A comparative study of human and rat hippocampal low-frequency oscillations during spatial navigation. *Hippocampus*, 23(8):656–661, 2013.

M. J. West, L. Slomianka, and H. J. G. Gundersen. Unbiased stereological estimation of the total number of neurons in the subdivisions of the rat hippocampus using the optical fractionator. *The Anatomical Record*, 231:482–497, 1991.

John H Williams and Julie A Kauer. Properties of carbachol-induced oscillatory activity in rat hippocampus. *Journal of neurophysiology*, 78(5):2631–2640, 1997.

M.P. Witter, A.W. Griffioen, B. Jorritsma-Byham, and J.L.M. Krijnen. Entorhinal projections to the hippocampal CA1 region in the rat: an underestimated pathway. *Neurosci Lett*, 85(2):193–198, 1988.

L Wittner, DA Henze, L Záborszky, and G Buzsáki. Three-dimensional reconstruction of the axon arbor of a CA3 pyramidal cell recorded and filled in vivo. *Brain Struct. Funct.*, 12:75–83, 2007.

W. Woodson, L. Nitecka, and Y. Ben-Ari. Organization of the GABAergic system in the rat hippocampal formation: A quantitative immunocytochemical study. *J. Comp. Neurol.*, 280:254–271, 1989.

F.G. Wouterlood, E. Saldana, and M.P. Witter. Projection from the nucleus reuniens thalami to the hippocampal region: Light and electron microscopic tracing study in the rat with the anterograde tracer Phaseolus vulgaris-leucoagglutinin. *J. Comp. Neurol.*, 296(2):179–203, 1990.

Chiping Wu, Hui Shen, Wah Ping Luk, and Liang Zhang. A fundamental oscillatory state of isolated rodent hippocampus. *The Journal of physiology*, 540(2):509–527, 2002.

Megan S Wyeth, Nianhui Zhang, Istvan Mody, and Carolyn R Houser. Selective reduction of cholecystokinin-positive basket cell innervation in a model of temporal lobe epilepsy. *J Neurosci*, 30(26):8993–9006, 2010.

Aarne Ylinen, Iván Soltész, Anatol Bragin, Markku Penttonen, Attila Sik, and György Buzsáki. Intracellular correlates of hippocampal theta rhythm in identified pyramidal cells, granule cells, and basket cells. *Hippocampus*, 5(1):78–90, 1995.

GLF Yuen and D Durand. Reconstruction of hippocampal granule cell electrophysiology by computer simulation. *Neuroscience*, 41(2):411–423, 1991.